Measurement cell for sound speed in liquids: The 3-way pulse method

THESIS FOR THE DEGREE

MASTER OF SCIENCE
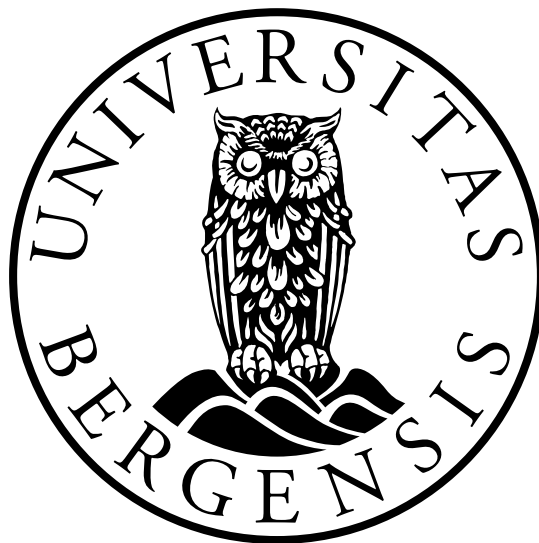
IN

MARINE MEASUREMENT SYSTEMS

ACOUSTICS

BY

JOACHIM GJESDAL KRISTENSEN

DEPARTMENT OF PHYSICS AND TECHNOLOGY

UNIVERSITY OF BERGEN

AUGUST, 2022

Abstract

In the oil and gas industry, high precision sound velocity measurements are vital to estimate the water cut of extracted oils. The water content is of great importance as it plays a crucial part in determining parameters such as production rates and custody transfer [1]. While models such as the UNESCO-algorithm can be used to calculate the sound velocity in water, such models are not always available for oils, as they depend on the exact composition of hydrocarbons. Since water cut is found from accurate sound velocity measurements of the different phases in an emulsion, devices capable of measuring sound velocity with high precision are essential.

In this thesis, a high-precision measurement cell for sound velocity measurements in liquids, with a relative expanded uncertainty limit of 1000 ppm at 95% confidence level, is developed and tested. The measurement cell is based on the 3-way pulse method. Some preferences were set in advance by XSENS Flow Solutions, and have been implemented into the design of the measurement cell.

Sound velocity measurements have been performed on distilled water, saline water at 20, 35 and 50 ppt salinity, respectively, and Exxsol D120 oil. Two signal processing methods; the zerocrossing method (ZCM) and the Fourier spectrum method (FSM) have been utilized, and two different diffraction correction methods have been applied to the measurements. The experimental sound velocities have been compared to modelled sound velocities throughout the project. The best agreement between the experimental and modelled sound velocities was within 628 ppm in distilled water and 744 ppm in saline water. Only the experimental sound velocities found with the ZCM that are corrected for diffraction using Method 2 are within 1000 ppm of the modelled sound velocity across all measurements in this work.

A number of different uncertainty contributors have been identified throughout the project. They are treated in different uncertainty models, and an example uncertainty budget has been carried out for the experimental sound velocity in distilled water at $25^\circ C$. The relative expanded uncertainty at 95% confidence level was found to be 422 ppm. Diffraction correction was found to be the main uncertainty contributor.

Acknowledgment

The present thesis is a cooperation between the Department of Physics and Technology at the University of Bergen and XSENS Flow Solutions. It is devoted to an investigation of the 3-way pulse method in a high precision measurement cell for liquids. The project started in early 2021, but most of the work was carried out between August 2021 and August 2022.

First and foremost, I would like to express my gratitude to my two supervisors Prof. Per Lunde (UiB) and Tarjei Rommetveit (XSENS) for the invaluable guidance they have given me throughout the project. The process would not have been the same without your guidance and support.

A special thanks to Charles Sebastiampillai and the rest of the staff at the mechanical workshop at the Department of Physics and Technology for manufacturing the measurement cell, and helping me whenever problems occurred. Inger Johanne Fjellanger and the Department of Chemistry also deserves my gratitude for providing me with liquid samples and a temperature regulating waterbath for testing - it is greatly appreciated.

Thanks to Everyone in the Acoustics group. Mathias Myrtveit Sæther and Audun Oppedal Pedersen are especially acknowledged for their input with the experimental setup and signal processing methods. Your willingness to help has been vital for this project.

Finally, I would like to thank my amazing family and friends for supporting me throughout the project and keeping me motivated. My years as a student would not have been the same without you.

Joachim Gjesdal Kristensen

Bergen, 08.08.2022

Contents

List of some frequently used symbols

Description	Symbol	Unit
Sound velocity	c	[m/s]
Hydrostatic pressure	P	[bar]
Gauge pressure	P_G	[bar]
Density	ρ	[kg/m^3]
Depth	h	[m]
Salinity	S	[g/l] or ppt
Temperature	T	[°C]
Reference temperature	T_0	[°C]
Transit time of Pulse A	t_A	[s]
Transit time of Pulse B	t_B	[s]
Transit time difference	Δt	[s]
Correction term	t^{corr}	[s]
Transducer distance at temperature T	L	[m]
Transducer distance at temperature T_0	L_0	[m]
Thermal expansion coefficient	K_T	
Linear thermal expansion coefficient	α	[°C^{-1}]
Frequency	f	[Hz]
Angular frequency	ω	[rad/s]
Wave number	k	[m^{-1}]
Time shift due to diffraction correction of Pulse A	t_A^{dif}	[s]
Time shift due to diffraction correction of Pulse B	t_B^{dif}	[s]
Reflection coefficient	R	
Effective transducer radius	a_{eff}	[m]
Half power angle	θ_{3dB}	[rad]

Chapter 1

Introduction

1.1 Background and motivation

Measurements of sound velocity dates all the way back to the 1600s, when naturalist and philosopher Pierre Gassendi measured the sound velocity in air [2, 3]. He used exploding gunpowder to estimate the time delay between the flash of the explosion and the following sound waves [3]. Admittedly, the measured values were about 40% higher than the actual value, but it laid the foundation for more accurate measurements in years to come.

Today, sound velocity measurements can be carried out with associated relative uncertainties as low as 1 ppm in both liquids [4] and gases [5]. Acoustic devices are getting more complex and advanced every year, and the development of accurate signal processing tools is evergrowing. They play an important role in a wide range of fields, such as seismology, SONAR, process control, nondestructive testing, oceanography, medical research and many more.

One of the more acoustic dependent fields is the oil and gas industry. In this sector, acoustic signals with varying frequencies are used to accomplish several duties within production, security, fabrication and more. Low-frequency signals (tens of Hertz) can be used to delineate hydrocarbon reservoirs, mid-frequency signals (thousands of Hertz) are applied in the evaluation of well integrity, and high-frequency signals (hundreds of kilohertz) are vital in characterization of rock fabric and near wellbore stress effects, to mention some [6].

A common instrument used to measure the flow rate of oil is ultrasonic flowmeters, USFMs, which are based on time detection of acoustic signals. For example, USFMs based on transit time measures the time difference between sound waves propagating upstream and downstream in a pipe. The differential transit time is directly proportional to the fluid velocity, which, in turn, is proportional to the flow rate [7]. In recent years, flow meters such as XSENS Flow Solutions' XACT flow rate and fractions meter [8], and Weatherford's ForeSite flowmeter [9], have been developed to measure both flow rate and water cut. During oil extraction, the extracted liquid is never 100% pure oil, but a mixture of crude oils and water. The water content in such oil-water emulsions is of great importance as it plays a crucial part in determining production rates, custody transfer and pipeline oil quality control

[1]. Using acoustic principles, the sound velocity can be measured for each of the different phases of an extracted emulsion, after they have been separated. When the sound velocity of each phase is known, they can be implemented in formulas to measure the water cut, e.g. [10].

Accurate sound velocity measurements of the phases in an emulsion are critical in the estimation of water cut. For water, existing models such as the UNESCO algorithm [11, 12] and Del Grosso's equation [12, 13] can be used to calculate the sound velocity as a function of temperature, pressure and salinity. On the contrary, oils are more complex and the sound velocity is dependent on the exact composition of hydrocarbons. Hence, devices capable of measuring sound velocity with high precision are essential in the estimation of water cut.

In this work, the three-way pulse method, first proposed by Lunde and Vestrheim in 1998 [14], will be applied to a sound velocity measurement cell designed by the author. The measurement cell will later be used by XSENS Flow Solutions to measure the sound velocity of single phase liquids, which, in turn, can be used to measure water cut and the different phases of oil-water mixtures.

1.2 Related work

In the field of measurement technology, there is a wide range of various acoustic measurement cells with the purpose of measuring sound velocity in different media. Each cell has its own design, and a corresponding measurement method based on acoustic principles.

In 1998, a feasibility study was carried out at Christian Michelsen Research to investigate the accuracy and traceability of sound velocity measurements using some candidate methods in a high-precision measurement cell [14]. The study includes a review and evaluation of available literature on existing methods. Norli [15] carried out an updated survey on the topic, including a synthesis of [14]. Although the candidate methods in [14] and [15] are examined based on sound velocity measurements on pressurized gases, many of them are equally applicable for liquids.

One method that was briefly evaluated in the feasibility study is the double pulse method with two reflectors. Kortbeek et al. [16] designed a double-pulse measurement cell consisting of two reflectors at unequal distance from a single edge-supported quartz transducer. The measurement cell was created for measurements in gases, but the same principle can be used for liquids, e.g. [17]. At the start of the measurement procedure, the transducer generates a single pulse which travels in both directions and is reflected at both reflectors. Before the echo from the farthest reflector has propagated back to the transducer, a second pulse is generated. The time difference between generating the first and the second pulse is adjusted such that the longer travelling echo of the first pulse and the shorter travelling echo of the second pulse coincide at reception at the transducer surface. The phase difference between the two echoes can then be used to calculate the sound velocity in the specimen. Kortbeek et al. reported uncertainties down to 200 ppm, using this method [16].

The double-pulse method with two reflectors was later used by e.g. Zhang and Schouten [18] and Benedetto et al. [17]. Zhang and Schouten applied the method to measure the sound velocity of a

mixture of helium and dinitrogen over a temperature span from 157 K to 298 K and at pressures up to 10 kbar. The overall uncertainty in the sound velocity measurements were about 1500 ppm [18]. Benedetto et al. performed a similar experiment, but with pure water over a temperature span from 274 K to 394 K and pressures up to 900 bar. The results were in agreement to within 1000 ppm compared to the IAPWS-95 formulation [19] throughout the temperature and pressure span examined [17].

Papadakis [20] reviewed another popular method, the pulse-echo overlap method, in 1967. The method is based on time detection of pairs of echoes and is considered to be both very versatile and highly accurate [20, 21, 22, 23]. An advantage with this technique is that the transducer is not required to be in direct contact with the specimen. Instead, a buffer rod may be interposed between the transducer and the cavity in which the specimen is to be filled. The pulse-echo overlap method with a buffer rod is widely used due to its simplicity and low cost. It is also relatively robust in regards to high temperature applications since the buffer protects the transducer from the specimen [24].

Nesse [10] made two measurement cells based on the pulse-echo overlap method with a buffer rod for sound velocity measurements in emulsions. Even though the method is capable of handling diffraction correction [20, 22], this was neglected in Nesse's work, and the total uncertainty in the measured sound velocity was found to be 1 m/s. Two of the main uncertainty contributors in this method is potential coherent noise from mode converted waves [25] as well as diffraction effects in the buffer rod [26]. The coherent noise may act as spurious echoes and interfere with the desired signal, resulting in a reduced signal-to-noise ratio. These noise sources may not be a problem in other methods that does not rely on a buffer rod.

A buffer-less method proposed in [14] and [15] is the three-way pulse method, which is the method used for this project. The method differs from many other techniques as it neither includes a buffer rod nor a reflector. Instead, it utilizes two transducers where the transducers themselves acts as reflectors. Only the sample of interest separates them. One of the transducers serves as a transmitting transducer while the other one acts as a receiver. The transmitting transducer generates a pulse which propagates through the sample towards the receiving transducer. Upon impact, part of the signal is transmitted into the receiver, while the rest is reflected back towards the transmitter. The reflected signal is reflected a second time at the surface of the transmitter, before propagating back to the receiver again. The transit time difference between the direct propagating signal and the two-time reflected signal can then be used to calculate the sound velocity. Solberg [27] applied the three-way pulse method to sound velocity measurements in tap water at room temperature. The relative uncertainty of the measurements was found to vary from 800 ppm to 2500 ppm depending on transducer type and diffraction correction method.

The three-way pulse method is one of the two methods in [14] considered to be most promising in regards to achieving the desired accuracy. To the authors knowledge, the method has not been investigated by anyone other than Lunde and Norli et al. [14, 15, 28] and Solberg [27]. The knowledge of this method is thus limited, and the measurement cell used in this work will be developed based on the findings in those articles.

1.3 Objective

The objective of the project is to develop and test a measurement cell for high precision sound velocity measurements in liquids. The measurement cell will be based on the 3-way pulse method, previously described in [14, 15, 27, 28]. A maximum relative expanded uncertainty of 1000 ppm at 95% confidence level is desirable.

Two important criteria were set in connection to the design of the measurement cell. Firstly, the measurement cell should be portable and small in size for easy transportation, and to ensure that the amount of liquid needed for measurements is not excessive. Secondly, the operating frequency should fit the industrial application for XSENS Flow Solutions. After consulting my supervisors, it was concluded that two 500 kHz immersion transducers would be fitting, and a maximum volume of 0.5 l was set for the cavity of the measurement cell.

Sound velocity measurements will be carried out over the temperature range from room temperature to about $45^\circ C$, which is just below the temperature limit of the transducers. The temperature will be regulated with a circulating water bath.

1.4 Thesis outline

The organization of this thesis is described in the following. The present introduction chapter presents background and motivation, some related work and literature, as well as the objective of this thesis. Theory about sound velocity and how the expression for it is derived, along with correction terms, are given in Chapter 2. Chapter 3 provides information on how the measurement cell was designed and explains the setups used for various measurements and calibration. The signal processing methods used in this work are also explained here. All uncertainty models and the respective formulas used for uncertainty calculations for the different parameters are given in Chapter 4. Experimental results of the measured sound velocity and other measured parameters are presented in Chapter 5. In addition, example budgets showing how the uncertainty of the measured sound velocity is calculated are provided throughout the chapter. In Chapter 6, the experimental results are reviewed along with a discussion on the different challenges and problems that occurred during the process. Finally, Chapter 7 gives concluding remarks on the work as a whole and some suggestions for further work.

Chapter 2

Theory

Chapter 2 provides the theoretical background for this work. It is divided into nine sections. Section 2.1 gives a description of the theoretical sound velocity in oils and water, and how they may vary due to change in different parameters. Section 2.2 explains how the sound velocity can be measured using the 3-way pulse method. Correction terms needed to account for non-ideal effects are presented in Section 2.3. Moreover, the sound velocity will be measured at increasing temperatures. Theory regarding the thermal expansion due to the temperature increase is given in Section 2.4. System models and derivation of formulas needed to calculate the sound velocity in the time domain and frequency domain is provided in Section 2.5 and 2.6, respectively. In Section 2.7, the theoretical sound field from ideal transducers are presented, and theory concerning how the effective transducer radius can be found from the actual sound field is given in Section 2.8. Lastly, a short explanation of signal-to-noise ratio is provided in Section 2.9.

2.1 Sound velocity

Sound velocity measurements will be performed on various liquid samples. The properties of the medium affects how the sound velocity changes with parameters such as temperature and pressure. It should also be noted that the concept of sound velocity depends on whether the media is dispersive or nondispersive [14]. For nondispersive media, the sound velocity is independent on frequency, and depends only on the physical properties of the medium. On the contrary, for dispersive media, the sound speed is dependent on frequency, with higher frequencies traveling faster than lower frequencies [29]. This will cause the sound waves to spread out and change shape as they propagate [30]. Also, for dispersive media, the sound velocity can be split into three different velocities: (1) The phase velocity, c_p, (2) the group velocity, c_g, and (3) the signal velocity, c_s [31]. How each of them is measured is briefly explained later.

2.1.1 Sound velocity in water

Sound velocity in water is close to independent on frequency and it is thus assumed that the measured value of c for water is equal to $c = c_p = c_g = c_s$. The three main parameters influencing the speed of sound in water are (1) temperature, (2) pressure and (3) salinity [32, 33]. In this project, reference measurements will be taken on both distilled and saline water. The sound velocity in distilled water is only dependent on temperature and pressure. Kinsler et. al. [29] provide a simplified equation for the sound velocity in distilled water. This equation is independent on salinity and will be used for sound velocity calculations of the distilled water used in this work. The equation is given as [29]

$$c(P_G, t) = 1402.7 + 488t - 482t^2 + 135t^3 + (15.9 + 2.8t + 2.4t^2) \cdot \frac{P_G}{100}, \tag{2.1}$$

where P_G is the gauge pressure in bar and $t = T/100$, with T in degrees Celsius. The uncertainty of Eq. 2.1 is 0.05% for $0 < T < 100°C$ and $0 < P_G < 200$ bar [29]. Gauge pressure is defined as the difference between the hydrostatic pressure, P, where the sound velocity is measured, and the atmospheric pressure, $P_{atm} = 1.01325$ bar [34], i.e.

$$P_G = P - P_{atm}. \tag{2.2}$$

The hydrostatic pressure is given as the sum of the pressure at the surface of the fluid, P_0, and the pressure due to the fluid itself [34], i.e.

$$P = P_0 + \rho g h \cdot 10^{-5}. \tag{2.3}$$

Here, ρ is the density of the fluid, g is the acceleration due to gravity and h is the depth below the surface. The last term is multiplied by 10^{-5} to convert from Pascal to bar. The sound velocity of distilled water is thus a function of both temperature, pressure, density and depth. The gravitational acceleration is assumed to be constant and equal to 9.81 m/s^2 [35].

A more complex equation is needed to describe sound velocity in saline water. Although several algorithms and equations exist, most of them are functions of depth rather than pressure. The two most accepted algorithms that takes pressure as an input are the UNESCO algorithm and the Del Grosso equation. In this work, the UNESCO algorithm is preferred due to its wider validity range for temperature and salinity. It is valid for temperatures between 0 and $40°C$ and salinity between 0 and 40 parts per thousand, for pressures up to 1000 bar [36]. It is also accepted as the International Standard algorithm [36].

The UNESCO algorithm was derived by Chen and Millero [11] in 1977 and recalculated coefficients were found by Wong and Zhu [12] in 1995. It should be noted that the algorithm is empirically derived from sound velocity measurements in *sea* water, while in this work, saline water will be made by mixing the desired amount of salt into distilled water. Hence, minerals and other particles that can be

found in the ocean will not be present in the saline water samples in this project, potentially causing a slight deviation from the UNESCO-algorithm. The UNESCO-algorithm consists of a set of equations and coefficients, and is presented in Appendix D.

The pressure in both Eq. 2.1 and D.1 is dependent on the density of the water. Additionally, the density is dependent on temperature. Thus, an equation describing the density of water as a function of temperature is needed. Fofonoff and Millard (1983) derived an accurate empirical expression describing the density of water as a function of temperature and salinity. It is given by the following equations [37]:

$$
\begin{aligned}
\rho(T, S) = \ & \rho_0 + \left(b_0 + b_1 T + b_2 T^2 + b_3 T^3 + b_4 T^4\right) S + \\
& \left(c_0 + c_1 T + c_2 T^2\right) S^{3/2} + d_0 S^2
\end{aligned}
$$

$$
\rho_0(T) = \ \ a_0 + a_1 T + a_2 T^2 + a_3 T^3 + a_4 T^4 + a_5 T^5,
$$

(2.4)

where T is the temperature in degrees Celsius and S is the salinity in Practical Salinity Units (parts per thousand). The equations are valid for temperatures between 0 and 40$°C$, salinity between 0 and 42 parts per thousand, and pressures up to 10 bar. The numerical values of the coefficients are given in Table 2.1

Table 2.1: Numerical values for the coefficients in Eq. 2.4 [37].

Coefficients	Numerical values	Coefficients	Numerical values
b_0	0.82449	d_0	$4.8314 \cdot 10^{-4}$
b_1	$-4.0899 \cdot 10^{-3}$	a_0	999.842594
b_2	$7.6438 \cdot 10^{-5}$	a_1	$6.793952 \cdot 10^{-2}$
b_3	$-8.2467 \cdot 10^{-7}$	a_2	$-9.095290 \cdot 10^{-3}$
b_4	$5.3875 \cdot 10^{-9}$	a_3	$1.001685 \cdot 10^{-4}$
c_0	$-5.72466 \cdot 10^{-3}$	a_4	$-1.120083 \cdot 10^{-6}$
c_1	$1.0227 \cdot 10^{-4}$	a_5	$6.536332 \cdot 10^{-9}$
c_2	$-1.6546 \cdot 10^{-6}$		

To illustrate how the speed of sound is affected by temperature and salinity, the speed of sound as a function of temperature for salinity values 0 g/liter, 10 g/liter, 20 g/liter, 30 g/liter and 40 g/liter is plotted in Fig. 2.1. A salinity of 1 g/liter is equivalent to 1 ppt.
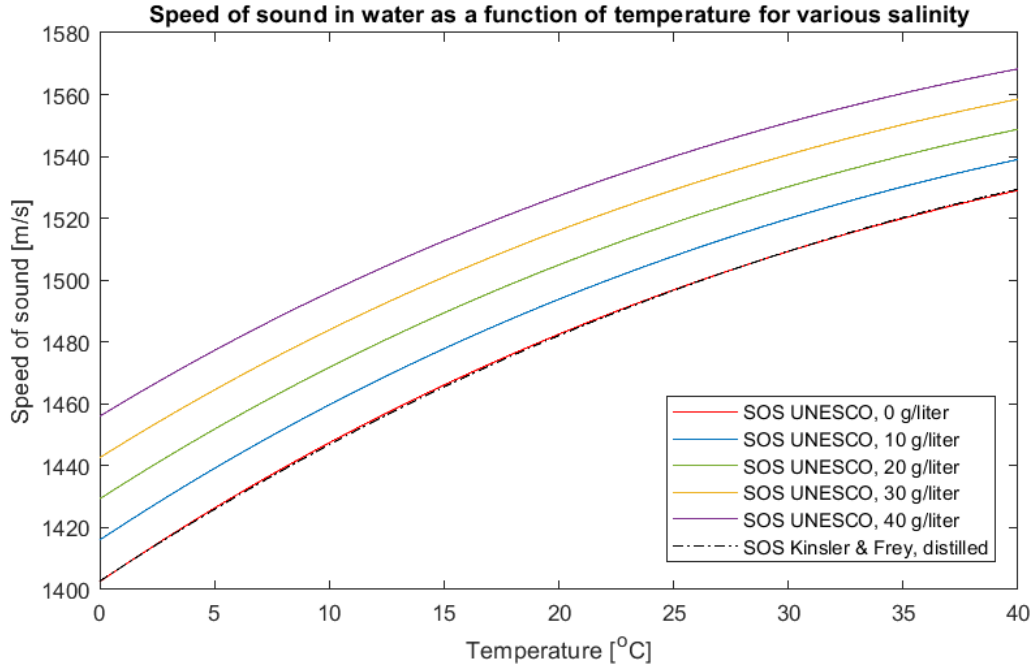
Figure 2.1: Calculated speed of sound (SOS) at depth $h = 3.0$ cm as a function of temperatures between 0 and $40°C$ for salinity values of 0 g/liter, 10 g/liter, 20 g/liter, 30 g/liter and 40 g/liter. The pressure at the surface of the water is set to 1.020 bar.

As some water will evaporate during measurements, a slight increase in salinity over time may be observed. The salinity at the start of an experiment may thus be less than the salinity at the end of the same experiment. An increase in salinity results in an increase in density, which in turn entails a higher pressure at a given depth, and thus, a corresponding increase in sound velocity at this depth. The evaporation rate is given as [38]

$$g_s = \frac{\theta A (x_s - x)}{3600},$$
(2.5)

where A is the surface area of the water, x_s is the maximum humidity ratio of saturated air (at the same temperature as the water surface) and x is the current humidity ratio of the air. θ is the evaporation coefficient given by [38]

$$\theta = (25 + 19\nu),$$
(2.6)

where ν is the velocity of the air above the measurement cell.

It should be noted that both Eq. 2.1 and D.1 are found empirically. Neither can be stated as "theoretically" correct as they are not derived from theory. Hence, sound velocities calculated from the models presented above will be referred to as *modelled* sound velocities throughout the rest of the project.

2.1.2 Sound velocity in oils

In contrary to water, the speed of sound in oils can be heavily dependent on frequency. Consequently, the phase velocity c_p, the group velocity c_g and the signal velocity c_s in oils will not necessarily be equal. For such dispersive media, it can therefore be challenging to measure the speed of sound, as different results may be obtained depending on where time detection is taken in the pulse. If the pulse is long enough to contain a steady state region, time detection in this part of the pulse will give the *phase* velocity at the carrier frequency [14]. Further, the *group* velocity can be found through time detection of the envelope of the pulse. It is the propagation velocity of a group of sound waves that differ somewhat in frequency [14]. Lastly, the *signal* velocity can be measured with time detection of the true signal onset. However, this would demand a high signal-to-noise ratio and a large bandwidth as the first period of the pulse often has a low amplitude. If the SNR is low, time detection of the true signal onset could potentially be deviating, causing the resulting signal velocity to be inaccurate [14]. It should be noted that the considerations made in [14] are made for gas, and conditions for sound velocity measurements in liquids are often better. There is usually less dispersion in liquids, and the absorption coefficient is generally lower in liquids than in gases [39]. This causes greater signal-to-noise ratios in liquids, making it easier to detect the signal onset than in gases [40].

The sound velocity of different crude oils are to be measured for various temperatures. The term "crude oil" includes all unrefined liquid petroleum products containing different hydrocarbon chains of different molecular weight [41]. The oils can vary in composition and purity, and various hydrocarbons in a given oil may have different boiling points. This has to be taken into consideration when heating an oil sample, as the hydrocarbons with the lowest boiling point may start to evaporate, causing a potential change in the acoustic properties during measurements.

Crude oils are usually classified based on how heavy they are. They can range anywhere from light to extra heavy, and a widely used classification is the American Petroleum Institute gravity, API gravity [42]. The API gravity is a measure of how heavy an oil is compared to water, and is often the only available specific description of it. The lower the API gravity, the heavier the oil. Equation of state for oils are almost always dependent on the exact composition of the oil, making it difficult to derive a general equation. Despite this, some general observations has been made regarding the sound speed in oils. For example, it is shown that the sound speed is generally greater in oils with lower API gravity [43]. Also, higher temperature and lower pressure cause a lower sound speed [43]. The oil used in this work is Exxsol D120, which has an API gravity of approximately 40° API [44].

2.2 The 3-way pulse method (3PM)

The 3-way pulse method, named 3PM in the following, is an acoustic measurement method that will be used to measure the speed of sound in various media in this project. It was first proposed by Lunde and Vestrheim in 1998 [14], and has later been investigated in [15, 27, 28].

In this method, two acoustic transducers, one transmitter and one receiver, are mounted in a solid

structure surrounding an acoustic cavity to be filled with a sample. The transducers are mounted axially concentric on opposite sides of the structure, separated by a distance L. Fig. 2.2 shows a sketch of the measurement principle with the two transducers and the solid structure.
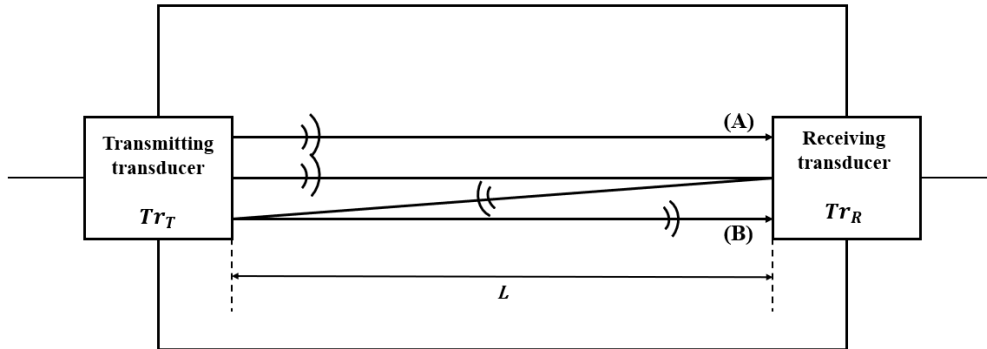
Figure 2.2: Illustration of the principle of the 3PM.

The transmitting transducer, Tr_T, generates an acoustic pulse that propagates to the receiving transducer, Tr_R. Upon impact with the surface of the receiving transducer, a part of the pulse, A, is transmitted into the receiving transducer. Another part, B, is reflected back towards the transmitting transducer, where it is partly reflected again, and then partly received by the receiving transducer. Either the transit time difference or the phase difference between the direct propagating signal and the two-time reflected signal can be used to calculate the sound velocity, c, in the sample. Using the transit time difference, Δt, between the two signals, the equation for c may be written as

$$c = \frac{2L}{\Delta t - t^{corr}},\tag{2.7}$$

where t^{corr} is a correction term accounting for non-ideal effects. The correction term will be explained in the next section. The corresponding equation using the phase difference can easily be found through the relationship

$$\text{time shift} = -\frac{\text{phase shift}}{\omega},\tag{2.8}$$

where ω is the angular frequency of the sound waves. This definition has been used in e.g. [27, 45, 46] to switch between the time domain and frequency domain.

2.3 Correction terms

When performing sound velocity measurements, there will be some non-ideal effects contributing to a time delay in the signals. These effects must be accounted for in order to calculate accurate values for the speed of sound. The main contributors to the time delay are the phase shift due to diffraction effects on reception of the pulses at the receiving transducer, the phase shift due to secondary

acoustic reflections from the interior of the transducers and phase shift due to thermal and viscous boundary layers on the transducer surfaces. These contributors will be discussed in the following subsections.

2.3.1   Diffraction correction

When a transducer generates sound waves, the waves will not propagate like perfectly plane waves. Instead, they will have a curved unfoldment, causing the waves to make impact on the receiving transducer over a finite time period. The center of the receiving transducer will detect the waves first, and some time will pass before the edges of the transducer detects them. The principle is shown in figure 2.3.
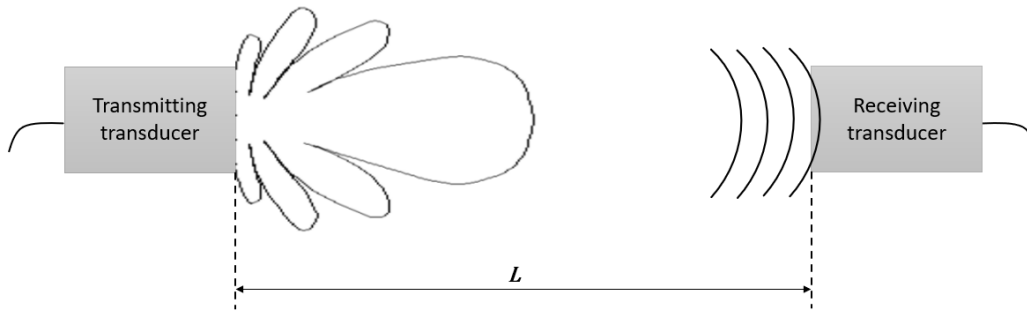
Figure 2.3: Diffraction of sound waves. The waves generated by the transmitting transducer will not be planar, but have a curved shape.

To account for this effect, a diffraction correction term is included when the speed of sound is being estimated. The diffraction correction for Signal A is denoted D_A^{dif} and the diffraction correction for Signal B is denoted D_B^{dif}. D_A^{dif} represents the phase shift due to diffraction effects on reception of the direct propagating pulse at the receiving transducer. D_B^{dif} consists of three terms: (1) phase shift due to diffraction effects on reflection at the receiving transducer, (2) phase shift due to diffraction effects on reflection at the transmitting transducer, (3) phase shift due to diffraction effects on reception of the double-reflected pulse at the receiving transducer. The diffraction correction terms can be written as [47]

$$D_A^{dif} = \frac{\langle p_A \rangle}{p_A^{plane}}, \qquad D_B^{dif} = \frac{\langle p_B \rangle}{p_B^{plane}}, \tag{2.9}$$

where $\langle p_A \rangle$ and $\langle p_B \rangle$ are the averaged free field sound pressure over the surface of the receiving transducer when the receiving transducer is absent, and p_A^{plane} and p_B^{plane} are the plane wave sound pressures at respective axial distances L and $3L$ from the transmitting transducer, for signal A and B respectively. Khimunin [48, 49] investigates the diffraction by introducing a dimensionless distance

$$S = \frac{z\lambda}{a^2} = \frac{2\pi z}{ka \cdot a}. \tag{2.10}$$

Here, z is the axial distance from the surface of the transmitting transducer, λ is the wave length of the sound waves, a is the radius of the transmitting transducer and k is the wave number in the medium. In the following, it is assumed that the transmitting transducer is oscillating like a plane circular piston mounted in a rigid baffle of infinite extent. This way of describing a transducer will hereafter be called "the baffled piston model". Using the baffled piston model, the diffraction correction can be written as a function of the dimensionless distance S and the ka-number [47]. For signal A, this yields

$$D_A^{dif}(S, ka) = 1 - \frac{4}{\pi} \int_0^{\pi/2} e^{-i\frac{(ka)^2 S}{2\pi}\left(\sqrt{1+\left(\frac{4\pi}{S \cdot ka}\right)^2 \cos^2\theta}-1\right)} \sin^2\theta \, d\theta \tag{2.11}$$

which corresponds to the formula Khimunin found from Williams' mathematical description of diffraction. It is important to note that continuous waves are assumed in this approach, and that the diffraction correction thus is dependent on the length of the pulse [50]. The equivalent diffraction correction as a function of distance z and wave number k is given as [47]

$$D_A^{dif}(z, k) = 1 - \frac{4}{\pi} \int_0^{\pi/2} e^{-ikz\left(\sqrt{1+4\left(\frac{a}{z}\right)^2 \cos^2\theta}-1\right)} \sin^2\theta \, d\theta \tag{2.12}$$

For signal B, the sound waves will propagate the same path as in signal A three times. The diffraction due to propagation all three ways must be accounted for, and can be treated in two separate ways [14, 27], labelled "Method 1" and "Method 2" in the following:

1. Method 1: The sound waves are thought to be transmitted "anew" after reflection at each transducer front. This description is illustrated in Fig. 2.4. Here, the time shift, t_B^{dif}, due to diffraction in Signal B, will be three times the time shift, t_A^{dif}, due to diffraction in Signal A. This results in a total time shift due to diffraction of $t^{dif} = t_B^{dif} - t_A^{dif} = 3t_A^{dif} - t_A^{dif} = 2t_A^{dif}$ [14, 27]. This description may be reasonable to use if the width of the main lobe of the sound beam is comparable in size to the front surface of the receiving transducer [14, 51].
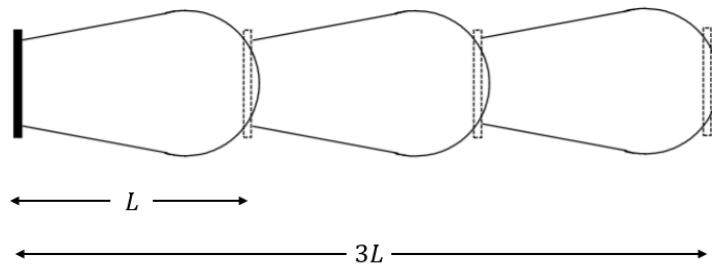
Figure 2.4: Illustration of diffraction for signal B, Method 1. From [27]

2. Method 2: The sound waves are thought to be reflected as if the transducer fronts are mirrors. Fig. 2.5 illustrates how this sound beam would look like if the mirrored images are "unfolded". Here, the diffraction correction for signal B would be the same as the diffraction correction for signal A, if the separation between the transducers were $3L$ [27]. This description may be rea-

sonable to use if the sound beam does not cover the whole surface area on which it is reflected
[40].
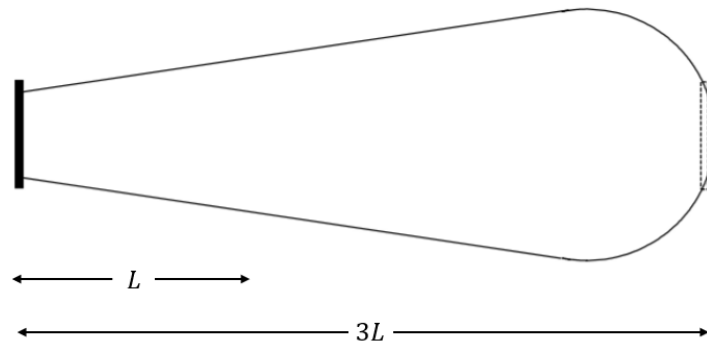
Figure 2.5: Illustration of diffraction for signal B, Method 2. From [27]

The integral in Eq. 2.11 can be solved using numeric methods. Khimunin carried out the modulus
[48] and phase [49] of the diffraction correction on a BESM-4 computer using Simpson's method. The
results of the modulus and phase calculations vs. dimensionless distance S, are given in Appendix
A.1. New and more advanced technology makes it possible to do these calculations more accurately.
Hence, new values for the amplitude and phase of the diffraction correction has been carried out
using Simpson's 1/3 rule with smaller steps in MATLAB. The rule is given by the formula [52]

$$\int_a^b f(x)dx \approx \frac{h}{3}\left(f_0 + f_n + 4\cdot\sum_{i=1,3,5}^{n-1} f_i + 2\cdot\sum_{i=2,4,6}^{n-2} f_i\right), \tag{2.13}$$

where $[a,b]$ is the integration range, h is the segment size and f is the expression to be integrated.
The calculated values are also given in Appendix A.

In Fig. 2.6 and 2.7, the amplitude and phase of the diffraction correction has been plotted against
the dimensionless distance S by implementing Eq. 2.11 in MATLAB, see Appendix E.1.1. The diffrac-
tion correction is shown for five different ka-values, and Simpson's method was used to calculate the
integral.
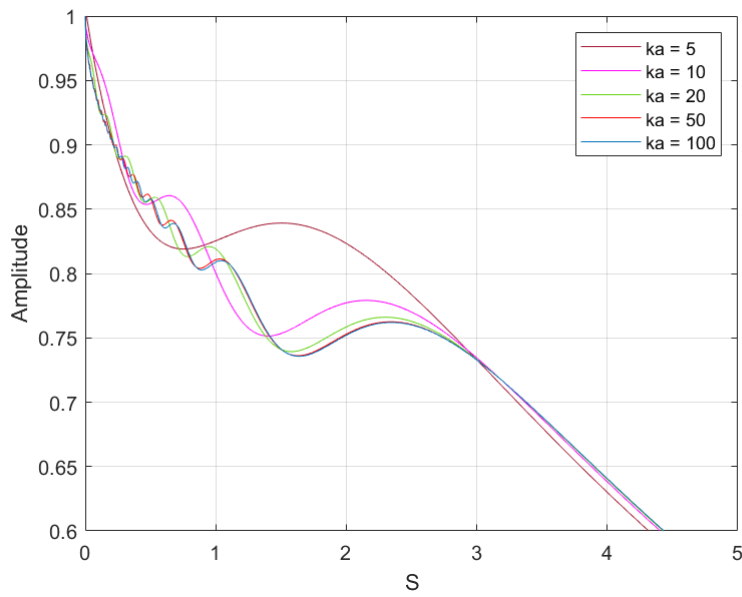
Figure 2.6: Amplitude of the diffraction correction as a function of dimensionless distance S for some ka-values.
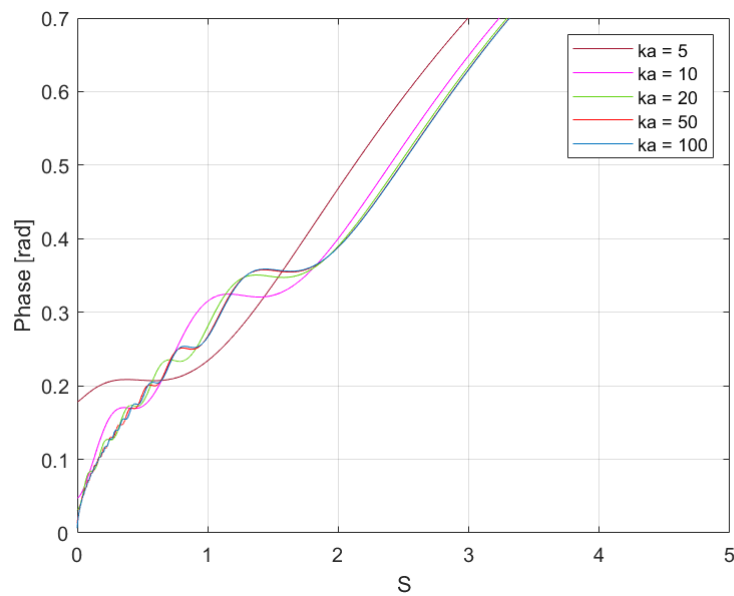
Figure 2.7: Phase of the diffraction correction as a function of dimensionless distance S for some ka-values.

Both the amplitude and the phase of the diffraction correction converges as the distance, S, from the transmitting transducer increases. This is because a receiver will perceive the sound waves as more planar further away from the transmitting transducer. In addition, the diffraction correction in the near field will be more detailed for larger ka-numbers. The fluctuations at low S-values are due to interference from sound waves from different points on the source.

2.3.2   Reflection coefficient for internal transducer reflections

A reflection coefficient is needed for sound velocity calculations due to the propagation path of signal B. Signal B is reflected two times, one time at the surface of the receiving transducer, and another time at the surface of the transmitting transducer, before being detected by the receiving transducer. Upon reflection, a part of the signal will propagate into the transducer, and secondary acoustic reflections from the interior of the transducer may propagate back into the sample and cause a phase shift depending on the impedance difference between the sample and the transducers.

A piezoelectric transducer is a layered medium, often consisting of a backing layer and one or more matching layers who's purpose is to optimize the transmission and reception of signals [53, 54]. For transmitting transducers, an important criteria is usually that the matching layer is chosen such that maximum power is transferred from the piezoelectric element and into the sample [55]. This is achieved when the thickness of the matching layer is 1/4 of the wavelength of the transmitting transducers center frequency [56].

Fig. 2.8 shows three layers: A piezoelectric element with characteristic acoustic impedance z_t, a matching layer with characteristic acoustic impedance z_k and a sample with characteristic acoustic impedance z_0. It can be shown that the specific acoustic impedance, z_{in}, that the sample will experience from the piezoelectric element via the matching layer is given as [55]

$$z_{in} = \frac{\frac{z_t}{z_k} + i \tan(k_k l)}{1 + i(\frac{z_t}{z_k}) \tan(k_k l)} z_k, \tag{2.14}$$

where k_k is the wave number in the matching layer and l is the thickness of the matching layer. The following simplifying assumptions are made:

- The sound waves propagate as plane waves.

- The boundary between each layer is plane.

- All layers are fluids (solids require more extensive treatment, involving mode conversion and shear waves [57]).

To achieve quarter wave matching it is required that the thickness of the matching layer is $l = \frac{\lambda_k}{4}$, or equivalently, $k_k l = \frac{\pi}{2}$. Then, $\tan(k_k l) = \infty$ and the expression for z_{in} can be reduced to

$$z_{in} = \frac{z_k^2}{z_t}. \tag{2.15}$$

In addition to choosing the thickness, l, the characteristic acoustic impedance of the matching layer should be chosen as the geometric mean of z_0 and z_t, i.e.

$$z_k = \sqrt{z_0 z_t}. \tag{2.16}$$

Insertion of Eq. 2.16 into Eq. 2.15 yields

$$z_{in} = \frac{z_0 z_t}{z_t} = z_0.$$

(2.17)

Consequently, the sample will experience a specific acoustic impedance corresponding to the characteristic acoustic impedance of the sample itself, and thus, quarter wave matching is achieved.
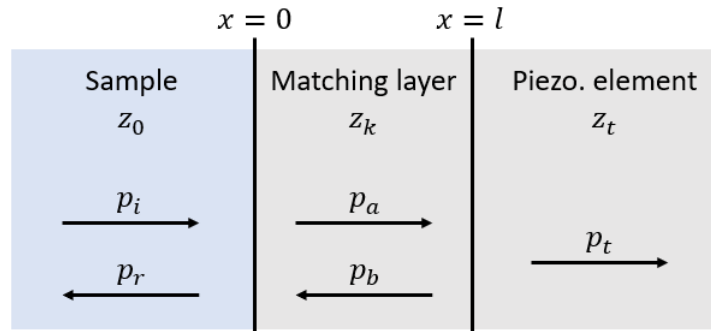
Figure 2.8: Three layers of different material. The two layers in gray are the piezoelectric element and matching layer in the transducer. The layer in blue is the sample. The two boundaries are at $x = 0$ and $x = l$ respectively.

In Fig. 2.8, $p_i = P_i e^{i(\omega t - k_0 x)}$ is the initial incident sound wave where ω is the angular frequency and k_0 is the wavenumber in the sample. This sound wave is split into a reflected part, $p_r = P_r e^{i(\omega t + k_0 x)}$, and a transmitted part, $p_a = P_a e^{i(\omega t - k_k x)}$, upon interaction with the sample-matching layer interface [29]. Similarly, p_a will be split into a reflected part, $p_b = P_b e^{i(\omega t + k_k x)}$, and a transmitted part, $p_t = P_t e^{i(\omega t - k_t x)}$, where k_t is the wavenumber in the piezoelectric element, upon interaction with the matching layer-piezoelectric element interface. p_i, p_r, p_a, p_b, p_t, P_i, P_r, P_a, P_b and P_t are all complex quantities.

If the sound wave is a pulse with length longer than $2l$, interference needs to be accounted for [57]. This is done by using the boundary conditions between the different layers in Fig. 2.8. The boundary conditions are [29]:

- Continuity of acoustic pressure across the boundary.

- Continuity of the normal component of particle velocity across the boundary.

The boundary conditions at $x = 0$ and $x = l$ yields the following two equations [29] :

$$\frac{P_i + P_r}{P_i - P_r} = \frac{z_k}{z_0} \frac{P_a + P_b}{P_a - P_b},$$

(2.18)

$$\frac{P_a e^{-ik_k l} + P_b e^{ik_k l}}{P_a e^{-ik_k l} - P_b e^{ik_k l}} = \frac{z_t}{z_k}.$$

(2.19)

In [57] it is shown how algebraic manipulation of Eq. 2.18 and 2.19 yields the complex pressure reflection coefficient

$$R = \frac{\left(1 - \frac{z_0}{z_t}\right)\cos k_k l + i\left(\frac{z_k}{z_t} - \frac{z_0}{z_k}\right)\sin k_k l}{\left(1 + \frac{z_0}{z_t}\right)\cos k_k l + i\left(\frac{z_k}{z_t} + \frac{z_0}{z_k}\right)\sin k_k l}.$$
(2.20)

The reflection coefficient gives rise to a phase shift $\angle R$ and a corresponding time shift given by

$$t^R = -\frac{\angle R}{\omega}.$$
(2.21)

The transducers used in this work are quarter wave matched to water. Fig. 2.9 shows the magnitude and phase of the complex reflection coefficient as a function of sample impedance, where the following assumptions are made based on [40]:

- The transducer is quarter wave matched to water with impedance 1.5 Mrayl.

- The sound velocity of the matching layer is 3000 m/s.

- The impedance of the piezoelectric element is 33 Mrayl

- The frequency of the sound waves are 500 kHz.

- The piezoelectric element extends infinitely. (The waves transmitted into the piezoelectric element will not be reflected back).
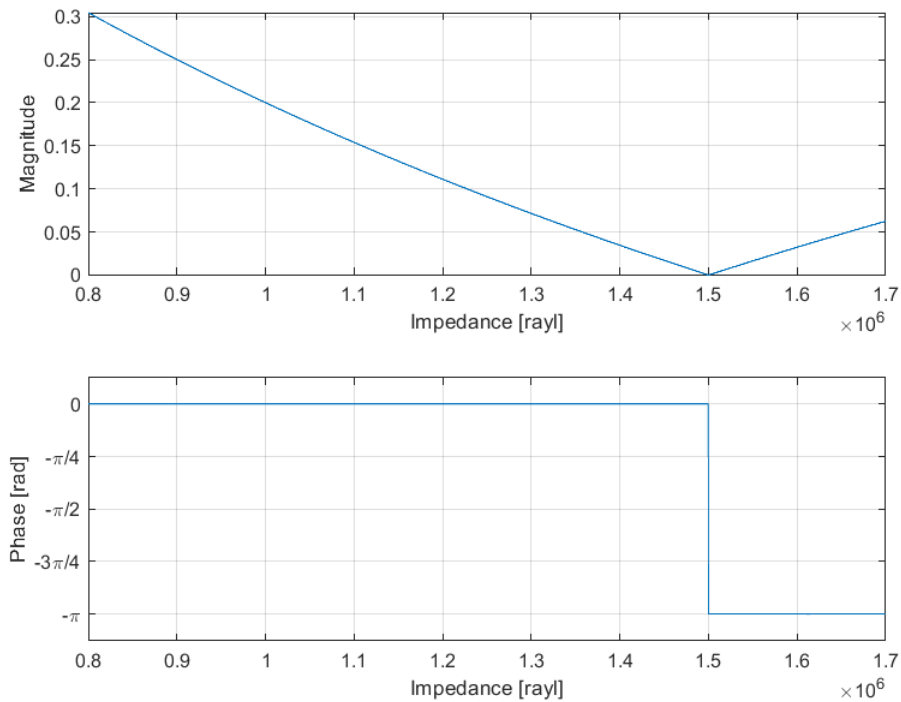
Figure 2.9: Magnitude (top) and phase (bottom) of the complex reflection coefficient as a function of sample impedance. The sound waves are propagating from the sample and into the matching layer which is connected to a piezoelectric element.

From the figures, it is clear that a phase shift of $-\pi$ radians occurs when the sample has an impedance higher than the impedance of water. To illustrate what this implies for the sound waves, a MATLAB-program, developed by Tarjei Rommetveit [40], is utilised. The program uses the complex reflection coefficient to compute the pulse echo response of a 1D layered structure. Fig. 2.10 and 2.11 show how the pulse unfolds when the sample impedance is lower and higher than that of water, respectively. A pulse length of 10 periods is used in both cases.
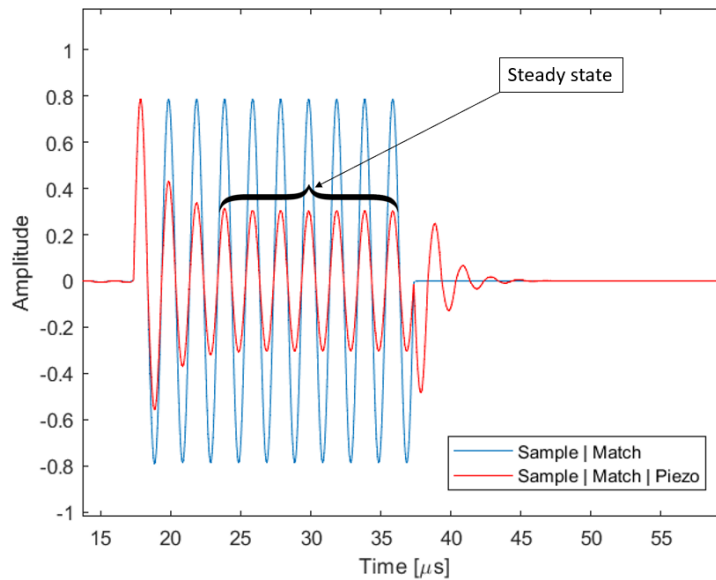
Figure 2.10: Pulse echo response based on the complex reflection coefficient when the sample impedance is 0.8 Mrayl. The assumptions listed above are applied. The pulse length is set to be 10 periods long.
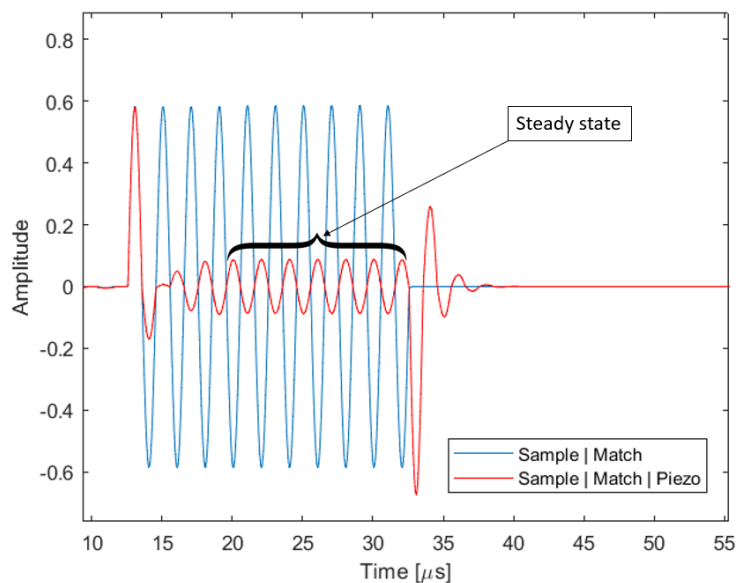
Figure 2.11: Pulse echo response based on the complex reflection coefficient when the sample impedance is 1.8 Mrayl. The assumptions listed above are applied. The pulse length is set to be 10 periods long.

The blue waveform represents the case where there is only two layers: The sample and the matching layer. The matching layer is treated as an infinite half-space, meaning that there will not be any secondary reflections where the transmitted sound waves are reflected back towards the sample. However, if the piezoelectric element is added, the transmitted sound waves will propagate back and forth in the matching layer between the two boundaries. For each reflection at the matching layer-sample boundary, a part of the pulse will be transmitted back into the sample and interfere with the signal of interest. Two things needs to be considered here:

1. The part that is transmitted back into the sample will either be 0 or 180 degrees out of phase with the signal of interest, depending on whether it has been reflected on the matching layer-sample interface an odd or even amount of times.

2. There will be a half wavelength delay for every time the sound waves have travelled back and forth in the matching layer.

These two cases will ensure that every time a part of the pulse is transmitted back into the sample, it is 180 degrees out of phase with the signal of interest. Consequently, the steady state part of the red waveform in Fig. 2.10 has the same phase as the blue waveform, while it is 180 degrees out of phase in Fig. 2.11, due to the sample impedance being lower and higher than 1.5 Mrayl, respectively.

Pulse B will experience two such reflections, one at the receiving transducer, and another at the transmitting transducer, before being detected. The steady state region in Fig. 2.11 will consequently be flipped back into phase at the second reflection. Consequently, the phase shift due to internal transducer reflections can be neglected if the assumptions above are correct. If information about the internal structure of the transducers was available, a more precise analysis of internal transducer reflections could have been carried out. However, such information is confidential, and contributions from internal transducer reflections to the total correction term will thus be omitted in the following.

2.3.3   Thermal and viscous boundary layers

In addition to phase shift due to internal reflections within the transducers, another phase shift will occur when thermal and viscous boundary layers are generated at the front surface of the transducers [14, 27, 58]. These layers arise due to interaction between the liquid medium and the solid transducer surfaces [14]. The thin layer of medium with different impedance causes a slight phase shift and a corresponding time delay upon reflection at the transducer surface. The principle is illustrated in Fig. 2.12. The thickness of the thin boundary layer is exaggerated in the figure. It is also assumed that the sound waves have normal incidence on the transducer surfaces due to them being axially concentric.
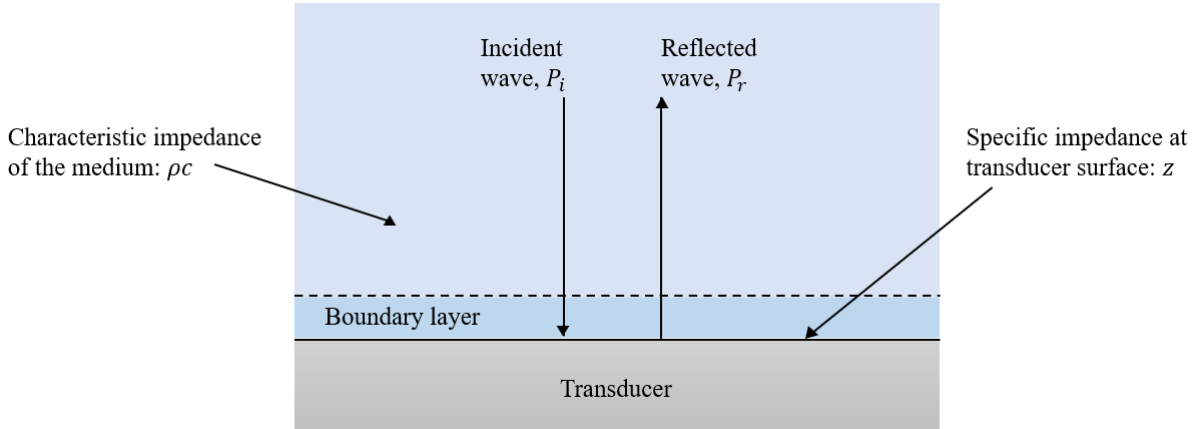
Figure 2.12: Illustration of reflection of a plane wave when thermal conduction and viscosity are taken into account. The transducer is assumed rigid.

The apparent specific admittance of the transducer surface (when thermal and viscous boundary layer effects are taken into account) is given as [58]

$$y = \frac{1}{z} = \frac{e^{-i\pi/4}}{\rho c} \sqrt{\frac{\omega \mu}{\rho c^2}} \frac{\gamma - 1}{\sqrt{Pr}}. \tag{2.22}$$

Here, the transducers are assumed rigid and it is assumed that the sound waves have a normal angle of incidence. z is the apparent specific impedance of the transducer surface, ρ is the density of the sample, c is the sound velocity in the sample, μ is the shear viscosity of the sample and γ is the heat capacity ratio of the sample. Pr is the Prandtl number of the sample and is given by [58]

$$Pr = \frac{\mu c_p}{\kappa}, \tag{2.23}$$

where c_p is the specific heat at constant pressure and κ is the coefficient of thermal conductivity. Solving Eq. 2.22 for z gives the apparent specific impedance of the transducer surface

$$z = e^{i\pi/4} \rho c \sqrt{\frac{\rho c^2}{\omega \mu}} \frac{\sqrt{Pr}}{\gamma - 1}. \tag{2.24}$$

The parameters in this equation depends on the medium and can be found in various tables and reference works, e.g. [10, 29]. Further, the complex pressure reflection coefficient for a plane wave with normal incidence is given by [29]

$$R = \frac{P_r}{P_i} = \frac{z - \rho c}{z + \rho c} \tag{2.25}$$

where P_i is the complex pressure amplitude of the incident wave and P_r is the complex pressure amplitude of the reflected wave. The complex pressure reflection coefficient, where effects from thermal and viscous boundary layers are taken into account, can then be found by inserting Eq. 2.24 into Eq.

2.25. The change in transit time due to these effects is given by

$$t^{bl} = -\frac{\angle R}{\omega} \tag{2.26}$$

In this work, the sound velocity of the sample liquids will be measured for various temperatures. The parameters in Eq. 2.24 are temperature dependent, and will change when the sample is heated. Nesse [10] found whether these parameters will increase or decrease with a small increase in temperature near room temperature. The results are different for water and oils, and are given in Table 2.2. The + sign indicates that the value of the parameter *increases* with increasing temperature, while the - sign indicates that the value of the parameter *decreases* with increasing temperature.

Table 2.2: Overview of the sign of the temperature derivative of the thermophysical parameters in Eq. 2.24 for water and oil near room temperature [10].

Parameters	SI-units	Water	Oil
Density (ρ)	kg/m^3	-	-
Sound speed (c)	m/s	+	-
Shear viscosity (μ)	kg/(m s)	-	-
Heat capacity ratio (γ)	1	+	-
Specific heat at constant pressure (c_p)	J/(kg K)	-	+
Thermal conductivity (κ)	W/(m K)	+	-

For water, one can find equations and tabulated values for the parameters, and use interpolation or polynomial regression to investigate how the parameters will alter when the temperature is changed. This is not as easy for oils, as such equations and tabulated values may not exist for certain organic liquids. However, these parameters are found at $21.9°C$ for some oils in Tables 4.2 to 4.6 in [10]. The time shifts calculated from these parameters for each oil are listed in Table 2.3.

Table 2.3: Time shift due to thermal and viscous boundary layers for some oils and water. The time shifts are calculated using the tabulated values from Tables 4.2 to 4.6 in [10] and 500 kHz frequency.

Liquid Sample	Time shift, t^{bl} [ps]
Dodecane	37.284
Hexadecane	34.346
Exxsol D80	34.094
Exxsol D100	36.256
Distilled water	1.4528

From the table, it is clear that the time shift in the oils are relatively similar, and greater than the time shift in distilled water. The oil tested in this work is Exxsol D120. Although some of the thermophysical properties for this oil are unavailable, an estimated time shift can be found by comparing available properties with properties of other oils. Several physical properties of Exxsol D120 are simi-

lar to Exxsol D100 [59]. It is thus assumed that the time shift in Exxsol D120 is comparable to the time shift in Exxsol D100. In Section 5.5.2, the diffraction correction is found to be between 0.147μs and 0.541μs, which is much higher than the time shifts presented in Table 2.3. Consequently, time shift due to thermal and viscous boundary layers are assumed negligible in this project.

2.4   Thermal expansion

In this work, sound velocity measurements are to be taken at temperatures ranging from room temperature up to the maximum temperature that the transducers can withstand. When the measurement cell is heated, it will expand with rising temperature, and the expansion will influence the transducer separation distance L. The thermal expansion must be adjusted for and an illustration of this principle is shown in Fig. 2.13. By introducing a thermal expansion coefficient, K_T, together with a transducer distance, L_0, measured at some reference temperature (e.g. at 20° C), the transducer separation distance can be written as

$$L = K_T L_0, \tag{2.27}$$

where the thermal expansion coefficient is [58]

$$K_T = 1 + \alpha_T \Delta T. \tag{2.28}$$

Here, α_T is the linear thermal expansion coefficient of the measurement cell material and $\Delta T = \bar{T} - T_0$ where T is the current temperature and T_0 is the reference temperature at which L_0 was measured. In this work, the measurement cell will be made out of plexiglas. The linear thermal expansion coefficient of plexiglas lies around $\alpha_T = (6.8 - 7.7) \cdot 10^{-5}\,°C^{-1}$ [60, 61, 62] depending on the supplier.
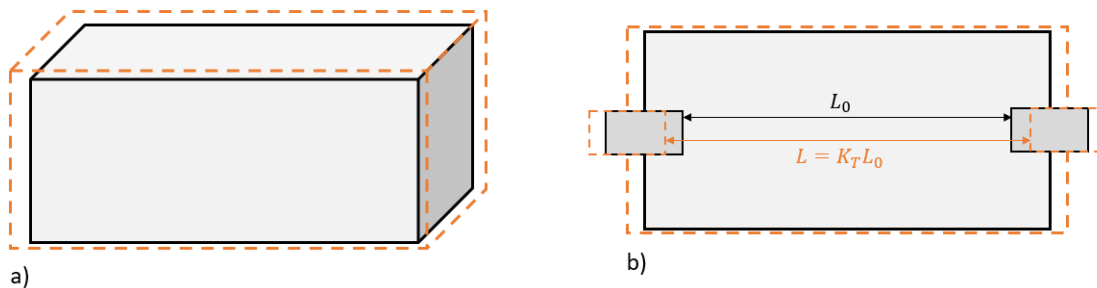
Figure 2.13: Illustration of how the measurement cell will expand when exposed to rising temperatures.

The casing of the transducers used in this project is made of 303 stainless steel [63, 64]. The linear thermal expansion coefficient of 303 stainless steel is approximately $\alpha_T = 1.73 \cdot 10^{-5}°C^{-1}$ [65], which is less than that of plexiglas. Other than that, the exact composition of the transducers are unknown, and thermal expansion of the interior of the transducers is difficult to quantify. Since the transducer

penetration depth is also much less than the length of the measurement cell, thermal expansion of
the transducers is neglected in this work.

2.5   Sound velocity measurements in the time domain

In the time domain, the sound velocity is calculated from measurements of the zerocrossings in Pulse
A and Pulse B, cf. Section 3.7.1. A given zerocross in Pulse A corresponds to the transit time of a given
point in Pulse A. Similarly, a given zerocross in Pulse B corresponds to the transit time of a given point
in Pulse B. The transit time of Pulse A and B is denoted t_A and t_B respectively. They correspond to the
time it takes for the signal to propagate from the signal generator until it is sampled by an oscilloscope,
and are schematically illustrated in Fig. 2.14 and 2.15.
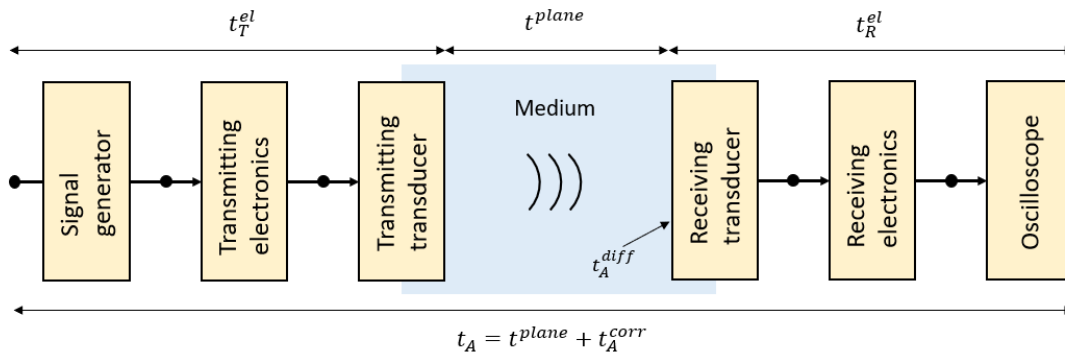
Figure 2.14: Model illustrating signal propagation for signal A.
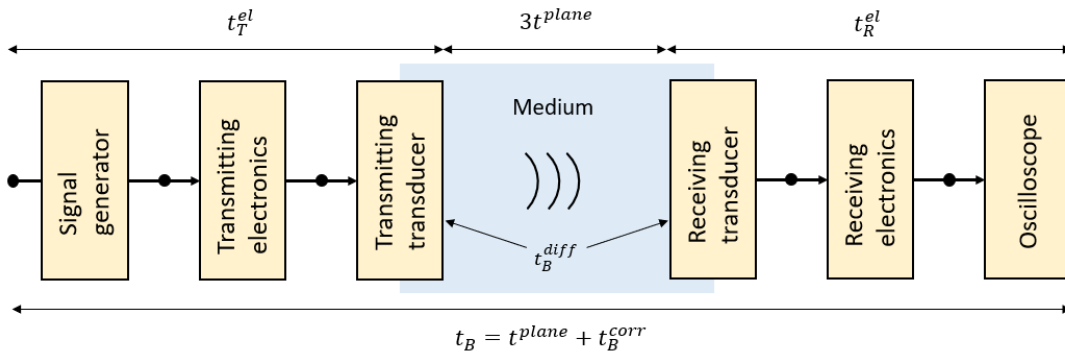
Figure 2.15: Model illustrating signal propagation for signal B.

t_A and t_B consist of several time components, and can be separated into

$$t_A = t^{plane} + t_A^{corr} \tag{2.29}$$

$$t_B = 3t^{plane} + t_B^{corr} \tag{2.30}$$

.

Here, t^{plane} is the plane wave travel time in the medium between the transducers, and t_A^{corr} and t_B^{corr}

are the correction terms for Pulse A and Pulse B, respectively. The correction terms contain all time components in t_A and t_B that are not due to the plane wave travel times. They can be written as

$$t_A^{corr} = t^{el} + t_A^{dif} \tag{2.31}$$

$$t_B^{corr} = t^{el} + t_B^{dif} + t^R + t_B^{bl}. \tag{2.32}$$

Here, $t^{el} = t_T^{el} + t_R^{el}$ where t_T^{el} is the time delay due to the signal generator, the transmitting electronics and the transmitting transducer, and t_R^{el} is the time delay due to the receiving transducer, the receiving electronics and the oscilloscope. In other words, it is the time it takes for the signal to be converted from an emitted voltage by the signal generator to plane wave sound pressure at the centre of the front of the transmitting transducer, plus the time it takes for the signal to be converted from free-field sound pressure at the front of the receiving transducer to a voltage signal that is read and displayed by the oscilloscope. t_A^{dif} is the time delay due to diffraction effects in Signal A. It represents the phase shift due to the diffraction effects on reception of the direct propagating pulse at the receiving transducer. t_B^{dif} is the time delay due to diffraction effects in signal B. It consists of three terms: (1) phase shift due to diffraction effects on reflection at the receiving transducer, (2) phase shift due to diffraction effects on reflection at the transmitting transducer, (3) phase shift due to diffraction effects on reception of the double-reflected pulse at the receiving transducer. The diffraction effects are described in more detail in Section 2.3.1. t^R is the time delay due to secondary acoustic reflections from the interior of the two transducers, and will be omitted in the following, cf. Section 2.3.2. t_B^{bl} is the time delay due to thermal and viscous boundary layers on reflection at the two transducer fronts, and will also be omitted in the following, cf. Section 2.3.3.

With L being the transducer distance and c being the sound speed in the sample, it is clear that

$$t^{plane} = \frac{L}{c}. \tag{2.33}$$

Thus, by using Eqs. 2.29 - 2.33, the sound speed of the medium can be derived as

$$c = \frac{2L}{(t_B - t_A) - (t_B^{dif} - t_A^{dif})}. \tag{2.34}$$

Also, the actual transducer distance is dependent on the temperature of the measurement cell, so the thermal expansion given in Eq. 2.27 must be inserted into equation, i.e.

$$c = \frac{2K_T L_0}{(t_B - t_A) - (t_B^{dif} - t_A^{dif} + t^R)}. \tag{2.35}$$

Defining $\Delta t = t_B - t_A$ and $t^{corr} = t_B^{dif} - t_A^{dif}$, this equation can be rewritten to

$$c = \frac{2K_T L_0}{\Delta t - t^{corr}}, \tag{2.36}$$

which corresponds to Eq. 2.7, but with thermal expansion taken into account.

2.6   Sound velocity measurements in the frequency domain

The complete setup required to measure the sound velocity in the frequency domain is described with block diagrams. Block diagrams split different parts of the measurement system into separate blocks [47]. Assuming the measurement system is a linear time-invariant system, a mathematical description of it can be derived if each block in the block diagrams is described with a transfer function. In this thesis, two block diagrams are needed: One for Pulse A and another for Pulse B. These two block diagrams are shown in Fig. 2.16 and 2.17. This way of representing an acoustic measurement system is described in [47], and has previously been used in e.g. [45, 66, 67].
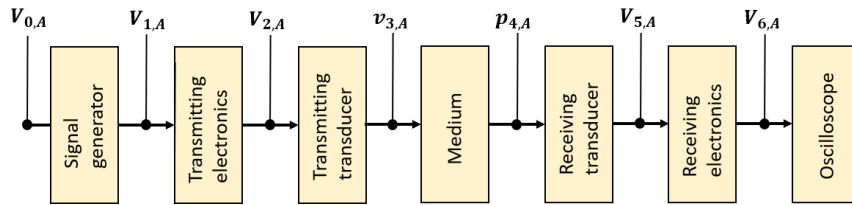
Figure 2.16: System model for Pulse A presented as a block diagram.
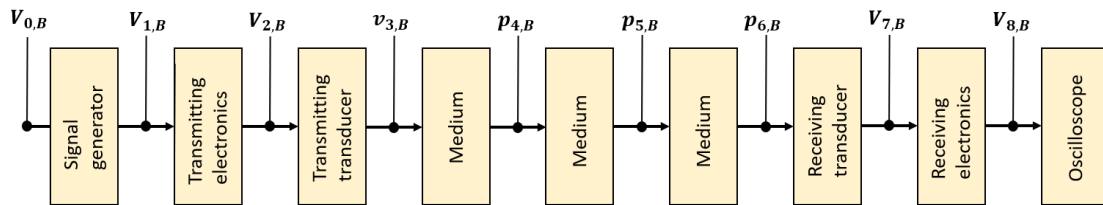
Figure 2.17: System model for Pulse B presented as a block diagram.

A node is defined between each block in the block diagrams. These nodes are used to define a physical quantity that represents the signal at the different "stages" of the measurement process. In the block diagrams shown in Fig. 2.16 and 2.17, there are three different possible physical quantities at the nodes: Voltage, V, on-axis pressure, p, and on-axis particle velocity, v. All variables are in the frequency domain, and the index "A" or "B" indicates whether the variables represents Pulse A or Pulse B. The variables are also indexed with a node number.

The input voltage on the signal generator, transmitting electronics and transmitting transducer is denoted $V_{0,A}$, $V_{1,A}$ and $V_{2,A}$ respectively for Pulse A, and $V_{0,B}$, $V_{1,B}$ and $V_{2,B}$ respectively for Pulse B. Similarly, the output voltage from the receiving transducer and the receiving electronics are denoted $V_{5,A}$ and $V_{6,A}$ respectively for Pulse A, and $V_{7,B}$ and $V_{8,B}$ respectively for Pulse B. For Pulse A, $v_{3,A}$ is the on-axis particle velocity at the front surface of the transmitting transducer, and $p_{4,A}$ is the on-axis free-field pressure at the front surface of the receiving transducer when the receiving transducer is absent. For signal B, $v_{3,B}$ is the on-axis particle velocity at the front surface of the transmitting

transducer, and $p_{6,B}$ is the on-axis free-field pressure at the front surface of the receiving transducer, after three-way propagation, when the receiving transducer is absent. Unlike Pulse A, Pulse B requires two additional pressure variables, $p_{4,B}$ and $p_{5,B}$. This is because Pulse B has propagated the distance between the transmitting and receiving transducer three times, compared to the one time for Pulse A. Thus, $p_{4,B}$ denotes the on-axis free-field pressure at the front surface of the receiving transducer, after one-way propagation, when the receiving transducer is absent. Similarly, $p_{5,B}$ denotes the on-axis free-field pressure at the front surface of the transmitting transducer, after two-way propagation, when the transmitting transducer is absent. For both measurements, it is assumed that the input voltage is the same as the emf of the signal generator. Also, $V_{6,A}$ and $V_{8,B}$ are the measured voltage amplitude of Pulse A and B, respectively, assuming the oscilloscope has an infinite terminal impedance.

The system model for Pulse A and B can mathematically be expressed as

$$V_{6,A} = V_{0,A} \frac{V_{1,A}}{V_{0,A}} \frac{V_{2,A}}{V_{1,A}} \frac{v_{3,A}}{V_{2,A}} \frac{p_{4,A}}{v_{3,A}} \frac{V_{5,A}}{p_{4,A}} \frac{V_{6,A}}{V_{5,A}} \tag{2.37}$$

$$V_{8,B} = V_{0,B} \frac{V_{1,B}}{V_{0,B}} \frac{V_{2,B}}{V_{1,B}} \frac{v_{3,B}}{V_{2,B}} \frac{p_{4,B}}{v_{3,B}} \frac{p_{5,B}}{p_{4,B}} \frac{p_{6,B}}{p_{5,B}} \frac{V_{7,B}}{p_{6,B}} \frac{V_{8,B}}{V_{7,B}} \tag{2.38}$$

This equation for the system model can be slightly modified by modelling the transmitting transducer as a uniformly vibrating, circular piston mounted in a rigid baffle of infinite extent (the baffled piston model). $v_{3,A}$ and $v_{3,B}$ are then the particle velocity across the whole surface of the transmitting transducer, and the description of the wave propagation can be split into two parts: A plane wave and a diffraction correction term. This way of describing the wave propagation has previously been used in e.g. [45, 47, 68]. The modified mathematical expression for the system model includes one extra fraction, $\frac{\langle p_{4,A} \rangle}{p_{4,A}}$ and $\frac{\langle p_{6,B} \rangle}{p_{6,B}}$, on the right hand side of Eq. 2.37 and 2.38 respectively. These fractions corresponds to D_A^{dif} and D_B^{dif} in Eq. 2.9 and represents the diffraction correction for Pulse A and B respectively. The system model can now be written as

$$V_{6,A} = V_{0,A} \frac{V_{1,A}}{V_{0,A}} \frac{V_{2,A}}{V_{1,A}} \frac{v_{3,A}}{V_{2,A}} \frac{p_{4,A}}{v_{3,A}} \frac{\langle p_{4,A} \rangle}{p_{4,A}} \frac{V_{5,A}}{\langle p_{4,A} \rangle} \frac{V_{6,A}}{V_{5,A}} \tag{2.39}$$

$$V_{8,B} = V_{0,B} \frac{V_{1,B}}{V_{0,B}} \frac{V_{2,B}}{V_{1,B}} \frac{v_{3,B}}{V_{2,B}} \frac{p_{4,B}}{v_{3,B}} \frac{p_{5,B}}{p_{4,B}} \frac{p_{6,B}}{p_{5,B}} \frac{\langle p_{6,B} \rangle}{p_{6,B}} \frac{V_{7,B}}{\langle p_{6,B} \rangle} \frac{V_{8,B}}{V_{7,B}} \tag{2.40}$$

or

$$V_{6,A} = V_{0,A} \frac{V_{1,A}}{V_{0,A}} \frac{V_{2,A}}{V_{1,A}} \frac{v_{3,A}}{V_{2,A}} \frac{p_{4,A}}{v_{3,A}} D_A^{dif} \frac{V_{5,A}}{\langle p_{4,A} \rangle} \frac{V_{6,A}}{V_{5,A}} \tag{2.41}$$

$$V_{8,B} = V_{0,B} \frac{V_{1,B}}{V_{0,B}} \frac{V_{2,B}}{V_{1,B}} \frac{v_{3,B}}{V_{2,B}} \frac{p_{4,B}}{v_{3,B}} \frac{p_{5,B}}{p_{4,B}} \frac{p_{6,B}}{p_{5,B}} D_B^{dif} \frac{V_{7,B}}{\langle p_{6,B} \rangle} \frac{V_{8,B}}{V_{7,B}}. \tag{2.42}$$

Here, $\langle p_{4,A} \rangle$ is the *average* incoming free-field pressure across the active surface of the receiving transducer due to Pulse A when the receiving transducer is absent. Similarly, for Pulse B, $\langle p_{6,B} \rangle$ is the *aver-*

age incoming free-field pressure across the active surface of the receiving transducer, after three-way propagation, when the receiving transducer is absent. Moreover, $p_{4,A}$, $p_{4,B}$, $p_{5,B}$ and $p_{6,B}$ denotes the pressure for *plane waves*. This rewriting of the system model is desirable in order to later obtain an expression used for calculating the sound velocity, c, of the medium.

For Pulse A, the transfer function for the medium block can be written as

$$\frac{p_{4,A}}{v_{3,A}} = \frac{e^{-ikL}}{e^{-ik\cdot 0}\frac{1}{\rho c}} = e^{-ikL}\rho c, \tag{2.43}$$

where L is the distance between the transducers and k is the wavenumber of the medium. The time convention $e^{i\omega t}$ is not included in the equation and will be omitted in the following. ρc is needed to convert the velocity to pressure using Euler's equation [29].

Similarly, the transfer function for the three medium blocks for Pulse B can be written as

$$\frac{p_{4,B}}{v_{3,B}}\frac{p_{5,B}}{p_{4,B}}\frac{p_{6,B}}{p_{5,B}} = \frac{p_{6,B}}{v_{3,B}} = \frac{e^{-ikL}Re^{-ikL}Re^{-ikL}}{e^{-ik\cdot 0}\frac{1}{\rho c}} = e^{-3ikL}R^2\rho c \tag{2.44}$$

where R is the plane wave reflection coefficient for the sample-transducer interface [29]. In Section 2.3.2 it was found that, since Pulse B is reflected two times, it does not experience a change in phase due to reflection on the transducer surfaces. Consequently, R is omitted in the following. Eq. 2.43 and 2.44 can be inserted into Eq. 2.41 and 2.42 respectively, giving

$$V_{6,A} = V_{0,A}\frac{V_{1,A}}{V_{0,A}}\frac{V_{2,A}}{V_{1,A}}\frac{v_{3,A}}{V_{2,A}}e^{-ikL}\rho c D_A^{dif}\frac{V_{5,A}}{\langle p_{4,A}\rangle}\frac{V_{6,A}}{V_{5,A}}, \tag{2.45}$$

$$V_{8,B} = V_{0,B}\frac{V_{1,B}}{V_{0,B}}\frac{V_{2,B}}{V_{1,B}}\frac{v_{3,B}}{V_{2,B}}e^{-3ikL}\rho c D_B^{dif}\frac{V_{7,B}}{\langle p_{6,B}\rangle}\frac{V_{8,B}}{V_{7,B}}. \tag{2.46}$$

An expression for c is obtained by first dividing the expression for Pulse B by the expression for Pulse A, i.e.

$$\frac{V_{8,B}}{V_{6,A}} = \frac{V_{0,B}\frac{V_{1,B}}{V_{0,B}}\frac{V_{2,B}}{V_{1,B}}\frac{v_{3,B}}{V_{2,B}}e^{-3ikL}\rho c D_B^{dif}\frac{V_{7,B}}{\langle p_{6,B}\rangle}\frac{V_{8,B}}{V_{7,B}}}{V_{0,A}\frac{V_{1,A}}{V_{0,A}}\frac{V_{2,A}}{V_{1,A}}\frac{v_{3,A}}{V_{2,A}}e^{-ikL}\rho c D_A^{dif}\frac{V_{5,A}}{\langle p_{4,A}\rangle}\frac{V_{6,A}}{V_{5,A}}} \tag{2.47}$$

Assuming that there are no unwanted acoustic reflections, the following transfer functions will cancel out since both Pulse A and B stems from the same generated burst:

- $\frac{V_{1,A}}{V_{0,A}}$ will cancel out $\frac{V_{1,B}}{V_{0,B}}$ because it is the same signal generator for both pulses.

- $\frac{V_{2,A}}{V_{1,A}}$ will cancel out $\frac{V_{2,B}}{V_{1,B}}$ because it is the same transmitting electronics for both pulses.

- $\frac{v_{3,A}}{V_{2,A}}$ will cancel out $\frac{v_{3,B}}{V_{2,B}}$ because it is the same transmitting transducer for both pulses.

- $\frac{V_{5,A}}{\langle p_{4,A}\rangle}$ will cancel out $\frac{V_{7,B}}{\langle p_{6,B}\rangle}$ because it is the same receiving transducer for both pulses.

- $\frac{V_{6,A}}{V_{5,A}}$ will cancel out $\frac{V_{8,B}}{V_{7,B}}$ because it is the same receiving electronics for both pulses.

In addition, $V_{0,A}$ will cancel out $V_{0,B}$ since they are the exact same voltage. Thus, Eq. 2.47 can be reduced to

$$\frac{V_{8,B}}{V_{6,A}} = \frac{e^{-2ikL} D_B^{dif}}{D_A^{dif}}.$$

(2.48)

Now, c can be derived by examining the phase of Eq. 2.48, i.e.

$$\angle \left(\frac{V_{8,B}}{V_{6,A}} \right) = \angle \left(\frac{e^{-2ikL} D_B^{dif}}{D_A^{dif}} \right).$$

(2.49)

This equation can be rewritten to

$$\angle V_{8,B} - \angle V_{6,A} = \angle D_B^{dif} - \angle D_A^{dif} - 2kL.$$

(2.50)

By inserting Eq. 2.27 and $k = \frac{\omega}{c}$, Eq. 2.50 can be solved for c, i.e.

$$c = \frac{2K_T L_0}{\left(-\frac{\angle V_{8,B}}{\omega} + \frac{\angle V_{6,A}}{\omega} \right) - \left(-\frac{\angle D_B^{dif}}{\omega} + \frac{\angle D_A^{dif}}{\omega} \right)}.$$

(2.51)

Defining $\Delta t = -\frac{\angle V_{8,B}}{\omega} + \frac{\angle V_{6,A}}{\omega}$ and $t^{corr} = -\frac{\angle D_B^{dif}}{\omega} + \frac{\angle D_A^{dif}}{\omega}$, this equation can be rewritten to

$$c = \frac{2K_T L_0}{\Delta t - t^{corr}},$$

(2.52)

which corresponds to Eq. 2.7, but with thermal expansion taken into account. The equation above is thus valid in both the time domain and the frequency domain through the relationship in Eq. 2.8.

2.7   Sound field and directivity

Using the baffled piston model to describe the transmitting transducer enables a theoretical description of the ideal sound field generated by the transducer. The actual sound field will be somewhat deviating, but it gives an indication of the approximate directivity function for the transducer. When using the baffled piston model, one can define the far field of the transmitting transducer to be the field where the distance from the transducer is greater than the Rayleigh distance. The Rayleigh distance, r', is given as [29]

$$r' = \frac{\pi a^2 f}{c},$$

(2.53)

where a is the radius of the active surface of the transmitting transducer, f is the frequency and c is the sound velocity of the medium in which the sound waves are propagating. In the far field, the sound pressure is given as the product between the axial pressure amplitude $P_{ax}(r)$ and the directivity term $H(\theta)$ [29], i.e.

$$|\mathbf{p}(r,\theta)| = P_{ax}(r)H(\theta). \tag{2.54}$$

The directivity term, also known as the "Bessel directivity", can be written as [29]

$$H(\theta) = \left|\frac{2J_1(ka\sin\theta)}{ka\sin\theta}\right|, \tag{2.55}$$

where θ is the angle relative to the acoustic axis and J_1 is the first order Bessel function of the first kind. The angular dependence of $H(\theta)$ reveals that there are pressure nodes and pressure maximas in the beam pattern. There will be a main lobe centered on the axis through the center of the transmitting transducer, and several side lobes at different angles θ. An example of the lobe structure from a plane circular piston is shown in figure 2.18.
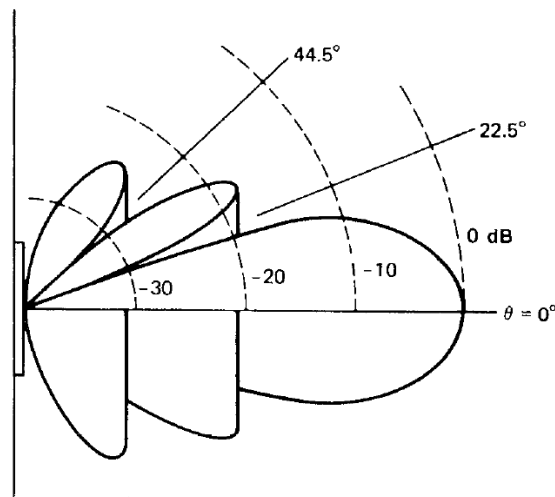
Figure 2.18: Example of beam pattern from a circular plane piston using the baffled piston model. From [29].

The form of the lobes depends on the radius of the radiating piston, the frequency of the sound waves and the sound velocity of the medium in which the sound waves are propagating. It is important to note that the directivity of the receiving transducer will also influence how the generated signal is perceived. Consequently, the directivity of both transducers must be taken into consideration. This can be done by multiplying the directivity of both transducers with each other [69], i.e.

$$H(\theta)_{tot} = H(\theta)_T \cdot H(\theta)_R, \tag{2.56}$$

where $H(\theta)_T$ is the directivity of the transmitting transducer, $H(\theta)_R$ is the directivity of the receiving

transducer and $H(\theta)_{tot}$ is the total directivity. Fig. 2.19 shows the beam pattern as a function of angle relative to the acoustic axis for two identical transducers constituting a transmitter and a receiver. See Appendix E.2.2 for MATLAB-script.
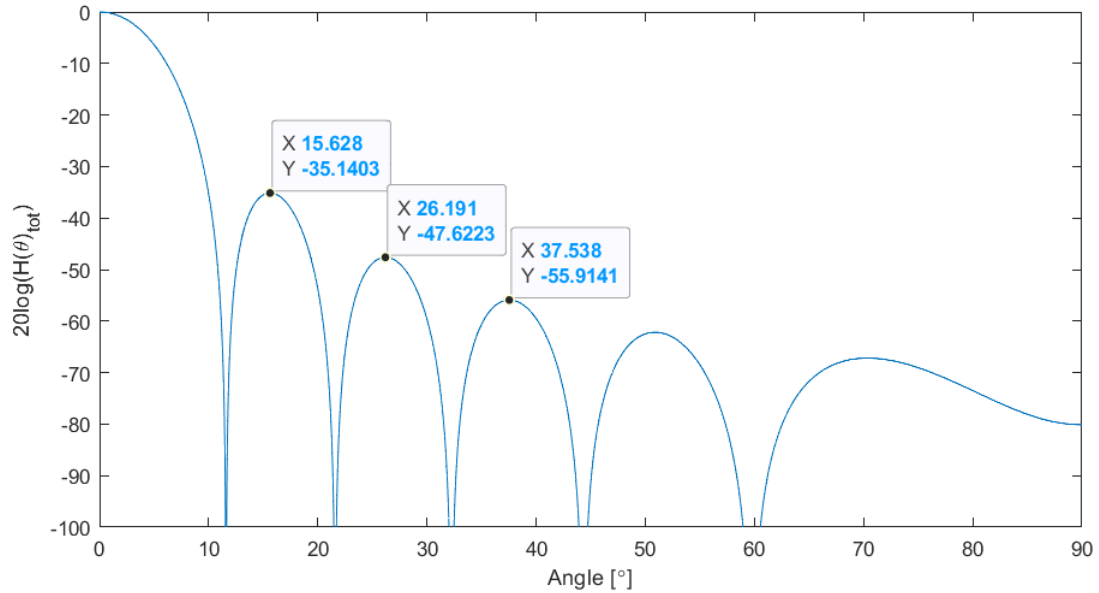
Figure 2.19: Total directivity for two transducers with radius $a = 9.67$ mm and frequency $f = 500$ kHz. The medium is set to be 50 ppt saline water at $60°C$ with sound velocity $c = 1593$ m/s. The dB-level of the peak of the first three side lobes are highlighted with data tips.

2.8 Effective transducer radius

Both transducers used in this work are V318-SU transducers which have the same nominal transducer radius specified by the manufacturer [63, 64]. However, the *effective* transducer radius will vary slightly, as it would be almost impossible to construct two completely identical transducers. Additionally, the baffled piston model assumes that the active surface of the transducers moves uniformly [29]. This is an idealized assumption, and the center and edges of the transducers will in reality oscillate with unequal amplitudes. The nominal transducer radius should thus be replaced with a measured effective transducer radius, a_{eff}, measured from the actual sound field of the transducer.

a_{eff} should be measured for both the transmitting and the receiving transducer, and is obtained by investigating the directivity of the transducers. A common way of doing this is to measure the beam width of the transmitted sound waves [27, 70]. The beam width is defined as the angular separation, in which the magnitude of the radiation pattern decreases by 50% (or -3dB) from the peak of the main lobe. The peak of the main lobe is at the acoustic axis, and the angular separation can be denoted $2\theta_{3dB}$ where θ_{3dB} is the half power angle [69]. This is illustrated in Fig. 2.20.
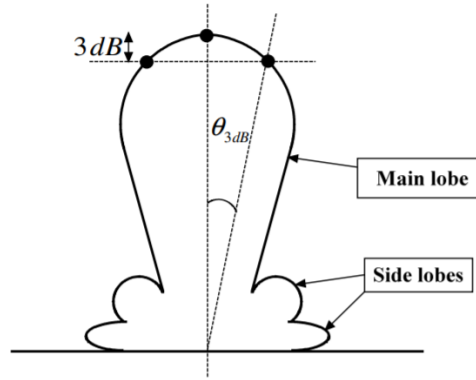
Figure 2.20: Illustration of where θ_{3dB} may be located relative to the peak of the main lobe. From [27].

Using the Bessel function of the first kind of order 1, it can be shown from Eq. 2.55 that the half power angle from a plane circular piston is given as [71]

$$\theta_{3dB} = \sin^{-1}\left(\frac{1.6163}{ka}\right), \tag{2.57}$$

using the baffled piston model. Here, $k = \omega/c$ is known and θ_{3dB} is measured. Thus, the effective transducer radius can be found as

$$a_{eff} = c/\omega \cdot \frac{1.6163}{\sin\theta_{3dB}} \tag{2.58}$$

A hydrophone can be used to find θ_{3dB} by measuring the amplitude of the signal whilst altering the transducer carefully around its front center. The angle where the amplitude has decayed 3 dB is noted and used to calculate a_{eff}. The process is described more thoroughly in Section 3.6.

2.9 Signal-to-noise ratio (SNR)

When measuring the sound velocity, one has to be aware that noise may cause errors in the measurements. Larger noise magnitude may entail a bigger measurement error. Thus, the ratio between the signal and the noise should be kept as high as possible. The signal-to-noise ratio, SNR, is defined as the ratio between the power of the signal to the power of noise, and is commonly specified in decibels as [7]

$$SNR = 10\log_{10}\left(\frac{W_S}{W_N}\right) = 20\log_{10}\left(\frac{V_S^{rms}}{V_N^{rms}}\right) \tag{2.59}$$

where W_S is the power of the signal, W_N is the power of the noise, V_S^{rms} is the root-mean-square voltage of the signal and V_N^{rms} is the root-mean-square voltage of the noise. Noise sources are often divided into incoherent noise and coherent noise. While coherent noise has the same frequency as the signal of interest, but different amplitude and phase, incoherent noise consists of both spatially

and temporal random noise with no definite phase shift relative to the signal of interest [72]. Some examples of potential noise sources are incoherent background noise from all the instruments in the laboratory, coherent noise due to reflections in the side walls of the measurement cell and acoustical cross talk from e.g. vibrations in the measurement cell. The signal-to-noise ratio may be improved through filtering. This is discussed further in Section 3.7.3.

Chapter 3

Experimental setup and measurement methods

Chapter 3 provides a description of the experimental setups and measurement methods used in this work. It is divided into seven sections with some of the sections also containing subsections. Section 3.1 gives a short description of the various instruments included in the measurement setup used for sound velocity measurements. Details about the measurement cell itself and how it was designed is given in Section 3.2. Moreover, considerations regarding the sound field inside the measurement cell are discussed in Section 3.3. Information about the setups and instruments used for temperature and pressure measurements are provided in Sections 3.4 and 3.5, respectively. Further, the setup used to measure the effective transducer radii is presented in Section 3.6. Finally, Section 3.7 explains the two signal processing methods used in this work, namely the zerocrossing method and the Fourier spectrum method, as well as filtering.

3.1 Setup used to measure sound velocity

The sound velocity of a liquid sample is calculated based on the sound waves that propagates back and forth in the medium between the transmitting and receiving transducer in the measurement cell. In short, a signal generator generates an electric signal that is converted to sound waves at the transmitting transducer. The sound waves propagates to the receiving transducer, where they are perceived and converted back to an electrical signal to be sampled by an oscilloscope. The sampled waveform is then imported to MATLAB [73] where the sound velocity is calculated. Fig. 3.1 shows a schematic drawing of all instruments in the measurement setup that are connected together during experiments. The setup is also depicted in Fig. 3.2. Table 3.1 lists all the utilized components.
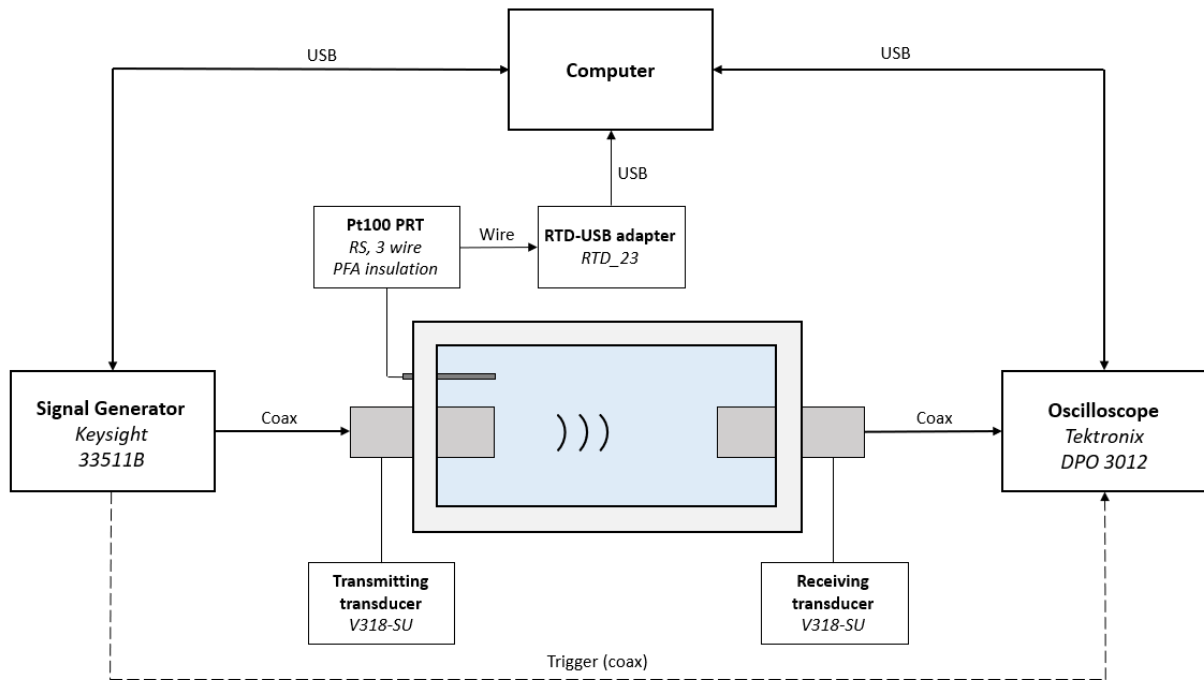
Figure 3.1: Schematic overview of the setup used for measurements. The measurement cell is submerged in a water bath shown in Fig. 3.9.
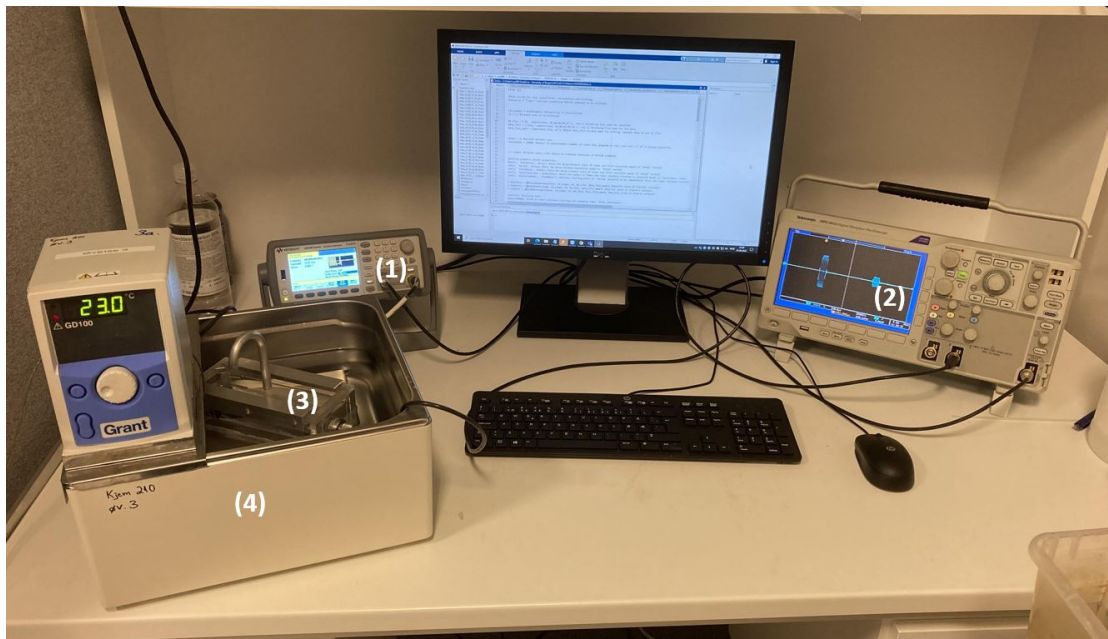
Figure 3.2: Image of the measurement setup. (1) Signal generator, (2) oscilloscope, (3) measurement cell with transducers and temperature probe, (4) water bath. The temperature probe is connected to the computer through a RTD-USB adapter (not shown here).

Table 3.1: List of components used in the setup made for sound velocity measurements.

Component	Manufacturer	Model	Serial Number
Signal Generator	Keysight	33511B	MY57300358
Oscilloscope	Tektronix	DPO 3012	C024018
Transmitting transducer	Olympus	V318-SU	1339737
Receiving transducer	Olympus	V318-SU	1339734
RTD-USB adapter	Dracal	RTD_23	E16381/E18753
Temperature probe	RS	Pt100 PRT	N/A
Water bath	Grant Instruments	GD100	N/A

3.1.1 Transmitting and receiving transducer

Two 500 kHz V318-SU immersion transducers from Olympus [63, 64] are used in this work. The transducers are depicted in Fig. 3.3. One of the transducers serves as a transmitting transducer while the other one serves as a receiving transducer. The transmitting transducer is connected to the signal generator, while the receiving transducer is connected to the oscilloscope. They are connected via coaxial cables with UHF-connectors coupled to the transducers, and BNC-connectors to the signal generator and oscilloscope. The dimensions of the V318-SU transducers are shown in Fig. 3.4.

Figure 3.3: Picture of the two V318-SU transducers used in this work.
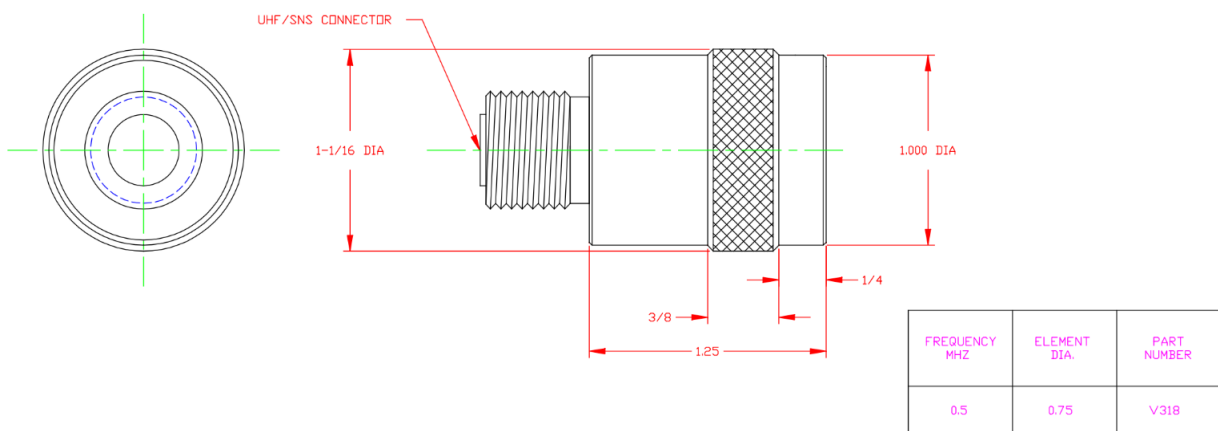
Figure 3.4: Schematic drawing of the dimensions of the V318-SU transducers, provided by a contact person at Olympus [74]. Dimensions are given in inches. The fractions are fractions of 1 inch (25.4 mm).

The *nominal* element diameter of the transducers is specified by the manufacturer to be 19.05 mm. In addition, the element is surrounded by corrosion resistant 303 stainless steel casing [63]. The steel casing affects the sound waves that impacts on the side of the transducers, which is treated in Section 3.3.1. This type of stainless steel has a density of ρ_0 = 8030 kg/m^3 [75] and the sound velocity in the material is c = 5640 m/s [76]. The acoustic impedance of the material is given as [29]

$$z = \rho_0 c = 45.29 \cdot 10^{-6} \, Rayl \tag{3.1}$$

In reality, even if the transducers are of the same kind, the performance can vary significantly. Hence, standard test forms with records of the actual RF waveform and frequency spectrum is provided by the manufacturer [74] for each individual transducer. The test forms includes measurements of the bandwidth, peak and center frequencies and upper and lower -6 dB frequencies. Table 3.2 shows a summary of the specifications for each transducer.

Table 3.2: Technical specifications for the transmitting and receiving transducer. The specifications are retrieved from the certificates provided by the manufacturer [74], given in Appendix B.

Transducer	Serial number	Center frequency	Peak frequency	-6 dB Bandwidth		
				Lower limit	Upper limit	Percentage
V318-SU Transmitter	1339737	0.54 MHz	0.51 MHz	0.32 MHz	0.76 MHz	82.33%
V318-SU Receiver	1339734	0.51 MHz	0.49 MHz	0.30 MHz	0.73 MHz	83.45%

3.1.2 Signal generator

A signal generator is needed in order to generate the signal that will be used to calculate the sound velocity of the sample. In this work, a Keysight 33511B waveform generator is connected to the transmitting transducer, as shown in Fig. 3.1. Additionally, there is a direct connection to the oscilloscope through the "sync" output, serving as a trigger. The signal generator is set to generate sinusoidal bursts of 10 periods. The frequency range of the sine wave is from 1 μHz to 20 MHz with 1 μHz resolution, and the accuracy is $\pm$(1 ppm of set frequency + 15 pHz) for one year at $(23 \pm 5)°C$ [77]. A log of the calibration history for the signal generator is not available. Hence, it is assumed that the instrument was calibrated within the last year. Consequently, the accuracy of the signal generator is assumed to be $\pm$0.5 Hz at room temperature, when driving the transmitting transducer at 500 kHz.

The amplitude range of the signal generator is from 1 mV to 10 V into 50 Ω with 4-digit resolution, and the accuracy of the amplitude is $\pm$(1% of set amplitude in V) $\pm$(1 mV) at $(23 \pm 5)°C$ [77]. The signal generator will be set to generate a signal with amplitude 10 V which entails an uncertainty of $\pm$(0.1 V) $\pm$(1 mV) at $(23 \pm 5)°C$. Table 3.3 shows the signal generator settings used during measurements. The signal generator is depicted in Fig. 3.5.

Table 3.3: Settings used in Keysight 33511B waveform generator during measurements.

Function	Frequency	Amplitude	Offset	Start phase	Cycles	Burst period
Sine (burst)	500 kHz	10 V	0 V	0°	10	10 ms

Figure 3.5: Keysight 33511B waveform generator.

3.1.3 Oscilloscope

A Tektronix DPO 3012 oscilloscope is used to sample the signal detected by the receiving transducer. The oscilloscope is shown in Fig. 3.6. From the oscilloscope, the data is transferred to a computer where it can be implemented and treated in MATLAB. According to the datasheet [78], the oscilloscope has a maximum sample rate of 2.5 GS/s which corresponds to $4 \cdot 10^{-10}$ s resolution along the horizontal time axis. The vertical resolution is 8 bits. Further, the time-base range is from 1 ns to 1000 s and the time-base accuracy is ±10 ppm over any interval above 1 ms. The input sensitivity range (at 1 MΩ) is 1 mV/div to 10 V/div and the corresponding accuracy is ±1.5% for sensitivity ranges of 5 mV/div and above.

The oscilloscope has a display which shows the waveform of the signal. Only the part of the waveform shown in this display is extracted when data is imported to the computer. Therefore, it is important to relocate the waveform in the display such that both the direct propagating signal and the two-time reflected signal are observable. The acquired waveform is averaged 512 times and contains 100 000 samples, using a sample frequency of 250 MHz.

Figure 3.6: Tektronix DPO 3012 oscilloscope.

3.1.4 Temperature sensor

A temperature sensor is needed in order to measure the temperature at which the sound velocity measurements are taken. In this work, a 3 wire Pt100 PRT Probe with PFA Insulation from RS [79] is utilized, see Fig. 3.7. It is 3 mm in diameter and 30 mm long, and measures temperature based on changes in the resistance. The temperature sensor has a class A type accuracy, which means that the uncertainty is given as [80]

$$\pm (0.15 + 0.002 \cdot |T|)^\circ C \tag{3.2}$$

at 95% confidence level, where $|T|$ is the absolute value of the measured temperature. Table 3.4 summarizes the specifications of the temperature sensor

Table 3.4: Specifications of the 3 wire Pt100 PRT Probe with PFA Insulation from RS [79] used in this work.

Sensor type	Wires	Diameter	Length	Uncertainty
Pt100 PRT	3	3 mm	30 mm	$\pm(0.15 + 0.002 \cdot |T|)^\circ C$

Figure 3.7: 3 wire Pt100 PRT Probe with PFA Insulation from RS [79].

3.1.5   PRT sensor to USB adapter

The temperature sensor is wired to a USB-RTD_23 adapter [81] which is connected to the computer, ref Fig. 3.1. The adapter has a 3-position terminal block and supports the 3-wire RS Pt100 RTD sensor. It has an operating range of -200°C to +600°C, an uncertainty of ±0.06°C (95% confidence level) or better at 25°C and a typical resolution of ±0.02°C [81]. The temperature is calculated using the DIN 43760 coefficients. The adapter is depicted in Fig. 3.8.

Figure 3.8: USB-RTD_23 adapter with a 3-position terminal block.

3.1.6   Water bath

The temperature is controlled with a GD100 general purpose stirred thermostatic water bath from Grant Instruments [82], shown in Fig. 3.9. It consists of a tub to be filled with water and a heating element mounted on the tub. The heating element also contains a propeller which circulates the water inside the bath. This is vital to decrease the temperature gradient in the water bath, and thus inside the measurement cell which is placed inside the bath.

Figure 3.9: Picture of the Grant Instruments' GD100 general stirred thermostatic waterbath.

3.2   Constructing the measurement cell

3.2.1   Transducer selection

For the measurement cell, it was requested that relatively low frequency transducers were used. In general, sound waves with low frequencies have a lower absorption rate than sound waves with higher frequencies [83]. Additionally, low frequencies will make far field conditions more obtainable, which is desirable in order to investigate potential interference due to side wall reflections etc., cf. Section 3.3. The Rayleigh distance is proportional to both the frequency of the sound waves and to the square of the element radius. Thus, the transducers should ideally also be small in size. However, low frequency transducers are usually bigger than high frequency transducers, since a large element surface is necessary to obtain slower vibrations. Moreover, the diffraction correction is dependent on both transducer radius and frequency, and the dependency is dependent on which diffraction correction method is used. For example, a larger effective transducer radius will cause a smaller diffraction correction in Method 1, but a bigger diffraction correction in Method 2, cf. Appendix A.2. It is therefore important to consider both the frequency and size, when selecting the transducer.

A preference was set by XSENS Flow Solutions in advance to use 500 kHz transducers. Since measurements will be performed on liquids, the transducers should also be of the immersion type. After searching the web for 500 kHz immersion transducers, the V318-SU transducer from Olympus [63] [64], shown in Fig. 3.3, seemed to be the most fitting. To the authors knowledge, this is the smallest available 500 kHz immersion transducer acquirable.

3.2.2   Dimensions of the measurement cell

The measurement cell will be shaped as a cuboid where the entire top side is removable for easy cleaning and filling access. As the 3-way pulse method is the measurement principle used in the cell, there will be no material between the transducers other than the sample itself. This means that a relatively large sample volume is needed for sound velocity measurements compared to the volume needed in other methods, like the solid buffer method used in e.g. [10, 84]. To not waste an excessive amount of sample when performing measurements, a volume limit of 0.5 liters was set by XSENS Flow Solutions. This restricts the possibilities for the dimensions of the measurement cell as far field conditions are desirable in order to model the lobe structure, cf. Section 2.7.

The two transducers have a knurled section with a slightly larger diameter than elsewhere on the transducers, cf Fig. 3.4. The diameter of this section is 26.986 mm compared to the 25.400 mm on the smooth section. After consulting the workshop, it was concluded that the best way to incorporate the transducers would be to insert them by pressing the backside of the transducers out through the holes from the inside of the measurement cell, with the holes having the same diameter as the smooth section. This would both reduce the risk of leakage through the holes, and it allows for relatively thick and robust cell walls. By inserting the transducers this way, they will penetrate 15.875 mm into the cavity. Fig. 3.10 shows how the transducers are penetrating into the cavity.
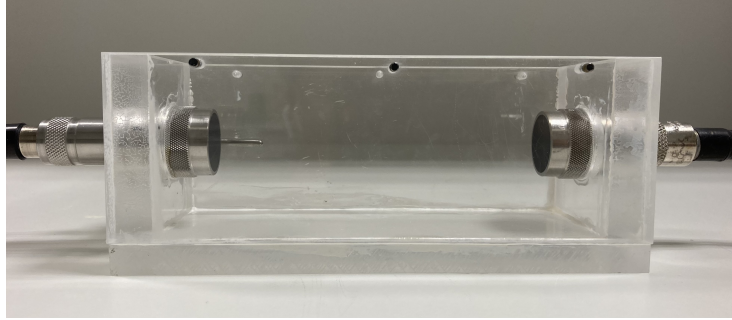
Figure 3.10: Image illustrating how the transmitting and receiving transducer penetrate into the cavity of the measurement cell.

As previously mentioned, it is desirable to have the transducers separated a distance larger than the Rayleigh distance in order to achieve far field conditions. However, the Rayleigh distance is inversely proportional to the sound velocity of the medium, cf. Eq. 2.53. Thus, the Rayleigh distance will change when the sample liquid is changed. Therefore, it is important to find a transducer distance that fulfills far field conditions for all samples that will be used during measurements. Following XSENS Flow Solutions' preferences, the transducer distance was based on an assumed minimum sound velocity of $c = 1154$ m/s. For the V318-SU transducers, this corresponds to a Rayleigh distance

$$r' = \frac{\pi \cdot (\frac{19.05 \ mm}{2})^2 \cdot 500 \ kHz}{1154 \ m/s} = 123.5 \ mm, \tag{3.3}$$

using the nominal transducer radius (the effective transducer radius could at this point not be measured since the transducers was yet to arrive). In other words, the transducers should be at least 123.5 mm apart. To have some margin, this is rounded up to 125 mm. A transducer distance of 125 mm will require the measurement cell to be approximately 157 mm long due to the transducer penetration depth.

The height and width of the measurement cell should be the same so that reflections in the side walls can be treated in the same way as reflections in the top and bottom walls, assuming the sound field is symmetric about the acoustic axis. A volume of 0.5 l and a cell length of 157 mm allows for a cell width and cell height of 57 mm. However, the height will be made to be 62 mm to compensate for a 5 mm deep lid on top of the cell. The handle on the lid is made hollow and will serve as an escape route when the sample expands due to increasing temperatures. Fig. 3.11 and 3.12 show schematic drawings of the measurement cell and lid.
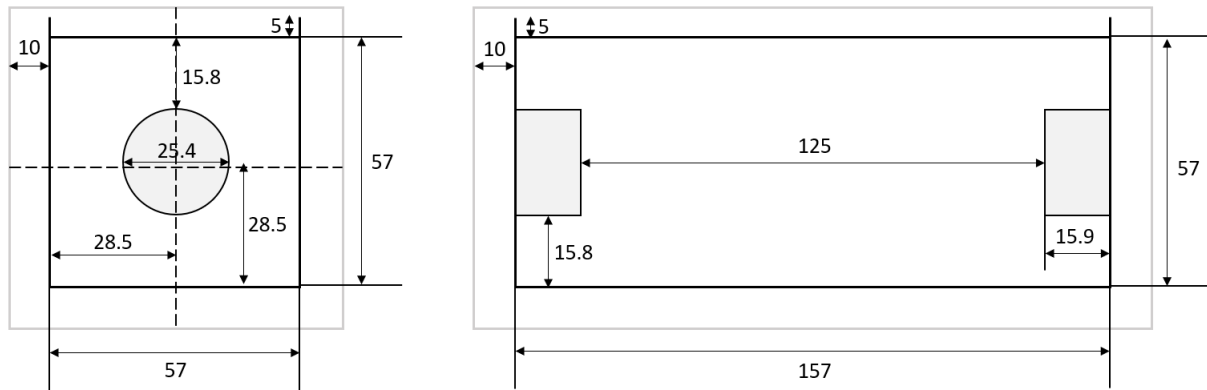
Figure 3.11: Dimensions of the design of the measurement cell. Dimensions are in mm.
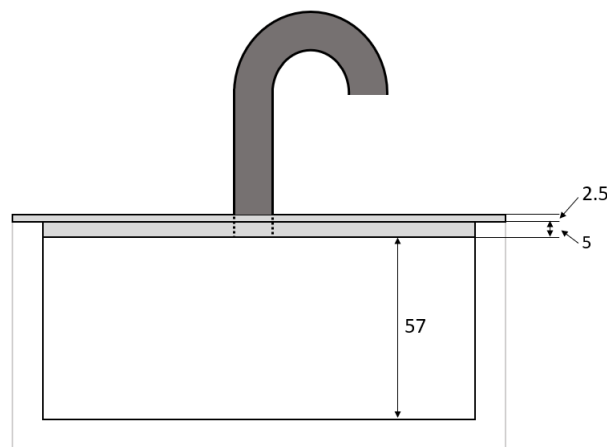
Figure 3.12: Dimensions of the measurement cell lid. Dimensions are in mm.

By reducing the width and height of the cell, one could increase the length of the cell to get further into the far field. However, as will be evident later, a reduction of width and height would reduce the difference in transit time between the main lobe signal and side wall reflections.

The initial plan was to have the transducers at a height such that their center axis would be straight in the middle of the liquid sample (28.5 mm from the bottom of the cell). However, there was a misunderstanding at the workshop, and the transducers were inserted in the middle of the total height of the measurement cell (31 mm from the bottom of the cell). Thus, the center axis of the transducers is located 31 mm from the bottom, 28.5 mm from each side wall and 26 mm from the lid. Consequently, reflections on the lid will occur before reflections on the other walls, potentially causing more interference with the signals of interest.

One solution to this problem would be to construct a completely new measurement cell with correct transducer height. However, this would be time consuming and cause delays. Thus, a simpler solution was opted for, where a new and narrower lid was created. The new lid is only 1.5 mm deep compared to the 5 mm of the original lid. As a result, the distance to the lid is now 29.5 mm. The dimensions of the final measurement cell are shown in Fig. 3.13.
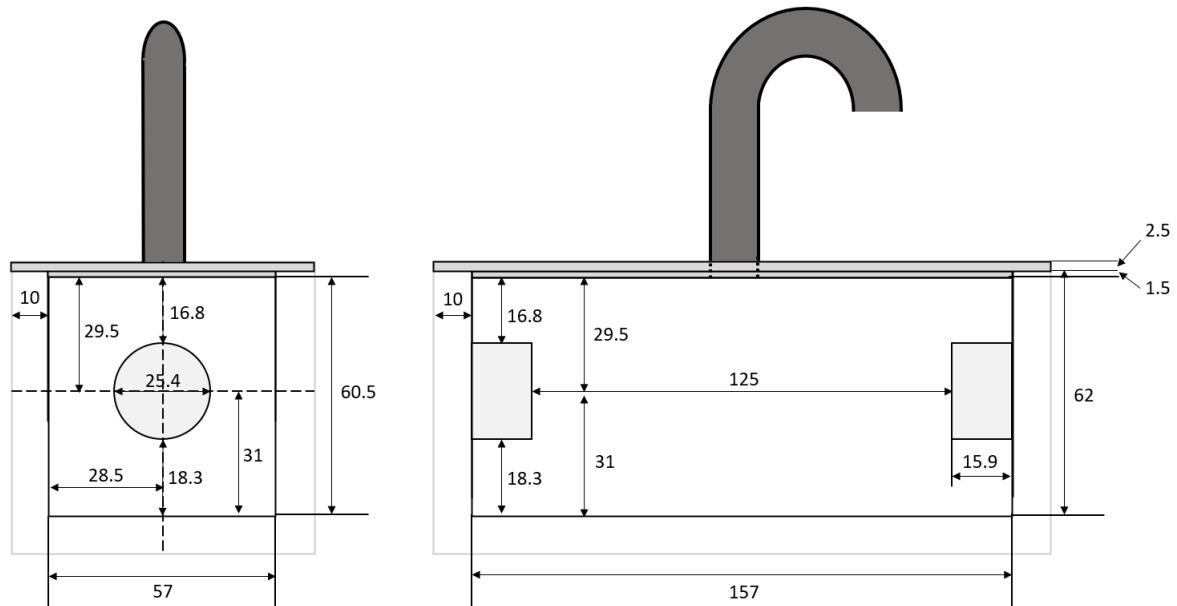
Figure 3.13: Dimensions of the final measurement cell. Dimensions are in mm.

3.2.3   Material of the measurement cell

After much consideration and consultation with both of my supervisors and the workshop, it was concluded that making the measurement cell out of plexiglas would be the best solution. Firstly, the acoustic impedance of plexiglass is closer to that of oils and water, compared to the acoustic impedance of metals. This is an advantage since it reduces the reflection coefficient at the boundary between the sample and the cell walls. The reflection coefficient at the boundary between water at $20°C$ and plexiglas is 0.38, while it for most metals may lie closer to 1. For example, the corresponding reflection coefficient at a water/aluminium boundary and a water/stainless steel boundary is 0.84 and 0.94, respectively. A smaller reflection coefficient ensures a smaller amplitude in the side wall reflected signals, and thus less coherent noise.

Another key advantage with plexiglas is that it is transparent, making it easier to detect potential dirt and sample remains that should be cleaned. It is also a light and solid material that is easy to handle.

The main downside of plexiglas, compared to e.g. aluminium, is the relatively large thermal expansion coefficient. Thus, a larger expansion must be compensated for when heating the sample than what would be the case for an aluminium cell. However, the staff at the workshop has stated that a heating to $50°C$, which is the temperature limit for the V318-SU transducers, should not be a problem as long as all cell walls are made out of the same material. Having the cell made out a single material, ensures that the cell will expand uniformly. Hence, cracks and tears in the cell walls will presumably not occur, as it did in the measurement cell constructed by Nesse [10], where both aluminium and plexiglas were used in the same cell. The final design of the measurement cell is shown in Fig. 3.14

Figure 3.14: The final design of the measurement cell.

3.3 Considerations regarding the sound field

The generated sound waves will have a beam pattern consisting of a main lobe and several side lobes. The side lobes are directed towards the side walls of the measurement cell, giving rise to side wall reflections. If the signal of interest overlaps with side wall reflections at the receiving transducer, interference will occur. Assuming a symmetric sound field about the acoustic axis, simple geometry may be used to calculate the time arrivals of the signal of interest and the side wall reflections. The propagation path of the side lobe signals is dependent on the sound velocity of the medium. Consequently, the following simulations are carried out for a set maximum and minimum sound velocity. The maximum sound velocity is set to $c_{max} = 1593$ m/s, which is the theoretical sound velocity of saline water at 50 ppt salinity and $60°C$, according to the UNESCO-algorithm [11, 12]. On the other hand, the minimum sound velocity is set to be $c_{min} = 1154$ m/s, which was used to find the maximum Rayleigh distance in Section 3.2.2. In Fig. 3.15 and 3.16, ray tracing is used to illustrate the propagation direction of the first four side lobes for those two sound velocities, respectively. The simulations are performed in MATLAB with the script provided in Appendix E.2.1. The simulations are based on the baffled piston model, using a piston radius equal to the nominal transducer radius of 9.525 mm and a set frequency of 500 KHz.

Rays that hit one side wall, and reflects back across the sample to the opposite side wall, before reaching the wall with the receiving transducer, are ignored. They have a dB-level corresponding to the third side lobe at max, which lies around -55 dB. A SNR of 55 dB corresponds to a time shift of $5.7 \cdot 10^{-10}$ s according to the numerical analysis of coherent noise, presented in Section 4.2.4. This is far less than the transit time uncertainty presented in the sensitivity analysis in Section 4.3, and these side wall reflections are henceforth considered negligible. Also, it should be noted that transmission into the actual side walls of the measurement cell is not included in these simulations. The rays are only plotted on one side to keep the diagrams as clear as possible.
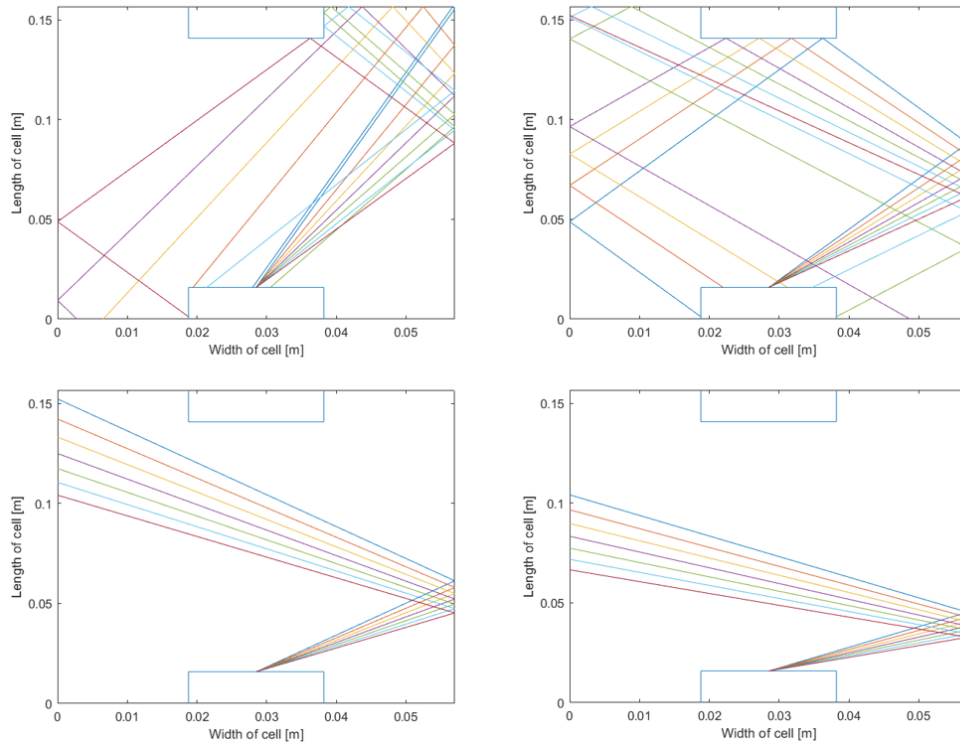
Figure 3.15: Ray tracing of side lobes when the sample has sound velocity $c = 1593\ m/s$. Top left: first side lobe. Top right: second side lobe. Bottom left: third side lobe. Bottom right: fourth side lobe. The piston radius is 9.525 mm, and the frequency is 500 KHz, resulting in a ka-number, $ka = 18.78$
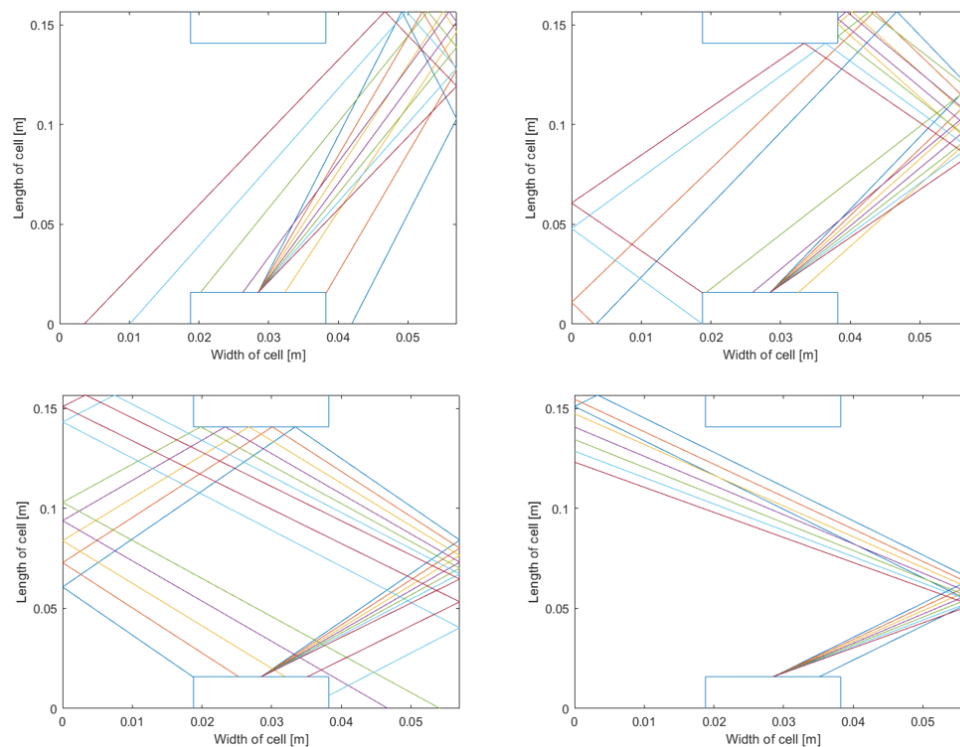
Figure 3.16: Ray tracing of side lobes when the sample has sound velocity $c = 1154\ m/s$. Top left: first side lobe. Top right: second side lobe. Bottom left: third side lobe. Bottom right: fourth side lobe. The piston radius is 9.525 mm, and the frequency is 500 KHz, resulting in a ka-number, $ka = 25.93$

For the sample with sound velocity $c = 1593$ m/s, it is primarily the second side lobe that hits the active surface of the receiving transducer. Similarly, for sample with sound velocity $c = 1154$ m/s, it is primarily the third side lobe that hits the active surface of the transducer. In addition, some of the side wall reflections will hit the steel casing surrounding the transducer. The different parts of the signal that impacts on different areas on the transducer are investigated more in the following three subsections.

3.3.1 Side wall reflections hitting the steel casing of the transducer

The transmission coefficient for sound waves travelling from the liquid sample and into the stainless steel casing is given as [29]

$$T = 1 + \frac{z_2 \cos\theta_i - z_1 \cos\theta_t}{z_2 \cos\theta_i + z_1 \cos\theta_t}, \tag{3.4}$$

where z_1 is the impedance of the liquid sample, z_2 is the impedance of the stainless steel casing, θ_i is the angle of the incident sound waves and θ_t is the angle of the transmitted sound waves, as illustrated in Fig. 3.17.
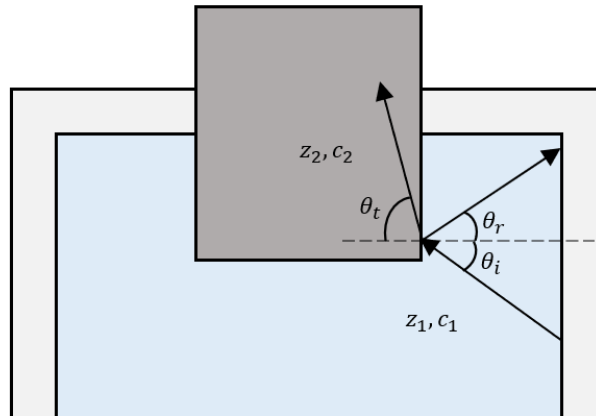
Figure 3.17: Illustration of the incident, reflected and transmitted rays at the interface between the liquid sample and the transducer steel casing.

θ_t can be found using Snells law, given as [29]

$$\frac{\sin\theta_i}{c_1} = \frac{\sin\theta_t}{c_2}, \tag{3.5}$$

where c_1 and c_2 is the sound velocity of the liquid sample and the stainless steel casing, respectively. Additionally, the critical angle θ_c is defined by [29]

$$\sin\theta_c = \frac{c_1}{c_2}. \tag{3.6}$$

If the angle of incidence is larger than the critical angle, the transmitted sound wave will have an

angle of 90° relative to the axis normal to the transducer casing. Assuming the sound velocity of the stainless steel casing is 5640 m/s [76], the largest critical angle in this work will not exceed

$$\theta_c = \sin^{-1}\left(\frac{1593 \; m/s}{5640 \; m/s}\right) = 16.41°, \tag{3.7}$$

which is far less than the incident angle. Consequently, the sound waves will propagate along the boundary between the two layers, with the amplitude decaying perpendicular to the boundary [29]. Even though the transmitted sound waves possesses energy, none of the energy propagates into the steel casing in the steady state. The propagation vector of the transmitted sound waves is parallel to the boundary, and the waves "clings" to the interface [29]. It is therefore assumed that the sound waves that hits the steel casing of the receiving transducer will not have an impact on the signal of interest.

3.3.2   Side wall reflections hitting the active surface of the transducer

Fig. 3.15 and 3.16 show propagation of sound rays in a sample with the approximate highest and lowest sound velocity that will be measured in this work, respectively. The top left plot in both figures indicates that only a small part of the side wall reflections due to the first side lobe will make impact on the active surface of the receiving transducer. The maximum magnitude of this part is found by investigating the side wall reflection which impacts on the edge of the active surface of the transducer, as illustrated in Fig 3.18. Simple trigonometric calculations show that this ray is transmitted at an angle of 20.72° relative to the normal axis through the transducer surface. Using the "data tip" function in MATLAB [73] on Fig. 2.19, it can be shown that the corresponding dB-level of this ray is approximately -64.77 dB. This is lower than the peak of the second side lobe, which is at approximately -47.62 dB. Hence, the side wall reflections due to the second side lobe will cause the biggest disturbances.

The interference due to side wall reflections can be avoided by choosing a pulse length short enough to ensure that the main lobe signal is perceived before the side wall reflections arrive. One way of finding this pulse length is to plot the transit time of the signals of interest and side wall reflections along the same time axis. If the one-way main lobe signal, the shortest travelling one-way side wall reflection, the three-way main lobe signal, and the shortest travelling three-way side wall reflection are plotted in the same diagram, one can check where interference may occur. This has been done in Fig. 3.18. Also, the longest travelling one-way side wall reflection is plotted to check whether it interferes with the three-way main lobe signal. The longest travelling one-way side wall reflection corresponds to the ray that is transmitted with an azimuth angle such that it hits one of the corners of the cell wall. This is illustrated in Fig. 3.19.
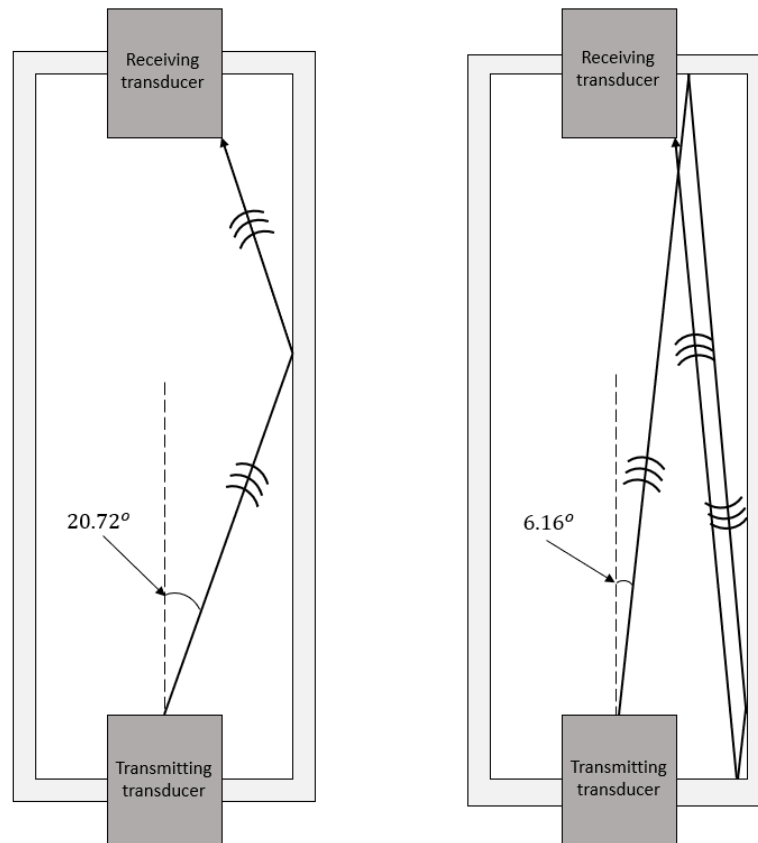
Figure 3.18: The shortest possible propagation path to reception at the receiver for one-way (left) and three-way (right) side wall reflection, respectively. Signals that are reflected on both side walls are not included due to the low dB-level.
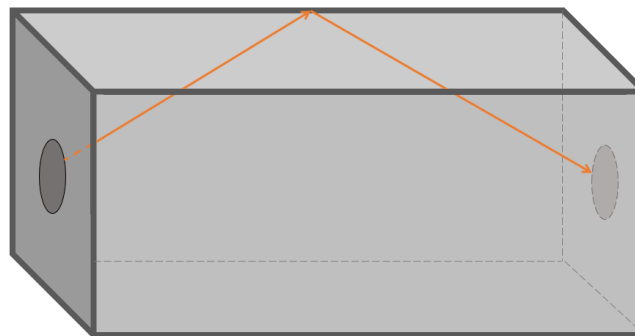
Figure 3.19: The path of the slowest one-way side wall reflection. The ray is reflected at the corner of the measurement cell, which is further from the acoustic axis than the middle of the side walls.
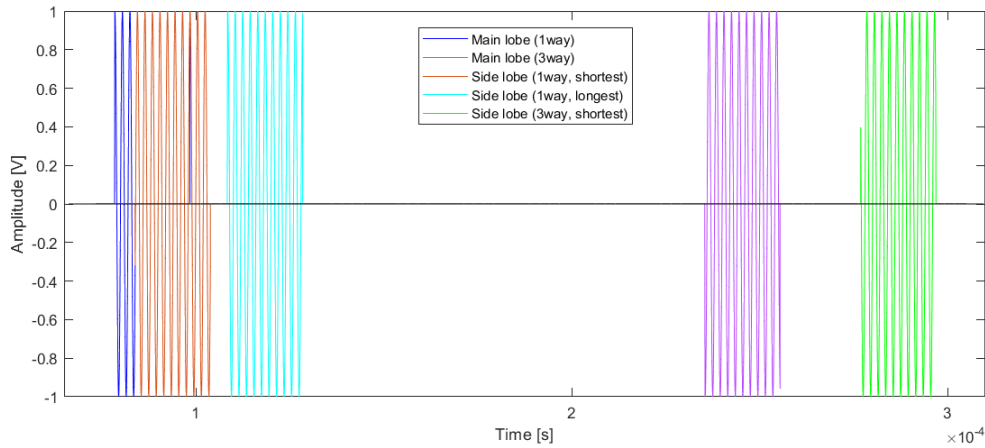
Figure 3.20: One-way signal of interest, shortest travelling one-way side wall reflection, longest travelling one-way side wall reflection, three-way signal of interest, and shortest travelling three-way side wall reflection plotted along the same time axis. The pulse length is set to 10 periods and the sound speed of the medium is set to 1593 m/s.

Fig 3.20 shows that interference with side wall reflections only occurs for Pulse A. The first three periods of the main lobe signal is detected before the first side wall reflection arrives. This means that the pulse length can be three periods at max in order to avoid interference with side wall reflections.

However, a problem with having a maximum pulse length of three periods is that the pulse will lack a steady state region. As explained in Section 2.1.2, a steady-state region is desirable when measurements are performed on dispersive media, due to the sound velocity being frequency dependent. Therefore, it might be necessary to use a longer pulse length, even if side wall reflections are present. Fig. 3.21 shows the waveform of Pulse A when the pulse length is 2, 5 and 10 periods, respectively.
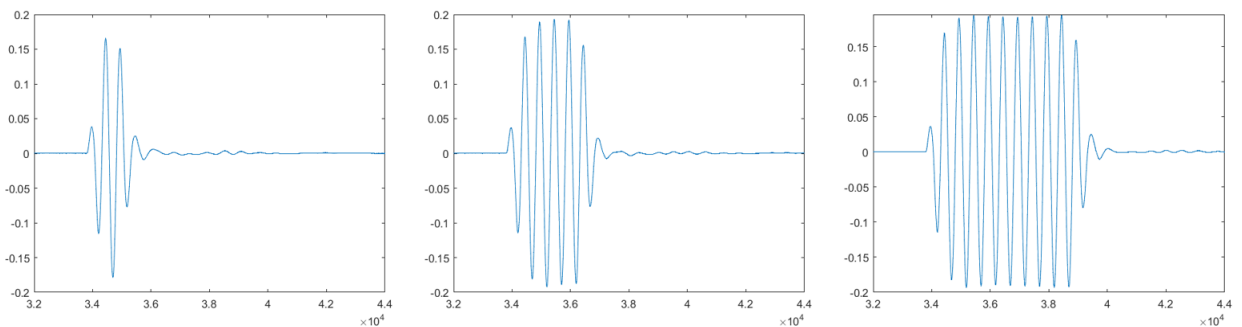
Figure 3.21: Waveform of Pulse A for various pulse lengths. Left: 2 periods, middle: 5 periods, right: 10 periods.

The shape of the waveform is seemingly equal for all three cases, with the exception of the length of the steady state part. It appears that the dB-level of the side wall reflections is low enough to not cause significant distortion in the signal of interest.

Some practical testing was performed in the laboratory to further explore potential interference due to side wall reflections. A metal block was placed next to each side wall in the measurement cell, with

various distance from the transmitting transducer, to investigate how the waveform would change. Fig. 3.22 shows the metal blocks placed in the middle of the transmitting and receiving transducer. They seemingly did not change the waveform around Pulse A. However, for Pulse B, there were a significant change in the noise signal. Fig. 3.23 and 3.24 shows how the waveform in the Pulse B region is affected by the metal block placement.
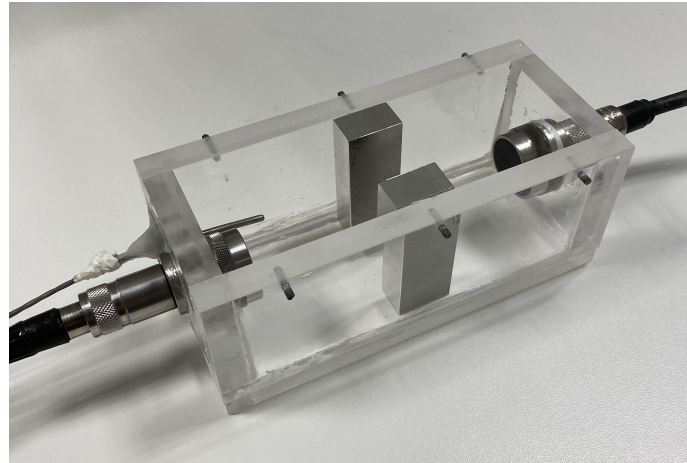
Figure 3.22: Image of the measurement cell with the two metal blocks used for testing.
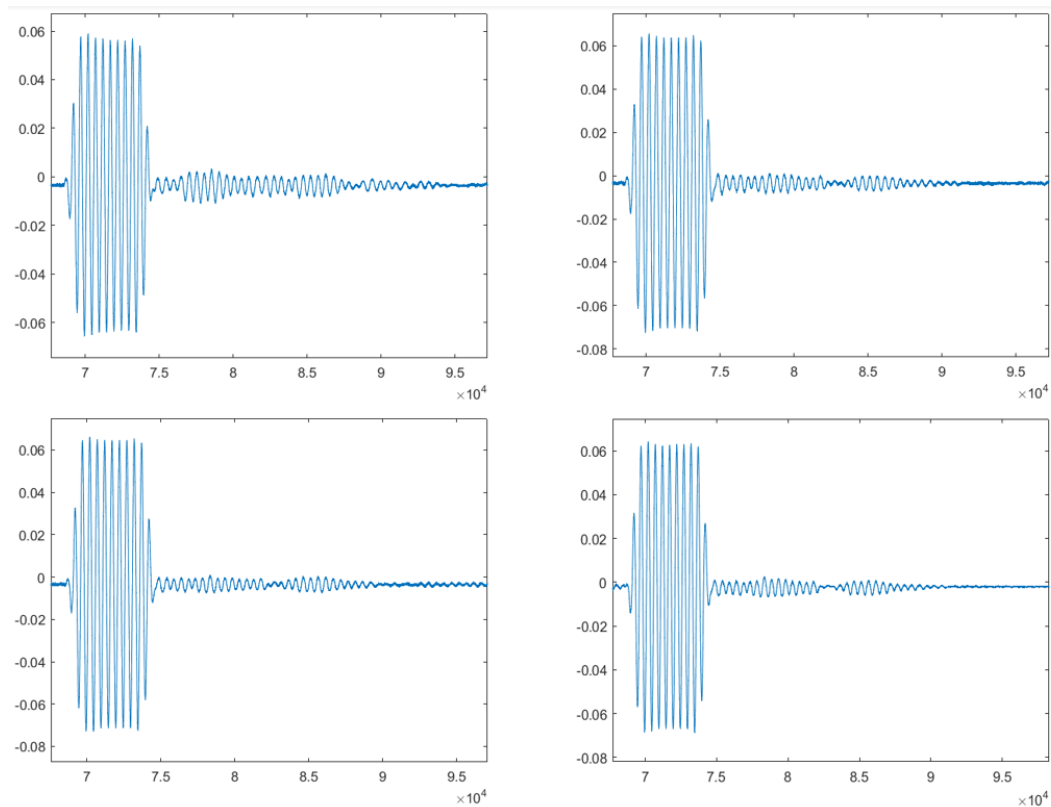
Figure 3.23: Comparison of the waveform at and after Pulse B for various placements of the metal blocks. Top left: no metal blocks. Top right: metal blocks placed by the transmitting transducer. Bottom left: metal blocks placed in the middle of the measurement cell. Bottom right: metal blocks placed by the receiving transducer. The pulse length is set to be 10 periods and the sample is distilled water at room temperature.
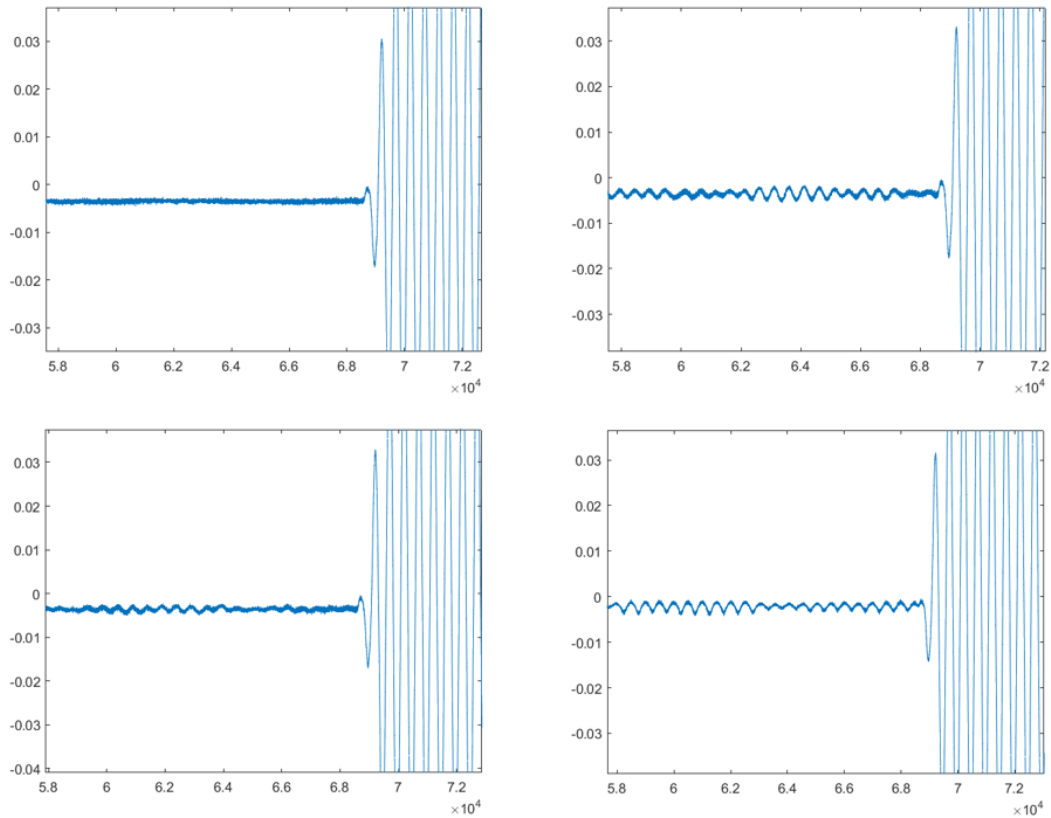
Figure 3.24: Comparison of the waveform prior to Pulse B for various placements of the metal blocks. Top left: no metal blocks. Top right: metal blocks placed by the transmitting transducer. Bottom left: metal blocks placed in the middle of the measurement cell. Bottom right: metal blocks placed by the receiving transducer. The pulse length is set to be 10 periods the sample is distilled water at room temperature.

Fig. 3.23 shows that the noise arriving after Pulse B is reduced when the metal blocks are placed in the measurement cell. However, the opposite applies prior to the pulse, where the metal blocks actually increase the noise to the point where it might be difficult to define the first arrival of the pulse.

To determine whether or not such metal blocks should be present during sound velocity measurements, the measured difference in transit time between Pulse A and Pulse B is investigated for different placements of the metal blocks. Fig. 3.25 shows ten measurements of the transit time difference for three different placements of the metal blocks as well as when the metal blocks are absent.
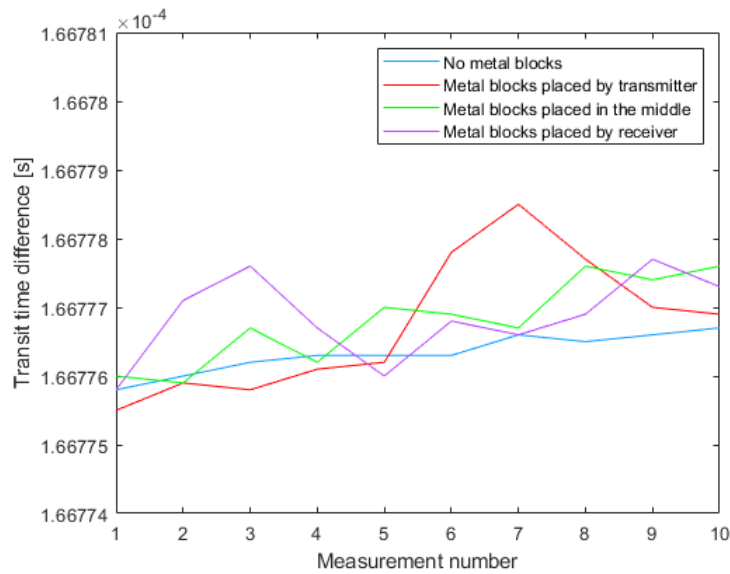
Figure 3.25: Ten measurements of the difference in transit time between Pulse A and Pulse B for three different placements of the metal blocks, as well as without the metal blocks. The pulse length is set to be 10 periods, and the zerocrosses in the steady state region were used to calculate the transit time difference. Measurements were taken every three seconds, and the sample is distilled water at room temperature.

Evidently, both the smallest and biggest transit time difference was measured with the metal blocks placed by the transmitting transducer, and there does not seem to be a systematic change caused by them. Other than measurement number 2 and 3 with the metal blocks placed by the receiver, and measurement number 6 and 7 with the metal blocks placed by the transmitter, there seems to be a slight systematic increase in transit time difference with increasing measurement number in each of the four cases. This indicates that the measurements may have been performed under unstable conditions where the temperature were slightly decreasing during measurements.

The small fluctuations are probably a result of white noise or noise from one or more of the instruments. The maximum fluctuation in transit time during the measurements were no more than 3 ns, which is far less than the maximum uncertainty in transit time difference calculated in the sensitivity analysis in Section 4.3. Hence, the influence of the metal blocks is not investigated further, and they will not be used during measurements in this work. Instead, the potential change in transit time due to the metal blocks will be treated as an uncertainty, cf. Section 5.5.1.

3.3.3 Main lobe signal bending around the edge of the transducer

Since the transducers are penetrating into the cavity of the measurement cell, coherent noise may also occur due to the main lobe being wider than the surface of the receiving transducer. Diffraction effects will cause part of the signal to "bend" around the edge of the receiving transducer. The waves will propagate along the side wall of the transducer, reflect on impact with the cell wall, and propagate back to the active surface of the receiving transducer [40]. This principle is illustrated in Fig. 3.26, and

may cause additional interference.
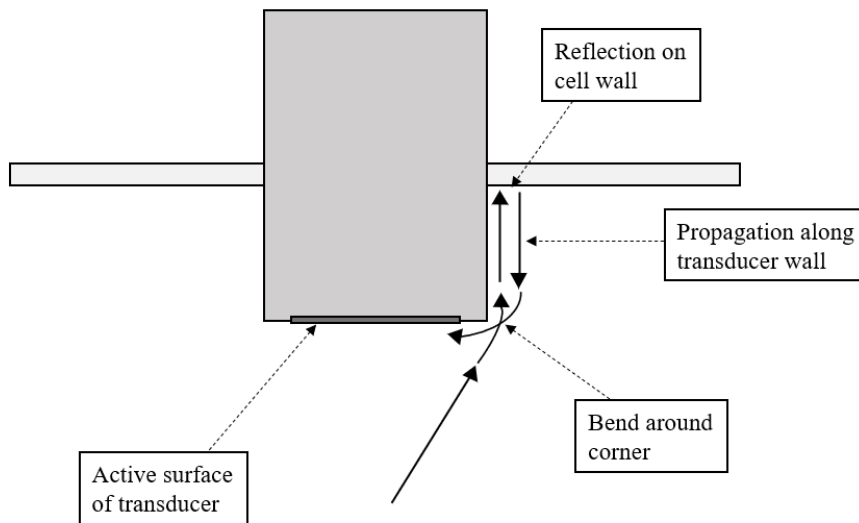
Figure 3.26: Illustration of how part of the signal in the main lobe will bend around the edge of the transducer, reflect at the cell wall, and propagate back to the active surface of the transducer.

The magnitude of this disturbance depends on the width of the main lobe, and thus, on the liquid sample in use. A wider main lobe results in a larger amplitude in the part of the signal bending around the corner. In order to investigate the magnitude of the potential interference, measurements were taken with and without a steel plate mounted flush with the receiving transducer, as shown in Fig. 3.27.
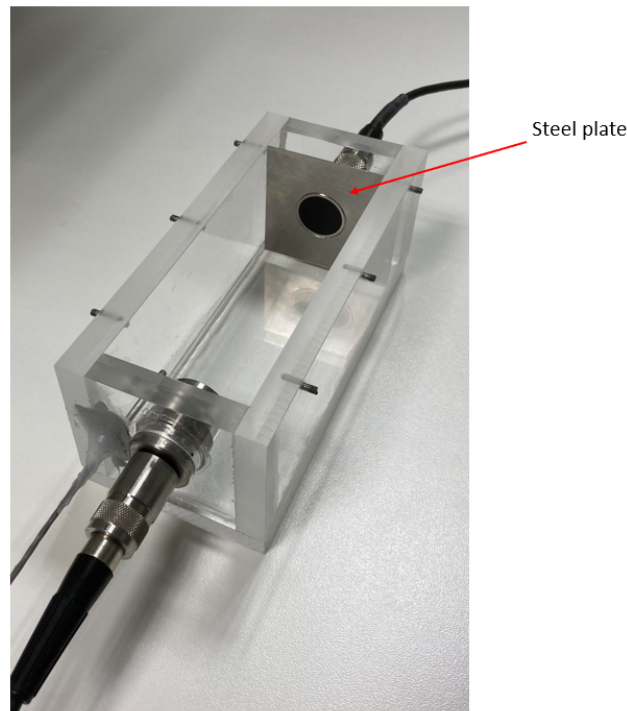
Figure 3.27: Image of the measurement cell with the steel plate mounted flush with the receiving transducer.

A comparison of the waveform acquired with and without the steel plate for Pulse A and B is given in Fig. 3.28 and 3.29, respectively.
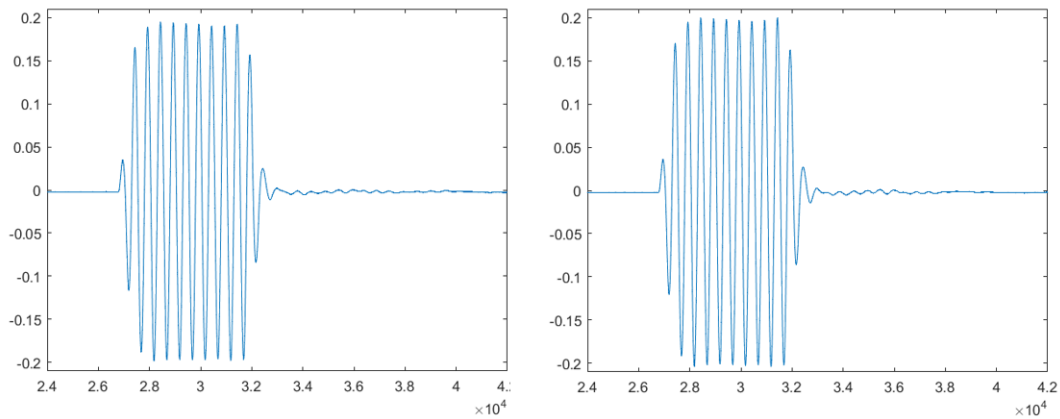
Figure 3.28: Comparison of Pulse A without the steel plate (left), and with the steel plate (right). The pulse length is set to be 10 periods and the sample is distilled water at room temperature.
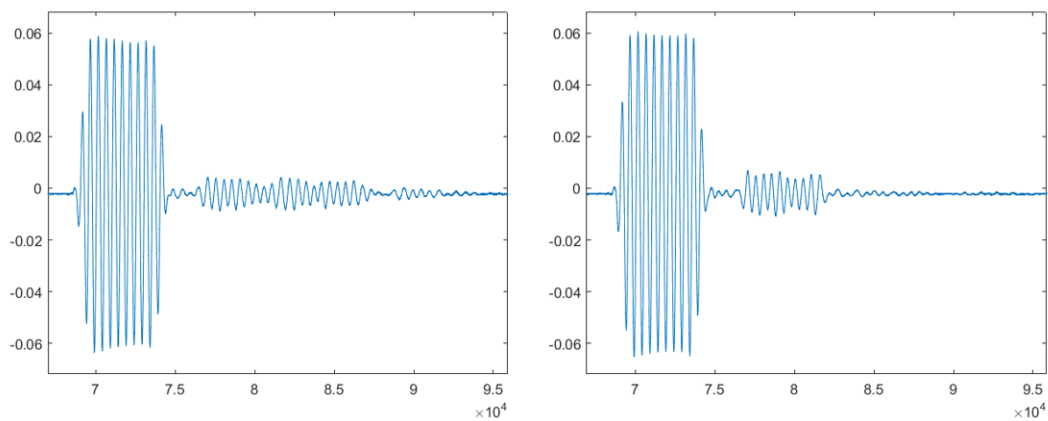
Figure 3.29: Comparison of Pulse B without the steel plate (left), and with the steel plate (right). The pulse length is set to be 10 periods and the sample is distilled water at room temperature.

Fig. 3.29 shows that the noise trailing Pulse B seems to be cut off when the steel plate is inserted. Also, the amplitude of each peak in the pulse seem slightly more stable with the steel plate inserted. However, ten measurements of the transit time difference between Pulse A and Pulse B is performed with and without the steel plate, respectively, to increase the confidence regarding the noise due to the main lobe. The measurements are plotted in Fig. 3.30.
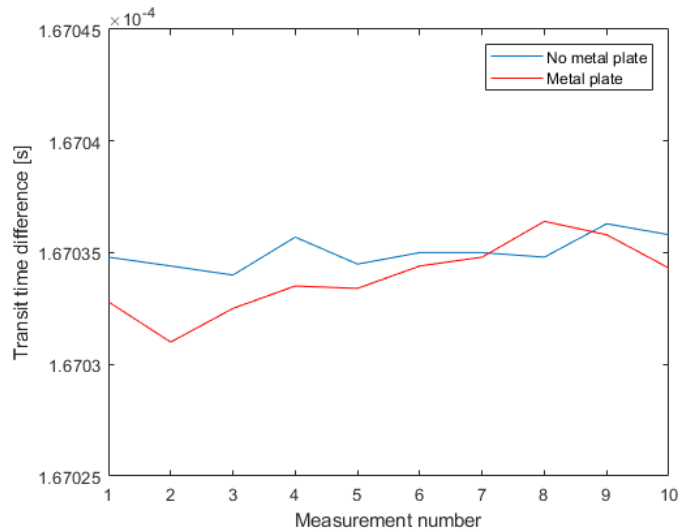
Figure 3.30: Ten measurements of the difference in transit time between Pulse A and Pulse B when the steel plate is inserted (red) and removed (blue). The pulse length is set to be 10 periods, and the zerocrosses in the steady state region were used to calculate the transit time. Measurements were taken every three seconds, and the sample is distilled water at room temperature.

For the first measurement numbers, the measured transit time differences seem to be slightly lower when the steel plate is inserted. However the maximum fluctuations observed is approximately 5 ns, which is far less than the maximum uncertainty in transit time difference calculated in the sensitivity analysis in Section 4.3. Hence, the influence of the steel plate is not investigated further, and the metal plate will not be used during measurements in this work. Instead, the potential change in transit time due to the steel plate will be treated as an uncertainty, cf. Section 5.5.1.

3.4 Setup used to measure temperature

A temperature sensor is needed in order to measure the temperature at which the sound velocity measurements are taken. As the density of the sample is dependent on temperature, the placement of the temperature sensor should be chosen carefully. Warm liquid has a lower density than cold liquid. Consequently, warm liquid rises to the top, while cold liquid sinks to the bottom. This may cause a temperature gradient in the sample, and thus, a varying speed of sound. In order to minimize the potential temperature difference between the liquid surrounding the temperature sensor and the liquid surrounding the transducers, the temperature sensor is mounted with its center at the same height as the center of the transducers, as shown in Fig. 3.31. Both the temperature sensor and the transducer will have its center 31 mm from the bottom of the cell.
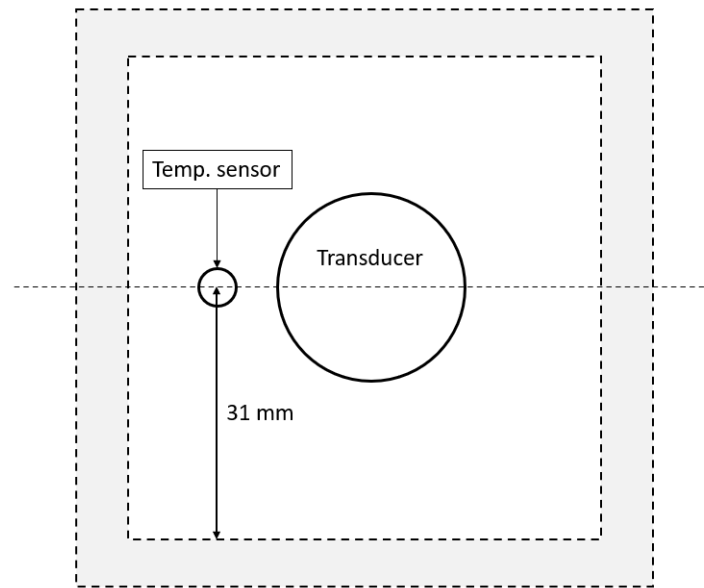
Figure 3.31: Sketch showing the placement of the temperature sensor in the measurement cell.

The temperature sensor should ideally be small in size to not cause unwanted reflections due to the side lobes. After doing some research, the temperature sensor that seemed the most fitting was the 3 Wire Pt100 PRT Probe with PFA Insulation from RS [79]. It is 3 mm in diameter, 30 mm long, and measures temperature based on changes in the resistance. PRT probes do not require more than two wires, but the additional wire increases the accuracy. This is because the third wire measures the resistance in the actual wires and subtracts this resistance from the read value [85, 86, 87]. Thus, lead wire resistance is compensated for. Three wire PRT probes provide good accuracy and repeatability, and has become the standard type of sensor for all major temperature transmitter manufacturers [85]. When it comes to four wire PRTs they are more accurate than three wire PRTs, but also more complex and expensive [86, 87]. There was also no available four wire PRTs with the same small size at the time of purchase. Hence, the three wire PRT probe was opted for.

Fig. 3.32 shows a simulation of the fourth side lobe, using ray tracing and the baffled piston model, when the medium is water with sound velocity 1593 m/s. The simulation is performed with the MATLAB-script provided in Appendix E.2.1. The temperature sensor has been implemented in the plot. It is clear that only a small part of the fourth side lobe impacts on the temperature sensor. In addition, the sound velocity in oils are generally lower than that in water, and lower sound velocity makes the side lobes narrower. Consequently, for all liquids tested in this work, it can be assumed that no part of the first three side lobes will impact on the temperature sensor.
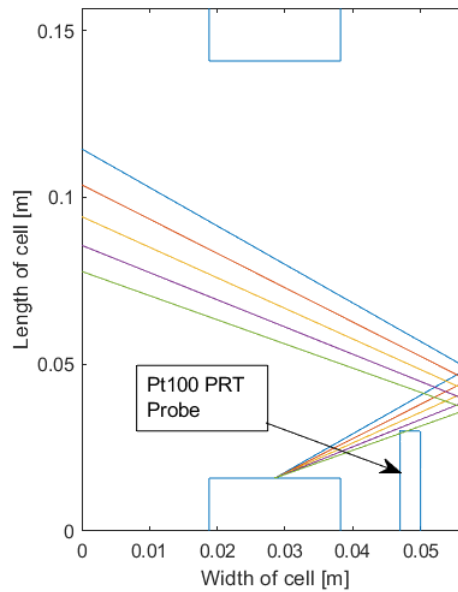
Figure 3.32: Simulation of the fourth side lobe in the measurement cell with the Pt100 PRT Probe implemented. The medium is set to be saline water at 50 ppt salinity and $60°C$, with sound velocity $c = 1593m/s$. The nominal transducer radii are used in the simulation.

3.4.1   Setup used to calibrate temperature sensor

The temperature sensor has a class A type accuracy, which means that the uncertainty is given as [80]

$$\pm (0.15 + 0.002 \cdot |T|)°C \tag{3.8}$$

where $|T|$ is the absolute value of the measured temperature. In addition, the temperature sensor may be biased, and always measure a higher or lower temperature than what it should. In order to reduce this potential bias, the sensor is calibrated with another temperature sensor with higher accuracy. The calibration is performed using a Fluke 1586A SUPER-DAQ precision temperature scanner together with a Fluke 1586-2588 DAQ-STAQ multiplexer. A Fluke 9102S dry-well calibrator is used to perform the calibration over a desired temperature span. The setup is illustrated in Fig. 3.33 and 3.34.
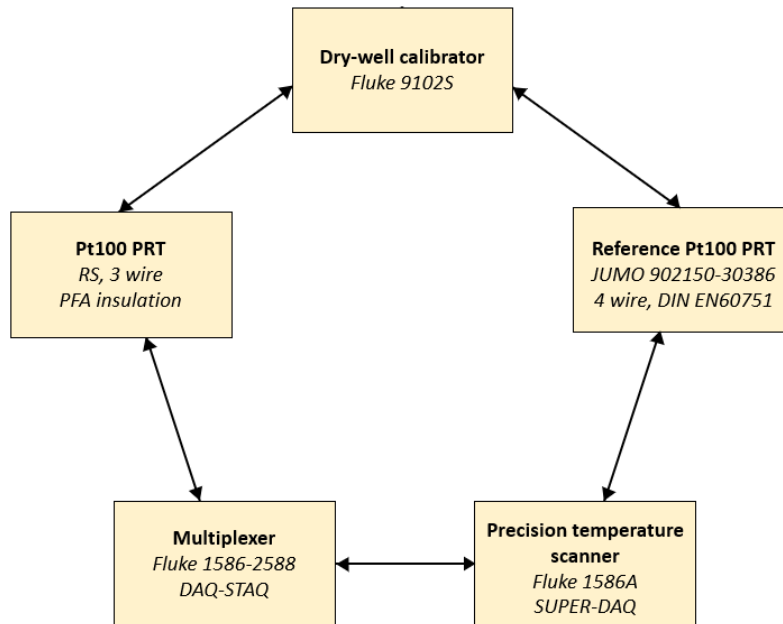
Figure 3.33: Schematic overview of the setup used when calibrating the temperature sensor.
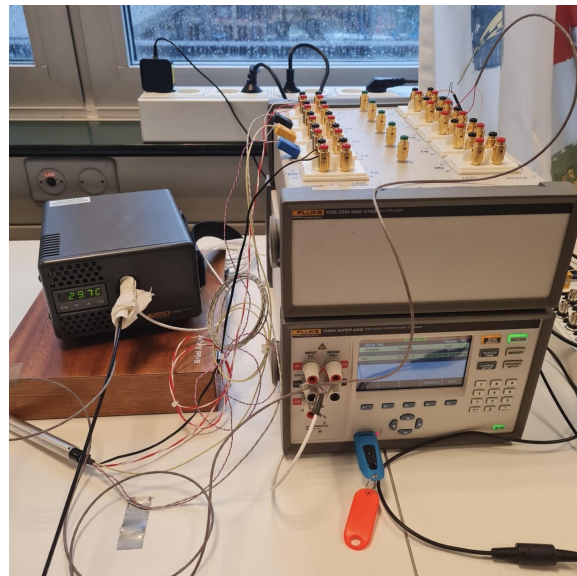
Figure 3.34: Picture of the setup used when calibrating the temperature sensor.

The temperature sensor to be calibrated is inserted into a hole in the dry-well calibrator where the temperature is changed. From here, it is connected to the precision temperature scanner through one of the channels on the multiplexer. The reference temperature sensor is connected directly to the precision temperature scanner from the dry-well calibrator. It is calibrated per DIN EN60751 [88] and assumed to show the "real" temperature in the dry-well calibrator.

The calibration is performed by taking 100 measurements with both temperature sensors for every $3°C$ from $15°C$ to $60°C$. The following three settings were implemented [?]: (1) tolerance: $±0.15°C$, (2) stability: $±0.15°C$ and (3) soaktime: 6 minutes. Tolerance is the interval in which the reference

probe temperature must be for a scan to proceed. Stability is the interval in which the temperature must be for a duration equal to the soaktime before the scan proceeds. In other words, the deviation between measurements had to be less than $0.15°C$ for 6 minutes straight for every setpoint before the 100 measurements were taken.

The characteristic of the Pt100 element to be calibrated is given by the polynomial equation [89]

$$R_T = R_0(1 + \alpha T + \beta T^2),$$
(3.9)

where R_0 is the resistance at 0°C (i.e. 100Ω), $\alpha = 3.9083 \cdot 10^{-3}\,°C^{-1}$ and $\beta = -5.775 \cdot 10^{-7}\,/°C^{-2}$. Higher order terms are neglected. The equation represents the nonlinear relationship between temperature and resistance. The coefficients represent the standard coefficients for a regular platinum element. They are implemented in the precision temperature scanner before starting a measurement sequence. When the series of measurements are completed, `cftool` in MATLAB [73] is used to plot the measurements taken from the uncalibrated sensor against the values taken from the reference sensor. Then, curve fitting is used to find new and more accurate values for the coefficients in Eq. 3.9. The old coefficients are then replaced by the new ones to find an updated characteristic equation for the sensor.

3.5   Setup used to measure pressure

Pressure measurements are necessary to calculate the modelled sound velocity of distilled and saline water. Both the equation presented by Kinsler et. al. [29] and the UNESCO-algorithm [11, 12] take pressure as an input. A Paroscientific Digiquartz precision pressure instrument model 740 is used to measure the pressure in the laboratory. The uncertainty of the instrument is ±0.015% (95% confidence level) of the measured value at room temperature and atmospheric pressure, according to the manufacturer [90]. The instrument is shown in Fig. 3.35.

Figure 3.35: Picture of the Paroscientific Digiquartz precision pressure instrument model 740 used for pressure measurements.

3.6 Setup used to measure effective transducer radius

The effective transducer radius, a_{eff}, is calculated from directivity measurements performed in a water tank with the setup shown in Fig. 3.36. First, the transmitting transducer is submerged into the water by attaching it to a metal holder in the tank. Then, a 1.0 mm needle hydrophone from Precision Acoustics [91] is submerged by controlling a motor through MATLAB [73]. The transducer and hydrophone are highlighted in Fig. 3.37. The distance between the hydrophone and transducer is approximately 65 cm, assuring far field conditions, cf. Eq 3.3. Several MATLAB-scripts were used to regulate the position of the transducer and the hydrophone. The original scripts can be found in [92].

Both the depth, breadth and angle must be carefully adjusted to keep the transducer and hydrophone aligned as axially concentric as possible. A satisfactory alignment is found by slightly altering the angle of the transducer and the position of the hydrophone, while constantly observing the amplitude of the sound waves on an oscilloscope. The acoustic axis is said to be found when the observed amplitude is at its highest. After alignment, the signal generator is set to generate a 100 period sinusoidal burst at 500 KHz and amplitude 10 V peak-to-peak. Measurements are then taken at angles from $-7°$ to $7°$ around the initial orientation, in steps of $0.05°$, assuring that the whole span of the beam width is covered. For each measurement, the oscilloscope is set to average the signal 512 times before sampling the waveform. After completing a measurement series for the transmitting transducer, the process is repeated for the receiving transducer.
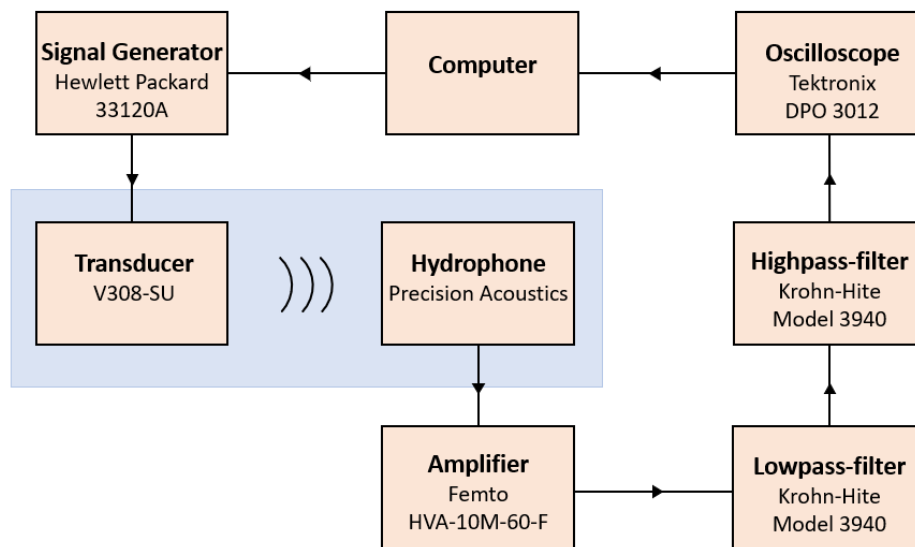
Figure 3.36: Schematic overview of the setup used to measure a_{eff}. The blue rectangle represents the water tank.
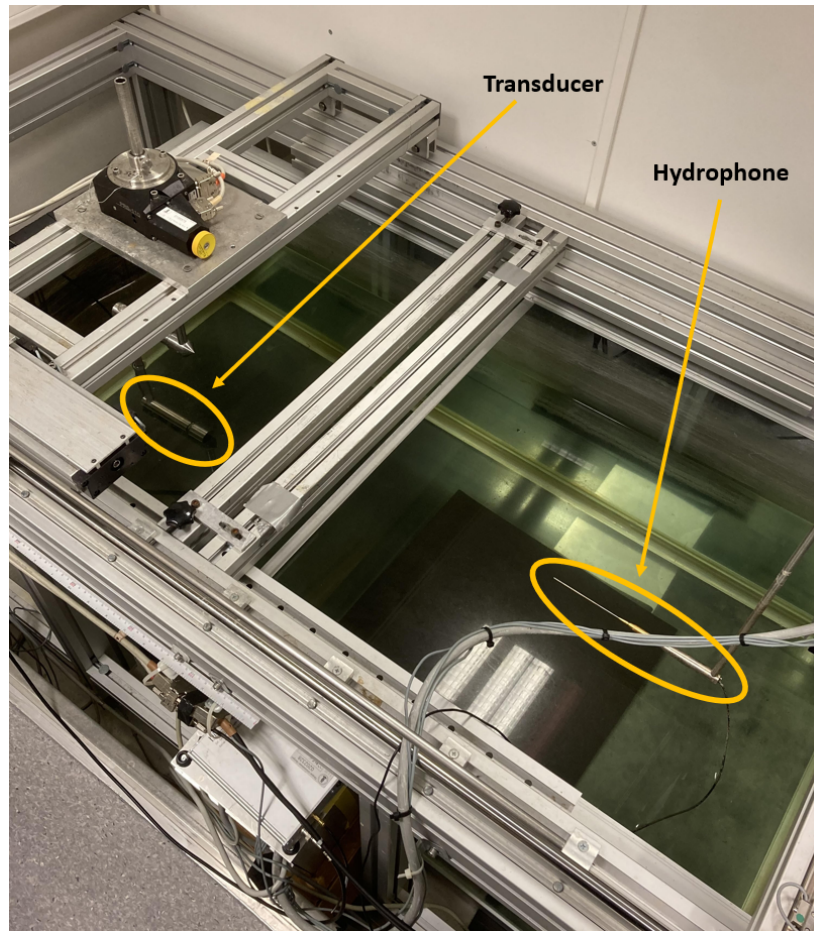
Figure 3.37: Picture of the water tank where a hydrophone is used to measure the directivity of a transducer.

3.7   Signal processing

In this section, two different signal processing methods used for calculation of the sound velocity will be explained. As mentioned earlier, the sound velocity can be calculated in both the time domain and in the frequency domain. For measurements in the time domain, detection of zerocrossings is used to measure the transit time, and thus the speed of sound. This method will in the following be called the zerocrossing method (ZCM). For measurements in the frequency domain, a method called the Fourier spectrum method (FSM) is used to calculate the sound velocity by performing a Fourier transformation of the pulses. Both methods are used and compared in this work. A pulse length of ten periods is applied in both methods throughout the project, and only the steady state part is utilized for sound velocity measurements. Usage of the steady state part is desirable since the diffraction correction assumes continuous waves, cf. Section 2.3.1. A ten-period pulse length will ensure that a steady state part is present. The only downside of using a ten-period pulse is that some coherent noise will interfere with the signal of interest, as shown in Section 3.3. However, these coherent noise sources are treated as an uncertainty later. All signal processing is performed with the MATLAB-scripts provided in Appendix E.3.

3.7.1   Zero-crossing method

The zero-crossing method is based on using direct measurements of the difference in transit time between Pulse A and B to calculate the sound velocity of the sample. It is a widely used method [15, 27, 45], but can be somewhat inaccurate if the pulses are too short to contain a steady state region. The reason is that there are other frequencies in the transient part of the pulse as the driving frequency has not yet been reached. Thus, if the medium is dispersive, time detection in the transient part may cause erroneously measurements. Additionally, the time shift between the zerocrosses in the transient part of the pulses fluctuates more than between the zerocrosses in the steady state part due to a lower SNR.

The transit time difference is measured by detecting the same part of the pulse in both the direct propagating pulse and the two-time reflected pulse. This can be done by detecting the time difference between the same zerocross number in both pulses, as illustrated with the eighth zerocross in Fig. 3.38.
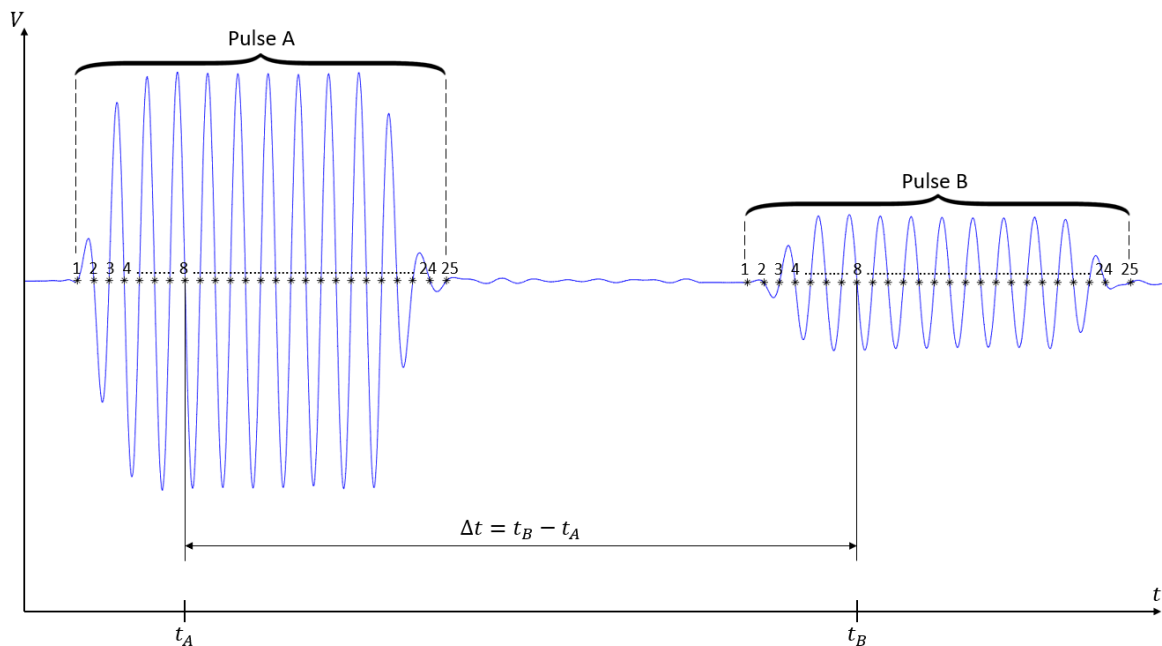
Figure 3.38: Illustration of how a zerocross in Pulse A, and the corresponding zerocross in Pulse B, can be used to calculate the difference in transit time between the two pulses. In this example, zerocross number 8 is used. The pulse length is set to be 10 periods.

Higher accuracy is obtained by averaging the transit time difference over all zerocrosses in the steady state part of the pulses.

When a signal is sampled by an oscilloscope, it is built up of several discrete points constituting the waveform. Thus, none of the points are actually located exactly at zero. The zerocrosses must therefore be localized manually after the waveform has been sampled. One solution may be to first locate approximate zerocrosses by finding the indices, i, of the waveform where the amplitude swaps sign. Then, linear interpolation is used on index number i and $i + 1$ for all those points in the waveform.

Linear interpolation is a curve fitting method using linear polynomials to calculate intermediate data between two adjacent known data points [93]. The principle is illustrated in Fig. 3.39.
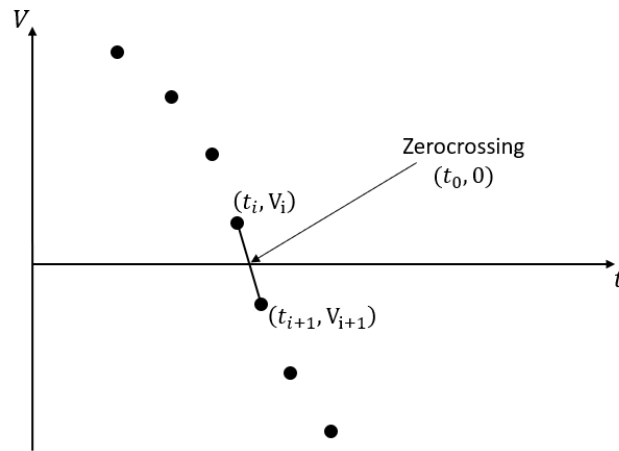
Figure 3.39: Illustration of the principle of linear interpolation.

Fig. 3.39 shows how a zerocross is found at $(t_0, 0)$ by using interpolation between points (t_i, V_i) and (t_{i+1}, V_{i+1}). In mathematical terms, the point-slope equation [94] is used to find the slope between the two adjacent known data points. The slope is given as

$$m = \frac{V_{i+1} - V_i}{t_{i+1} - t_i}.$$

(3.10)

Now, swapping t_{i+1} for t_0 and V_{i+1} for 0 in Eq. 3.10, and solving for t_0 gives

$$t_0 = t_i - \frac{V_i}{m},$$

(3.11)

where both t_i, V_i and m are known. Since the frequency and amplitude of the waveforms in this work is relatively high, the part of the pulses around zero will be close to linear. Hence, linear interpolation is assumed to be sufficient for finding the zerocrosses [27].

It is important to remember to distinguish the zerocrosses in the noise from the zerocrosses in the signals of interest. Fig. 3.40 shows that, initially, there are zerocrosses across the whole waveform.
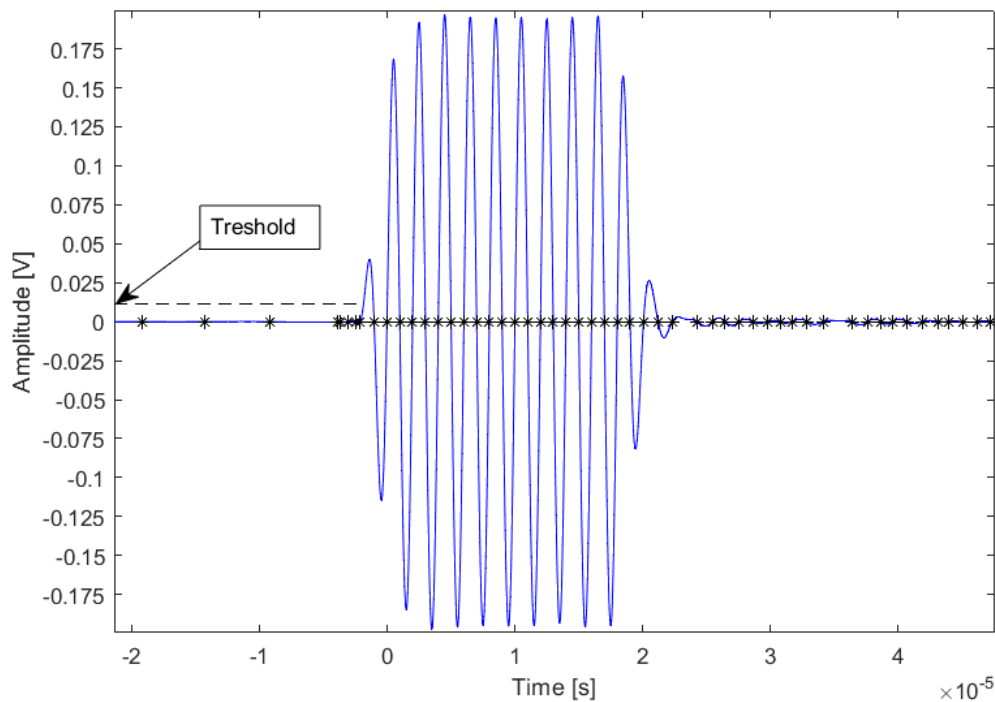
Figure 3.40: Plot of a waveform sampled by an oscilloscope and filtered in MATLAB [73]. The waveform is generated by a signal generator set to generate a 10 period long pulse. The black stars represent the zerocrosses.

The zerocrosses that do not represent the signals of interest are removed by setting a treshold value. The treshold value must be higher than the noise, but low enough to detect the start of the pulses. When the treshold value is exceeded, it indicates that the next zerocrosses are within the signal of interest. For the waveform in Fig. 3.40, a treshold value of e.g. 0.01 would be sufficient. The end of the pulses is found by only keeping the first $n-1$ zerocrosses subsequent to the first zerocross. As the waveform crosses the zero-axis twice for each period, a ten period pulse would result in a total of $n = 20$ zerocrosses. However, it has been found that if the signal generator is set to generate a ten period pulse, the pulses will contain a total of 25 zerocrosses, which is five more than what is expected, cf. Fig. 3.38. This is due to the transducers needing time to start oscillating at the desired magnitude [95]. The same is observed for all pulse lengths between 1 and 10 periods. Consequently, the total number of zerocrosses that are of interest for each pulse is defined as $n+5$, where n is twice the number of periods set to be generated by the signal generator.

3.7.2   Fourier spectrum method

In the Fourier spectrum method, FSM, [45, 96, 97], the discrete Fourier transform, DFT, of Pulse A and Pulse B is used to calculate the sound velocity of the specimen in the frequency domain. The DFT is given as [98]

$$X_k = \sum_{n=0}^{N-1} x_n e^{-i\frac{2\pi}{N}kn} \qquad (3.12)$$

where a sequence of N complex numbers, $x_n = x_0, x_1, \dots x_{N-1}$, are transformed into another sequence of complex numbers, $X_k = X_0, X_1, \dots X_{N-1}$. The method is based on using the unwrapped phase angle of the DFT of Pulse A and B to calculate the sound velocity. Theory regarding calculations of sound velocity in the frequency domain is presented in Section 2.6, where a formula for c is given in Eq. 2.51. Here, the FSM will be explained using distilled water at room temperature as the liquid sample and a pulse length of ten periods at 500 kHz.

The first step when using the FSM to calculate the sound velocity, is to identify the pulses of interest. Using the zerocrossing method presented in the previous section, the start of the pulses are defined where the first zerocross is detected, and the end is defined at zerocrossing number $n + 5$, where n is twice the number of periods, for each pulse. For a ten period pulse, this means that the start is at zerocrossing number 1, and the end is at zerocrossing number 25, as mentioned above.

When the pulses are identified, the steady state part of each pulse is extracted. The waveform is essentially zero padded by setting all parts of the total signal except the steady state parts to zero. Fig. 3.41 shows the original waveform, and the waveform after zero padding. The waveform contains a total of 100 000 samples.

(a)

(b)
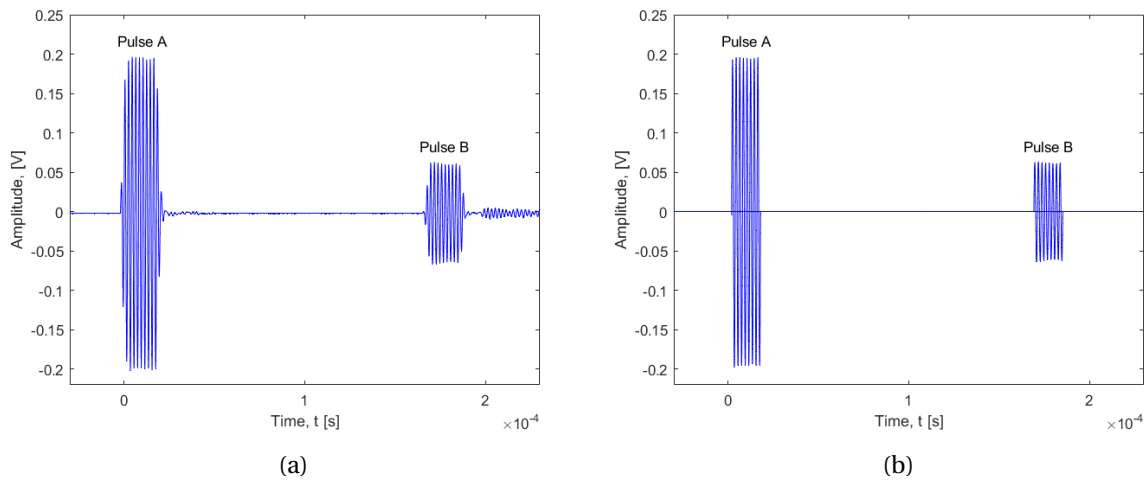
Figure 3.41: Original waveform and zero padded waveform of a ten-period pulse at 500 kHz in distilled water at room temperature. (a) Original waveform, (b) Zero padded waveform.

The DFT of the steady state part of Pulse A and B is computed using a fast Fourier transform (FFT) algorithm in MATLAB [73]. Only the steady state part is used since it was found that an inclusion of the transient parts resulted in more unstable results. It should be noted that abruptly truncating the signal by extracting only the steady state parts of the pulses may cause aliasing effects [45]. However, the potential aliasing effects are assumed to be small by comparing the measured sound velocities in Fig. 3.42.
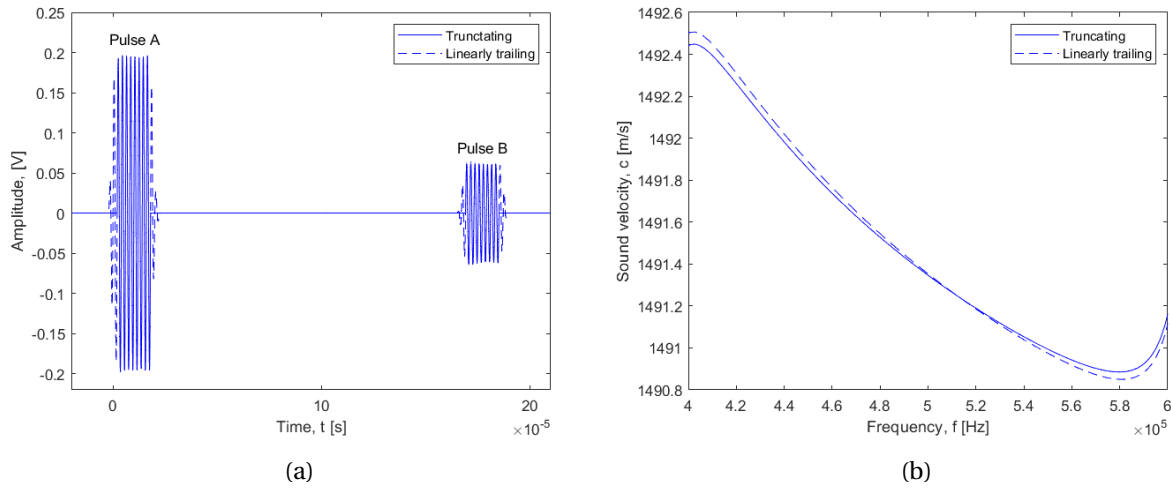
Figure 3.42: Original waveform and zero padded waveform of a 10 period pulse at 500 kHz in distilled water at room temperature. (a) Original waveform, (b) Zero padded waveform.

The figure compares the sound velocities found from abruptly truncating the signal at each end of the steady state region and linearly trailing the signal in the transient part of the pulses. A small change in measured sound velocity as a function of frequency can be seen between the two cases. However, at the frequency of interest, i.e. 500 kHz, the measured sound velocities are almost identical. For the truncated signal, the measured sound velocity is $c = 1491.346$ m/s, while for the linearly trailed signal, the measured sound velocity is $c = 1491.353$ m/s. The difference is only 0.007 m/s which is assumed to be negligible, and it will thus be treated as an uncertainty. The corresponding uncertainty in transit time difference is found to be

$$u(\Delta t)_{trunc} = \frac{2 \cdot 125\ mm}{1491.346\ m/s} - \frac{2 \cdot 125\ mm}{1491.353\ m/s} = 7.87 \cdot 10^{-10}\ s, \qquad (3.13)$$

using Eq. 2.33. The exact temperature was unfortunately not measured during these tests, but they were performed at room temperature. A transducer distance of 125.00 mm is therefore assumed as that was found to be the transducer distance at $22.8°C$, cf. Section 5.3.1. The measured sound velocities above are not corrected for diffraction.

For the sound velocity calculations, the unwrapped phase angle of the DFT of the pulses is used. When MATLAB computes the DFT, the angles are given as wrapped phase angles, meaning that the angles are oscillating within the interval $[-\pi, \pi]$, as shown in Fig. 3.43b [73]. By subtracting 2π to the wrapped phase angles at all frequencies where there is a phase-jump, the unwrapped phase angle is obtained. The unwrapped phase is found with the *unwrap* command in MATLAB [73], and is shown in Fig. 3.43c. Some small jumps can be observed in the unwrapped phase spectrum, indicated with circles. These distortions are a result of noise interfering with the signal of interest outside the bandwidth, where the signal-to-noise ratio is low. Comparison of the magnitude and phase spectra in Fig. 3.43 shows that the phase-jumps in the unwrapped phase spectra are found at the frequencies where there is a dip in the magnitude spectra, i.e. where the SNR is low. The possible impact of the jumps

in the phase spectra are discussed further in Chapter 6. The unwrapped phase angle of the DFT of Pulse A and B corresponds to $\angle V_{6,A}$ and $\angle V_{8,B}$, respectively, in Eq. 2.51, and will be used to calculate the sound velocity.
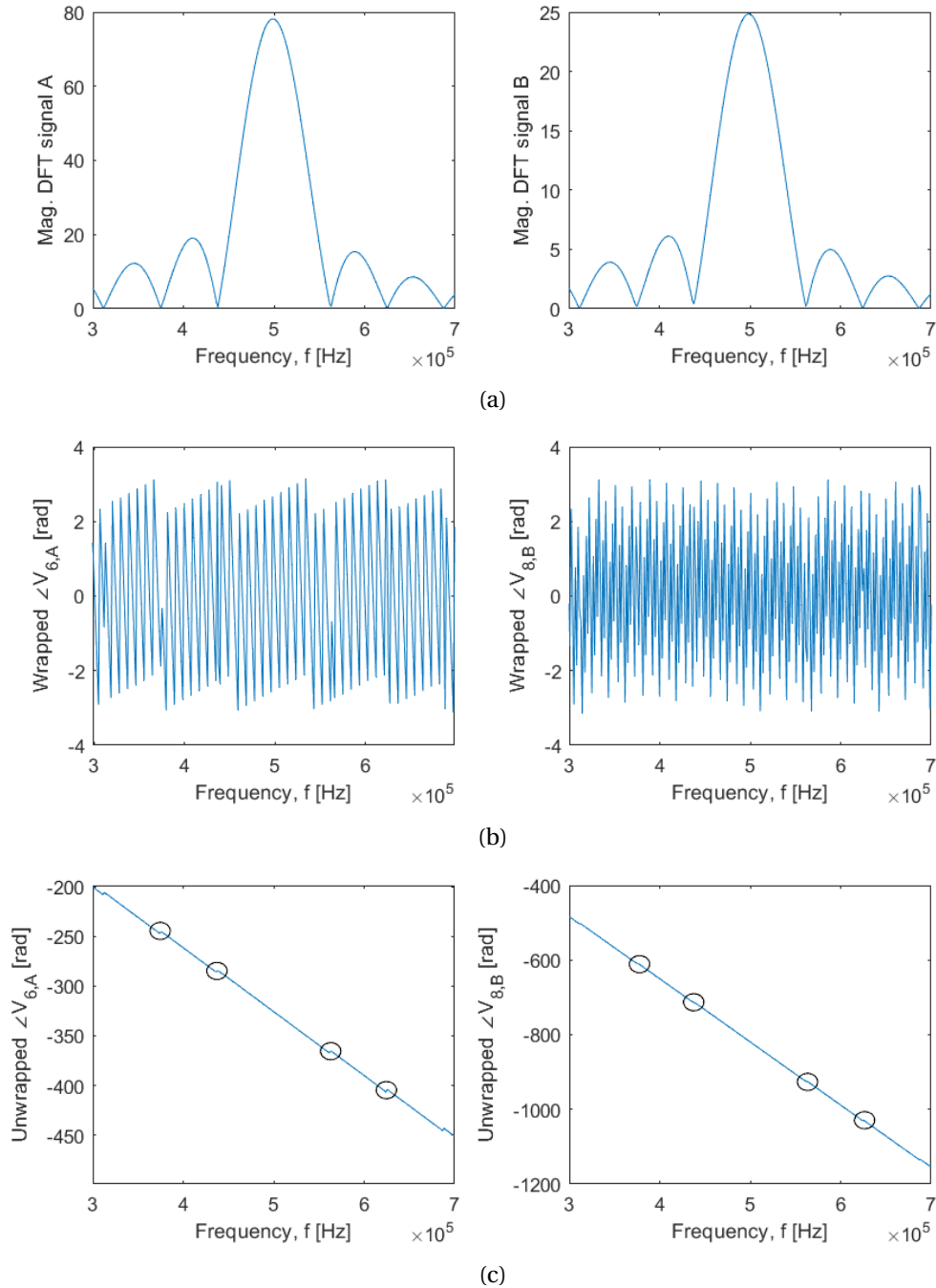
Figure 3.43: The magnitude and phase angle of the DFT of the steady state part of Pulse A (to the left) and Pulse B (to the right). (a) Magnitude of the DFT of the pulses as a function of frequency. (b) Wrapped phase of the DFT of the pulses as a function of frequency. (c) Unwrapped phase of the DFT of the pulses as a function of frequency. The output signal is set to be 10 periods at 500 kHz frequency and the waveform is averaged 512 times. The circles highlight the distortions in the unwrapped phase spectra.

3.7.3   Filtering

As mentioned in Section 2.9, the signal-to-noise ratio should be kept as high as possible to reduce the probability of measurement errors. Coherent noise is discussed in Section 3.3. Incoherent noise is reduced by through averaging. Additionally, noise with frequencies other than the frequency of the signal of interest is further reduced through filtering. Both analog and digital filters can be applied to reduce noise. While analog filters consist of analog components such as inductors, capacitors and resistors connected in a circuit, digital filters are usually embedded in a chip such as a digital signal processor (DSP) [99, 100]. Both analog and digital filters remove noise outside of the passband frequencies [99], but it may be more challenging to make changes to an analog filter than a digital filter [40]. All analog signals must be digitized before passing through a digital filter.

Originally, two analog Krohn-Hite Model 3940 filters [101] were implemented in the measurement circuit. One of the filters served as a lowpass filter with cut-off frequency 800 kHz, while the other served as a highpass filter with cut-off frequency 200 kHz. Fig. 3.45 shows an example of how the filtering affects the sampled signal when the transmitting transducer generates sound waves at 500 kHz and length 10 periods.
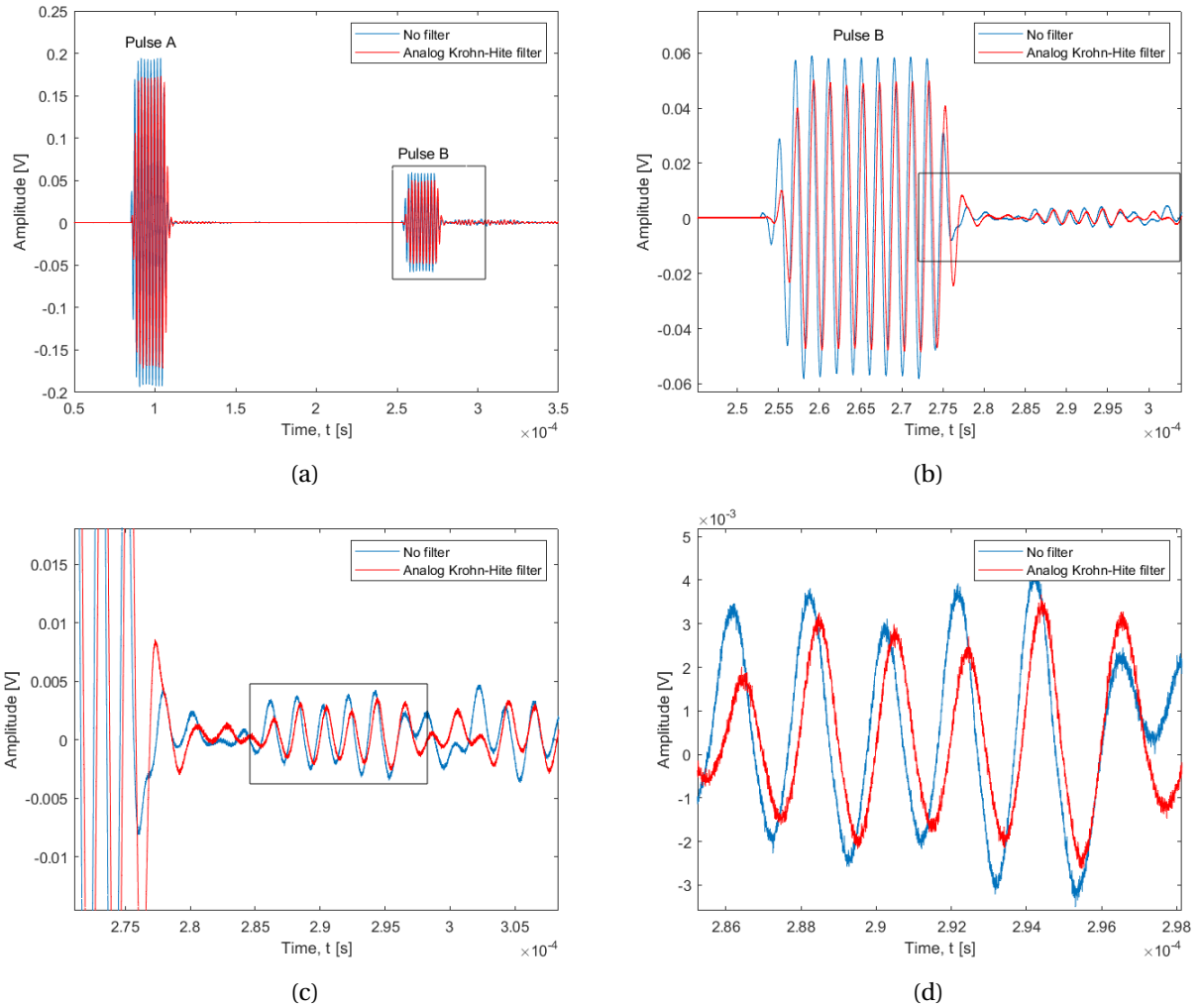
Figure 3.44: Sampled waveform when the generated signal is transmitted at 500 kHz and pulse length 10 periods. The blue waveform represents the raw signal while the red waveform represents the signal after it has been filtered by two analog Krohn-Hite filters: one of which serve as a lowpass filter with cut-off frequency 800 kHz, and another serving as a highpass filter with cut-off frequency 200 kHz. The filter gain is set to 1 for both filters. (a) Complete sampled waveform, (b) Enlargement of the area inside the black rectangle in (a), (c) Enlargement of the area inside the black rectangle in (b), (d) Enlargement of the area inside the black rectangle in (c).

Evidently, the Krohn-Hite filters cause a significant reduction in the amplitude of Pulse A and B, even if the filter gain is set to be equal to 1. It can also be seen that the filters give rise to a phase shift of approximately one eighth of a period and the first peak prior to Pulse B has been reduced to the point where it is difficult to define the start of the pulse. Consequently, a digital filter is opted for instead.

A number of digital filters were tested to find the most promising one. Eventually, a digital Butterworth filter combined with a lowpass Chebyshev Type I filter was found to be the most fitting. Before applying the filters, the sampled waveform is decimated. Decimation is the process of digitally resampling the signal with a lower sample rate [102]. In MATLAB, decimation is performed through the function `decimate(x,r)`, where the sample rate of x is reduced by a factor r [73]. In this work, the signal is decimated with a factor 5, reducing the sample frequency from 250 MHz to 50 MHz, making

it less demanding to process the data. The function then applies a lowpass Chebyshev Type I infinite impulse response (IIR) filter of order 8 to ensure that the Nyquist-Shannon theorem [7] is fulfilled after decimation. The filter has a default normalized cut-off frequency of 0.8 divided by the decimation factor, resulting in 0.16 for this work.

Further, the digital Butterworth filter is applied. The Butterworth filter is a signal processing filter that have a relatively high roll-off and a frequency response that is optimally flat in the passband [103]. Similarly to the Chebyshev Type I filter, it is an infinite-impulse-response (IIR) filter which entails that it has an impulse response $h(t)$ that does not become exactly zero past a certain point [93]. They are also often referred to as *recursive* filters. The output of such filters is computed based on a feedback system where both previously computed values of the output signal as well as values of the input signal are used [93]. The Z-transform may be used in calculation of the frequency response of recursive filters [104]. The Z-transfer function $G(z)$ of a recursive filter can be written as [93]

$$G(z) = \frac{a_0 + a_1 z^{-1} + a_2 z^{-2} + ... + a_n z^{-n}}{1 + b_1 z^{-1} + b_2 z^{-2} + ... + b_m z^{-m}},$$
(3.14)

where $a_0...a_n$ and $b_1...b_m$ are the filter coefficients and z is, in general, a complex number given as

$$z = Ae^{j\phi},$$
(3.15)

where A is the magnitude of z, j is the imaginary unit and ϕ is the angle. In MATLAB, the function "butter" can be used to design a Butterworth filter for the sampled signal [73]. The function takes the desired filter order and bandpass cut-off frequencies as input, and returns the filter coefficients of the transfer function in descending powers of z. In this work, the lower and higher cut-off frequency are set to 100 kHz and 1 MHz, respectively, and the filter order is set to 4. The designed filter is then applied to the sampled signal by using the filter coefficients together with the MATLAB command `filtfilt` [73]. Filtfilt adds a second backward application of the filter which cancels out the phase delay of the filter [73, 104]. The filtfilt command is also automatically applied whenever 'decimate' is used, to remove phase distortion from the Chebyshev filter.
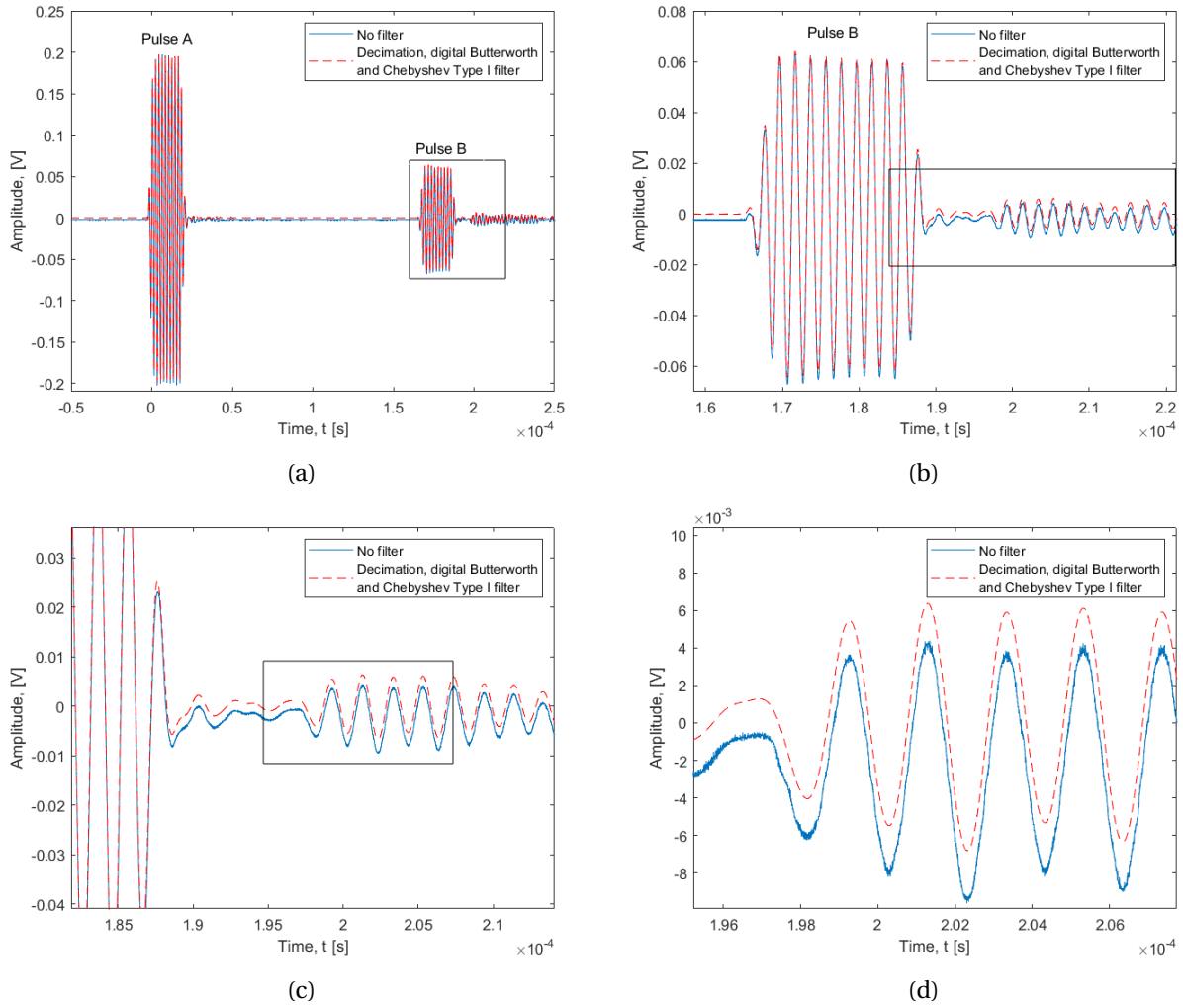
Figure 3.45: Sampled waveform when the generated signal is transmitted at 500 kHz and pulse length 10 periods. The blue waveform represents the raw signal while the red waveform represents the signal after it has been decimated and digitally filtered with a Butterworth filter and a Chebyshev Type I filter. The Butterworth filter has lower and higher cut-off frequencies 100 kHz and 1 MHz, respectively, and filter order 4. The Chebyshev filter has a default normalized cut-off frequency of 0.8 divided by the decimation factor [73], resulting in 0.16 for this application. (a) Complete sampled waveform, (b) Enlargement of the area inside the black rectangle in (a), (c) Enlargement of the area inside the black rectangle in (b), (d) Enlargement of the area inside the black rectangle in (c).

The white noise and DC-component of the generated signal is removed by the filters. Also, there are no apparent phase delay due to the filter, which is expected when using filtfilt [73]. However, by greatly zooming in on a zerocross in either of the pulses, a small phase delay can be seen. In the figure below, the original signal (after only removing the DC-component) and the filtered signal are plotted on top of each other. The time difference between each zerocrossing in the original and filtered signal is calculated through a simple for-loop in MATLAB [73]. A vector of the time difference of each zerocross is generated, and the maximum difference is found at zerocrossing number 22, which is highlighted in Fig. 3.46. The maximum time difference will be treated as an uncertainty in transit time, and is found to be $u(\Delta t)_{filt} = 1.15 \cdot 10^{-9}$ s.
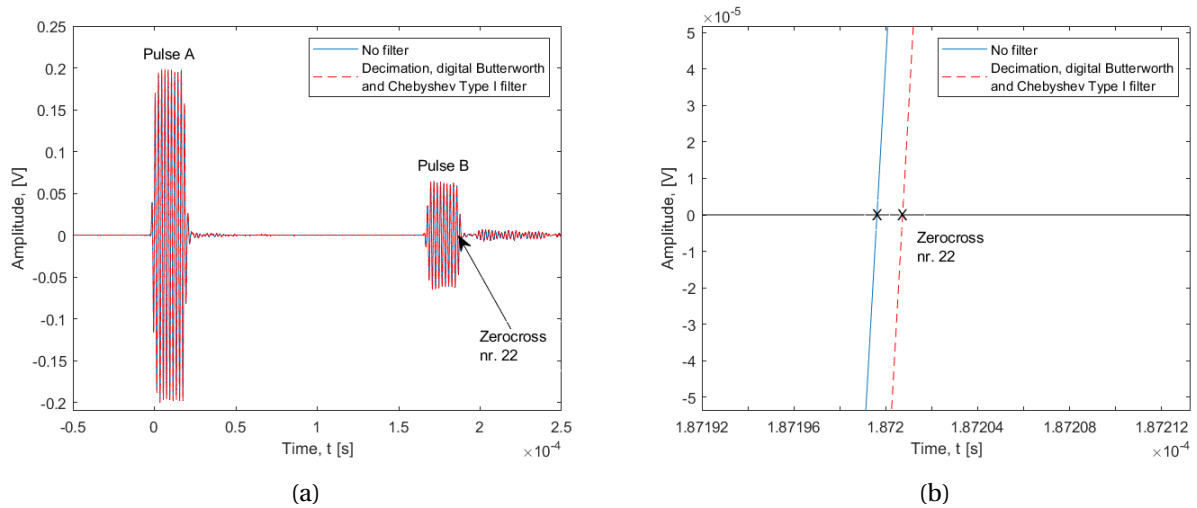
Figure 3.46: Sampled waveform when the generated signal is transmitted at 500 kHz and pulse length 10 periods. The blue waveform represents the raw signal (with the DC-component removed) while the red waveform represents the signal after it has been decimated and digitally filtered with a Butterworth filter and a Chebyshev Type I filter. The Butterworth filter has lower and higher cut-off frequencies 100 kHz and 1 MHz, respectively, and filter order 4. The Chebyshev filter has a default normalized cut-off frequency of 0.8 divided by the decimation factor [73], resulting in 0.16 for this application. (a) Complete sampled waveform, (b) Enlargement of zerocrossing number 22.

Chapter 4

Uncertainty model and sensitivity analysis

One of the main objectives in this master's thesis is to construct a measurement cell that can measure the sound velocity with a *relative expanded uncertainty* at 95 % confidence level of maximum 1000 ppm. Chapter 4 describes the uncertainty models used for uncertainty calculations in this work. A sensitivity analysis carried out prior to constructing the measurement cell is also provided here. Only the models and derivation of formulas is included in this chapter. Experimental results of sound velocity measurements, and their corresponding uncertainties, are given in Section 5.4. Example uncertainty budgets used to calculate the uncertainty of the experimental sound velocity are also provided throughout Chapter 5. As the value of some uncertainty contributors are acquired for each measurement, values for each of the uncertainty contributors constituting the total uncertainty, as well as how they are found or estimated for a given measurement, are also provided here.

Chapter 4 is divided into four main sections. Section 4.1 presents uncertainty notations used throughout the project. In Section 4.2, an uncertainty model for the experimental sound velocity is derived. Here, uncertainty models for each of the uncertainty contributors to the total uncertainty of the sound velocity is presented in subsections. A sensitivity analysis carried out prior to designing the measurement cell is provided in Section 4.3. Finally, Section 4.4 presents two uncertainty models for the modelled sound velocities: one for distilled water, and another for saline water. As the modelled sound velocities are pressure dependent, an uncertainty model for the measured pressure is also provided here.

All uncertainty models in this work follow the *International Bureau of Weights and Measures* [105] and [106]. The layout of the models is inspired by [46] and [84].

4.1   Notations used in uncertainty calculations

To clarify notations used in the uncertainty models in this chapter, the applied symbols are listed in Table 4.1. The notations are based on notations used in [107] which follows [105].

Table 4.1: Uncertainty notations used throughout the project. Notations are based on [107] which follows [105].

Standard uncertainty of measurand x	$u(x)$
Combined standard uncertainty of measurand x, where x is a function of n variables, $f(x) = f(x_1, x_2, ..., x_n)$	$u_c(x)$
Sensitivity coefficient of variable x_i, $i = 1, 2, ..., n$	$\frac{\partial f(x)}{\partial x_i}$
Coverage factor	k
Expanded uncertainty of measurand x	$U(x) = u(x) \cdot k$
Relative standard uncertainty of measurand x	$E_x = \frac{u(x)}{x}$
Relative expanded uncertainty of measurand x	$E_x \cdot k$

More information about the uncertainty standards used in this work is provided in Appendix C.

4.2 Uncertainty model for the measured sound velocity

A model for the combined standard uncertainty of the experimental sound velocity measurements is presented in this section. The model serve as a base for the sensitivity analysis presented in the next section, and is used in the uncertainty budgets carried out in Chapter 5.

In Chapter 2, a formula for the measured sound velocity in both the time domain and the frequency domain was derived. For clarification, the formula is repeated here:

$$c = \frac{2K_T L_0}{\Delta t - t^{corr}}.$$ (4.1)

According to [105] the combined standard uncertainty of c, within a 68% confidence level, assuming uncorrelated parameters, can be expressed as

$$u_c^2(c) = \left(\frac{\partial c}{\partial L_0} \cdot u_c(L_0) \right)^2 + \left(\frac{\partial c}{\partial t^{corr}} \cdot u_c(t^{corr}) \right)^2 + \left(\frac{\partial c}{\partial \Delta t} \cdot u_c(\Delta t) \right)^2 + \left(\frac{\partial c}{\partial K_T} \cdot u_c(K_T) \right)^2$$ (4.2)

where $u_c(L_0)$, $u_c(t^{corr})$, $u_c(\Delta t)$ and $u_c(K_T)$ are the combined standard uncertainties of L_0, t^{corr}, Δt and K_T, respectively. The partial derivatives in Eq. 4.2 can be derived to get the following expression:

$$u_c^2(c) = \left(\frac{2K_T}{\Delta t - t^{corr}} \cdot u_c(L_0) \right)^2 + \left(\frac{2K_T L_0}{(\Delta t - t^{corr})^2} \cdot u_c(t^{corr}) \right)^2$$
$$+ \left(-\frac{2K_T L_0}{(\Delta t - t^{corr})^2} \cdot u_c(\Delta t) \right)^2 + \left(\frac{2L_0}{\Delta t - t^{corr}} \cdot u_c(K_T) \right)^2.$$ (4.3)

The *expanded* uncertainty is a quantity that defines an interval that is expected to contain a large fraction of the values of the measurements that has been taken [105]. The probability of a measure-

ment having a value within this interval is dependent on the coverage factor k. Multiplication of the combined standard uncertainty with k results in an expanded uncertainty with a confidence level associated with the value of k, i.e.

$$U^2(c) = k \cdot \left(\left(\frac{2K_T}{\Delta t - t^{corr}} \cdot u_c\left(L_0\right) \right)^2 + \left(\frac{2K_T L_0}{(\Delta t - t^{corr})^2} \cdot u_c\left(t^{corr}\right) \right)^2 \right.$$
$$\left. + \left(-\frac{2K_T L_0}{(\Delta t - t^{corr})^2} \cdot u_c(\Delta t) \right)^2 + \left(\frac{2L_0}{\Delta t - t^{corr}} \cdot u_c\left(K_T\right) \right)^2 \right), \tag{4.4}$$

where $k = 2$ for a 95% confidence level [105]. By inserting Eq. 4.1, this equation may be simplified to

$$U^2(c) = k \cdot \left(\left(\frac{c}{L_0} \cdot u_c\left(L_0\right) \right)^2 + \left(\frac{c}{\Delta t - t^{corr}} \cdot u_c\left(t^{corr}\right) \right)^2 \right.$$
$$\left. + \left(-\frac{c}{\Delta t - t^{corr}} \cdot u_c(\Delta t) \right)^2 + \left(\frac{c}{K_T} \cdot u_c\left(K_T\right) \right)^2 \right). \tag{4.5}$$

Division of all terms in Eq. 4.5 by c^2 gives

$$\frac{U^2(c)}{c^2} = k \cdot \left(\left(\frac{u_c\left(L_0\right)}{L_0} \right)^2 + \left(\frac{u_c\left(t^{\text{corr}}\right)}{\Delta t - t^{\text{corr}}} \right)^2 + \left(-\frac{u_c(\Delta t)}{\Delta t - t^{\text{corr}}} \right)^2 + \left(\frac{u_c\left(K_T\right)}{K_T} \right)^2 \right). \tag{4.6}$$

If the sample is 50 ppt saline water at $60°C$, the difference in transit time between Pulse A and B is approximately

$$\Delta t = \frac{2L_0}{c} = \frac{2 \cdot 125 \, mm}{1593 \, m/s} = 157 \, \mu s. \tag{4.7}$$

Given that oils generally have lower sound velocity than water, this will be roughly the lowest value of Δt in this work. Moreover, the correction term t^{corr} is dominated by diffraction correction. Pulse A will have a diffraction correction corresponding to a time shift of less than a quarter of a period [47]. The corresponding diffraction correction for Pulse B is thus less than three quarters of a period, according to diffraction correction Method 1, cf. Section 2.3.1. As a result, the total time shift due to diffraction correction will be less than half a period. In Method 2, both Pulse A and B has a diffraction correction corresponding to a time shift of less than a quarter of a period. The correction term will thus never exceed a value of

$$t^{corr} = \frac{1}{2} \cdot \frac{1}{500\text{kHz}} = 1\mu s. \tag{4.8}$$

Consequently, $\Delta t >> t^{corr}$, and Eq. 4.6 can be further simplified to

$$\frac{U^2(c)}{c^2} = k \cdot \left(\left(\frac{u_c(L_0)}{L_0} \right)^2 + \left(\frac{u_c\left(t^{\mathrm{corr}}\right)}{\Delta t} \right)^2 + \left(-\frac{u_c(\Delta t)}{\Delta t} \right)^2 + \left(\frac{u_c(K_T)}{K_T} \right)^2 \right).$$ (4.9)

The relative standard uncertainty, E, for each variable, is introduced as $E_{L_0} = \frac{u_c(L_0)}{L_0}$, $E_{t^{corr}} = \frac{u_c(t^{corr})}{t^{corr}}$, $E_{\Delta t} = \frac{u_c(\Delta t)}{\Delta t}$ and $E_{K_T} = \frac{u_c(K_T)}{K_T}$ for L_0, t^{corr}, Δt and K_T respectively. In addition $E_c \cdot k = \frac{U(c)}{c}$ is the relative expanded uncertainty of c. Using these notations, Eq. 4.9 may be expressed in terms of relative uncertainties, i.e.

$$k \cdot E_c = k \cdot \sqrt{E_{L_0}^2 + E_{K_T}^2 + E_{\Delta t}^2 + \frac{(t^{\mathrm{corr}})^2}{(\Delta t)^2} E_{t^{corr}}^2}.$$ (4.10)

An uncertainty model for each of the uncertainty contributors in Eq. 4.2 is presented in the following. Also, since most of the parameters are temperature dependent, an uncertainty model for the combined standard uncertainty of the measured temperature, $u_c(T)$, is introduced.

4.2.1 Uncertainty model for temperature measurements

The temperature is measured with the calibrated Pt100 element described in Section 3.4. The temperature sensor has Class A type accuracy, and there are uncertainties connected to the calibration. The adapter used to read temperature data from the sensor also carries its own uncertainty, and there will be uncertainties related to variation in temperature during measurements. The combined standard uncertainty of the temperature measurements can be modelled as

$$u_c^2(T) = u^2(T)_{Pt100} + u^2(T)_{drift} + u^2(T)_{ref.Pt100} + u^2(T)_{ref.drift}$$
$$+ u^2(T)_{scanner} + u^2(T)_{temp.dev.} + u^2(T)_{RTD-USB} + u^2(T)_{temp.var.} + u^2(T)_{other}$$ (4.11)

assuming all terms are uncorrelated and that all sensitivity coefficients are equal to 1. Table 4.2 shows an overview of the different contributors, and a corresponding description.

Table 4.2: Description of the uncertainty contributors to the combined standard uncertainty of measured temperature.

Uncertainty contributor	Description
$u(T)_{Pt100}$	Standard uncertainty of the 3 wire RS Pt100 sensor. Class A type accuracy [79].
$u(T)_{drift.}$	Standard uncertainty due to drift because of ageing of the 3 wire RS Pt100 sensor [108].
$u(T)_{ref.Pt100}$	Standard uncertainty of the 4 wire JUMO reference Pt100 sensor, used for calibration [109]. 1/10 DIN type accuracy.
$u(T)_{ref.drift}$	Standard uncertainty due to drift because of ageing of the 4 wire JUMO reference Pt100 sensor [108].
$u(T)_{scanner}$	Standard uncertainty in the Fluke 1586A temperature scanner used for calibration [110].
$u(T)_{dev.}$	Standard uncertainty due to deviation from the 4 wire JUMO reference Pt100 sensor after calibration.
$u(T)_{RTD-USB}$	Standard uncertainty of the Dracal RTD-USB adapter [81].
$u(T)_{temp.var.}$	Standard uncertainty due to observed variation in temperature during stable conditions (5 min.).
$u(T)_{other}$	Standard uncertainty due to other sources.

4.2.2 Uncertainty model for the thermal expansion

Rising temperatures will cause the measurement cell to expand. The increase in transducer distance due to the thermal expansion is found from the thermal expansion coefficient, introduced in Section 2.4. The combined standard uncertainty of the thermal expansion coefficient can be written as

$$u_c^2(K_T) = (\Delta T \cdot u(\alpha_T))^2 + (\alpha_T \cdot u(\Delta T))^2, \tag{4.12}$$

using Eq. 2.28. Table 4.3 summarizes the uncertainty contributors with an associated description.

Table 4.3: Description of the uncertainty contributors to the combined standard uncertainty of the thermal expansion coefficient.

Uncertainty contributor	Description
$u(\alpha_T)$	Standard uncertainty in the linear thermal expansion coefficient [60, 61, 62].
$u(\Delta T)$	Standard uncertainty in the temperature difference between the reference temperature, T_0, at which L_0 was measured, and the current temperature, T.

4.2.3 Uncertainty model for length measurements

The transmitting and receiving transducer are mounted on opposite sides of the measurement cell, as explained in Section 3.1.1. The distance between the transducers is measured with a digital Sylvac S_Cal PRO caliper [111]. The caliper has a max error, specified by the manufacturer. In addition, there will be uncertainties related to caliper drift and resolution, repeatability of measurements, as well as orientation and roughness of the transducer surfaces. The combined standard uncertainty of

the length measurements can be modelled as

$$u_c^2(L_0) = u^2(L_0)_{caliper} + u^2(L_0)_{drift} + u^2(L_0)_{resolution}$$
$$+ u^2(L_0)_{repeatability} + u^2(L_0)_{surface} + u^2(L_0)_{other}, \tag{4.13}$$

assuming all sensitivity coefficients are equal to 1 and no correlation between the terms. Table 4.4 shows an overview of the different contributors, and a corresponding description.

Table 4.4: Description of the uncertainty contributors to the combined standard uncertainty of the measured transducer distance L_0.

Uncertainty contributor	Description
$u(L_0)_{caliper}$	Standard uncertainty in the Sylvac S_cal PRO caliper (max error) [111].
$u(L_0)_{drift}$	Standard uncertainty due to caliper stability and drift.
$u(L_0)_{resolution}$	Standard uncertainty due to the resolution of the caliper display [111].
$u(L_0)_{repeatability}$	Standard uncertainty due to repeatability of measurements.
$u(L_0)_{surface}$	Standard uncertainty due to roughness and orientation of transducer surfaces.
$u(L_0)_{other}$	Standard uncertainty due to other sources.

4.2.4 Uncertainty model for the transit time difference

Both signal processing methods presented in Section 3.7 are applied to measure the difference in transit time between Pulse A and B. While the transit time difference is measured directly from zero-crossings in the zerocrossing method, it is estimated from the phase of Pulse A and B in the Fourier Spectrum method. Consequently, the uncertainty in transit time difference, $u_c(\Delta t)$, is dependent on which signal processing method is used. Hence, two slightly different uncertainty models for $u_c(\Delta t)$ are provided: One for the ZCM, and another for the FSM.

The combined standard uncertainty of the transit time difference using the ZCM can be modelled as

$$u_c^2(\Delta t)_{ZCM} = u_c^2(\Delta t)_{coh.noise} + u^2(\Delta t)_{rand.noise} + u^2(\Delta t)_{osc.} + u^2(\Delta t)_{el.}$$
$$+ u^2(\Delta t)_{dis.} + u^2(\Delta t)_{filt.} + u^2(\Delta t)_{zc.var.} + u^2(\Delta t)_{w.bath} + u^2(\Delta t)_{other}. \tag{4.14}$$

Similarly, the combined standard uncertainty of the transit time difference using the FSM can be modelled as

$$u_c^2(\Delta t)_{FSM} = u_c^2(\Delta t)_{coh.noise} + u^2(\Delta t)_{rand.noise} + u^2(\Delta t)_{osc.} + u^2(\Delta t)_{el.}$$
$$+ u^2(\Delta t)_{dis.} + u^2(\Delta t)_{filt.} + u^2(\Delta t)_{trunc.} + u^2(\Delta t)_{w.bath} + u^2(\Delta t)_{other}. \tag{4.15}$$

All sensitivity coefficients are assumed to be 1 for both models, and the terms are assumed to be un-

correlated. The uncertainty contributors related to the measured difference in transit time between Pulse A and Pulse B are listed in Table 4.5 with an associated description.

Table 4.5: Description of the uncertainty contributors to the combined standard uncertainty of the measured difference in transit time between Pulse A and B.

Uncertainty contributor	Description
$u_c(\Delta t)_{coh.noise}$	Combined standard uncertainty due to different coherent noise sources.
$u(\Delta t)_{rand.noise}$	Standard uncertainty due to random noise from unknown sources.
$u(\Delta t)_{osc.}$	Standard uncertainty due to time resolution in the Tektronix DPO 3012 Digital Phosphor Oscilloscope [78].
$u(\Delta t)_{el.}$	Standard uncertainty due to instability in electrical components such as cables, power supply, etc..
$u(\Delta t)_{dis.}$	Standard uncertainty due to discretization of signals (bit resolution, incoherent noise and sampling frequency).
$u(\Delta t)_{filt.}$	Standard uncertainty due to time shift/phase delay in the digital filters.
$u(\Delta t)_{zc.var.}$	Standard uncertainty due to spread in time shift of zerocrossing pairs in Pulse A and B.
$u(\Delta t)_{trunc.}$	Standard uncertainty due to abruptly truncating the signal.
$u(\Delta t)_{w.bath}$	Standard uncertainty due to vibration from water bath.
$u(\Delta t)_{other}$	Standard uncertainty due to other sources.

Calculation of $u_c(\Delta t)_{coh.noise}$ and $u(\Delta t)_{dis.}$ are described in the following two subsections, respectively.

Uncertainty in Transit Time due to Coherent Noise

Coherent noise may have the same frequency as the signal of interest, but different amplitude and phase. Possible sources of coherent noise are reverberation, ringing and acoustical crosstalk, to mention some. This kind of noise can not be reduced through averaging, as can be done for incoherent noise.

In the following, the possible influence of coherent noise on the signal of interest will be investigated. The method is based on the analysis carried out by Lunde et. al. in [112]. First, let the signal of interest and the noise signal be given by

$$S_S = A\sin(\omega t) \tag{4.16}$$

and

$$S_N = B\sin(\omega t + \phi), \tag{4.17}$$

respectively. Adding the signals together will result in the combined signal

$$S_C = C\sin(\omega t + \theta) \tag{4.18}$$

with amplitude

$$C = A\sqrt{1 + \left(\frac{B}{A}\right)^2 + 2\left(\frac{B}{A}\right)\cos\phi} \tag{4.19}$$

and phase

$$\theta = \tan^{-1}\left(\frac{(B/A)\sin\phi}{1 + (B/A)\cos\phi}\right). \tag{4.20}$$

Following [46], a worst case scenario would be if the phase difference between the signal of interest and the noise signal is $\phi = \pm 90°$. In such a case, the phase of the combined signal may be expressed as

$$\theta = \pm\tan^{-1}\left(\frac{B}{A}\right), \tag{4.21}$$

which corresponds to a time shift

$$\delta t = \frac{\theta}{\omega} = \frac{\theta}{2\pi f}. \tag{4.22}$$

The relationship between a time shift and the corresponding signal-to-noise ratio that will result in such time shift can be estimated by combining Eq. 4.21, Eq. 4.22 and Eq. 2.59 to get

$$SNR = 20\log_{10}\left(\frac{A}{B}\right) = 20\log_{10}\left(\frac{1}{\tan(2\pi f \cdot \delta t)}\right). \tag{4.23}$$

Thus, if the signal-to-noise ratio is known, the worst case resulting time shift can be calculated. Fig 4.1 shows the worst case resulting time shift as a function of signal-to-noise ratios from 10 to 60 dB.
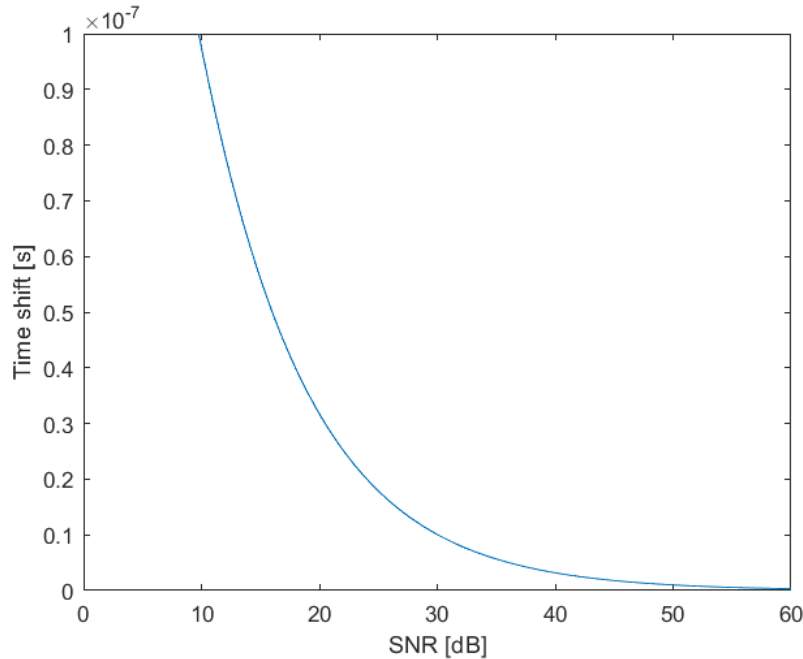
Figure 4.1: Worst case time shift as a function of signal-to-noise ratio from 10 dB to 60 dB.

This diagram is used to find the worst case resulting time shift from coherent noise sources.

Uncertainty in transit time due to discretization of signals

Time detection is performed through digital signal processing methods where the original signal is sampled and discretized. The sampling frequency should be at least twice the highest frequency in the analogue signal, according to the Nyquist-Shannon theorem [7]. The sampled signal consists of a series of points of time- and amplitude values. Both the time-axis and the amplitude-axis are discrete, where the steps in the time-axis are determined by the sampling frequency, and the steps in the amplitude-axis are determined by the bit resolution. The uncertainty due to the sampling frequency and bit resolution is treated in the following, together with uncertainty due to incoherent noise. These uncertainties are treated in a similar manner to the method used in [46].

Firstly, the combined standard uncertainty of the sampled voltage amplitude, V, due to bit resolution and incoherent noise, can be expressed as

$$u_c(V) = \sqrt{u^2(V)_{inc} + u^2(V)_{bit}}, \tag{4.24}$$

where $u(V)_{inc}$ is the standard uncertainty due to incoherent noise and $u(V)_{bit}$ is the standard uncertainty due to the bit resolution of the oscilloscope. Both sensitivity coefficients are assumed to be 1. Incoherent noise can be reduced by averaging the waveform when sampling a signal [7]. The oscilloscope used in this work is capable of averaging the waveform 512 times, which significantly reduces the incoherent noise. However, some incoherent noise will always remain. If the mean of the incoherent noise is zero, the standard deviation is equal to the root-mean-square of the incoherent noise [7]. This will be used to estimate the uncertainty due to incoherent noise.

Only the part prior to the first arrival of Pulse A is used to approximate the uncertainty. This is because it is the only part of the signal where there is only incoherent noise. The part is illustrated with a black ellipse in Fig. 4.2.
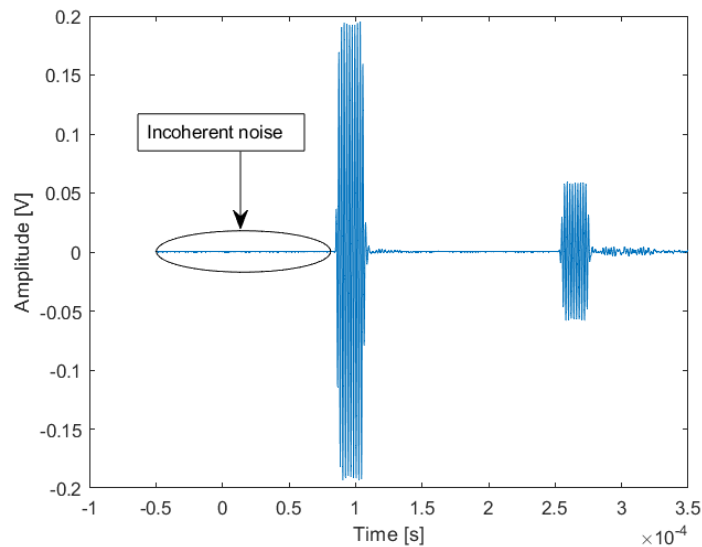
Figure 4.2: Part of signal used to calculate the RMS value of the amplitude of the incoherent noise.

After sampling a waveform, the waveform is first shifted such that the mean of the amplitude values in the ellipse in Fig. 4.2 is zero. Then the root-mean-square of those data points is used to represent the uncertainty in voltage amplitude due to incoherent noise [7]. This process will be performed in MATLAB for each acquired waveform using the script provided in Appendix E.3.4.

Further, the uncertainty in voltage amplitude due to bit resolution corresponds to the maximum quantization error, and is given as [7]

$$u(V)_{bit} = \frac{\Delta V_q}{2},$$

(4.25)

where ΔV_q is the quantization interval given by

$$\Delta V_q = \frac{V_{osc}^{max} - V_{osc}^{min}}{2^b - 1}.$$

(4.26)

Here, V_{osc}^{max} and V_{osc}^{min} are the maximum and minimum value of the oscilloscope display range, and b is the number of bits used in the quantization.

An illustration of how the uncertainty in sampled voltage amplitude due to incoherent noise and bit resolution limits the uncertainty in zerocrossing times are shown in Fig. 4.3.
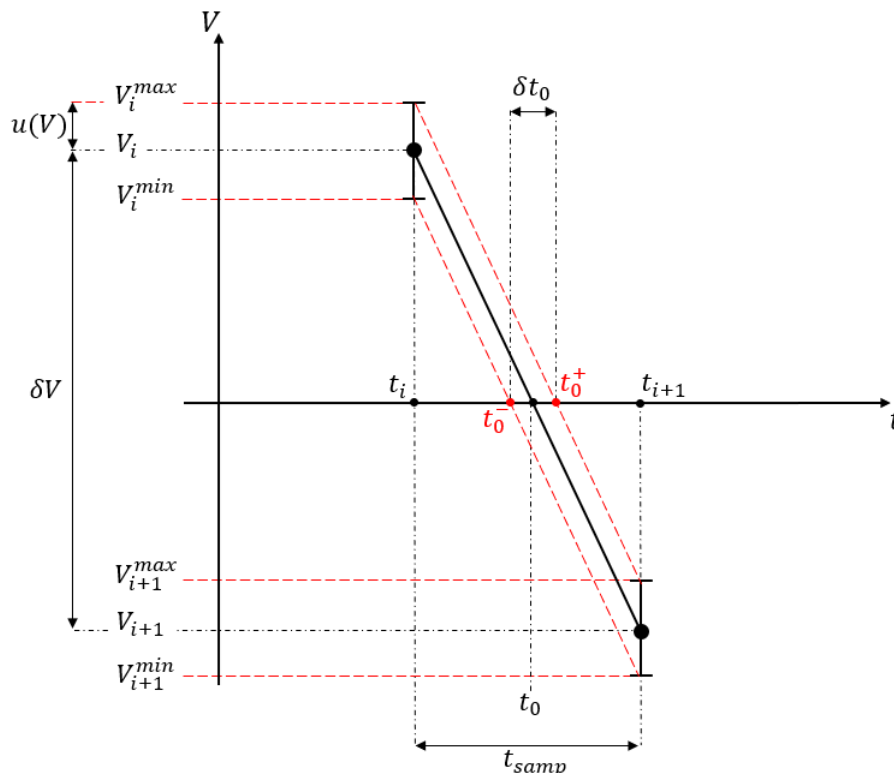
Figure 4.3: Illustration of how uncertainty in zerocrossing times are affected by the uncertainty in voltage amplitude due to bit resolution and incoherent noise. The illustration is inspired by Fig. 4.13 in [46].

In the figure, the time of sample number i, which is the sample just before a zerocross, is defined

as t_i. Consequently, t_{i+1} is the time of the sample just after the same zerocross. Correspondingly, V_i and V_{i+1} are the voltage amplitudes of sample number i and $i+1$, respectively. The maximum amplitudes V_i^{max} and V_{i+1}^{max} and minimum amplitudes V_i^{min} and V_{i+1}^{min}, for sample number i and $i+1$ respectively, are used to find the time error for the calculated zerocrossings due to bit resolution and incoherent noise. Using Eq. 3.10, the slope, m^+, through points (t_i, V_i^{max}) and (t_{i+1}, V_{i+1}^{max}) can be written as

$$m^+ = \frac{V_{i+1}^{max} - V_i^{max}}{t_{i+1} - t_i}. \tag{4.27}$$

Here, $V_i^{max} = V_i + u(V)$ and $V_{i+1}^{max} = V_{i+1} + u(V)$, as shown in Fig. 4.3. Insertion into Eq. 4.27 gives

$$m^+ = \frac{(V_{i+1} + u(V)) - (V_i + u(V))}{t_{i+1} - t_i} = \frac{V_{i+1} - V_i}{t_{i+1} - t_i}, \tag{4.28}$$

which is the same expression as in Eq. 3.10. The same can be shown for a slope, m^-, through the points (t_i, V_i^{min}) and (t_i, V_i^{min}). Hence, $m = m^+ = m^-$, assuming the incoherent noise is constant for all samples. The maximum positive error, t_0^+, is found from the maximum values of voltage amplitudes, while the maximum negative error, t_0^-, is found from the minimum values of voltage amplitudes. The error interval, δt_0, for the zerocrossing, is the difference between the positive and negative error, i.e.

$$\delta t_0 = t_0^+ - t_0^- = (t_0 + e(t_0)) - (t_0 - e(t_0)) = 2e(t_0), \tag{4.29}$$

where $e(t_0)$ is the zerocrossing time error. Inserting Eq. 3.11 into the equation above gives

$$\delta t_0 = t_0^+ - t_0^- = \left(t_i - \frac{V_i^{max}}{m}\right) - \left(t_i - \frac{V_i^{min}}{m}\right) = \frac{1}{m}\left(V_i^{min} - V_i^{max}\right) = 2e(t_0). \tag{4.30}$$

Now, solving Eq. 4.30 for $e(t_0)$ after inserting $V_i^{max} = V_i + u_c(V)$, $V_i^{min} = V_i - u_c(V)$ and Eq. 3.10 gives

$$\pm e(t_0) = \pm \frac{t_{i+1} - t_i}{V_{i+1} - V_i} \cdot \frac{(V_i - u_c(V)) - (V_i + u_c(V))}{2} = \pm \frac{t_s}{\delta V} \cdot u_c(V), \tag{4.31}$$

where the sampling period t_s and voltage difference δV are given by $t_s = t_{i+1} - t_i$ and $\delta V = V_{i+1} - V_i$, respectively, as shown in Fig. 4.3. The sampling frequency, f_s, corresponding to the sampling period, is given by

$$f_s = 1/t_s. \tag{4.32}$$

As mentioned in Section 3.1.3, the waveform sampled by the oscilloscope contains 100 000 data points. This corresponds to a sampling period

$$t_s = \frac{t_{osc}^{max} - t_{osc}^{min}}{100000},$$

(4.33)

where t_{osc}^{max} and t_{osc}^{min} are the maximum and minimum value of the time axis displayed by the oscilloscope, respectively. Eq. 4.33 may be inserted into Eq. 4.31 to find the zerocrossing time error. The calculated error will differ slightly for each zerocrossing, so the uncertainty in t_0 may be estimated by finding the average error for all zerocrosses. Hence,

$$u(t_0) \approx \bar{e}(t_0) = \frac{1}{N} \sum_{i=1}^{N} e_i(t_0)$$

(4.34)

for all N zerocrosses.

4.2.5 Uncertainty model for the correction term

Time shift due to internal reflections within the transducers and time shift due to thermal and viscous boundary layers on the transducer surfaces are neglected in this work, cf. Section 2.3.2 and 2.3.3, respectively. Consequently, the uncertainty in the correction term t^{corr} in Eqs. 2.36 and 2.52 is equal to the uncertainty in the diffraction correction, i.e.

$$u(t^{corr}) = u(t^{dif}),$$

(4.35)

where $t^{dif} = t_B^{dif} - t_A^{dif}$ in the time domain, and $t^{dif} = -\frac{\angle D_B^{dif}}{\omega} + \frac{\angle D_A^{dif}}{\omega}$ in the frequency domain, cf. Section 2.5 and 2.6, respectively.

Uncertainty in diffraction correction

In this work, two different diffraction correction methods have been used, cf. Section 2.3.1. The uncertainty of the diffraction correction is dependent on the method. In Appendix A.2 it is shown that, for Method 1, the greatest diffraction correction is obtained by choosing the longest transducer distance and the smallest effective transducer radius. On the contrary, the smallest diffraction correction is obtained by choosing the shortest transducer distance and the greatest effective transducer radius. Quite the opposite applies for Method 2. Hence, the uncertainty due to diffraction correction is estimated by inserting the measured values of a_{eff} and L which results in the greatest and smallest diffraction correction, respectively, for Method 1 and 2. The uncertainty is then represented as the deviation between the biggest and smallest diffraction correction. In order to not underestimate the uncertainty, the greatest uncertainty of the two methods is chosen as the uncertainty of the correction term. The uncertainty is calculated in Section 5.5.2.

It should be noted that the diffraction correction model presented by Khimunin [48, 49], which is the model used in this project, carry its own uncertainty. It is difficult to quantify the uncertainty of the model itself. However, the tabulated data presented in Appendix A.1 show great correspondence

between the values found by Khimunin and the values found in this project, and the uncertainty of the diffraction correction model is thus neglected in this work.

4.3   Sensitivity analysis

In this section a sensitivity analysis for the measured sound velocity is carried out. The purpose of the sensitivity analysis is to investigate how sensitive the uncertainty of the measured sound velocity is to the uncertainty of the other parameters. This is important in order to get an indication of how the measurement cell should be constructed in order to achieve the desired uncertainty target of less than 1000 ppm at 95% confidence level. The sensitivity analysis is comparable to the approach used in [27], and the calculations are based on the uncertainty model for, c, presented in the previous section. As the analysis is made prior to constructing the measurement cell, the assumptions listed below are preliminary.

Distilled water will be used as reference medium in the sensitivity analysis. It is assumed that the total uncertainty of c is temperature dependent, and increases with increasing temperature. The reason is that: (1) The measurement cell will probably be assembled at room temperature (whereas measurements will be taken up to the temperature limit of the transducers), (2) higher temperatures lead to increased change in cell dimensions due to thermal expansion, (3) the amount of disturbing air bubbles will presumably increase when the temperature increases, and (4) the transit time difference between the signal of interest and side wall reflections is probably less at higher temperatures due to an increase in sound velocity. Hence, a tentative temperature of $60°C$, just exceeding the limit of most standard transducers from Olympus [63], will be used in this analysis.

The following assumptions are made:

- The measurement cell is made out of plexiglas

- $c = 1551.1$ m/s - approximate sound velocity in distilled water at $60°C$ and 1 atm. following Eq. 2.1.

- $L_0 = 125$ mm - transducer distance at $22°C$.

- $T_0 = 22°C$ - reference temperature at which L_0 was measured.

- $\alpha_T = 7.25 \cdot 10^{-5}°C^{-1}$ - linear thermal expansion coefficient of plexiglas [60, 61, 62].

- $f = 500$ kHz - frequency of the sound waves.

Since L_0 is assumed to be measured at reference temperature, $T_0 = 22°C$, thermal expansion must be compensated for. Using Eq. 2.28, the thermal expansion coefficient for plexiglas at $60°C$ is

$$.K_T = 1 + 7.25 \cdot 10^{-5}°C^{-1} \cdot (60 - 22)°C = 1.0028. \tag{4.36}$$

Consequently, the transducer distance at $60°C$ is equal to

$$L = 125 \text{ mm} \cdot 1.0028 = 125.35 \text{ mm}. \tag{4.37}$$

A transducer distance of 125.35 mm corresponds to a transit time difference

$$\Delta t = \frac{2L}{c} = \frac{2 \cdot 125.35 \text{ mm}}{1551.1 \text{ m/s}} = 162 \, \mu s. \tag{4.38}$$

In Section 4.2 it is shown that the diffraction correction will be less than 1 μs. The correction term is therefore set to be $t^{corr} = 1 \mu s$ for the time being. Now, assuming each term in Eq. 4.10 contributes with the same amount, E, to the total uncertainty of c, the equation may be simplified to

$$k \cdot E_c = k \cdot \sqrt{4E^2}. \tag{4.39}$$

With a limit for the relative expanded measurement uncertainty of 1000 ppm at 95% confidence level, each of the four terms can contribute with 250 ppm at most at 68% confidence level. That is, if all terms contribute with the same amount. If one of the terms contributes more, one or more of the other terms has to compensate for this. In Eq. 4.10, the squared of the relative standard uncertainty of the correction term, $E_{t^{corr}}^2$, is multiplied with the relative sensitivity coefficient $\frac{(t^{corr})^2}{(\Delta t)^2}$. The preliminary values of Δt and t^{corr} is applied to find the maximum accepted value of $E_{t^{corr}}$, i.e.

$$\frac{(t^{corr})^2}{(\Delta t)^2} E_{t^{corr}}^2 = \frac{(1 \, \mu s)^2}{(162 \, \mu s)^2} E_{t^{corr}}^2 < (250 \, ppm)^2 \implies E_{t^{corr}} < 40500 \, ppm. \tag{4.40}$$

Using the tentative assumptions for the different parameters, a preliminary uncertainty budget is calculated in Table 4.6. The table shows the contribution of each term to the total uncertainty of c, when each term contribute equally, and the uncertainty limit is 1000 ppm at 95% confidence level.

Table 4.6: Preliminary uncertainty budget for the experimental sound velocity. Each term contributes equally to the total uncertainty. The medium is assumed to be distilled water, having a sound velocity of 1551.1 m/s at $60°C$.

Variable	Value	Relative standard uncertainty (68% c.l.)	Relative expanded uncertainty (95% c.l.)	Absolute expanded uncertainty (95% c.l.)
L_0	125 mm	250 ppm	500 ppm	0.0625 mm
K_T	1.0028	250 ppm	500 ppm	0.0005
Δt	162 μs	250 ppm	500 ppm	0.0810 μs
t^{corr}	1 μs	40500 ppm	81000 ppm	0.0810 μs
c	1551.1 m/s	500 ppm	1000 ppm	1.5511 m/s

Now, some adjustments will be made regarding the contribution of each term to the total uncertainty. This will result in a more realistic uncertainty budget that will serve as a base for the development of

the measurement cell.

Firstly, the combined standard uncertainty of K_T was presented in Section 4.2.2. It can be rewritten to

$$u_c\left(K_T\right) = \sqrt{\left(\Delta T \cdot u\left(\alpha_T\right)\right)^2 + \left(\alpha_T \cdot u(\Delta T)\right)^2}. \tag{4.41}$$

Some algebraic manipulation can be performed to find the corresponding relative combined standard uncertainty of K_T as a function of the relative standard uncertainties $E_{\alpha_T} = \frac{u(\alpha_T)}{\alpha_T}$ and $E_{\Delta T} = \frac{u(\Delta T)}{\Delta T}$, i.e.

$$E_{K_T} = \sqrt{\left(\frac{\alpha_T \Delta T}{1 + \alpha_T \Delta T}\right)^2 E_{\alpha_T}^2 + \left(\frac{\alpha_T \Delta T}{1 + \alpha_T \Delta T}\right)^2 E_{\Delta T}^2}. \tag{4.42}$$

Since the measurement cell is assumed to be made out of plexiglas with linear thermal expansion coefficient $\alpha_T = 7.25 \cdot 10^{-5}{}^{\circ}C^{-1}$ [60, 61, 62], it is clear that $\alpha_T \Delta T << 1$ and Eq. 4.42 can be reduced to

$$E_{K_T} = \sqrt{(\alpha_T \Delta T)^2 E_{\alpha_T}^2 + (\alpha_T \Delta T)^2 E_{\Delta T}^2} \tag{4.43}$$

Assuming both terms contribute with the same amount, Y, to E_{K_T}, the equation may be simplified to

$$E_{K_T} = \sqrt{2Y^2}, \tag{4.44}$$

resulting in $Y = 176$ ppm for $E_{K_T} = 250$ ppm, which is the current assumption. Consequently,

$$(\alpha_T \Delta T)\, E_{\Delta T} = 176\,\text{ppm}, \tag{4.45}$$

where the preliminary values of α_T and ΔT can be inserted to get

$$E_{\Delta T} = \frac{176\,\text{ppm}}{7.25 \cdot 10^{-5}{}^{\circ}C^{-1} \cdot (60 - 22){}^{\circ}C} = 63884\,\text{ppm}. \tag{4.46}$$

The corresponding absolute uncertainty of ΔT is

$$u(\Delta T) = \Delta T \cdot E_{\Delta T} = (60 - 22){}^{\circ}C \cdot 63884\,\text{ppm} = 2.43{}^{\circ}C \tag{4.47}$$

which is unreasonably high. In this work, a PT100 temperature sensor with Class A type accuracy will most likely be used. The uncertainty of such temperature probes at $60{}^{\circ}C$ is $0.27{}^{\circ}C$ (95% confidence level), according to [113]. Using the same approach as in Eqs. 4.43 through 4.47, it can be shown that a reduction of E_{K_T} from 250 ppm to 50 ppm, results in a reduction of $u(\Delta T)$ from $2.43{}^{\circ}C$ to just under $0.50{}^{\circ}C$, which is far more realistic.

For the transducer distance, L_0, the absolute expanded uncertainty is stated to be 0.0625 mm in Table

4.6. This seems reasonable as it covers the uncertainty of a standard digital high precision caliper in the workshop at the Department for Physics and Technology, which has a maximum measurement error of 0.03 mm [111]. However, since the measurement cell will be put together of several cut out cell walls, and the transducer surfaces might be slightly skewed relative to each other, the relative standard uncertainty of L_0 is increased from 250 ppm to 400 ppm. This corresponds to an increase of absolute expanded uncertainty from 0.0625 mm to 0.1 mm, reducing the likelihood of underestimating the uncertainty.

Adjustments to the relative standard uncertainty of Δt and t^{corr} are based on findings in [27]. Solberg applied the 3PM to measure the sound velocity in tap water, using both V301-SU and V302-SU transducers [63]. For the V301-SU transducers, a relative standard uncertainty of 35 ppm and 750 000 ppm for Δt and t^{corr} was reported, respectively, when driving the transducers at 330 kHz. For the V302-SU transducer, a relative standard uncertainty of 35 ppm and 2 186 000 ppm for Δt and t^{corr} was reported, respectively, when driving the transducer at 600 kHz. Since the measurement principle in this work is the same as in [27], it is assumed that the reported uncertainty of 35 ppm is a reasonable estimation for this project. Hence, the relative standard uncertainty of Δt is reduced from 250 ppm to 50 ppm to have some margin. With a limit for the relative expanded measurement uncertainty of 1000 ppm at 95% confidence level, this leaves 292 ppm for the relative standard uncertainty of t^{corr}. Taking the same relative sensitivity coefficient into account, a new value of $E_{t^{corr}}$ can be found, i.e.

$$\frac{(t^{corr})^2}{(\Delta t)^2} E^2_{t^{corr}} = \frac{(1\ \mu s)^2}{(162\ \mu s)^2} E^2_{t^{corr}} < (292\ ppm)^2 \implies E_{t^{corr}} < 47304\ ppm. \tag{4.48}$$

This is far less than the values found by Solberg. However, the relative sensitivity coefficient in this analysis is accounting for worst case scenario, where Δt is the lowest it can be and t^{corr} is the highest it can be, given that the medium is distilled water. Realistically, the sensitivity coefficient will be smaller for the actual experiments, resulting in a higher upper limit for the uncertainty of t^{corr}.

A new preliminary uncertainty budget is calculated in Table 4.7, based on the updated uncertainties. The table shows the contribution of each term to the total uncertainty of c, when the uncertainty limit is 1000 ppm at 95% confidence level.

Table 4.7: Updated preliminary uncertainty budget for the experimental sound velocity. The medium is assumed to be distilled water, having a sound velocity of 1551.1 m/s at $60°C$.

Variable	Value	Relative standard uncertainty (68% c.l.)	Relative expanded uncertainty (95% c.l.)	Absolute expanded uncertainty (95% c.l.)
L_0	125 mm	400 ppm	800 ppm	0.10 mm
K_T	1.0028	50 ppm	100 ppm	$1.0028 \cdot 10^{-4}$
Δt	162 μs	50 ppm	100 ppm	0.0162 μs
t^{corr}	1 μs	47304 ppm	94608 ppm	0.0946 μs
c	1551.1 m/s	500 ppm	1000 ppm	1.5511 m/s

4.4   Uncertainty model for the modelled sound velocities

4.4.1   Uncertainty model for pressure measurements

The modelled sound velocity in both distilled and saline water is dependent on pressure. Hence the uncertainty of the modelled sound velocities are dependent on the uncertainty of the measured pressure. A model for the uncertainty of the measured pressure is derived in the following.

The combined standard uncertainty of the hydrostatic pressure at transducer depth, h, is given as

$$u_c^2(P) = u_c^2(P_0) + u_c^2(P_h), \tag{4.49}$$

where P_0 is the measured pressure at the sample surface and P_h is the pressure due to the depth and density of the specimen. The combined standard uncertainty of P_0 is given as

$$u_c^2(P_0) = u^2(P_0)_{barometer} + u^2(P_0)_{resolution} + u^2(P_0)_{var.} + u^2(P_0)_{stab.} + u^2(P_0)_{other}, \tag{4.50}$$

assuming all sensitivity coefficients are equal to 1 and uncorrelated terms. Table 4.8 lists the uncertainty contributors with a corresponding description. The combined standard uncertainty of P_h is more complex. P_h is given as [34]

$$P_h = \rho g h \cdot 10^{-5}, \tag{4.51}$$

where ρ is the density of the sample, g is the gravitational acceleration and the unit of P_h is bar. The combined standard uncertainty of P_h (in units of bar) is given as

$$u_c^2(P_h) = (10^{-5} g h \cdot u_c(\rho))^2 + (10^{-5} \rho h \cdot u(g))^2 + (10^{-5} \rho g \cdot u_c(h))^2, \tag{4.52}$$

where the standard uncertainty due to gravitational acceleration, $u(g)$, will be neglected in the following. The depth, h is measured with the same Sylvac S_cal PRO caliper that was used to measure the transducer distance. Hence, the uncertainty due to transducer depth, $u_c(h)$, corresponds to the combined standard uncertainty due to $u(L_0)_{caliper}$, $u(L_0)_{drift}$, $u(L_0)_{resolution}$ and $u(L_0)_{repeatability}$, listed in Table 4.4. The density is calculated according to Eq. 2.4. It is dependent on both temperature and salinity, and its combined standard uncertainty can be expressed as

$$u_c^2(\rho) = \left(\frac{\partial \rho}{\partial T} \cdot u_c(T)\right)^2 + \left(\frac{\partial \rho}{\partial S} \cdot u(S)\right)^2, \tag{4.53}$$

where $u_c(T)$ is the combined standard uncertainty of temperature and $u(S)$ is the standard uncertainty due to salinity. The sensitivity coefficients are found through differentiation of Eq. 2.4, i.e.

$$\frac{\partial \rho}{\partial T} = \begin{aligned} & a_1 + 2a_2 T + 3a_3 T^2 + 4a_4 T^3 + 5a_5 T^4 + \\ & \left(b_1 + 2b_2 T + 3B_3 T^2 + 4b_4 T^3 \right) S + \\ & (c_1 + 2c_2 T) S^{3/2} \end{aligned} \qquad (4.54)$$

$$\frac{\partial \rho}{\partial S} = \begin{aligned} & b_0 + b_1 T + b_2 T^2 + b_3 T^3 + b_4 T^4 + \\ & \frac{3}{2} \left(c_0 + c_1 T + c_2 T^2 \right) S^{1/2} + 2d_0 S. \end{aligned} \qquad (4.55)$$

Using Eq. 4.49, 4.50, 4.52 and 4.53, the combined standard uncertainty of the hydrostatic pressure can be expressed as

$$u_c^2(P) = \begin{aligned} & (u^2(P_0)_{barometer} + u^2(P_0)_{resolution} + u^2(P_0)_{stab} + u^2(P_0)_{var.} + u^2(P_0)_{other} + \\ & \left(10^{-5} gh \cdot \frac{\partial \rho}{\partial T} \cdot u_c(T) \right)^2 + \left(10^{-5} gh \cdot \frac{\partial \rho}{\partial S} \cdot u(S) \right)^2 + (10^{-5} \rho h \cdot u(g))^2 + (10^{-5} \rho g \cdot u_c(h))^2 \end{aligned} \qquad (4.56)$$

All uncertainty contributors related to the hydrostatic pressure are listed in Table 4.8 with an associated description.

Table 4.8: Description of the uncertainty contributors to the combined standard uncertainty of hydrostatic pressure.

Uncertainty contributor	Description
$u(P_0)_{barometer}$	Standard uncertainty in the Paroscientific Digiquartz Model 740 barometer used to measure pressure at the sample surface [90].
$u(P_0)_{resolution}$	Standard uncertianty due to the resolution of the barometer.
$u(P_0)_{stab.}$	Standard uncertainty due to long term stability in barometer.
$u(P_0)_{var.}$	Standard uncertainty due to variation in pressure at sample surface during measurements.
$u(P_0)_{other}$	Standard uncertainty in measured pressure at the sample surface due to other sources.
$u_c(T)$	Combined standard uncertainty of measured temperature.
$u(S)$	Standard uncertainty due to the resolution of the display of the UWE NJW-3000 scale used for salinity adjustments.
$u(g)$	Standard uncertainty due to gravitational acceleration.
$u_c(h)$	Combined standard uncertainty due to transducer depth.

The atmospheric pressure is assumed to have a negligible uncertainty. Hence, the gauge pressure P_G is assumed to have the same uncertainty as the hydrostatic pressure, $u_c(P) = u(P_G)$. It is assumed that the effects of evaporation can be neglected due to the measurement cell lid.

4.4.2 Uncertainty model for the modelled sound velocity in distilled water

The formula used to calculate the sound velocity in distilled water is given in Eq. 2.1. The equation has an uncertainty of 0.05% for $0 < T < 100°C$ and $0 < P_G < 200$ bar [29]. This is the uncertainty

of the model itself. Additionally, there are uncertainties related to the gauge pressure, P_G, and the temperature, T. The combined standard uncertainty of the modelled sound velocity in distilled water, can be expressed as

$$u_c(c) = \sqrt{\left(\frac{\partial c}{\partial P_G} \cdot u_c(P_G)\right)^2 + \left(\frac{\partial c}{\partial T} \cdot u_c(T)\right)^2 + u^2(c)_{model}}.$$ (4.57)

assuming all terms are uncorrelated. The sensitivity coefficients are found by differentiating Eq. 2.1, i.e.

$$\frac{\partial c}{\partial P_G} = 0.159 + 2.8 \cdot 10^{-4} T + 2.4 \cdot 10^{-6} T^2,$$ (4.58)

$$\frac{\partial c}{\partial T} = 4.88 - 0.0964 T + 405 \cdot 10^{-6} T^2 + 2.8 \cdot 10^{-4} P_G + 4.8 \cdot 10^{-6} T P_G.$$ (4.59)

The uncertainty contributors to the combined standard uncertainty of the modelled sound velocity in distilled water are listed in Table 4.9.

Table 4.9: Description of the uncertainty contributors to the combined standard uncertainty of the modelled sound velocity in distilled water, calculated using the model derived by Kinsler et. al. [29].

Uncertainty contributor	Description
$u_c(P_G)$	Combined standard uncertainty due to the gauge pressure.
$u_c(T)$	Combined standard uncertainty due to the measured temperature.
$u(c)_{model}$	Standard uncertainty in the sound velocity model presented by Kinsler et. al.

4.4.3   Uncertainty model for the modelled sound velocity in saline water

The formula used to calculate the sound velocity in seawater is given in Eq. D.1. The model carries its own uncertainty, and there are uncertainties related to the temperature, T, hydrostatic pressure, P, and salinity, S. Assuming T, P and S are uncorrelated, the combined standard uncertainty of the modelled sound velocity, c, in seawater, can be expressed as

$$u_c(c) = \sqrt{\left(\frac{\partial c}{\partial P} \cdot u_c(P)\right)^2 + \left(\frac{\partial c}{\partial T} \cdot u_c(T)\right)^2 + \left(\frac{\partial c}{\partial S} \cdot u(S)\right)^2 + u^2(c)_{model}}.$$ (4.60)

The sensitivity coefficients are found by differentiating Eq. D.1. They are given in Appendix D. All uncertainty contributors are listed in Table 4.10 with an associated uncertainty.

Table 4.10: Description of the uncertainty contributors to the combined standard uncertainty of the modelled sound velocity in seawater, calculated using the UNESCO algorithm.

Uncertainty contributor	Description
$u_c(P)$	Combined standard uncertainty of the hydrostatic pressure.
$u_c(T)$	Combined standard uncertainty of the measured temperature.
$u(S)$	Standard uncertainty due to salinity. Equivalent to the uncertainty of the scale used for adjusting salinity values.
$u(c)_{model}$	Standard uncertainty in the UNESCO sound velocity model for seawater.

Chapter 5

Experimental results

Chapter 5 is divided into five sections presenting the results of the experiments carried out in this project. All uncertainty budgets calculated in this chapter is calculated according to the uncertainty models presented in Chapter 4. In Section 5.1, the measurements of the effective transducer radius for both the transmitting and receiving transducer are provided. Further, results of the calibration of the temperature sensor is presented in Section 5.2 along with uncertainty budgets for the temperature and pressure measurements. Measurements and calculated uncertainties of the transducer distance are given in Section 5.3. Uncertainties concerning both the reference transducer distance at a given temperature, and the thermal expansion coefficient is treated here. Section 5.4 is the main section and presents the measured sound velocities in this work. All measured sound velocities are presented graphically together with the modelled sound velocities. Associated tables listing the sound velocities at selected temperature set points are provided for further investigation of the results. The tables also list the associated measurement uncertainty to each experimental sound velocity in terms of ppm. Some comments regarding the results with main focus on maximum calculated uncertainties will be made consecutively throughout the section, as the main goal of this thesis is to design a measurement cell with a maximum uncertainty of 1000 ppm at 95% confidence level. Finally, in Section 5.5, an example uncertainty budget for the experimental sound velocity is derived. Results are commented consecutively throughout the chapter. However, a more thorough discussion regarding the results is presented in Chapter 6.

5.1 Measurements of the effective transducer radius

The effective transducer radius is calculated from directivity measurements, according to Section 2.8. Measurements were taken at angles from $-7°$ to $7°$ in steps of $0.05°$. Two sets of measurements were carried out on each transducer. Fig. 5.1 and Fig. 5.2 show the two sets of voltage amplitude measurements as a function of angle from the center axis for the transmitting and receiving transducer, respectively.
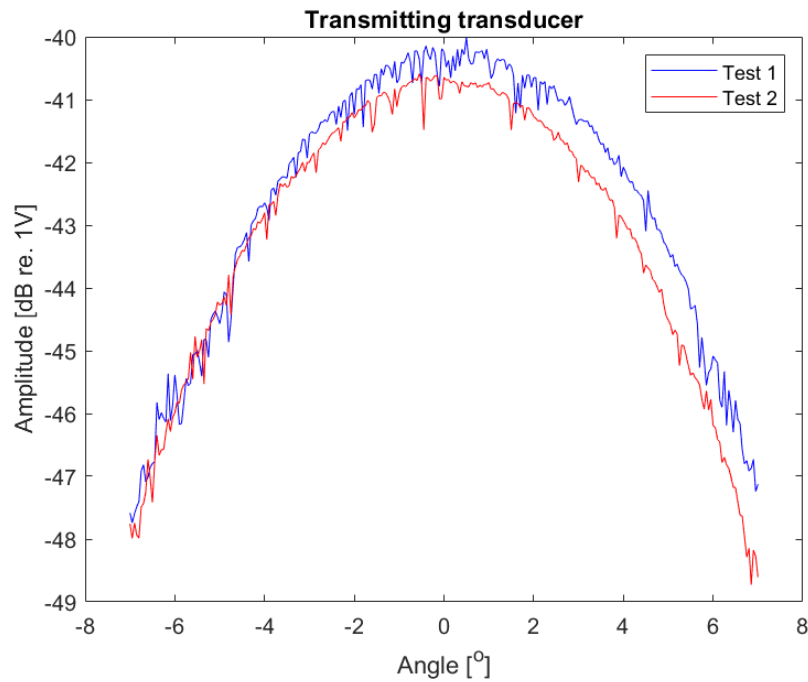
Figure 5.1: Measured amplitude in dB re. 1V as a function of angle displacement relative to the acoustic axis for the transmitting transducer. Test 1 represents the first measurement series, while Test 2 represent the second measurement series.
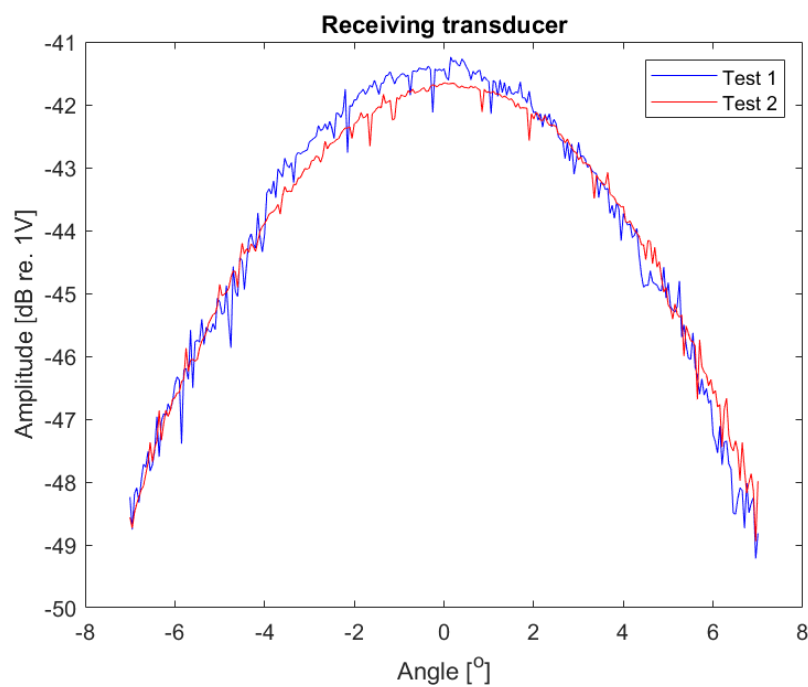
Figure 5.2: Measured voltage amplitude in dB re. 1V as a function of angle displacement relative to the acoustic axis for the receiving transducer. Test 1 represents the first measurement series, while Test 2 represent the second measurement series.

From the plotted curves, it is clear that the two tests were slightly more coinciding for the receiving transducer than for the transmitting transducer. The reason for the deviation between the two tests is

probably due to a slight displacement of the transducer holder during mounting of the transducers.

The tests were performed in the following order: (1) Test 1 for the transmitting transducer, (2) Test 1 for the receiving transducer, (3) Test 2 for the transmitting transducer and (4) Test 2 for the receiving transducer. Consequently, after every test, the tested transducer was disassembled from the transducer holder and replaced by the other transducer. This may have caused a slight displacement and change of angle to the transducer holder, resulting in a slightly different starting position in the following test. Attempts were made to reduce this error by carefully altering the position of the transducer until the signal had the same amplitude as in the previous test.

Moreover, the measurements do not constitute smooth curves. All four curves are "jumpy" which implies that the measurements were taken under unstable conditions. The jumps might be due to acoustic noise from one or more of the instruments.

In order to find a_{eff}, a second order polynomial was used in MATLAB [73] to plot a regression curve for each of the four measurement series. A horizontal line was then plotted where the amplitude of the regression curve had decayed by 3 dB from the top. The 3 dB-angle, $\theta_{3\,dB}$, corresponds to the angles where the intersection between the regression curve and the horizontal line takes place. This is illustrated with the first test for the transmitting transducer in Fig. 5.3.
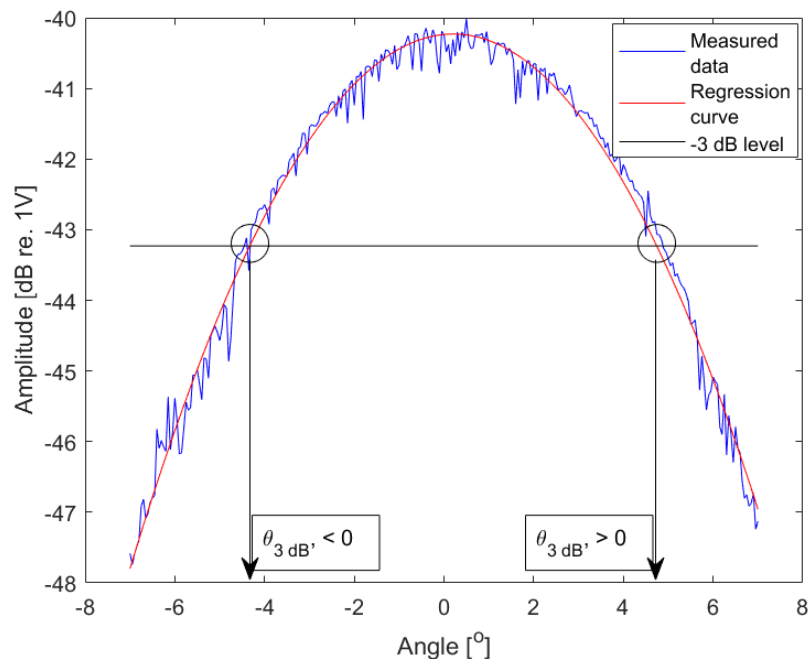
Figure 5.3: First set of measurements for the transmitting transducer (Test 1) and the second order polynomial regression curve. The negative and positive value for $\theta_{3\,dB}$ are the angles corresponding to the two circles in the plot, respectively.

The intersection points between the regression curve and the horizontal line were read manually by zooming in on the figures. Since there are two intersection points, the measured value of $\theta_{3\,dB}$ for each test is defined as the average of the magnitude of the negative and the positive angle. Further, a_{eff} for each transducer is equal to the average of the measured a_{eff} in the two tests.

Table 5.1: Measured values of $\theta_{3\,dB}$ and a_{eff} based on the regression curves for each of the four measurement sets in Fig. 5.1 and Fig. 5.2. T stands for transmitting transducer and R for receiving transducer.

Transducer type	Test	-3 dB angles, $\theta_{3\,dB}$, [°]			Effective element radius, a_{eff}, [mm]	
		Negative, $\theta_{3\,dB}$	Positive, $\theta_{3\,dB}$	Average, $\overline{\theta_{3\,dB}}$	By test, a_{eff}	Average, $\overline{a_{eff}}$
T	1	$-4.33°$	$4.74°$	$4.54°$	9.61 mm	9.71 mm
	2	$-4.51°$	$4.38°$	$4.45°$	9.80 mm	
R	1	$-4.54°$	$4.41°$	$4.48°$	9.73 mm	9.63 mm
	2	$-4.42°$	$4.73°$	$4.58°$	9.52 mm	

Fig. 5.1 and Fig. 5.2 show that the first test with the transmitting transducer and the second test with the receiving transducer is marginally shifted to the right compared to the other test. To compensate for this bias, the average of the negative and positive value for $\theta_{3\,dB}$ was used to calculate a_{eff}. A total of four values for a_{eff} were found, two for the transmitting transducer, and two for the receiving transducer. The average a_{eff} for both the transmitting and receiving transducer were found to be slightly larger than the nominal transducer radius.

Initially, more directivity measurements should was supposed be carried out for each transducer. However, during the third measurement series, some distortion of the signal found place around the -3 dB angle. This continued to occur the following tests as well. Two plots, one for the transmitting transducer, and another for the receiving transducer, where signal distortion occured, are shown in Fig. 5.4.

(a)

(b)
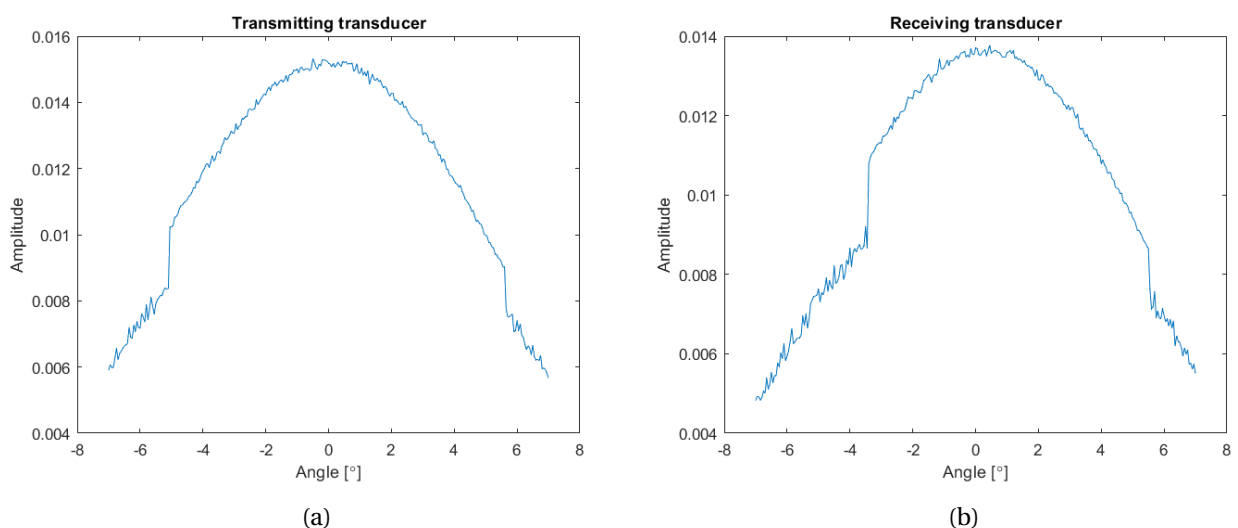
Figure 5.4: Example of how the amplitude was distorted during directivity measurements of (a) the transmitting transducer and (b) the receiving transducer.

The signal is clearly distorted at around -5° and 5.5° for the transmitting transducer, and around -3.5° and 5.5° for the receiving transducer.

The problem was never resolved, and due to time limitation, the transducers had to be delivered to the workshop before additional measurements without distortion could be carried out.

5.2   Temperature and pressure measurements

Both the temperature and pressure in the measurement cell are measured continuously throughout all sound velocity measurement series. The temperature sensor is calibrated prior to being implemented in the measurement cell to reduce the uncertainty. The current section presents the calibration results and the uncertainty of the temperature and pressure measurements.

5.2.1   Calibration of temperature sensor

Two measurement series were performed with the 3 wire RS Pt100 temperature sensor. In the first measurement series, the standard coefficients in Eq. 3.9 for a regular platinum element was used. The coefficients were implemented in the precision temperature scanner, and are repeated here: $R_0 = 100\,\Omega$ (i.e. the temperature at $0^\circ C$), $\alpha = 3.9083 \cdot 10^{-3}\,^\circ C^{-1}$ and $\beta = -5.775 \cdot 10^{-7}\,^\circ C^{-2}$. Fig. 5.5 shows the values measured with the uncalibrated sensor plotted against the values measured with the reference probe. Using Eq. 3.9, the measured temperatures are converted to the corresponding measured resistances. `cftool` in MATLAB [73] was used to plot these resistances against the measured temperature values found with the reference probe to find the new coefficients for the characteristic equation. The new coefficients were found to be $R_0 = 100.3\,\Omega$, $\alpha = 3.733 \cdot 10^{-3}\,^\circ C^{-1}$ and $\beta = -4.784 \cdot 10^{-7}\,^\circ C^{-2}$. New measurements taken with these coefficients are shown in Fig. 5.6. The measurements from before calibration are kept in the figure to illustrate the effect of the calibration.
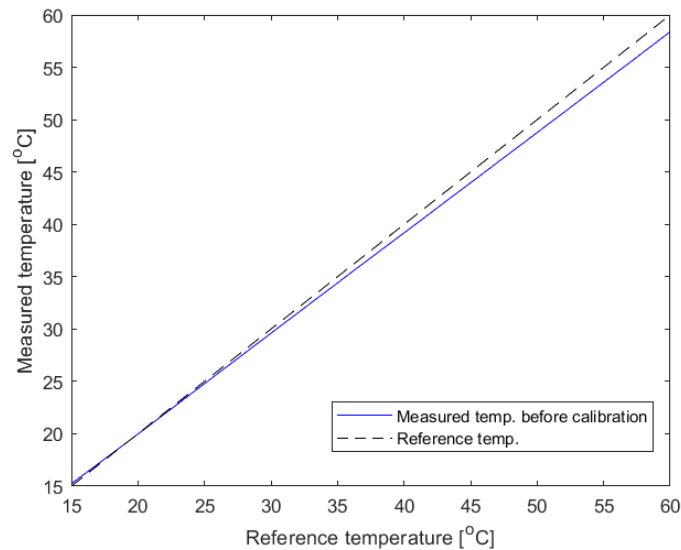
Figure 5.5: Values measured with the uncalibrated temperature sensor plotted against the values measured with the reference probe. The coefficients used when performing the measurements are $R_0 = 100\,\Omega$, $\alpha = 3.9083 \cdot 10^{-3}\,^\circ C^{-1}$ and $\beta = -5.775 \cdot 10^{-7}\,^\circ C^{-2}$.
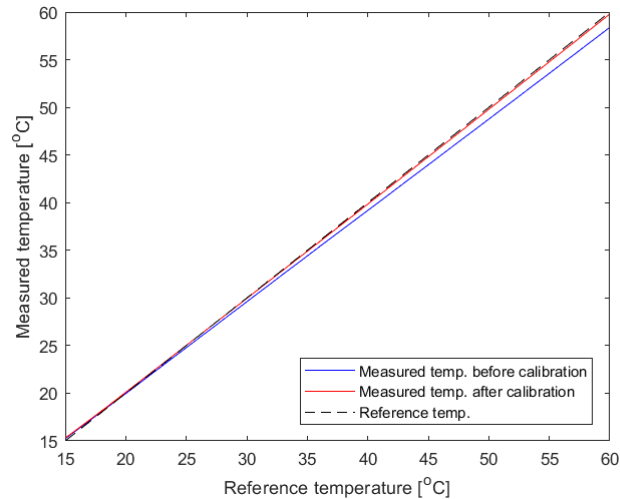
Figure 5.6: Values measured with the calibrated temperature sensor plotted against the values measured with the reference probe. The coefficients used when performing the measurements are $R_0 = 100.3\,\Omega$, $\alpha = 3.733 \cdot 10^{-3}\,°C^{-1}$ and $\beta = -4.784 \cdot 10^{-7}\,°C^{-2}$.

From Fig. 5.5 it is clear that the RS-temperature sensor measures relatively accurate temperatures around $20°C$ before calibration. However, the deviation between the measured values and the reference values increases with increasing temperature. In Fig. 5.6, the red line represents measurements after calibration. It is clear that this line lies closer to the dashed black line for most temperatures. The effect of the calibration is greatest for high temperatures.

The deviation from the temperature measured with the reference probe, before and after calibration, is plotted in Fig. 5.7. Evidently, the measurements actually lie closer before calibration for the lowest temperatures. However, when the temperature exceeds $24°C$, the measurements is far more accurate after calibration. Another trend that can be seen, is that in both cases, the measurements are greater than the reference values for lower temperatures, while they are lower for higher temperatures
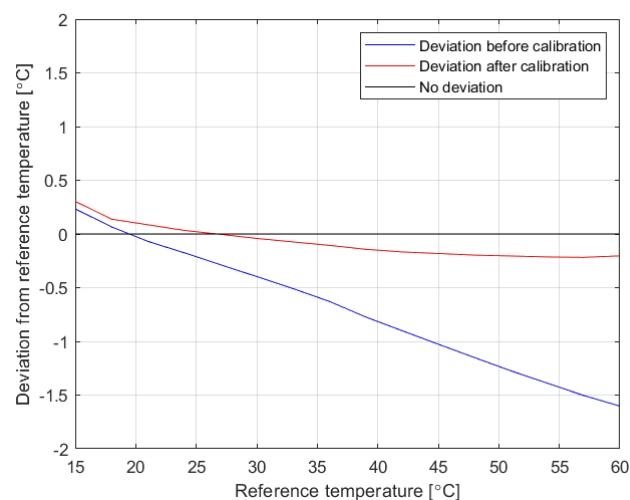
Figure 5.7: Deviation from the temperature measured with the reference probe before calibration (red) and after calibration (blue).

5.2.2   Uncertainty in temperature measurements

In Section 4.2.1, an uncertainty model for the temperature measurements is presented. Here, this model is used to calculate the uncertainty of the temperature measurements at $25°C$, which proved to be the temperature that generally caused the greatest relative expanded uncertainties for the experimental sound velocities. Table 5.2 lists values for all uncertainty contributors, and an associated description for each uncertainty contributor is found in Table 4.2. The uncertainty of the temperature measurements is calculated in the uncertainty budget in Table 5.3.

Table 5.2: List of the uncertainties contributing to the uncertainty of the temperature measurements using a 3 wire Pt100 PRT Probe with PFA Insulation from RS [79]. A description of each contributor is provided in Table 4.2. The values are presented for $T = 25°C$ and each value has been multiplied with its associated coverage factor. The coverage factor for each contributor is $k = 2$ unless otherwise is specified.

Uncertainty contributor	Value	Note
$u(T)_{Pt100}$	$0.2°C$	Specified by the manufacturer to have Class A type accuracy: $0.15°C + 0.002 \cdot T$ [79]. Follows IEC 60751 [113].
$u(T)_{drift.}$	$0.05°C$	Max over a five year period according to [108].
$u(T)_{ref.Pt100}$	$0.045°C$	Found from interpolation of tabulated values in [109]. 1/10 DIN type accuracy.
$u(T)_{ref.drift}$	$0.05°C$	Max over a five year period according to [108].
$u(T)_{scanner}$	$0.155°C$	Specified by the manufacturer [110].
$u(T)_{dev.}$	$0.0367°C$	Found from Fig 5.7.
$u(T)_{RTD-USB}$	$0.06°C$	Specified by the manufacturer [81].
$u(T)_{temp.var.}$	$0.003°C$	Observed during stable conditions over 5 mins. Coverage factor $k = \sqrt{3}$ assumed.
$u(T)_{other}$	N/A	N/A

Table 5.3: Uncertainty budget for the uncertainty of the temperature measurements for $T = 25°C$. The values are taken from Table 5.2, and the budget is calculated according to Eq. 4.11.

Uncertainty Contributor	Input Uncertainty				Combined Uncertainty	
	Expand. uncert. [°C]	Conf. level & distribut.	Cov. fact., k	Standard uncertainty [°C]	Sens. coeff.	Variance [°C²]
$u(T)_{Pt100}$	0.2	95% (norm)	2	0.1	1	0.01
$u(T)_{drift}$	0.05	95% (norm)	2	0.025	1	$6.25 \cdot 10^{-4}$
$u(T)_{ref.Pt100}$	0.045	95% (norm)	2	0.0225	1	$5.063 \cdot 10^{-4}$
$u(T)_{ref.drift}$	0.05	95% (norm)	2	0.025	1	$6.25 \cdot 10^{-4}$
$u(T)_{scanner}$	0.155	95% (norm)	2	0.0775	1	$6.006 \cdot 10^{-3}$
$u(T)_{dev.}$	0.0367	95% (norm)	2	0.0184	1	$3.367 \cdot 10^{-4}$
$u(T)_{RTD-USB}$	0.06	95% (norm)	2	0.03	1	$9.00 \cdot 10^{-4}$
$u(T)_{temp.var.}$	0.003	100% (rect)	$\sqrt{3}$	$1.732 \cdot 10^{-3}$	1	$3.00 \cdot 10^{-6}$
Sum of variances, $u_c^2(T)$						$0.019°C^2$
Combined standard uncertainty, $u_c(T)$						$0.138°C$
Expanded uncertainty (95% confidence level, $k = 2$), $U(T)$						$0.276°C$
Operating temperature, T						$25°C$
Relative expanded uncertainty (95% confidence level, $k = 2$), $U(T)/T$						1.103%

5.2.3 Uncertainty in pressure measurements

The environmental pressure is measured continuously with a Paroscientific Digiquartz Model 740 barometer [90] throughout the measurement series, and is used to calculate the hydrostatic pressure inside the measurement cell. The barometer is not connected to any other device in the experimental setup. The pressure measurements are needed for calculation of the modelled sound velocities, using the formula derived by Kinsler et. al. [29] and the UNESCO-algorithm [11, 12].

The uncertainty of the hydrostatic pressure is calculated according to the uncertainty model presented in Section 4.4.1. It is dependent on several other parameters such as the density of the sample, temperature and transducer depth. The density is calculated from the empirical expression presented by Fofonoff and Millard [37], see Eq. 2.4. Further, the uncertainty is calculated for the case where the temperature is $25°C$ and the sample is distilled water. The environmental pressure was measured to be $P_0 = 1.020$ bar. Table 5.4 shows the value of each uncertainty contributor and how it is found. A description of each term is provided in table 4.8.

Table 5.4: List of the uncertainties contributing to the uncertainty of the hydrostatic pressure, when the sample is distilled water at 25°. A description of each uncertainty contributor is provided in Table 4.8. Each value has been multiplied with its associated coverage factor.

Uncertainty contributor	Value	Note
$u(P_0)_{barometer}$	$1.530 \cdot 10^{-4}$ bar	Specified by the manufacturer to be $\pm 0.015\%$ of the measured value [90]. Coverage factor $k = 2$ assumed.
$u(P_0)_{resolution}$	$1 \cdot 10^{-5}$ bar	Due to the number of digits on the barometer display. Coverage factor $k = 2$ assumed.
$u(P_0)_{stab.}$	N/A	N/A
$u(P_0)_{var.}$	$5.00 \cdot 10^{-5}$	Observed variations in pressure during measurements. Coverage factor $k = \sqrt{3}$ assumed.
$u(P_0)_{other}$	N/A	N/A
$u_c(T)$	$0.276°C$	Calculated in Table 5.3. Coverage factor $k = 2$ assumed.
$u(S)$	$1 \cdot 10^{-4}$ kg	Due to the number of digits on the scale display. Coverage factor $k = 1$ assumed.
$u(g)$	N/A	N/A
$u_c(h)$	0.0159 mm	Equal to the combined standard uncertainty of the caliper used for length measurements, see Table 5.9 and [111]. Coverage factor $k = 1$ assumed.

Table 5.5: Uncertainty budget for the total uncertainty of the hydrostatic pressure in distilled water at $25°C$. The values are taken from Table 5.4, and the budget is calculated according to Eq. 4.56.

Uncertainty Contributor	Input Uncertainty				Combined Uncertainty	
	Expand. uncert.	Conf. level & distribut.	Cov. fact., k	Standard uncertainty	Sens. coeff.	Variance [bar^2]
$u(P_0)_{barometer}$	$1.530 \cdot 10^{-4}$ bar	95% (norm)	2	$7.650 \cdot 10^{-5}$ bar	1	$5.852 \cdot 10^{-9}$
$u(P_0)_{resolution}$	$1.00 \cdot 10^{-5}$ bar	95% (norm)	2	$5.00 \cdot 10^{-6}$ bar	1	$2.50 \cdot 10^{-11}$
$u(P_0)_{var.}$	$5.00 \cdot 10^{-5}$ bar	100% (rect)	$\sqrt{3}$	$2.887 \cdot 10^{-5}$ bar	1	$8.333 \cdot 10^{-10}$
$u_c(T)$	$0.276°C$	95% (norm)	2	$0.138°C$	$-7.4157 \cdot 10^{-6}$	$1.044 \cdot 10^{-12}$
$u(S)$	-	-	-	-	-	-
$u_c(h)$	$0.0159 \cdot 10^{-3}$ m	68% (norm)	1	$0.0159 \cdot 10^{-3}$ m	0.9781	$2.419 \cdot 10^{-10}$
Sum of variances, $u_c^2(P)$						$6.953 \cdot 10^{-9}$ bar^2
Combined standard uncertainty, $u_c(P)$						$8.338 \cdot 10^{-5}$ bar
Expanded uncertainty (95% confidence level, $k = 2$), $U(P)$						$1.668 \cdot 10^{-4}$ bar
Hydrostatic pressure at $25°C$ in distilled water, P.						1.049 bar
Relative expanded uncertainty (95% confidence level, $k = 2$), $U(P)/P$						0.0159%

The atmospheric pressure is assumed to have a negligible uncertainty. Hence, the gauge pressure P_G is assumed to have the same uncertainty as the hydrostatic pressure at transducer depth, h.

As mentioned in Section 2.1.1, evaporation will have a slight impact on the total pressure. This is not included in the uncertainty budget as it is assumed that the lid will make these effects negligible.

5.3 Transducer distance measurements

Sound velocity measurements are conducted over a temperature span from approximately 25 to $45°C$ in this work. Due to thermal expansion of the measurement cell, the distance between the transmitting and receiving transducer will change depending on the temperature. The transducer distance, L_0, is therefore measured at a reference temperature, T_0, and a thermal expansion coefficient, K_T, is used to calculate the transducer distance at different temperatures. The current section presents measurements of L_0, as well as the uncertainty of both L_0 and K_T.

5.3.1 Measurements of L_0

A total of 50 transducer distance measurements were performed using the Sylvac S_cal PRO caliper [111]. First, ten measurements were performed on the distance between the center of each transducer. These measurements give an indication of the repeatability of the length measurements. Afterwards, 40 measurements were taken at different sections of the transducer surfaces to also investigate the orientation of the transmitting and receiving transducer relative to each other, as well as the roughness of the transducer surfaces. An illustration of where measurements were taken are shown in Fig. 5.8. Series of ten measurements with main focus on the top, bottom, left- and right-hand section were performed, respectively. The results are shown in Table 5.6 and 5.7, respectively. The standard deviation of the measurements is calculated according to Eq. C.2 [105]. The standard uncertainty is represented as the standard uncertainty of the mean of the individual values, given by Eq. C.4 [105]. Also, the degrees of freedom is specified in each table, calculated according to Eq. C.3 [105].
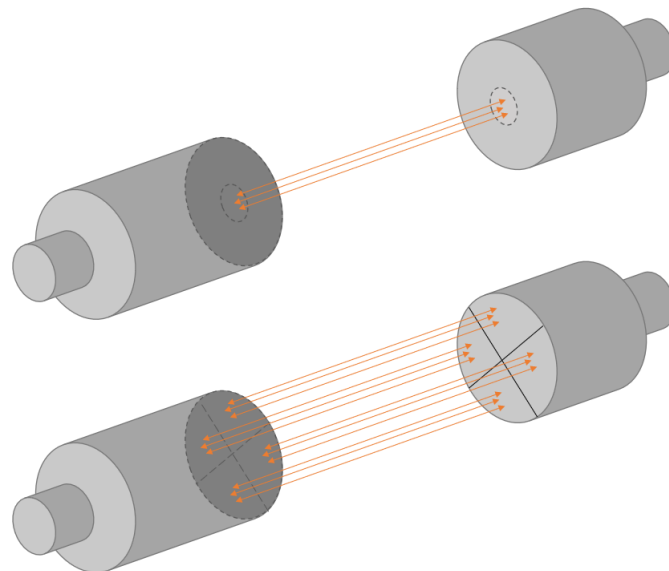
Figure 5.8: Top: measured distance bewteen the center of each transducer. Bottom: measured distance between top, bottom, left-hand and right-hand section of the transducers.

Table 5.6: Measured transducer distance, L_0, between the center of each transducer. The distance is measured with a Sylvac S_cal PRO caliper [111] at reference temperature $T_0 = 22.8°C$. The number of degrees of freedom is 9.

Measurement number	Measured transducer distance [mm]
1	125.00
2	125.01
3	125.01
4	125.00
5	125.01
6	124.99
7	125.00
8	125.00
9	125.01
10	125.00
Mean	125.003
Standard deviation	0.0067
Standard uncertainty	0.0021
Expanded uncertainty (95% confidence level, $k = 2$)	0.0042

Table 5.7: Measured transducer distance, L_0, between the top, bottom, left-hand and right-hand section of each transducer. The distance is measured with a Sylvac S_cal PRO caliper [111] at reference temperature $T_0 = 22.8°C$. The number of degrees of freedom is 39.

Measurement number	Measured transducer distance [mm]			
	Top	Bottom	Left	Right
1	125.01	125.00	124.99	125.00
2	125.01	125.00	125.01	125.01
3	125.01	125.01	125.01	125.01
4	125.01	125.00	125.00	125.00
5	125.00	125.01	125.00	125.01
6	124.99	125.00	124.99	125.00
7	125.00	125.00	124.99	125.01
8	125.00	124.99	124.99	125.00
9	125.00	125.00	125.01	125.01
10	125.01	125.01	125.00	125.01
Mean	125.0028			
Standard deviation	0.0072			
Standard uncertainty	$1.138 \cdot 10^{-3}$			
Expanded uncertainty (95% confidence level, k = 2)	$2.277 \cdot 10^{-3}$			

The measurements in the tables indicate that the transducer distance is slightly over 125 mm, which is the value used for L_0 in calculations. However, all values are well within the uncertainty of the caliper, which is stated to be 0.03 mm by the manufacturer [111].

5.3.2 Uncertainty in measurements of L_0

The uncertainty of the transducer distance, L_0, is calculated according to the uncertainty model presented in Section 4.2.3. Table 5.8 lists the value of each uncertainty contributor to the total uncertainty of L_0. An associated description for each uncertainty contributor is found in Table 4.4. The uncertainty budget for L_0 is presented in Table 5.9.

Table 5.8: List of the uncertainties contributing to the total uncertainty of the transducer distance, L_0, measured at reference temperature, $T_0 = 22.8°C$. A description of each uncertainty contributor is provided in Table 4.4. Each value has been multiplied with its associated coverage factor.

Uncertainty contributor	Value	Note
$u(L_0)_{caliper}$	0.03 mm	Specified by the manufacturer [111].
$u(L_0)_{drift}$	N/A	N/A
$u(L_0)_{resolution}$	0.01 mm	Specified by the manufacturer [111].
$u(L_0)_{repeatability}$	0.0021 mm	Calculated according to Section 5.3.1.
$u(L_0)_{surface}$	$1.138 \cdot 10^{-3}$ mm	Calculated according to Section 5.3.1. Coverage factor $k = 1$ assumed.
$u(L_0)_{other}$	N/A	N/A

Table 5.9: Uncertainty budget for the total uncertainty of the measured transducer distance, L_0, at reference temperature, $T_0 = 22.8°C$. The values are taken from Table 5.8, and the budget is calculated according to Eq. 4.13.

Uncertainty Contributor	Input Uncertainty				Combined Uncertainty	
	Expand. uncert.	Conf. level & distribut.	Cov. fact., k	Standard uncertainty	Sens. coeff.	Variance $[mm^2]$
$u(L_0)_{caliper}$	0.03 mm	95% (norm)	2	0.015 mm	1	$2.250 \cdot 10^{-4}$
$u(L_0)_{drift}$	N/A	N/A	N/A	N/A	N/A	N/A
$u(L_0)_{resolution}$	0.01 mm	95% (norm)	2	0.005 mm	1	$2.500 \cdot 10^{-5}$
$u(L_0)_{repeatability}$	0.0021 mm	95% (norm)	2	$1.05 \cdot 10^{-3}$ mm	1	$1.103 \cdot 10^{-6}$
$u(L_0)_{surface}$	$1.138 \cdot 10^{-3}$ mm	68% (norm)	1	$1.138 \cdot 10^{-3}$ mm	1	$1.300 \cdot 10^{-6}$
$u(L_0)_{other}$	N/A	N/A	N/A	N/A	N/A	N/A
Sum of variances, $u_c^2(L_0)$						$2.524 \cdot 10^{-4}\ mm^2$
Combined standard uncertainty, $u_c(L_0)$						$0.0159\ mm$
Expanded uncertainty (95% confidence level, $k = 2$), $U(L_0)$						$0.0318\ mm$
Transducer distance at reference temperature 22.8°C, L_0						$125.00\ mm$
Relative expanded uncertainty (95% confidence level, $k = 2$), $U(L_0)/L_0$						0.0254%

5.3.3 Uncertainty in thermal expansion

The uncertainty model for the thermal expansion coefficient is presented in Section 4.2.2. Here, the model is used to calculate an uncertainty budget for the uncertainty of K_T. The uncertainty is calculated for the case where the temperature is $T = 25°C$, which proved to be the temperature that caused the greatest relative expanded uncertainties in the experimental sound velocities. Table 5.10 lists values for the two uncertainty contributors, and an associated description for each uncertainty contributor is found in Table 4.3. It should be noted that the thermal expansion of the transducers are neglected due to the exact composition of the transducer interior being unknown.

Table 5.10: List of the uncertainties contributing to the total uncertainty of the thermal expansion coefficient when the temperature is $T = 25°C$. Each value has been multiplied with its associated coverage factor.

Uncertainty contributor	Value	Note
$u(\alpha_T)$	$4.5 \cdot 10^{-6°}C^{-1}$	Based on tabulated values in [60, 61, 62]. Coverage factor $k = \sqrt{3}$ assumed.
$u(\Delta T)$	0.243°C	Equal to the square root of the sum of the variance for T (see Table 5.3) and T_0, respectively ($u_c(T) = u_c(T_0)$ assumed). Coverage factor $k = 1$ assumed.

Table 5.11: Uncertainty budget for the total uncertainty of the thermal expansion coefficient for $T = 25°C$. The values are taken from Table 5.10, and the budget is calculated according to Eq. 4.12.

Uncertainty Contributor	Input Uncertainty				Combined Uncertainty	
	Expand. uncert.	Conf. level & distribut.	Cov. fact., k	Standard uncertainty	Sens. coeff.	Variance
$u(\alpha_T)$	$4.50 \cdot 10^{-6}°C^{-1}$	100% (rect)	$\sqrt{3}$	$2.60 \cdot 10^{-6}°C^{-1}$	2.2	$3.27 \cdot 10^{-11}$
$u(\Delta T)$	$0.243°C$	68% (norm)	1	$0.243°C$	$7.25 \cdot 10^{-5}$	$3.10 \cdot 10^{-10}$
Sum of variances, $u_c^2(K_T)$						$3.43 \cdot 10^{-10}$
Combined standard uncertainty, $u_c(K_T)$						$1.85 \cdot 10^{-5}$
Expanded uncertainty (95% confidence level, $k = 2$), $U(K_T)$						$3.70 \cdot 10^{-5}$
Thermal expansion coefficent for plexiglas at 25°C, K_T						1.000016
Relative expanded uncertainty (95% confidence level, $k = 2$), $U(K_T)/K_T$						0.0037%

5.4 Sound velocity measurements

Sound velocity measurements have been carried out on distilled water, saline water and Exxsol oil over a temperature span from approximately 25 to 45°C. For all measurements, the signal generator was set to generate a ten period pulse at 500 kHz frequency and 10 V amplitude. Only the steady state part of the pulses is used to measure the sound velocity, after being averaged 512 times, both in the ZCM and the FSM, cf. Section 3.7.1 and 3.7.2. In the following subsections, there are figures showing the measured and modelled sound velocities as a function of temperature. The following notations are applied:

- c_{ZCM}: Measured sound velocity using the ZCM, not corrected for diffraction.

- $c_{ZCM,M1}$: Measured sound velocity using the ZCM and diffraction correction Method 1.

- $c_{ZCM,M2}$: Measured sound velocity using the ZCM and diffraction correction Method 2.

- c_{FSM}: Measured sound velocity using the FSM, not corrected for diffraction.

- $c_{FSM,M1}$: Measured sound velocity using the FSM and diffraction correction Method 1.

- $c_{FSM,M2}$: Measured sound velocity using the FSM and diffraction correction Method 2.

- $c_{K\&F}$: Modelled sound velocity calculated using the formula presented by Kinsler et. al. [29].

- c_{UNESCO}: Modelled sound velocity calculated using the UNESCO algorithm [11, 12].

Before initiating each measurement series, the measurement cell was thoroughly cleaned. After cleaning, the liquid sample was filled in the cavity, and the measurement cell was placed in the water bath.

The water bath was filled to just below the height of the measurement cell and set to have a temperature of just under $25°C$. When the temperature in the cell and water bath had stabilized, the measurement series were initiated.

For further investigation, the values for the measured and modelled sound velocities at temperature set points 25, 30, 35, 40 and $45°C$ are inserted into tables along with associated measurement uncertainties. To not overload the tables with columns, the uncertainties are only presented as relative expanded uncertainties (ppm), as the main target of this thesis is to design a measurement cell with a max relative uncertainty of 1000 ppm at 95% confidence level. It should be noted that the uncertainties presented in the tables are the measurement uncertainties calculated according to the uncertainty model presented in Chapter 4. It is not the deviation from the modelled sound velocities $c_{K\&F}$ and c_{UNESCO}. The experimental sound velocities are compared to the modelled sound velocities in normalized plots throughout the section, where a deviation up to 1000 ppm from the modelled sound velocities are marked in green.

In the tables, values from both measurement series are listed together for comparison reasons. Since the temperatures at which the sound velocities are measured varies slightly for each measurement series, linear interpolation is used on the two measurements closest to each temperature set point to find a value for the sound velocity at the temperatures specified in the tables.

Moreover, sound velocity measurements are investigated over a frequency span from 275 to 600 kHz, following [84]. The frequency test is performed on distilled water, saline water at 50 ppt salinity and Exxsol D120 oil, and gives an indication as to whether the measurement cell can be used to measure sound velocity at other frequencies.

All measured sound velocities are found from waveforms acquired every three seconds from the oscilloscope through an automated MATLAB-script, see Appendix E.3.1 and E.3.4. The corresponding relative uncertainties are calculated according to the uncertainty model presented in Chapter 4, using the MATLAB-script presented in Appendix E.3.5.

Some comments will be made regarding the results and uncertainties throughout the next subsections. However, a more thorough and detailed discussion is provided in Chapter 6.

5.4.1   Sound velocity measurements in distilled water

In total, two sets of measurements have been performed on distilled water. The measured sound velocities are plotted together with the modelled sound velocities in Fig. 5.9. Both the UNESCO algorithm [11] [12] and the formula presented by Kinsler et. al. [29] are used to calculate the modelled sound velocity. Also, the normalised measured sound velocity is plotted with respect to $c_{K\&F}$ and c_{UNESCO} in Fig. 5.10 and 5.11, respectively, to further investigate the deviation from the modelled sound velocities. The hydrostatic pressure varied between 1.009 and 1.022 bar across the measurement series.
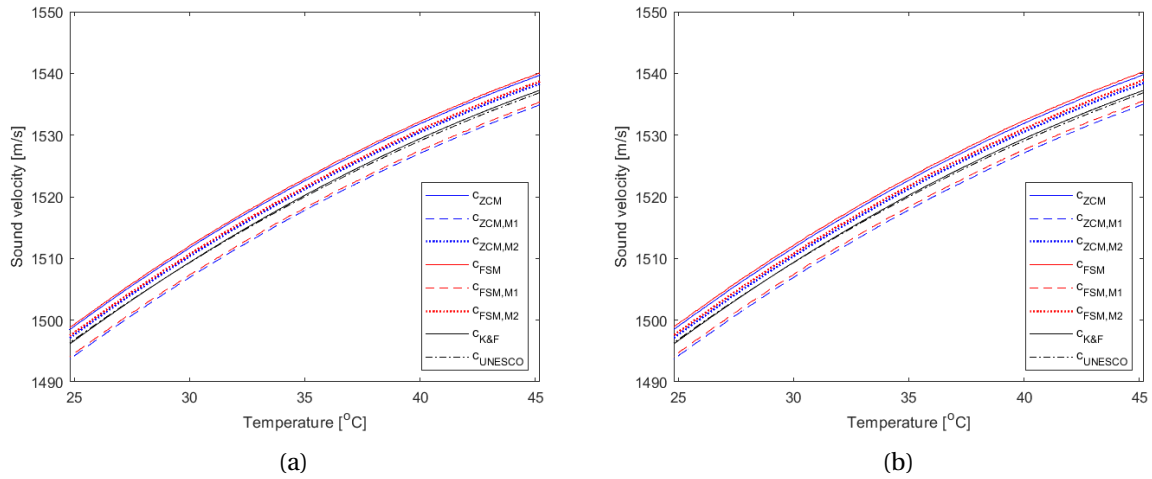
Figure 5.9: Measured and theoretical sound velocity in distilled water from 25 to $45°C$. The measured values are found using the steady state portion of a ten period pulse and averaging the waveform 512 times. The theoretical values for $c_{K\&F}$ and c_{UNESCO} are calculated using Eq. 2.1 and D.1, respectively. (a) Measurement series 1, (b) Measurement series 2.
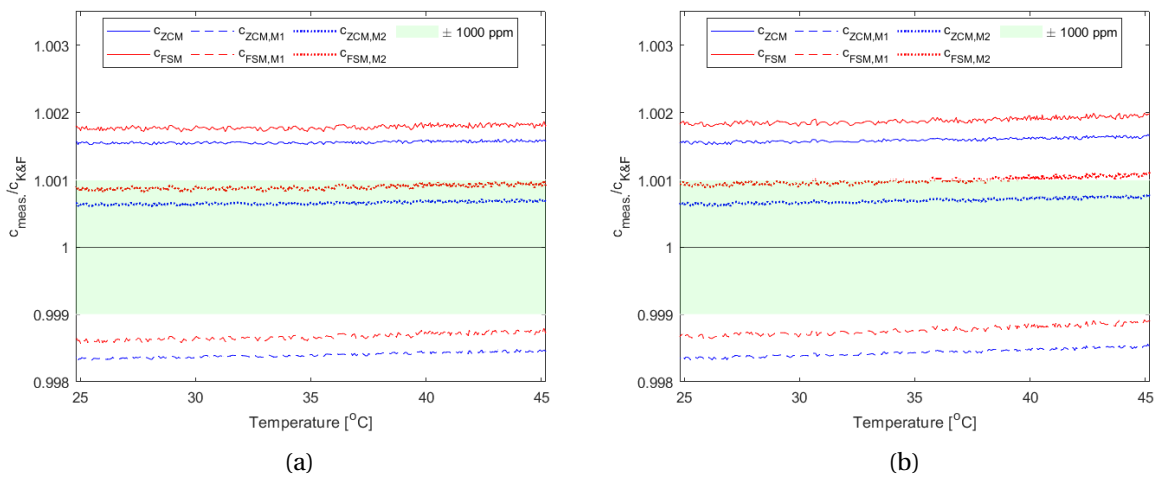
Figure 5.10: Normalised measured sound velocity in distilled water from 25 to $45°C$, with respect to the theoretical values calculated using Eq. 2.1. The measured values are found using the steady state portion of a ten period pulse and averaging the waveform 512 times. (a) Measurement series 1, (b) Measurement series 2.
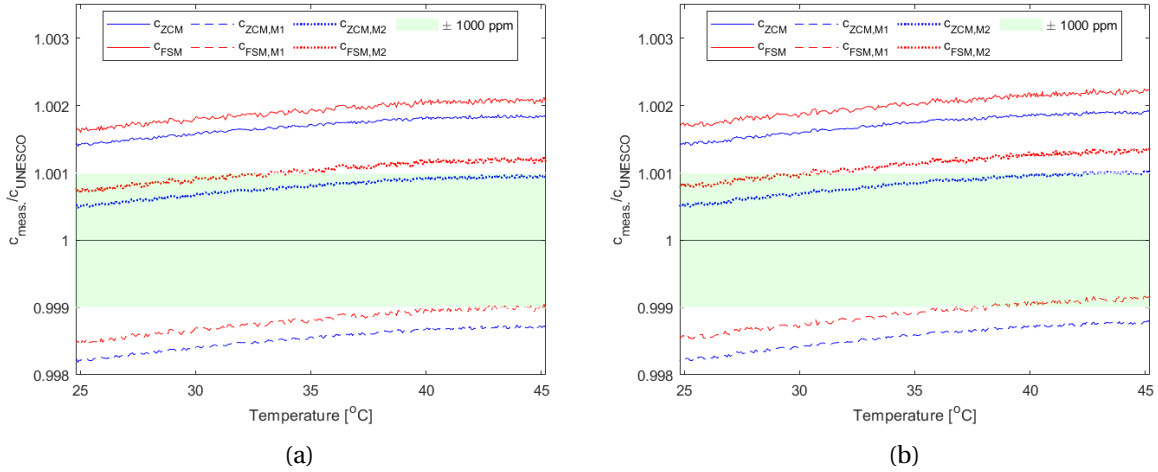
Figure 5.11: Normalised measured sound velocity in distilled water from 25 to $45°C$, with respect to the theoretical values calculated using Eq. D.1. The measured values are found using the steady state portion of a ten period pulse and averaging the waveform 512 times. (a) Measurement series 1, (b) Measurement series 2.

Table 5.12: Sound velocity measurements in distilled water using the ZCM on the steady state portion of a ten period pulse that is averaged 512 times. For each temperature, there are two measured sound velocities. The topmost value was measured during the first measurement series, while the bottom-most value was measured during the second measurement series.

Zerocrossing method							
	Modelled sound velocity		**Experimental sound velocity**			**Relative expanded uncertainty (95% c.l.)**	
Temp. [$°C$]	$c_{K\&F}$ [m/s]	c_{UNESCO} [m/s]	c_{ZCM} [m/s]	$c_{ZCM,M1}$ [m/s]	$c_{ZCM,M2}$ [m/s]	$E_{c_{ZCM,M1}}$ [ppm]	$E_{c_{ZCM,M2}}$ [ppm]
25	1496.69	1496.88	1499.01	1494.26	1497.63	422	393
			1499.02	1494.27	1497.63	428	398
30	1509.37	1509.32	1511.72	1506.94	1510.35	415	384
			1511.80	1507.01	1510.43	418	387
35	1520.25	1520.01	1522.62	1517.82	1521.25	413	381
			1522.69	1517.89	1521.32	414	382
40	1529.43	1529.06	1531.85	1527.03	1530.49	412	380
			1531.90	1527.09	1530.54	413	381
45	1537.01	1536.62	1539.43	1534.59	1538.08	414	382
			1539.46	1534.62	1538.12	413	381

Table 5.13: Sound velocity measurements in distilled water using the FSM on the steady state portion of a ten period pulse that is averaged 512 times. For each temperature, there are two measured sound velocities. The topmost value was measured during the first measurement series, while the bottom-most value was measured during the second measurement series.

Fourier spectrum method						
	Modelled sound velocity		Experimental sound velocity			Relative expanded uncertainty (95% c.l.)	
Temp. [$^\circ$C]	$c_{K\&F}$ [m/s]	c_{UNESCO} [m/s]	c_{FSM} [m/s]	$c_{FSM,M1}$ [m/s]	$c_{FSM,M2}$ [m/s]	$E_{c_{FSM,M1}}$ [ppm]	$E_{c_{FSM,M2}}$ [ppm]
25	1496.69	1496.88	1499.30	1494.63	1497.94	412	383
			1499.47	1494.80	1498.11	419	388
30	1509.37	1509.32	1512.17	1507.48	1510.82	406	375
			1512.32	1507.63	1510.97	408	377
35	1520.25	1520.01	1523.04	1518.34	1521.69	403	371
			1523.06	1518.36	1521.71	405	372
40	1529.43	1529.06	1532.23	1527.51	1530.89	402	370
			1532.39	1527.67	1531.05	403	372
45	1537.01	1536.62	1539.79	1535.05	1538.46	404	372
			1540.01	1535.27	1538.68	404	372

Fig. 5.9 - 5.11 and Table 5.12 - 5.13 show some clear trends in the measured sound velocities. Firstly, the sound velocities measured with the ZCM is slightly lower than the corresponding sound velocities measured with the FSM, over the complete temperature span. The difference is fluctuating, but seems to lie around 0.3 to 0.7 m/s. Based on the tabulated data, the difference between c_{ZCM} and c_{FSM} is 1512.32 m/s - 1511.72 m/s = 0.60 m/s at most, which is the difference at 30°C, taking both measurement series for both signal processing methods into account. For the measured sound velocities corrected for diffraction using Method 1, i.e. $c_{ZCM,M1}$ and $c_{FSM,M1}$, the maximum difference is 1507.63 m/s - 1506.94 m/s = 0.69 m/s, which is also at 30°C. Here, the uncertainty of $c_{ZCM,M1}$ is 415 ppm, which is equivalent to 0.63 m/s, and the uncertainty of $c_{FSM,M1}$ is 408 ppm, which is equivalent to 0.62 m/s. Evidently, the measured sound velocities $c_{ZCM,M1}$ and $c_{FSM,M1}$ are only within each others uncertainty if both uncertainties are taken into account.

For the measured sound velocities corrected for diffraction using Method 2, i.e. $c_{ZCM,M2}$ and $c_{FSM,M2}$, the maximum difference is also found at 30°C. The difference is 1510.97 m/s - 1510.35 m/s = 0.62 m/s, which is between the difference of the uncorrected sound velocities and the difference of the sound velocities corrected for diffraction using Method 1. The uncertainty of the value of $c_{ZCM,M2}$ is 384 ppm, which is equivalent to 0.58 m/s, while the uncertainty of $c_{FSM,M2}$ is 377 ppm, which is equivalent to 0.57 m/s. Again, it is clear that the two sound velocities are only within each others uncertainties if both uncertainties are taken into account. In other words, both the greatest deviation between the two signal processing methods and the greatest measurement uncertainties are found for the measured sound velocities corrected for diffraction using Method 1. Table 5.12 and 5.13 also

show that the relative uncertainties are highest at the lowest temperature, and diffraction correction Method 1 results in greater relative uncertainties than Method 2. In Chapter 6, this is discussed further with illustrating figures.

Fig. 5.10 shows the measured sound velocities relative to the sound velocities calculated from the model presented by Kinsler et. al. [29]. A deviation of 1000 ppm from the model is illustrated in green. The measured sound velocities closest to the modelled sound velocities are found using the ZCM and diffraction correction Method 2. However, the corresponding sound velocities found using the FSM are also within 1000 ppm of $c_{K\&F}$ for most temperatures. There seems to be a slight non linear relationship between $c_{K\&F}$ and the experimental sound velocities, where the experimental sound velocities are increasing at a higher rate. Also, the measured values in measurement series 2 is generally somewhat higher, causing $c_{FSM,M2}$ to be outside 1000 ppm of $c_{K\&F}$ when the temperature exceeds approximately $38°C$. The deviation between measurement series 1 and 2, as well as the non linearity, indicates that measurements might have been performed under unstable conditions. Additionally, 5.11 shows that the measured values does not follow the modelled sound velocity calculated with the UNESCO algorithm [11, 12]. The modelled sound velocity calculated with the formula presented by Kinsler et. al. [29] is clearly more matching. This is discussed more thoroughly in Chapter 6.

To investigate how the measurement cell functions at other frequencies, the measured sound velocity is investigated as a function of frequency from 275 kHz to 600 kHz, in steps of 25 kHz. Using the same experimental setup, the sound velocity was found by setting the desired frequency on the signal generator, and running the MATLAB-script presented in Appendix E.3.4. The temperature fluctuated between $24.991°C$ and $25.016°C$ during measurements. The experimental sound velocity as a function of frequency are shown in Fig. 5.12, and a list of the measured values is provided in Table 5.14.
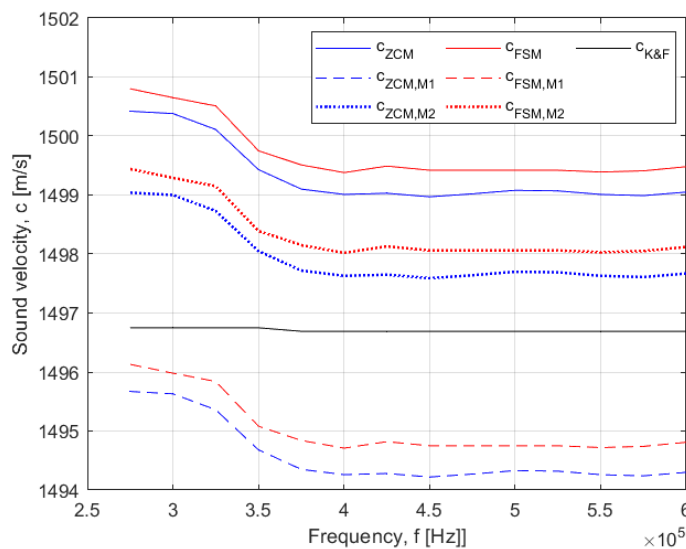
Figure 5.12: Measured sound velocity in distilled water as a function of frequency from 275 kHz to 600 kHz. The measured values are found using the steady state portion of a ten period pulse and averaging the waveform 512 times. The temperature was set to be $25°C$, but fluctuated between $24.991°C$ and $25.016°C$ during measurements.

Table 5.14: List of the modelled and measured sound velocities at each frequency set point between 275 kHz and 600 kHz. The measured values are found using the steady state portion of a ten period pulse and averaging the waveform 512 times. The temperature was set to be $25°C$, but fluctuated between $24.991°C$ and $25.016°C$ during measurements.

Frequency	Modelled sound velocity	Measured sound velocity ZCM			Measured sound velocity FSM		
f [kHz]	$c_{K\&F}$ [m/s]	c_{ZCM} [m/s]	$c_{ZCM,M1}$ [m/s]	$c_{ZCM,M2}$ [m/s]	c_{FSM} [m/s]	$c_{FSM,M1}$ [m/s]	$c_{FSM,M2}$ [m/s]
275	1496.75	1500.42	1495.67	1499.04	1500.80	1496.13	1499.44
300	1496.75	1500.38	1495.63	1499.00	1500.65	1495.98	1499.29
325	1496.75	1500.11	1495.36	1498.73	1500.51	1495.84	1499.15
350	1496.75	1499.43	1494.68	1498.05	1499.75	1495.08	1498.39
375	1496.69	1499.10	1494.35	1497.72	1499.51	1494.84	1498.15
400	1496.69	1499.01	1494.26	1497.63	1499.38	1494.71	1498.02
425	1496.69	1499.03	1494.28	1497.65	1499.49	1494.82	1498.13
450	1496.69	1498.97	1494.22	1497.59	1499.42	1494.75	1498.06
475	1496.69	1499.02	1494.27	1497.64	1499.42	1494.75	1498.06
500	1496.69	1499.08	1494.33	1497.70	1499.42	1494.75	1498.06
525	1496.69	1499.07	1494.32	1497.69	1499.42	1494.75	1498.06
550	1496.69	1499.01	1494.26	1497.63	1499.39	1494.72	1498.03
575	1496.69	1498.99	1494.24	1497.61	1499.41	1494.74	1498.05
600	1496.69	1499.05	1494.30	1497.67	1499.48	1494.81	1498.12

Fig. 5.12 shows that the measured sound velocity stabilize around 375 kHz, which corresponds well to the results found in [84]. This is the case for both the ZCM and the FSM. The increase in sound velocity at lower frequencies are thought to be due to an amplitude reduction of the pulses, and thus a lower SNR.

Uncertainty of the experimental sound velocity in distilled water

The uncertainty of the experimental sound velocity in distilled water is calculated according to the uncertainty model presented in Section 4.2. It is a result of several different uncertainty contributors found at different stages in the project. The values of the uncertainty contributors are also found in a number of different ways. Some are calculated during measurements or estimated through observations, while others may be found directly in datasheets or other tabulated data. An example uncertainty budget for the experimental sound velocity in distilled water is thus presented in Section 5.5.

Uncertainty of the theoretical sound velocity in distilled water

In Section 4.4.2, an uncertainty model for the sound velocity in distilled water, calculated using Eq. 2.1, was derived. According to Table 5.12 and 5.13, the maximum relative uncertainty for the measured sound velocity is found at $25°C$. Consequently, this temperature is also used in the derivation of the uncertainty budget for $c_{K\&F}$. The environmental pressure was measured by the barometer to be $P_0 = 1.020$ bar when the sound velocity was measured at $25°C$. Both the combined standard uncertainty of temperature and pressure is used to calculate the uncertainty of $c_{K\&F}$. They are calculated in Table 5.3 and 5.5, respectively. Table 5.15 lists the different uncertainty contributors to the total uncertainty of $c_{K\&F}$. An associated description to each uncertainty contributor can be found in Table 4.9.

Table 5.15: List of the uncertainties contributing to the total uncertainty of the modelled sound velocity, $c_{K\&F}$, when the temperature is $T = 25°C$ and the pressure measured by the barometer is $P_0 = 1.020$ bar. A description of each uncertainty contributor is provided in Table 4.9. Each value has been multiplied with its associated coverage factor.

Uncertainty contributor	Value	Note
$u_c(P_G)$	$1.668 \cdot 10^{-4}$ bar	Equal to $u_c(P)$, found in table 5.5. Coverage factor $k = 2$.
$u_c(T)$	$0.276°C$	Found in table 5.3. Coverage factor $k = 2$.
$u(c)_{model}$	0.748 m/s	0.05% of theoretical sound velocity, which is 1496.7 m/s at $25°C$ according to [29]. Coverage factor $k = 2$ assumed.

Table 5.16: Uncertainty budget for the total uncertainty of $c_{K\&F}$ in distilled at $T = 25°C$ and $P_0 = 1.020$ bar. The values are taken from Table 5.15, and the budget is calculated according to Eq. 4.57.

Uncertainty Contributor	Input Uncertainty				Combined Uncertainty	
	Expand. uncert.	Conf. level & distribut.	Cov. fact., k	Standard uncertainty	Sens. coeff.	Variance [$(m/s)^2$]
$u_c(P_G)$	$1.668 \cdot 10^{-4}$ bar	95% (norm)	2	$8.339 \cdot 10^{-5}$ bar	0.168	$1.951 \cdot 10^{-10}$
$u_c(T)$	$0.276°C$	95% (norm)	2	$0.138°C$	2.723	0.141
$u(c)_{model}$	0.748 m/s	95% (norm)	2	0.374 m/s	1	0.140
Sum of variances, $u_c^2(c)$						$0.281 \ (m/s)^2$
Combined standard uncertainty, $u_c(c)$						$0.530 \ m/s$
Expanded uncertainty (95% confidence level, $k = 2$), $U(c)$						$1.060 \ m/s$
Theoretical sound velocity in distilled water at $25°C$, c						$1496.7 \ m/s$
Relative expanded uncertainty (95% confidence level, $k = 2$), $U(c)/c$						0.071%

5.4.2 Sound velocity measurements in saline water

In total, six measurement series (two measurement series for each salinity concentration) were carried out on saline water with the following salinity concentrations: (1) 20 ppt, (2) 35 ppt and (3) 50 ppt. The desired salinity was achieved by weighing up the correct amount of salt, mixing it into distilled water, and waiting for it to be dissolved. This process was repeated for every measurement series. The measurement cell was also cleaned and dried in between each measurement series to keep the salinity as accurate as possible. In Fig. 5.13, 5.15, 5.18 and 5.14, 5.16, 5.19, the absolute and normalised sound velocities are plotted respectively for each salinity concentration together with the modelled sound velocities calculated with the UNESCO-algorithm. Also, the experimental sound velocity is investigated as a function of frequency for 50 ppt salinity. The results are shown in Fig. 5.20.

Sound velocity measurements in saline water at 20 ppt salinity

The hydrostatic pressure varied between 1.015 and 1.023 bar during measurements on 20 ppt saline water, and the following results were obtained:

(a)   (b)
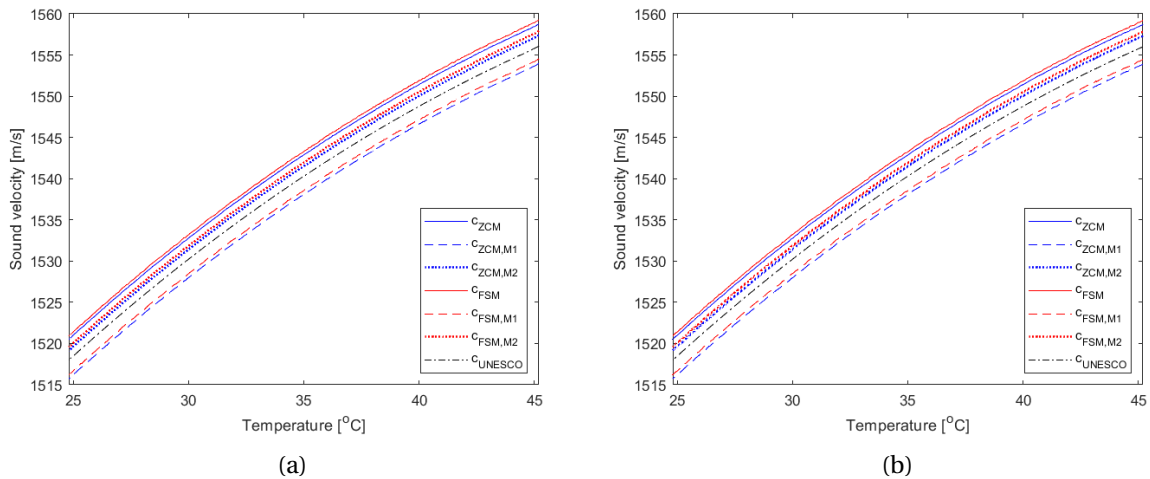
Figure 5.13: Measured and theoretical sound velocity in saline water at 20 ppt salinity from 25 to $45°C$. The measured values are found using the steady state portion of a ten period pulse and averaging the waveform 512 times. The theoretical values are calculated using Eq. D.1. (a) Measurement series 1, (b) Measurement series 2.
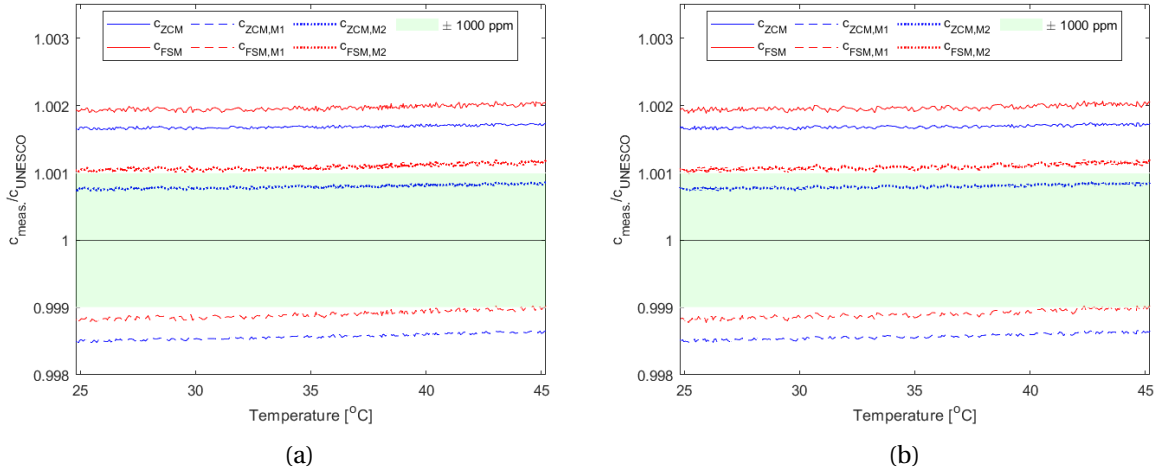
Figure 5.14: Normalised measured sound velocity in saline water at 20 ppt salinity from 25 to 45°C, with respect to the theoretical values calculated using Eq. D.1. The measured values are found using the steady state portion of a ten period pulse and averaging the waveform 512 times. (a) Measurement series 1, (b) Measurement series 2.

Table 5.17: Sound velocity measurements in saline water at 20 ppt salinity using the ZCM on the steady state portion of a ten period pulse that is averaged 512 times. For each temperature, there are two measured sound velocities. The topmost value was measured during the first measurement series, while the bottom-most value was measured during the second measurement series.

Zerocrossing method						
	Modelled sound velocity	Experimental sound velocity			Relative expanded uncertainty (95% c.l.)	
Temp. [°C]	c_{UNESCO} [m/s]	c_{ZCM} [m/s]	$c_{ZCM,M1}$ [m/s]	$c_{ZCM,M2}$ [m/s]	$E_{c_{ZCM,M1}}$ [ppm]	$E_{c_{ZCM,M2}}$ [ppm]
25	1518.49	1520.98	1516.21	1519.62	419	390
		1521.08	1516.30	1519.72	422	392
30	1530.24	1532.90	1528.11	1531.55	416	384
		1532.83	1528.04	1531.47	415	384
35	1540.30	1542.88	1538.07	1541.54	412	378
		1542.80	1537.99	1541.46	412	379
40	1548.78	1551.46	1546.63	1550.12	412	379
		1551.39	1546.56	1550.05	413	380
45	1555.75	1558.44	1553.59	1557.11	413	379
		1558.43	1553.57	1557.09	411	378

Table 5.18: Sound velocity measurements in saline water at 20 ppt salinity using the FSM on the steady state portion of a ten period pulse that is averaged 512 times. For each temperature, there are two measured sound velocities. The topmost value was measured during the first measurement series, while the bottom-most value was measured during the second measurement series.

Fourier spectrum method						
	Modelled sound velocity	**Experimental sound velocity**			**Relative expanded uncertainty (95% c.l.)**	
Temp. [°C]	c_{UNESCO} [m/s]	c_{FSM} [m/s]	$c_{FSM,M1}$ [m/s]	$c_{FSM,M2}$ [m/s]	$E_{c_{FSM,M1}}$ [ppm]	$E_{c_{FSM,M2}}$ [ppm]
25	1518.49	1521.35	1516.58	1519.99	408	379
		1521.47	1516.69	1520.11	412	381
30	1530.24	1533.31	1528.52	1531.95	406	374
		1533.27	1528.48	1531.91	404	373
35	1540.30	1543.28	1538.47	1541.93	402	368
		1543.20	1538.39	1541.84	402	369
40	1548.78	1551.91	1547.08	1550.57	401	368
		1551.82	1546.99	1550.49	402	369
45	1555.75	1558.91	1554.06	1557.58	401	368
		1558.95	1554.10	1557.62	401	368

Fig. 5.13 and 5.14 shows many of the same trends that was found in the results for distilled water. Firstly, it is clear that the FSM still measures a somewhat higher sound velocity than the ZCM. However, the deviation has a slightly lower ceiling at approximately 0.53 m/s, compared to 0.69 m/s for distilled water.

Based on the tabulated data in Table 5.17 and 5.18, the difference between c_{ZCM} and c_{FSM} is 0.52 m/s at most, which corresponds to the difference at both $40°C$ and $45°C$, taking both measurement series for both signal processing methods into account. For the measured sound velocities corrected for diffraction using Method 1, i.e. $c_{ZCM,M1}$ and $c_{FSM,M1}$, the maximum difference is 1554.10 m/s - 1553.57 m/s = 0.53 m/s, which is at $45°C$. The corresponding uncertainty of $c_{ZCM,M1}$ is 411 ppm, which is equivalent to 0.64 m/s, and the corresponding uncertainty of $c_{FSM,M1}$ is 401 ppm, which is equivalent to 0.62 m/s. Evidently, the measurement uncertainty covers the deviation between $c_{ZCM,M1}$ and $c_{FSM,M1}$.

For the measured sound velocities corrected for diffraction using Method 2, i.e. $c_{ZCM,M2}$ and $c_{FSM,M2}$, the maximum difference is also found at 45°. The difference is 1557.62 m/s - 1557.09 m/s = 0.53 m/s, which is the same that was found for the results using diffraction correction Method 1. The corresponding uncertainty of $c_{ZCM,M1}$ is 378 ppm, which is equivalent to 0.59 m/s, and the corresponding uncertainty of $c_{FSM,M1}$ is 368 ppm, which is equivalent to 0.57 m/s. The absolute uncertainty of $c_{ZCM,M2}$ and $c_{FSM,M2}$ is thus lower than the absolute uncertainty of $c_{ZCM,M1}$ and $c_{FSM,M1}$, but still high enough for the sound velocities to lie within each others uncertainty.

Furthermore, Fig 5.14 shows the same non linearity that was found in Fig 5.10, where the measured

sound velocities seem to be increasing at a higher rate than c_{UNESCO}, when the temperature is increasing. Similarly to distilled water, $c_{ZCM,M2}$ is the only measured sound velocity that is within 1000 ppm of the modelled sound velocity over the complete temperature span.

One additional observation that has been made is that measurement series 1 and 2 are more corresponding for saline water at 20 ppt salinity than distilled water. For distilled water, the deviation between measurement series 1 and 2 reached 0.22 m/s at $45°C$, cf. Table 5.13. The maximum deviation found for saline water at 20 ppt salinity is only 0.12 m/s, at $25°C$. Also, the tables show that measurement series 2 always measured higher sound velocities than measurement series 1 for distilled water. This was not the case for saline water, where the results of measurement series 1 and 2 were more alternating in regards to which was higher. The results are discussed further and more thoroughly in Chapter 6.

Sound velocity measurements in saline water at 35 ppt salinity

The hydrostatic pressure varied between 1.017 and 1.031 bar during measurements on 35 ppt saline water, and the following results were obtained:
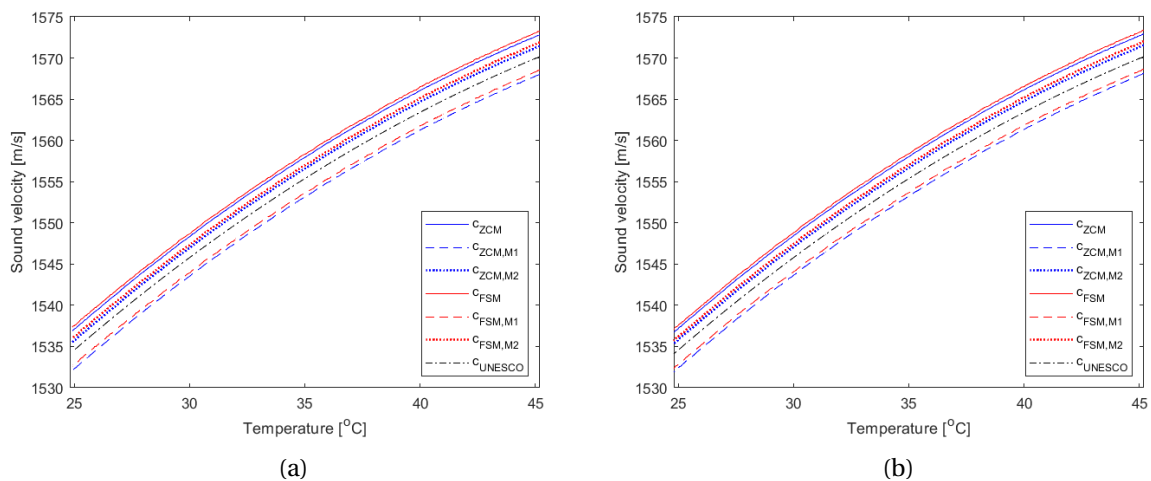
Figure 5.15: Measured and theoretical sound velocity in saline water at 35 ppt salinity from 25 to $45°C$. The measured values are found using the steady state portion of a ten period pulse and averaging the waveform 512 times. The theoretical values are calculated using Eq. D.1. (a) Measurement series 1, (b) Measurement series 2.
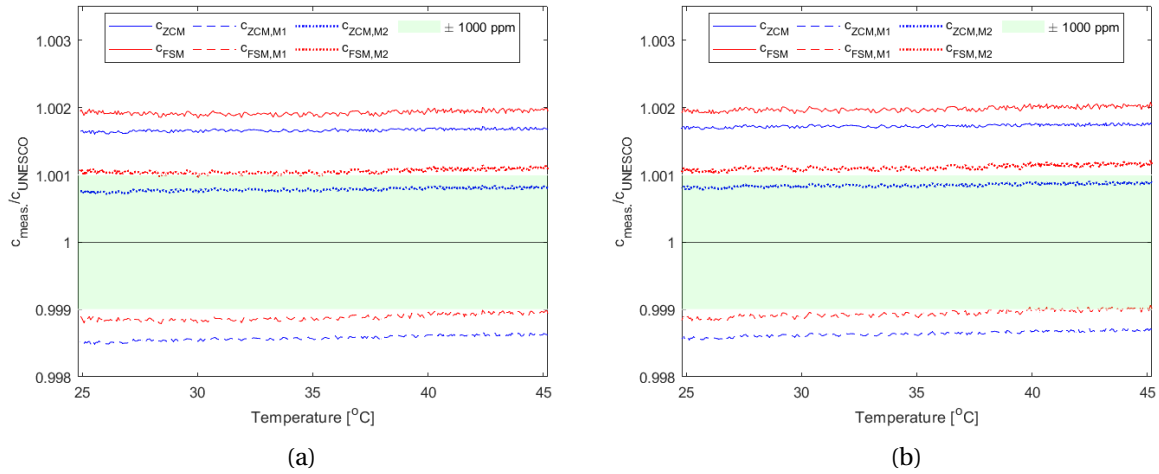
Figure 5.16: Normalised measured sound velocity in saline water at 35 ppt salinity from 25 to 45°C, with respect to the theoretical values calculated using Eq. D.1. The measured values are found using the steady state portion of a ten period pulse and averaging the waveform 512 times. (a) Measurement series 1, (b) Measurement series 2.

Table 5.19: Sound velocity measurements in saline water at 35 ppt salinity using the ZCM on the steady state portion of a ten period pulse that is averaged 512 times. For each temperature, there are two measured sound velocities. The topmost value was measured during the first measurement series, while the bottom-most value was measured during the second measurement series.

Zerocrossing method						
	Modelled sound velocity	**Experimental sound velocity**			**Relative expanded uncertainty (95% c.l.)**	
Temp. $[^{\circ}\text{C}]$	c_{UNESCO} $[\text{m/s}]$	c_{ZCM} $[\text{m/s}]$	$c_{\text{ZCM,M1}}$ $[\text{m/s}]$	$c_{\text{ZCM,M2}}$ $[\text{m/s}]$	$E_{c_{\text{ZCM,M1}}}$ $[\text{ppm}]$	$E_{c_{\text{ZCM,M2}}}$ $[\text{ppm}]$
25	1534.59	1537.15	1532.36	1535.81	411	382
		1537.28	1532.49	1535.94	420	390
30	1545.79	1548.36	1543.55	1547.03	410	378
		1548.51	1543.69	1547.18	418	388
35	1555.37	1557.92	1553.09	1556.60	409	381
		1557.99	1553.16	1556.67	416	386
40	1563.41	1566.07	1561.22	1564.75	409	381
		1566.15	1561.30	1564.83	415	384
45	1569.94	1572.63	1567.76	1571.32	408	374
		1572.74	1567.86	1571.43	415	383

Table 5.20: Sound velocity measurements in saline water at 35 ppt salinity using the FSM on the steady state portion of a ten period pulse that is averaged 512 times. For each temperature, there are two measured sound velocities. The topmost value was measured during the first measurement series, while the bottom-most value was measured during the second measurement series.

Fourier spectrum method						
	Modelled sound velocity	**Experimental sound velocity**			**Relative expanded uncertainty (95% c.l.)**	
Temp. [$^\circ$**C**]	c_{UNESCO} [**m/s**]	c_{FSM} [**m/s**]	$c_{FSM,M1}$ [**m/s**]	$c_{FSM,M2}$ [**m/s**]	$E_{c_{FSM,M1}}$ [**ppm**]	$E_{c_{FSM,M2}}$ [**ppm**]
25	1534.59	1537.56	1532.83	1536.23	403	374
		1537.64	1532.91	1536.31	412	382
30	1545.79	1548.69	1543.94	1547.37	401	371
		1548.85	1544.09	1547.53	411	381
35	1555.37	1558.31	1553.54	1556.99	398	368
		1558.35	1553.57	1557.03	408	378
40	1563.41	1566.53	1561.74	1565.22	397	367
		1566.52	1561.73	1565.21	408	378
45	1569.94	1573.03	1568.22	1571.73	397	368
		1573.17	1568.36	1571.88	407	377

The first measurement series conducted on saline water at 35 ppt salinity differs from the other ones, as it is the only measurement series that shows a clear decrease in the normalized sound velocity measured with the FSM at the lowest temperatures. This is clarified in Fig. 5.17, which zooms in on $c_{FSM,M2}/c_{UNESCO}$ for temperatures between 25 and 30$^\circ C$.
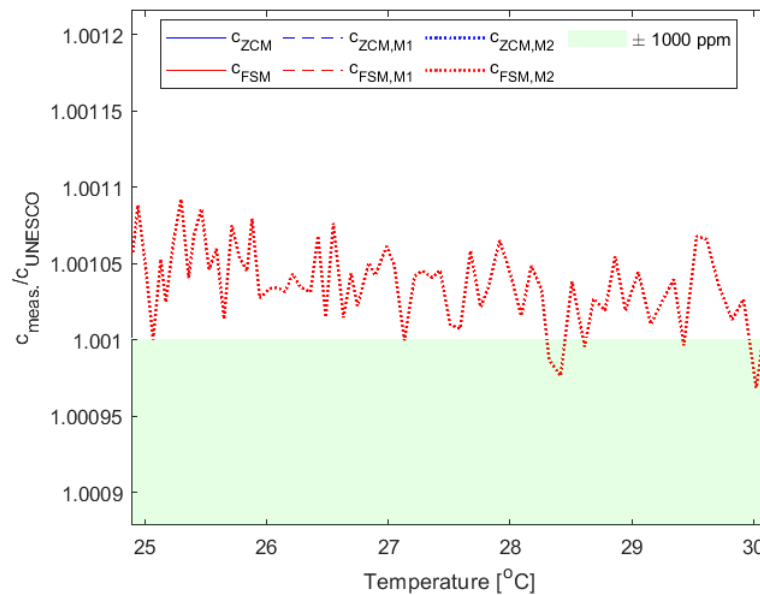
Figure 5.17: Measured sound velocity measured with the FSM using diffraction correction Method 2, $c_{FSM,M2}$, normalized with respect to the modelled sound velocity, c_{UNESCO}, over a temperature span from 25 to 30$^\circ C$. The figure is an extract from Fig. 5.16a.

Fig. 5.17 shows that the measurements are fluctuating, but there is an overall decrease causing $c_{FSM,M2}$ to not be within 1000 ppm of c_{UNESCO} until around $28.4°C$. In other words, the modelled sound velocity was increasing at a higher rate than the measured sound velocity at low temperatures. The reason behind this is discussed further in Chapter 6. Other than that, the same trends that was found in distilled water and water at 20 ppt salinity can be seen here. The FSM always measures higher sound velocities than the ZCM, and $c_{ZCM,M2}$ is the measured sound velocity that is closest to c_{UNESCO} over the complete temperature span.

Based on the tabulated data in Table 5.19 and 5.20, the deviation between the sound velocities measured with the ZCM and the FSM is always greatest at $45°C$. For the uncorrected sound velocities, the difference is 1573.17 m/s - 1572.63 m/s = 0.54 m/s at most. A small increase in difference is found for the sound velocities that are corrected according to diffraction correction Method 1, i.e. 1568.36 m/s - 1567.76 m/s = 0.60 m/s. The difference between the sound velocities measured using diffraction correction Method 2 lies in between the other two differences, and is found to be 1571.88 m/s - 1571.32 m/s = 0.56 m/s. The corresponding estimated uncertainties are 408, 407, 374 and 377 ppm, which is equivalent to 0.64, 0.64, 0.59 and 0.59 m/s for $c_{ZCM,M1}$, $c_{FSM,M1}$, $c_{ZCM,M2}$ and $c_{FSM,M2}$, respectively. Evidently, the uncertainty of the each measured sound velocity is high enough to cover the deviation to the corresponding sound velocity measured with the other signal processing method. This is the case for both diffraction correction methods. The tables also show that, (with exception of the measurements conducted with the FSM at $40°C$), the measured sound velocities is higher for measurement series 1 than 2. This was also the case for distilled water, but not for saline water at 20 ppt salinity.

Sound velocity measurements in saline water at 50 ppt salinity

The hydrostatic pressure varied between 1.012 and 1.029 bar during measurements on 50 ppt saline water, and the following results were obtained:
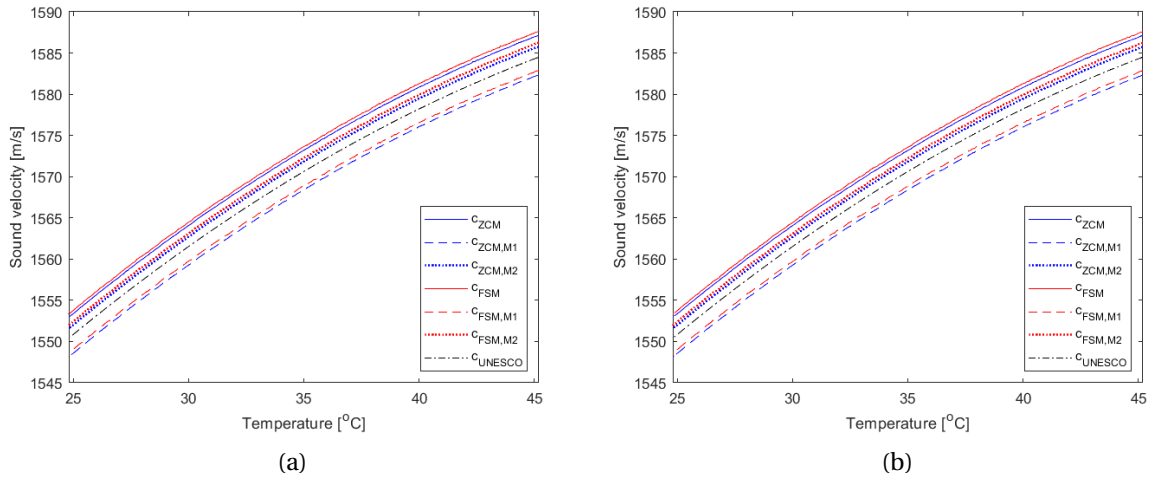
Figure 5.18: Measured and theoretical sound velocity in saline water at 50 ppt salinity from 25 to 45$^{\circ}C$. The measured values are found using the steady state portion of a ten period pulse and averaging the waveform 512 times. The theoretical values are calculated using Eq. D.1. (a) Measurement series 1, (b) Measurement series 2.
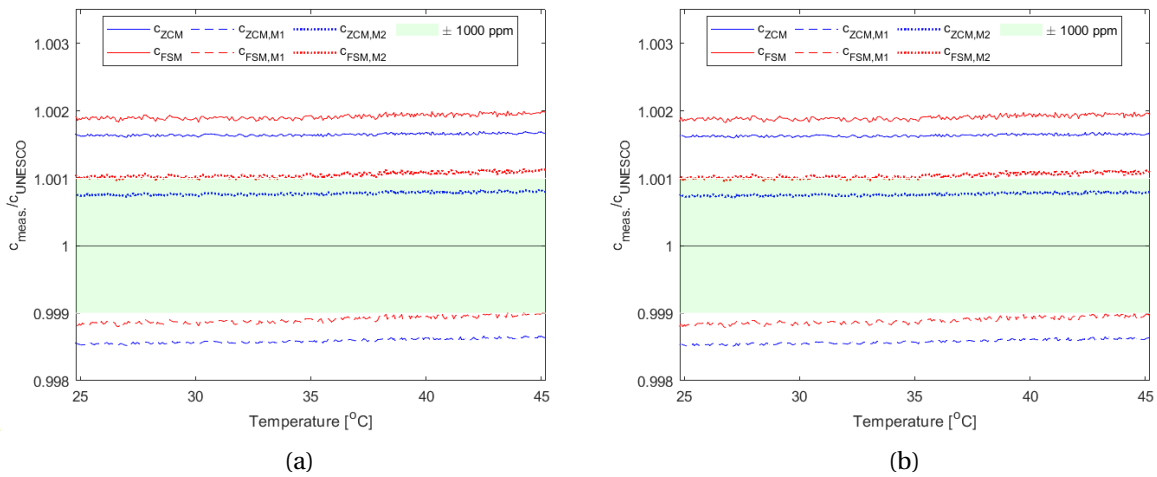
Figure 5.19: Normalised measured sound velocity in saline water at 50 ppt salinity from 25 to 45$^{\circ}C$, with respect to the theoretical values calculated using Eq. D.1. The measured values are found using the steady state portion of a ten period pulse and averaging the waveform 512 times. (a) Measurement series 1, (b) Measurement series 2.

Table 5.21: Sound velocity measurements in saline water at 50 ppt salinity using the ZCM on the steady state portion of a ten period pulse that is averaged 512 times. For each temperature, there are two measured sound velocities. The topmost value was measured during the first measurement series, while the bottom-most value was measured during the second measurement series.

Zerocrossing method						
	Modelled sound velocity	**Experimental sound velocity**			**Relative expanded uncertainty (95% c.l.)**	
Temp. [$^\circ$**C**]	c_{UNESCO} [**m/s**]	c_{ZCM} [**m/s**]	$c_{ZCM,M1}$ [**m/s**]	$c_{ZCM,M2}$ [**m/s**]	$E_{c_{ZCM,M1}}$ [**ppm**]	$E_{c_{ZCM,M2}}$ [**ppm**]
25	1550.87	1553.42	1548.60	1552.10	428	399
		1553.37	1548.54	1552.05	424	395
30	1561.53	1564.11	1559.37	1562.79	425	396
		1564.15	1559.41	1562.83	423	395
35	1570.63	1573.23	1568.45	1571.92	424	395
		1573.22	1568.45	1571.91	423	394
40	1578.21	1580.90	1576.10	1579.60	423	394
		1580.85	1576.05	1579.55	422	393
45	1584.29	1586.96	1582.14	1585.67	423	394
		1586.97	1582.15	1585.68	422	393

Table 5.22: Sound velocity measurements in saline water at 50 ppt salinity using the FSM on the steady state portion of a ten period pulse that is averaged 512 times. For each temperature, there are two measured sound velocities. The topmost value was measured during the first measurement series, while the bottom-most value was measured during the second measurement series.

Fourier spectrum method						
	Modelled sound velocity	**Experimental sound velocity**			**Relative expanded uncertainty (95% c.l.)**	
Temp. [$^\circ$**C**]	c_{UNESCO} [**m/s**]	c_{FSM} [**m/s**]	$c_{FSM,M1}$ [**m/s**]	$c_{FSM,M2}$ [**m/s**]	$E_{c_{FSM,M1}}$ [**ppm**]	$E_{c_{FSM,M2}}$ [**ppm**]
25	1550.87	1553.80	1549.06	1552.50	415	386
		1553.77	1549.03	1552.47	415	385
30	1561.53	1564.54	1559.78	1563.25	414	385
		1564.53	1559.77	1563.25	413	384
35	1570.63	1573.68	1568.90	1572.40	412	383
		1573.61	1568.83	1572.34	412	383
40	1578.21	1581.33	1576.53	1580.05	411	382
		1581.27	1576.47	1579.99	410	381
45	1584.29	1587.42	1582.60	1586.15	410	381
		1587.47	1582.65	1586.21	409	380

The measured sound velocities in saline water at 50 ppt salinity seem to increase at a similar rate to the increase that is seen for the other salinity concentrations (with exception of measurement series 1

for 35 ppt salinity), as the temperature increases. Again, the sound velocities measured with the FSM are always greater than the corresponding sound velocities measured with the ZCM, and $c_{ZCM,M2}$ is the only measured sound velocity that is within 1000 ppm of c_{UNESCO} over the complete temperature span.

The biggest deviation between sound velocities measured with the ZCM and the FSM is found for diffraction correction Method 2, where the maximum difference between $c_{ZCM,M2}$ and $c_{FSM,M2}$ is 1586.21 m/s - 1585.67 m/s = 0.54 m/s at $45°C$. The relative uncertainties for the associated sound velocity values are 394 ppm, which is equivalent to 0.62 m/s, for $c_{ZCM,M2}$, and 380 ppm, which is equivalent to 0.60 m/s, for $c_{FSM,M2}$. Further, both the uncorrected sound velocities and the corrected sound velocities using diffraction correction Method 1 show a maximum deviation of 0.51 m/s, at $45°C$, between the ZCM and FSM. They are calculated as 1587.47 m/s - 1586.96 m/s = 0.51 m/s and 1582.65 m/s - 1582.14 m/s = 0.51 m/s for the uncorrected and corrected sound velocities, respectively. The associated relative uncertainties to the values of $c_{ZCM,M1}$ and $c_{FSM,M1}$ are 423 ppm, which equivalent to 0.67 m/s, and 409 ppm, which is equivalent to 0.65 m/s, respectively.

The measured sound velocity in water at 50 ppt salinity was also investigated at different frequencies. Fig. ?? shows that the results are quite similar to the ones found for distilled water, see Fig 5.12. Again, it seems like the measured sound velocities stabilize around 375 kHz for both the ZCM and the FSM. The small change in c_{UNSECO} is due to the temperature not being completely stable. It varied between $24.986^c ircC$ and $25.011°C$ during measurements.
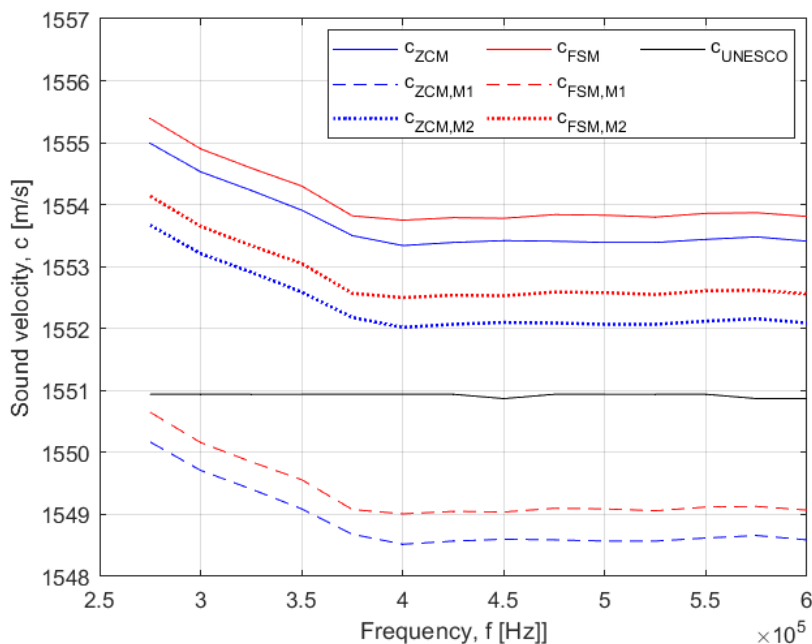
Figure 5.20: Measured sound velocity in saline water at 50 ppt salinity as a function of frequency from 275 kHz to 600 kHz. The measured values are found using the steady state portion of a ten period pulse and averaging the waveform 512 times. The temperature was set to be $25°C$, but fluctuated between $24.986°C$ and $25.011°C$ during measurements.

Table 5.23: List of the modelled and measured sound velocities at each frequency set point between 275 kHz and 600 kHz. The measured values are found using the steady state portion of a ten period pulse and averaging the waveform 512 times. The temperature was set to be 25°C, but fluctuated between 24.986°C and 25.011°C during measurements.

Frequency	Modelled sound velocity	Measured sound velocity ZCM			Measured sound velocity FSM		
f [kHz]	c_{UNESCO} [m/s]	c_{ZCM} [m/s]	$c_{ZCM,M1}$ [m/s]	$c_{ZCM,M2}$ [m/s]	c_{FSM} [m/s]	$c_{FSM,M1}$ [m/s]	$c_{FSM,M2}$ [m/s]
275	1550.94	1554.99	1550.17	1553.67	1555.39	1550.65	1554.14
300	1550.94	1554.53	1549.71	1553.21	1554.90	1550.16	1553.65
325	1550.94	1554.23	1549.41	1552.91	1554.59	1549.85	1553.34
350	1550.94	1553.91	1549.09	1552.59	1554.30	1549.56	1553.05
375	1550.94	1553.50	1548.68	1552.18	1553.82	1549.08	1552.57
400	1550.94	1553.34	1548.52	1552.02	1553.75	1549.01	1552.50
425	1550.94	1553.39	1548.57	1552.07	1553.79	1549.05	1552.54
450	1550.87	1553.42	1548.60	1552.10	1553.78	1549.04	1552.53
475	1550.94	1553.41	1548.59	1552.09	1553.84	1549.10	1552.59
500	1550.94	1553.39	1548.57	1552.07	1553.83	1549.09	1552.58
525	1550.94	1553.39	1548.57	1552.07	1553.80	1549.06	1552.55
550	1550.94	1553.44	1548.62	1552.12	1553.86	1549.12	1552.61
575	1550.87	1553.48	1548.66	1552.16	1553.87	1549.13	1552.62
600	1550.87	1553.41	1548.59	1552.09	1553.81	1549.07	1552.56

Change in salinity due to evaporation

During measurements, evaporation may cause a slight change in salinity when the sample is heated. To account for this, a CMD210 conductivity meter [114] was used to measure the conductivity of the sample before and after measurements were taken. The conductivity meter has an accuracy of ±0.2% of the measured value ±3 of the least significant digit [114]. All measured values are presented in Table. 5.24.

Table 5.24: Conductivity measurement on saline water before and after testing, using a CMD210 conductivity meter.

	20 ppt [mS/cm]		35 ppt [mS/cm]		50 ppt [mS/cm]	
	Before	After	Before	After	Before	After
Measurement series 1	32.07	32.10	53.06	53.08	75.13	75.18
Measurement series 2	32.07	32.09	53.04	53.07	75.16	75.20

Evidently, the change in salinity is miniscule. It falls within the uncertainty of the CMD210 instrument, and can thus be neglected.

Uncertainty of the experimental sound velocity in saline water

Section 5.5 provides an uncertainty budget for the uncertainty of the experimental sound velocity in distilled water. The budget is carried out according to the uncertainty model presented in Section 4.2. The same method can be used to calculate an uncertainty budget for the uncertainty of the experimental sound velocity in saline water, and is consequently not done here.

Uncertainty of the modelled sound velocity in saline water

In Section 4.4.3, an uncertainty model for the sound velocity in saline water, calculated using Eq. D.1 was derived. Here, the uncertainty model will be used to derive an uncertainty budget for c_{UNESCO}. The temperature and environmental pressure are set to be $T = 25°C$ and $P_0 = 1.020$ bar, respectively, which is the same that was used for the uncertainty budget for $c_{K\&F}$. Additionally, a salinity of 50 ppt is used, since it differs the most from distilled water. The desired salinity was achieved by using a UWE NJW-300 scale to measure the amount of salt required. A datasheet for the scale has not been found, and the uncertainty of the salinity is thus assumed to be equal to the resolution of the scale display, which is 0.1 g.

Table 5.25: List of the uncertainties contributing to the total uncertainty of the modelled sound velocity, c_{UNESCO}, when the temperature is $T = 25°C$, the environmental pressure is $P_0 = 1.020$ bar, and the salinity is 50 ppt. A description of each uncertainty contributor is provided in Table 4.10. Each value has been multiplied with its associated coverage factor.

Uncertainty contributor	Value	Note
$u_c(P)$	$1.668 \cdot 10^{-4}$ bar	Found in Table 5.5. Coverage factor $k = 2$ assumed.
$u_c(T)$	$0.276°C$	Found in Table 5.3. Coverage factor $k = 2$ assumed.
$u(S)$	$1.00 \cdot 10^{-4}$ kg	Due to the number of digits on the scale display. Coverage factor $k = 1$ assumed.
$u(c)_{model}$	0.15 m/s	Estimated in [115]. Coverage factor $k = 1$ assumed.

Table 5.26: Uncertainty budget for the total uncertainty of c_{UNESCO} in saline water at $T = 25°C$, $P_0 = 1.020$ bar and 50 ppt salinity. The values are taken from Table 5.25, and the budget is calculated according to Eq. 4.60.

Uncertainty	Input Uncertainty				Combined Uncertainty	
Contributor	Expand. uncert.	Conf. level & distribut.	Cov. fact., k	Standard uncertainty	Sens. coeff.	Variance $[(m/s)^2]$
$u_c(P)$	$1.668 \cdot 10^{-4}$ bar	95% (norm)	2	$8.339 \cdot 10^{-5}$ bar	0.168	$1.970 \cdot 10^{-10}$
$u_c(T)$	$0.276°C$	95% (norm)	2	$0.138°C$	2.674	0.136
$u(S)$	$1.00 \cdot 10^{-4}$ kg	68% (norm)	1	$1.00 \cdot 10^{-4}$ kg	1.094	$1.197 \cdot 10^{-8}$
$u(c)_{model}$	0.15 m/s	68% (norm)	1	0.15 m/s	1	0.0225
Sum of variances, $u_c^2(c)$						0.158 $(m/s)^2$
Combined standard uncertainty, $u_c(c)$						0.398 m/s
Expanded uncertainty (95% confidence level, $k = 2$), $U(c)$						0.796 m/s
Theoretical sound velocity in distilled water at $25°C$, c						1496.9 m/s
Relative expanded uncertainty (95% confidence level, $k = 2$), $U(c)/c$						0.053%

5.4.3 Sound velocity measurements in Exxsol D120 oil

In total, four measurement series were performed on Exxsol D120 oil. Two of the sets were taken on "new" oil, while the other two were taken on oil that had been temperature cycled from $25°C$ to $45°C$, and back to $25°C$ again. As explained in Section 2.1.2, heating of the oil may cause evaporation of some hydrocarbons in the oil composition. Consequently, the oil may have different acoustic properties after it has been temperature cycled. Hence, the main purpose of the last two measurement series is to investigate whether there would be a systematic change in sound velocity after the oil has been heated.

In contrary to distilled and saline water, there are no equation describing the sound velocity of Exxsol D120 oil as a function of temperature. Thus, the measured sound velocities cannot be compared to a corresponding modelled value.

Sound velocity measurements in uncycled Exxsol D120 oil

The hydrostatic pressure varied between 1.004 and 1.013 bar during measurements on uncycled Exxsol D120 oil, and the following results were obtained:
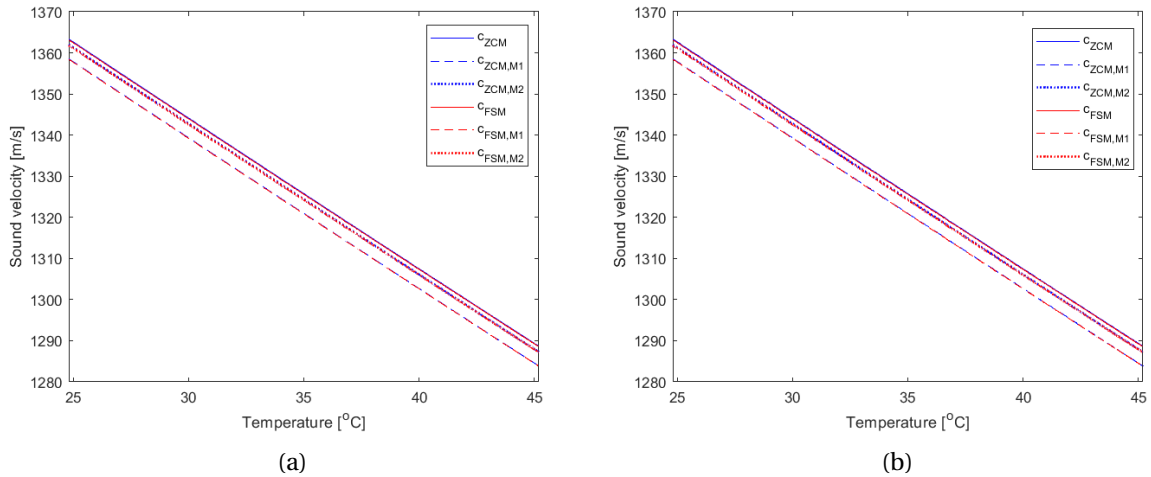
Figure 5.21: Measured sound velocity in Exxsol D120 oil from 25 to $45°C$. The measured values are found using the steady state portion of a ten period pulse and averaging the waveform 512 times. (a) Measurement series 1, (b) Measurement series 2.

Table 5.27: Sound velocity measurements in Exxsol D120 oil using the ZCM on the steady state portion of a ten period pulse that is averaged 512 times. For each temperature, there are two measured sound velocities. The topmost value was measured during the first measurement series, while the bottom-most value was measured during the second measurement series.

Zerocrossing method, not cycled					
	Experimental sound velocity			Relative expanded uncertainty (95% c.l.)	
Temp. [$°C$]	c_{ZCM} [m/s]	$c_{ZCM,M1}$ [m/s]	$c_{ZCM,M2}$ [m/s]	$E_{c_{ZCM,M1}}$ [ppm]	$E_{c_{ZCM,M2}}$ [ppm]
25	1362.65	1358.20	1361.27	410	382
	1362.64	1358.19	1361.26	410	382
30	1344.21	1339.80	1342.83	410	383
	1344.18	1339.77	1342.79	411	383
35	1325.87	1321.47	1324.46	409	381
	1325.89	1321.48	1324.47	410	382
40	1307.49	1303.11	1306.08	409	381
	1307.42	1303.04	1306.00	409	380
45	1289.54	1285.19	1288.12	408	380
	1289.53	1285.19	1287.11	409	381

Table 5.28: Sound velocity measurements in Exxsol D120 oil using the FSM on the steady state portion of a ten period pulse that is averaged 512 times. For each temperature, there are two measured sound velocities. The topmost value was measured during the first measurement series, while the bottom-most value was measured during the second measurement series.

Fourier spectrum method, not cycled				
	Experimental sound velocity			**Relative expanded uncertainty (95% c.l.)**
Temp. [°C]	c_{FSM} [m/s]	$c_{FSM,M1}$ [m/s]	$c_{FSM,M2}$ [m/s]	$E_{c_{FSM,M1}}$ [ppm]	$E_{c_{FSM,M2}}$ [ppm]
25	1362.45	1358.01	1361.07	402	374
	1362.48	1358.04	1361.10	401	373
30	1344.02	1339.60	1342.63	403	375
	1344.01	1339.59	1342.62	401	372
35	1325.71	1321.31	1324.31	402	374
	1325.71	1321.31	1324.30	400	372
40	1307.30	1302.92	1305.89	401	373
	1307.32	1302.94	1305.91	400	372
45	1289.36	1285.00	1287.94	401	373
	1289.38	1285.03	1287.96	398	369

Fig. 5.21 shows that the sound velocity of Exxsol D120 oil decreases as the temperature increases, which is expected, e.g. [116, 117, 118, 119]. The decrease seems to be relatively linear compared to the increase in sound velocity in water, which shows a slight arc when it is plotted against temperature.

Interestingly, the sound velocities measured with the FSM is slightly lower than the sound velocities measured with the ZCM, which is the opposite of what was observed for both distilled and saline water. This is the case for both the uncorrected sound velocities, and the sound velocities corrected for diffraction, over the complete temperature span.

Based on the values in the two tables, the deviation between the sound velocities measured with the ZCM and the FSM never exceeds 0.21 m/s, taking both measurement series into account. The difference between the uncorrected sound velocities, c_{ZCM} and c_{FSM}, are found to be 1344.21 m/s - 1344.01 m/s = 0.2 m/s at most, which is at 30°C (it is the same for 25°C). Further, the maximum deviation in the corrected sound velocities are 1339.80 m/s - 1339.59 m/s = 0.21 m/s for diffraction correction Method 1 and 1342.83 m/s - 1342.62 m/s = 0.21 m/s for diffraction correction Method 2, which are also found at 30°C. The associated relative uncertainties to each of these sound velocities are 410 ppm for $c_{ZCM,M1}$, which is equivalent to 0.55 m/s, 401 ppm for $c_{FSM,M1}$, which is equivalent to 0.54 m/s, 383 ppm for $c_{ZCM,M2}$, which is equivalent to 0.51 m/s, and 372 ppm for $c_{FSM,M2}$, which is equivalent to 0.50 m/s. Evidently, the sound velocities measured with the ZCM and FSM are within each others estimated measurement uncertainties. Moreover, measurement series 1 and 2 shows an agreement to within 0.08 m/s, where the biggest deviation is found for $c_{ZCM,M2}$ at 40°C. The results are examined in further details in Chapter 6.

Similarly to distilled water and 50 ppt saline water, the sound velocity of Exxsol D120 oil is investigated as a function of frequency. The results are presented in Fig. 5.22 and Table 5.29. Compared to distilled and saline water, the measurements seem to stabilize at a higher frequency for Exxsol D120 oil. While the sound velocity measurements were rather stable above 375 kHz for both distilled and saline water, they do not stabilize until approximately 425 kHz for the oil. There is a peak at 300 kHz where the measurements are roughly 2 m/s more than at the stable part. The reason is discussed further in Chapter 6.
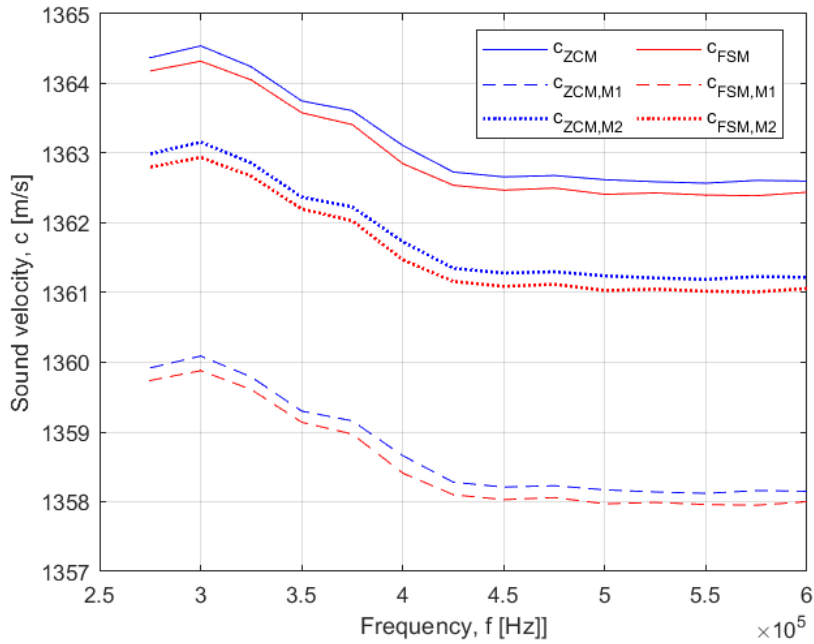
Figure 5.22: Measured sound velocity in Exxsol D120 oil as a function of frequency from 275 kHz to 600 kHz. The measured values are found using the steady state portion of a ten period pulse and averaging the waveform 512 times. The temperature was set to be $25°C$, but fluctuated between $24.986°C$ and $25.011°C$ during measurements.

Table 5.29: List of the measured sound velocities in Exxsol D120 at each frequency set point between 275 kHz and 600 kHz. The measured values are found using the steady state portion of a ten period pulse and averaging the waveform 512 times. The temperature was set to be $25°C$, but fluctuated between $24.986°C$ and $25.011°C$ during measurements.

Frequency	Measured sound velocity ZCM			Measured sound velocity FSM		
f [kHz]	c_{ZCM} [m/s]	$c_{ZCM,M1}$ [m/s]	$c_{ZCM,M2}$ [m/s]	c_{FSM} [m/s]	$c_{FSM,M1}$ [m/s]	$c_{FSM,M2}$ [m/s]
275	1364.37	1359.92	1362.99	1364.18	1359.74	1362.80
300	1364.54	1360.09	1363.16	1364.32	1359.88	1362.94
325	1364.24	1359.79	1362.86	1364.05	1359.61	1362.67
350	1363.75	1359.30	1362.37	1363.58	1359.14	1362.20
375	1363.61	1359.16	1362.23	1363.41	1358.97	1362.03
400	1363.11	1358.66	1361.73	1362.85	1358.41	1361.47
425	1362.73	1358.28	1361.35	1362.54	1358.10	1361.16
450	1362.66	1358.21	1361.28	1362.47	1358.03	1361.09
475	1362.68	1358.23	1361.30	1362.50	1358.06	1361.12
500	1362.62	1358.17	1361.24	1362.41	1357.97	1361.03
525	1362.59	1358.14	1361.21	1362.43	1357.99	1361.05
550	1362.57	1358.12	1361.19	1362.40	1357.96	1361.02
575	1362.61	1358.16	1361.23	1362.39	1357.95	1361.01
600	1362.60	1358.15	1361.22	1362.44	1358.00	1361.06

Sound velocity measurements in temperature cycled Exxsol D120 oil

The hydrostatic pressure varied between 1.005 and 1.018 bar during measurements on temperature cycled Exxsol D120 oil, and the following results were obtained:

(a)   (b)
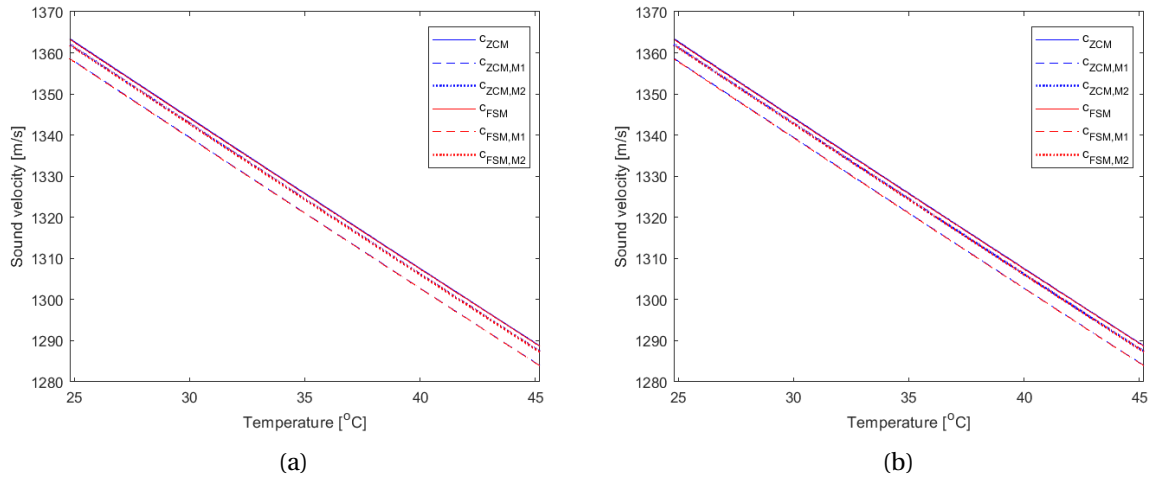
Figure 5.23: Measured sound velocity in Exxsol D120 oil from 25 to $45°C$. The oil has been tempera-
ture cycled once between 25 and $45°C$ prior to initiating the measurements. The measured values are
found using the steady state portion of a ten period pulse and averaging the waveform 512 times. (a)
Measurement series 1, (b) Measurement series 2.

Table 5.30: Sound velocity measurements in Exxsol D120 oil that has been temperature cycled from
25 to $45°C$, using the ZCM on the steady state portion of a ten period pulse that is averaged 512 times.
For each temperature, there are two measured sound velocities. The topmost value was measured
during the first measurement series, while the bottom-most value was measured during the second
measurement series.

Zerocrossing method, cycled					
	Experimental sound velocity			**Relative expanded uncertainty (95% c.l.)**	
Temp. [$°C$]	$\mathbf{c_{ZCM}}$ [**m/s**]	$\mathbf{c_{ZCM,M1}}$ [**m/s**]	$\mathbf{c_{ZCM,M2}}$ [**m/s**]	$\mathbf{E_{c_{ZCM,M1}}}$ [**ppm**]	$\mathbf{E_{c_{ZCM,M2}}}$ [**ppm**]
25	1362.78	1358.33	1361.40	412	384
	1362.82	1358.37	1361.44	411	383
30	1344.36	1339.95	1342.97	411	383
	1344.39	1339.97	1343.00	410	382
35	1326.01	1321.51	1324.60	409	382
	1326.00	1321.50	1324.59	408	380
40	1307.65	1303.11	1306.08	409	381
	1307.63	1303.08	1306.06	407	379
45	1289.71	1285.36	1288.31	408	379
	1289.74	1285.39	1288.34	406	378

Table 5.31: Sound velocity measurements in Exxsol D120 oil that has been temperature cycled from 25 to 45°C, using the FSM on the steady state portion of a ten period pulse that is averaged 512 times. For each temperature, there are two measured sound velocities. The topmost value was measured during the first measurement series, while the bottom-most value was measured during the second measurement series.

Fourier spectrum method, cycled					
	Experimental sound velocity			**Relative expanded uncertainty (95% c.l.)**	
Temp. [°C]	c_{FSM} [m/s]	$c_{FSM,M1}$ [m/s]	$c_{FSM,M2}$ [m/s]	$E_{c_{FSM,M1}}$ [ppm]	$E_{c_{FSM,M2}}$ [ppm]
25	1362.59	1358.14	1361.21	407	379
	1362.57	1358.12	1361.19	402	374
30	1344.18	1339.77	1342.80	406	378
	1344.22	1339.81	1342.84	403	375
35	1325.82	1321.32	1324.41	404	375
	1325.83	1321.32	1324.42	402	374
40	1307.44	1302.90	1305.87	404	376
	1307.41	1302.87	1305.85	401	373
45	1289.50	1285.15	1288.20	403	375
	1289.53	1285.18	1288.24	401	373

The sound velocity measurements of temperature cycled Exxsol D120 oil show similar trends to sound velocity measurements of Exxsol D120 oil that has not been temperature cycled. Again, it is clear that the ZCM generally results in higher measured sound velocities than the FSM, and measurement series 1 and 2 show great correspondence, agreeing to within a deviation of 0.04 m/s. This is the best match between the two measurement series across all tested liquids.

According to the tabulated data in Table 5.30 and 5.31, the biggest deviation between values found with the ZCM and FSM is at 25°C. Here, the difference between c_{ZCM} and c_{FSM} is 1362.82 m/s - 1362.57 m/s = 0.25 m/s. The same difference is found for the corrected sound velocities, i.e. 1358.37 m/s - 1538.12 m/s = 0.25 m/s for diffraction correction Method 1, and 1361.44 m/s - 1361.19 m/s = 0.25 m/s for diffraction correction Method 2. The associated uncertainties for the respective measurements are 411 ppm for $c_{ZCM,M1}$, which is equivalent to 0.56 m/s, 402 ppm for $c_{FSM,M1}$, which is equivalent to 0.55 ppm, 383 ppm for $c_{ZCM,M2}$, which is equivalent to 0.52 m/s, and 374 ppm for $c_{FSM,M2}$, which is equivalent to 0.51 m/s. Again, it is clear that the difference in the measured values found using the ZCM and FSM are covered by the estimated uncertainties.

By comparing Table 5.27 with Table 5.30, and Table 5.28 with Table 5.31, it is clear that the measured sound velocities are higher for the oil that has been temperature cycled, both for the ZCM and the FSM. This indicates that there might have been a potential change in the oil composition, due to the temperature cycling. The topic is discussed further in Chapter 6.

Uncertainty of the experimental sound velocity in Exxsol D120 oil

Section 5.5 provides an uncertainty budget for the uncertainty of the experimental sound velocity in distilled water. The budget is carried out according to the uncertainty model presented in Section 4.2. The same method can be used to calculate an uncertainty budget for the uncertainty of the experimental sound velocity in Exxsol D120 oil, and is consequently not done here.

5.5   Uncertainty in the experimental sound velocity

According to the results above, the relative expanded uncertainty of the experimental sound velocities generally seems to be higher for lower temperatures. An example of how the uncertainty of the experimental sound velocities is calculated is given in the following, using the measured sound velocity of distilled water at $25°C$ found with the ZCM using diffraction correction Method 1, during the first measurement series, which was $c = 1494.26$ m/s.

The uncertainty of the experimental sound velocity is a product of the uncertainties of K_T, L_0, Δt and t^{corr}. The uncertainty of K_T and L_0 are calculated in the uncertainty budgets presented in Table 5.11 and 5.9, respectively. The uncertainty of Δt and t^{corr} has not been found yet, and will be calculated in the following subsections. The uncertainty of the experimental sound velocity will eventually be calculated in Section 6.4b.

5.5.1   Uncertainty in the transit time difference

Uncertainty in transit time difference due to coherent noise

The pulse length is set to be ten periods long during measurements. In Section 3.3, it was found that side wall reflections will interfere with Pulse A if the pulse length is longer than three periods, see Fig 3.20. It was also found that the second side lobe will cause the biggest disturbances, as the peak of the first side lobe will not hit the active surface of the transducer. The peak of the second side lobe is approximately -47.62 dB, cf. Fig 2.19. Using the numerical analysis of coherent noise presented in Section 4.2.4, a corresponding worst case time shift of $1.324 \cdot 10^{-9}$ s is found. This will be one of the contributions to the uncertainty due to coherent noise.

The sound field from the transmitting transducer was investigated by placing metal blocks at different places in the cavity of the measurement cell, and by mounting a steel plate flush with the active surface of the receiving transducer. The setup, and how the waveform was affected, is described in more detail in Section 3.3. It was found that the steel plate slightly increased the first arriving noise trailing Pulse B, but cut off the noise further behind, cf. Fig. 3.29. On the other hand, the metal blocks reduced the noise trailing Pulse B. However, they also reduced the amplitude of Pulse B, and increased the noise prior to it, cf. Fig 3.23 and 3.24. The exact reason to why the waveform is changed the way it is has not been identified in this work, but some potential reasons is discussed in Chapter 6. Regardless, it was argued that neither the steel plate nor the metal blocks should be incorporated

during measurements. However, it has already been shown that they affect the shape of Pulse B, and changes to the waveform might have been different and more disastrous for other media or sound waves at different frequencies. Consequently, to account for worst case scenario, the max amplitude of the noise trailing Pulse B, will be used to estimate a corresponding uncertainty. This is illustrated in Fig. 5.24.
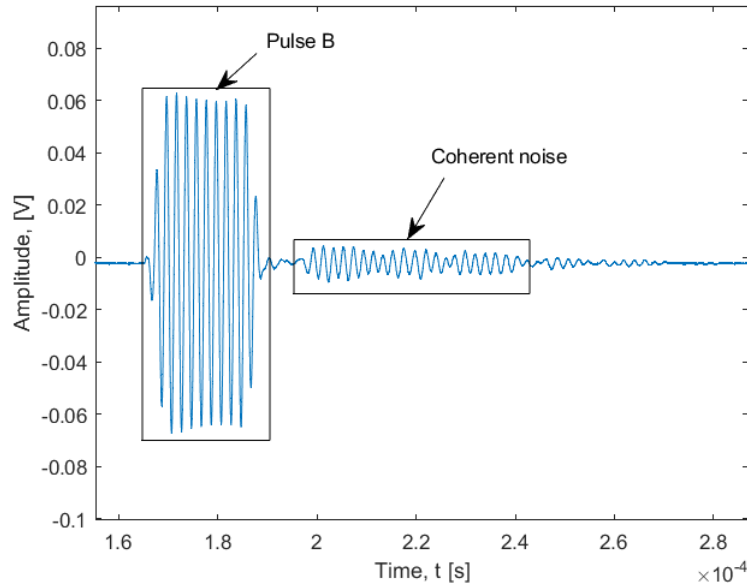
Figure 5.24: Pulse B and the trailing noise used to calculate a worst case time shift and a corresponding uncertainty due to coherent noise. The signal generator was set to generate a ten period pulse at 500 kHz, and the waveform is averaged 512 times.

The maximum amplitude of the signal of interest is 0.063 V, while the maximum amplitude of the noise is 0.0043 V. Using Eq. 2.59, this is equivalent to a signal-to-noise ratio of SNR = 23.32 dB. From the numerical analysis presented in Section 4.2.4, it is found that the corresponding worst case resulting time shift is $2.169 \cdot 10^{-8}$ s.

With the time shift due to the second side lobe signal interfering with Pulse A and the possible time shift due to coherent noise around Pulse B both being known, the uncertainty in transit time difference due to coherent noise can be calculated as

$$u_c(\Delta t)_{coh.noise} = \sqrt{(1.324 \cdot 10^{-9} \ s)^2 + (2.169 \cdot 10^{-8} \ s)^2} = 2.173 \cdot 10^{-8} \ s \qquad (5.1)$$

Uncertainty in transit time difference due to vibrations from water bath

The GD100 water bath that is used for temperature regulations contains a propeller that runs continuously whenever the water is being heated. This causes small vibrations that affects the measured transit times. Fig. 5.25 shows how an extract of the waveform is affected by the vibrations from the water bath.
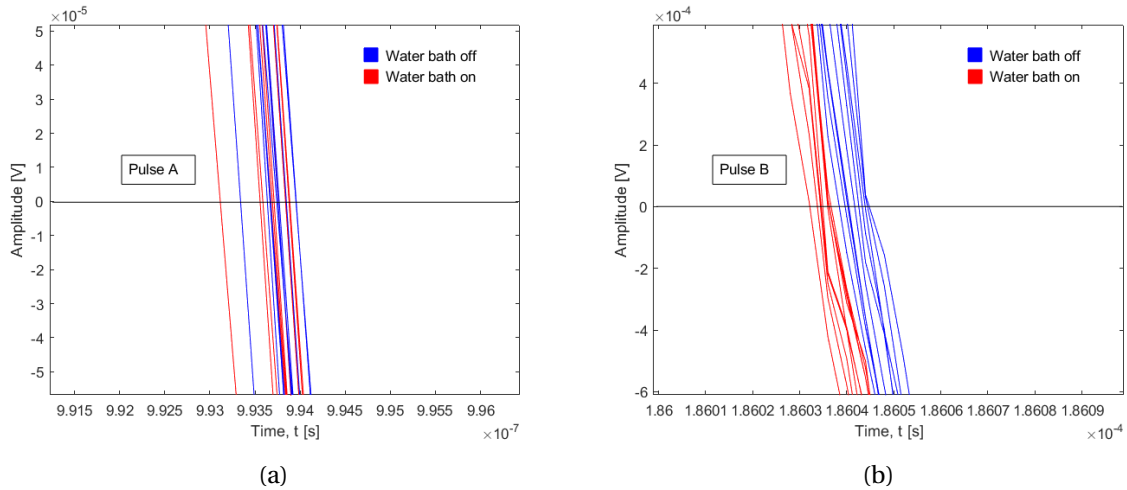
Figure 5.25: Enlargement of 20 distinct waveforms; ten of which were sampled when the water bath was turned off (blue) and another ten that were sampled when the water bath was turned on (red). The signal generator was set to generate a ten period pulse at 500 kHz, and the waveform is averaged 512 times. (a) Pulse A, (b) Pulse B.

There is a clear time shift due to vibrations from the water bath. Pulse B is shifted more to the left than Pulse A, causing the measured difference in transit time to be smaller than what it actually is. This is compensated for by introducing an uncertainty, $u(\Delta t)_{w.bath}$. The uncertainty is estimated by first calculating the mean of the transit time difference between Pulse A and B, for all ten waveforms when the water bath is turned off. The standard deviation is then found with Eq. C.2 and used to calculate the standard uncertainty, $u(\Delta t)_{w.bath\,OFF}$ with Eq. C.4. The same process is then repeated with the water bath turned on, in order to find $u(\Delta t)_{w.bath`\,ON}$. The transit time measurements with the water bath turned off and on is shown in Table 5.32.

Table 5.32: List of ten measurements with the water bath turned off, and another ten measurements with the water bath turned on. The number of degrees of freedom is 9 in both cases.

Waveform	Water bath off Δt [μs]	Water bath on Δt [μs]
1	166.78	166.77
2	166.78	166.77
3	166.78	166.78
4	166.78	166.78
5	166.78	166.77
6	166.78	166.77
7	166.77	166.78
8	166.78	166.77
9	166.78	166.77
10	166.78	166.77
Mean	166.779 μs	166.773 μs
Standard deviation	3.20 ns	4.80 ns
Standard uncertainty	1.07 ns	1.60 ns

Using $u(\Delta t)_{w.bath\ OFF} = 1.07$ ns and $u(\Delta t)_{w.bath\ ON} = 1.60$ ns, the value of $u(\Delta t)_{w.bath}$ is calculated:

$$u(\Delta t)_{w.bath} = \sqrt{(1.07\ ns)^2 + (1.60\ ns)^2} = 1.92\ ns. \tag{5.2}$$

Calculation of the uncertainty in transit time difference

The uncertainty in transit time difference is calculated according to the uncertainty model presented in Section 4.2.4. The values of the various uncertainty contributors are calculated at different stages during the project, and a summary of the values is given in Table 5.33. An associated description to each of the contributors is provided in Table 4.5.

Table 5.33: List of the uncertainties contributing to the total uncertainty of the transit time difference assuming the sample is distilled water at 25°C. Each value has been multiplied with its associated coverage factor.

Uncertainty contributor	Value	Note
$u_c(\Delta t)_{coh.noise}$	$2.17 \cdot 10^{-8}$ s	Calculated according to Section 4.2.4. Coverage factor $k = 2$ assumed.
$u(\Delta t)_{rand.noise}$	N/A	N/A
$u(\Delta t)_{osc.}$	$4 \cdot 10^{-10}$ s	Specified by the manufacturer to have a sample rate of 2.5 GS/s [78]. Coverage factor $k = 2$ assumed.
$u(\Delta t)_{el.}$	N/A	N/A
$u(\Delta t)_{dis.}$	$7.06 \cdot 10^{-9}$ s	Measured for each acquisition (measurement at 25°C used as an example). Coverage factor $k = 2$ assumed.
$u(\Delta t)_{filt.}$	$1.15 \cdot 10^{-9}$ s	Estimated by investigating the change in transit time difference with and without the digital filters, cf. Section 3.7.3. Coverage factor $k = 1$ assumed.
$u(\Delta t)_{zc.var.}$	$7.64 \cdot 10^{-9}$ s	Measured for each acquisition (measurement at 25°C used as an example). Coverage factor $k = 1$ assumed.
$u(\Delta t)_{trunc.}$	$7.87 \cdot 10^{-10}$ s	Estimated by investigating the difference in transit time, by truncating and linearly trailing the signal, cf. Section 3.7.2. Coverage factor $k = 1$ assumed.
$u(\Delta t)_{w.bath}$	$1.92 \cdot 10^{-9}$ s	Estimated by investigating the change in transit time difference with the water bath turned on and off, respectively. Coverage factor $k = 1$ assumed.
$u(\Delta t)_{other}$	N/A	N/A

Since the transit time difference is found with two different methods, two uncertainty budgets are presented in the following: one for the ZCM, and another for the FSM.

Table 5.34: Uncertainty budget for the transit time difference measured with the ZCM in distilled water at 25°C. The values are taken from Table 5.33, and the budget is calculated according to Eq. 4.14.

Uncertainty Contributor	Input Uncertainty				Combined Uncertainty	
	Expand. uncert.	Conf. level & distribut.	Cov. fact., k	Standard uncertainty	Sens. coeff.	Variance [s^2]
$u(\Delta t)_{coh.noise}$	$2.17 \cdot 10^{-8}$ s	95% (norm)	2	$1.09 \cdot 10^{-8}$ s	1	$1.18 \cdot 10^{-16}$
$u(\Delta t)_{osc.}$	$4 \cdot 10^{-10}$ s	95% (norm)	2	$2 \cdot 10^{-10}$ s	1	$4 \cdot 10^{-20}$
$u(\Delta t)_{dis.}$	$7.06 \cdot 10^{-9}$ s	95% (norm)	2	$3.53 \cdot 10^{-9}$ s	1	$1.24 \cdot 10^{-17}$
$u(\Delta t)_{filt.}$	$1.15 \cdot 10^{-9}$ s	68% (norm)	1	$1.15 \cdot 10^{-9}$ s	1	$1.35 \cdot 10^{-18}$
$u(\Delta t)_{zc.var.}$	$7.64 \cdot 10^{-9}$ s	68% (norm)	1	$7.64 \cdot 10^{-9}$ s	1	$5.84 \cdot 10^{-17}$
$u(\Delta t)_{w.bath}$	$1.92 \cdot 10^{-9}$ s	68% (norm)	1	$1.92 \cdot 10^{-9}$ s	1	$3.69 \cdot 10^{-18}$
Sum of variances, $u_c^2(\Delta t)_{ZCM}$						$1.940 \cdot 10^{-16}$ s^2
Combined standard uncertainty, $u_c(\Delta t)_{ZCM}$						$1.39 \cdot 10^{-8}$ s
Expanded uncertainty (95% confidence level, $k = 2$), $U(\Delta t)_{ZCM}$						$2.79 \cdot 10^{-8}$ s
Transit time difference in distilled water at 25°C, Δt						$1.67 \cdot 10^{-4}$ s
Relative expanded uncertainty (95% confidence level, $k = 2$), $U(\Delta t)_{ZCM}/\Delta t$						0.017%

Table 5.35: Uncertainty budget for the transit time difference measured with the FSM in distilled water at 25°C. The values are taken from Table 5.33, and the budget is calculated according to Eq. 4.15.

Uncertainty Contributor	Input Uncertainty				Combined Uncertainty	
	Expand. uncert.	Conf. level & distribut.	Cov. fact., k	Standard uncertainty	Sens. coeff.	Variance [s^2]
$u(\Delta t)_{coh.noise}$	$2.17 \cdot 10^{-8}$ s	95% (norm)	2	$1.09 \cdot 10^{-8}$ s	1	$1.18 \cdot 10^{-16}$
$u(\Delta t)_{osc.}$	$4 \cdot 10^{-10}$ s	95% (norm)	2	$2 \cdot 10^{-10}$ s	1	$4 \cdot 10^{-20}$
$u(\Delta t)_{dis.}$	$7.06 \cdot 10^{-9}$ s	95% (norm)	2	$3.53 \cdot 10^{-9}$ s	1	$1.24 \cdot 10^{-17}$
$u(\Delta t)_{filt.}$	$1.15 \cdot 10^{-9}$ s	68% (norm)	1	$1.15 \cdot 10^{-9}$ s	1	$1.35 \cdot 10^{-18}$
$u(\Delta t)_{trunc.}$	$7.87 \cdot 10^{-10}$ s	68% (norm)	1	$7.87 \cdot 10^{-10}$ s	1	$6.19 \cdot 10^{-19}$
$u(\Delta t)_{w.bath}$	$1.92 \cdot 10^{-9}$ s	68% (norm)	1	$1.92 \cdot 10^{-9}$ s	1	$3.69 \cdot 10^{-18}$
Sum of variances, $u_c^2(\Delta t)_{FSM}$						$1.36 \cdot 10^{-16}$ s^2
Combined standard uncertainty, $u_c(\Delta t)_{FSM}$						$1.17 \cdot 10^{-8}$ s
Expanded uncertainty (95% confidence level, $k = 2$), $U(\Delta t)_{FSM}$						$2.33 \cdot 10^{-8}$ s
Transit time difference in distilled water at 25°C, Δt						$1.67 \cdot 10^{-4}$ s
Relative expanded uncertainty (95% confidence level, $k = 2$), $U(\Delta t)_{FSM}/\Delta t$						0.014%

5.5.2   Uncertainty in the correction term

In Section 4.2.5, it was stated that the uncertainty of the correction term is equal to the uncertainty of the diffraction correction. Two different diffraction correction methods are investigated in this work. The uncertainty is calculated for both methods, and the greatest uncertainty is used as the uncertainty of the correction term in order to not underestimate the total uncertainty of the measured sound velocity. The uncertainties are calculated according to the approach described in 4.2.5.

At 25°C, the transducer distance is given as

$$L = L_0 \cdot K_T = 125.000 \; mm \cdot 1.000016 = 125.002 \; mm. \tag{5.3}$$

Using the combined standard uncertainty of L_0 and K_T in Table 5.9 and 5.11, respectively, the combined standard uncertainty of L can be found as

$$\begin{aligned} u_c(L) &= \sqrt{(K_T \cdot u_c(L_0))^2 + (L_0 \cdot u_c(K_T))^2} \\ &= \sqrt{(1.000016 \cdot 0.0159 \, \text{mm})^2 + (125.002 \, \text{mm} \cdot 1.852 \cdot 10^{-5})^2} \\ &= 0.016 \, \text{mm}. \end{aligned} \tag{5.4}$$

Hence, the longest possible transducer distance is L_{max} = 125.002 mm + 0.016 mm = 125.018 mm and the shortest possible transducer distance is L_{min} = 125.002 mm − 0.016 mm = 124.986 mm, assuming 95% confidence level, $k = 2$.

The effective element radius was measured using the setup described in Section 3.6. Unfortunately, only two sets of valid measurement data are taken for each transducer, as some unknown source caused large errors in the other measurement series. Hence, the biggest and smallest value of a_{eff} in Table 5.1 are used in the calculation of the uncertainty in diffraction correction. The standard uncertainty of the diffraction correction is calculated in Table 5.36 and 5.37 for Method 1 and 2, respectively.

Table 5.36: The biggest and smallest diffraction correction using diffraction corrected Method 1 in distilled water at 25°C.

	Biggest diff. corr.	Smallest diff. corr.
Trans. dist., L	125.018 mm	124.986 mm
Eff. element rad., a_{eff}	9.52 mm	9.80 mm
Diff. corr., t^{dif}	0.54112 μs	0.51726 μs
Diff. corr. std. uncertainty, $u(t^{dif})$	23.86 ns	

Table 5.37: The biggest and smallest diffraction correction using diffraction corrected Method 2 in distilled water at 25°C.

	Biggest diff. corr.	Smallest diff. corr.
Trans. dist., L	124.986 mm	125.018 mm
Eff. element rad., a_{eff}	9.80 mm	9.52 mm
Diff. corr., t^{dif}	0.15475 μs	0.14741 μs
Diff. corr. std. uncertainty, $u(t^{dif})$	7.34 ns	

Evidently, Method 1 results in the greatest deviation between the two values, and the uncertainty of the correction term is thus set to be $u(t^{corr})$ = 0.02386 μs. A coverage factor of $k = 1$ is assumed due to the lack of measurements of a_{eff}. Although the correction term only consists of one term, an uncertainty budget is calculated in Table 5.38 to find the relative expanded uncertainty of t^{corr}.

Table 5.38: Uncertainty budget for the correction term using the uncertainty found in diffraction correction Method 1. The value of the standard uncertainty of the diffraction correction is found in Table 5.36.

Uncertainty	Input Uncertainty				Combined Uncertainty	
Contributor	Expand. uncert.	Conf. level & distribut.	Cov. fact., k	Standard uncertainty	Sens. coeff.	Variance [s^2]
$u(t^{dif})$	$2.386 \cdot 10^{-8}$ s	68% (norm)	1	$2.386 \cdot 10^{-8}$ s	1	$5.693 \cdot 10^{-16}$
Sum of variances, $u_c^2(t^{corr})$						$5.693 \cdot 10^{-16}$ s^2
Combined standard uncertainty, $u_c(t^{corr})$						$2.386 \cdot 10^{-8}$ s
Expanded uncertainty (95% confidence level, $k = 2$), $U(t^{corr})$						$4.772 \cdot 10^{-8}$ s
Lowest diffraction correction corresponding to the given uncertainty, $t^{corr} = t^{dif}$						$5.173 \cdot 10^{-7}$ s
Relative expanded uncertainty (95% confidence level, $k = 2$), $U(t^{corr})/t^{corr}$						9.226%

5.5.3   Uncertainty in the measured sound velocity

In this section, an example uncertainty budget is derived for the measured sound velocity at $25°C$ in measurement series 1, using the ZCM and diffraction correction Method 1, cf. Table 5.12. The sound velocity is calculated according to Eq. 2.7. It is dependent on the transducer distance, L_0, thermal expansion coefficient, K_T, transit time difference, Δt, and correction term, t^{corr}. Consequently, the uncertainty of c is dependent on the uncertainty of L_0, K_T, Δt and t^{corr}, respectively. The uncertainty of L_0 and K_T is calculated in Section 5.3, and the uncertainty of Δt and t^{corr} is calculated Sections 5.5.1 and 5.5.2, respectively. Table 5.39 provides a summary of the values of L_0, K_T, Δt and t^{corr}, and their associated uncertainties. A corresponding uncertainty budget is derived in Table 5.40, using Eq. 4.3 in Section 4.2.

Table 5.39: Summary of the different uncertainty contributors to the uncertainty of the measured sound velocity. The values are found for measurement series 1 where the sample is distilled water at $25°C$ and the sound velocity is measured with the ZCM and diffraction correction Method 1, ref. Table 5.12.

Variable	Value	Uncertainty Contributor	Value	Note
L_0	125.00 mm	$U(L_0)$	0.0318 mm	Found in Table 5.9. Coverage factor $k = 2$.
K_T	1.000016	$U(K_T)$	$3.70 \cdot 10^{-5}$	Found in Table 5.11. Coverage factor $k = 2$.
Δt	$1.668 \cdot 10^{-4}$ s	$U(\Delta t)$	$2.79 \cdot 10^{-8}$ s	Found in Table 5.34. Coverage factor $k = 2$.
t^{corr}	$5.173 \cdot 10^{-7}$ s	$U(t^{corr})$	$4.772 \cdot 10^{-8}$ s	Found in Table 5.38. Coverage factor $k = 2$.

Table 5.40: Uncertainty budget for the measured sound velocity in distilled water at 25°C. The budget is derived for the sound velocity that was measured during measurement series 1, using the ZCM and diffraction correction Method 1.

Source	Input Uncertainty				Combined Uncertainty	
	Expand. uncert.	Conf. level & distribut.	Cov. fact., k	Standard uncertainty	Sens. coeff.	Variance [(m/s)^2]
$U(L_0)$	$3.18 \cdot 10^{-5}$ m	95% (norm)	2	$1.589 \cdot 10^{-5}$ m	12028	0.0365
$U(K_T)$	$3.70 \cdot 10^{-5}$	95% (norm)	2	$1.852 \cdot 10^{-5}$	1504	$7.750 \cdot 10^{-4}$
$U(\Delta t)$	$2.79 \cdot 10^{-8}$ s	95% (norm)	2	$1.393 \cdot 10^{-8}$ s	$-9.042 \cdot 10^6$	0.0159
$U(t^{corr})$	$4.772 \cdot 10^{-8}$ s	95% (norm)	2	$2.386 \cdot 10^{-8}$ s	$9.042 \cdot 10^6$	0.0465
Sum of variances, $u_c^2(c)$						0.0996 (m/s)^2
Combined standard uncertainty, $u_c(c)$						0.316 m/s
Expanded uncertainty (95% confidence level, $k = 2$), $U(c)$						0.631 m/s
Measured sound velocity at 25°C in distilled water, using ZCM and diff. corr. M1, c						1494.26 m/s
Relative expanded uncertainty (95% confidence level, $k = 2$), $U(c)/c$						0.0422%

In terms of ppm, the relative expanded uncertainty at 95% confidence level of the experimental sound velocity in distilled water at 25°C, in measurement series 1, is 422 ppm. By dividing each of the variances by the sum of the variances and multiplying with 422 ppm, it is found that the correction term contributes the most with 197 ppm. Further, the uncertainty of the transducer distance and transit time difference contributes with 155 and 67 ppm respectively, while the uncertainty of thermal expansion only contributes with 3 ppm.

Chapter 6

Discussion

In Chapter 6, the results presented in Chapter 5 are further discussed and examined. The chapter is divided into three sections. Section 6.1 presents a discussion on the sound velocity measurements, where general observations are reviewed and potential influences on the experimental sound velocities are analyzed. Section 6.2 assesses the uncertainty of both the experimental and modelled sound velocities in further detail. Lastly, Section 6.3 suggests some potential improvements for the measurement cell.

6.1   Discussion of sound velocity measurements

Sound velocity measurements have been carried out on distilled water, saline water at 20, 35 and 50 ppt salinity, respectively, and uncycled and temperature cycled Exxsol D120 oil. Two measurement series have been carried out on each sample to investigate the repeatability of the results.

The sound velocity measurements have been conducted through two different signal processing methods, namely the ZCM and the FSM. Additionally, diffraction has been corrected for with two different methods named Method 1 and Method 2. Thus, a total of four different diffraction corrected experimental sound velocities are found for each measured temperature. Also, two different modelled sound velocities for water are calculated at each temperature for comparison reasons. An explanation of the symbols for the different sound velocities is provided in the start of Section 5.4.

Benus [84] measured the sound velocity of distilled water and saline water at 20 ppt salinity. Both two- and six-period pulses were used in the experiments, and the sound velocities were found using the pulse-echo buffer rod method [10, 24, 84]. Other than the temperature control units, T/R switch and measurement cell, the exact same instruments were used. The signal generator was set to generate 500 kHz sound waves at 10 V amplitude, and the oscilloscope averaged the waveform 512 times, which is the same settings that are used in this work. Consequently, the experimental sound velocity in distilled water and saline water at 20 ppt salinity is compared to the results found in [84]. Since a ten-period pulse is used in this work, the results will primarily be compared to the six-period results rather than the two-period results in [84].

It should be noted that Benus used a self-built temperature control setup to control the temperature of the sample. The temperature control setup consisted of a waterbath and a temperature control unit, as well as a circulating water pump, heating element and temperature probe submerged into the waterbath. The setup is described in more detail in [84]. Due to the size of the waterbath, spatial temperature variations were observed during measurements. To minimize errors due to these variations the heating were stopped at chosen temperature set-points and measurements were taken when the temperature had stabilized [84]. These spatial temperature variations were not observable in this work. The GD100 general stirred thermostatic waterbath used in this project has a built-in propeller that constantly circulates the water and reduces the temperature gradient. Hence, stabilization at chosen temperature set points was not done here.

Tabulated results in [84] summarizes the mean of the measured sound velocities at the chosen temperature set points after stabilization, while the tabulated results in this work summarizes the sound velocity that was measured at given temperatures while the temperature was constantly increasing. The tabulated data will lay the foundation for the discussion in this chapter along with trends found graphically. A more thorough review of the results could be carried out by looping through every measured value and comparing them with each other, but that would be too time consuming and is consequently not done here.

6.1.1 General observations

Two sets of measurements were carried out on distilled water from approximately 25 to 45°C. There was a slight deviation in measured sound velocity between the measurement series which is discussed later. Also, Fig. 5.10 and 5.11 clearly shows that the experimental sound velocity has a more linear relationship with the modelled sound velocity calculated using the equation presented by Kinsler et. al. than with the modelled sound velocity calculated with the UNESCO-algorithm. The non-linearity might be due to the UNESCO-algorithm being empirically derived from sound velocity measurements in sea water containing several different minerals [11]. Additionally, the accuracy of the UNESCO-algorithm in low saline water is debated [115]. Hence, the experimental sound velocities in distilled water will primarily be compared to $c_{K\&F}$ rather than c_{UNESCO}.

For the experimental sound velocities corrected for diffraction using Method 1 in distilled water, the best agreement with the modelled sound velocity was found at 45°C. Here, $c_{ZCM,M1}$ and $c_{FSM,M1}$ agreed to within 1555 and 1132 ppm of $c_{k\&F}$, respectively. The biggest deviation was found at 25°C, with an agreement of 1624 and 1376 ppm for $c_{ZCM,M1}$ and $c_{FSM,M1}$, respectively. Further, for the experimental sound velocities corrected for diffraction using Method 2, the best agreement with the modelled sound velocity was found at 25°C. Here, $c_{ZCM,M2}$ and $c_{FSM,M2}$ agreed to within 628 and 835 ppm of $c_{k\&F}$, respectively. The biggest deviation was found at 45°C, with an agreement of 696 and 943 ppm for $c_{ZCM,M2}$ and $c_{FSM,M2}$, respectively. It can be seen that diffraction correction Method 1 has its best agreement at the highest temperatures, while diffraction correction Method 2 has its best agreement at the lowest temperatures. This is the case for almost all measurement series. The reason is that

uncorrected experimental sound velocities are around 2 to 3.5 m/s higher than the sound velocities calculated according to the models. While diffraction correction Method 1 reduces the experimental sound velocity by up to around 4.80 m/s, diffraction correction Method 2 reduces the experimental sound velocity by only 1.20 to 1.40 m/s. As a result, the experimental sound velocities with diffraction correction Method 1 is always less than the modelled sound velocity, while the opposite applies for diffraction correction Method 2. Since the experimental sound velocities generally increases at a slightly higher rate than the modelled sound velocities, with increasing temperature, it is expected that diffraction correction Method 1 has best agreement at high temperatures, while diffraction correction Method 2 has best agreement at low temperatures. The difference in how the experimental and modelled sound velocities increases with temperature is discussed later.

Using a six-period pulse, Benus found the best agreement in distilled water at $23.66°C$, where the ZCM and FSM agreed to within 100 ppm and 101 ppm, respectively, which is better than what is found here. However, by comparing the graphically presented normalized sound velocities in Section 5.4 with the normalized sound velocities in [84], it can also be seen that the measurements in [84] were more fluctuating and "jumpy" than the measurements carried out in this work. The reason might be the shorter pulse length used in [84]. A six-period pulse is shorter than a ten-period pulse, meaning that the transit time difference is calculated from fewer zerocrosses. Consequently, fluctuations in the zerocrossing times will have a bigger impact on the measured transit time difference.

While Benus found a better agreement than what is found here, it should be noted that the modelled sound velocity lies near the middle of the sound velocities corrected for diffraction using Method 1 and 2, respectively, in this work. Fig. 5.10 shows that it is impossible for both $c_{ZCM,M1}$ and $c_{ZCM,M2}$ to lie within 1000 ppm of $c_{K\&F}$ at the same temperature. The same applies for $c_{FSM,M1}$ and $c_{FSM,M2}$. However, it is observed that diffraction correction Method 2 results in sound velocities closer to $c_{K\&F}$. This was also the diffraction correction method used in [84], but with a slight twist where diffraction was corrected for in both the solid buffer and the sample.

For the experimental sound velocities corrected for diffraction using Method 1 in saline water at 20 ppt salinity, the best agreement with the modelled sound velocity was also found at at $45°C$. Here, $c_{ZCM,M1}$ and $c_{FSM,M1}$ agreed to within 1388 and 1061 ppm of c_{UNESCO}, respectively. The biggest deviation was found at $25°C$, with an agreement of 1501 and 1258 ppm for $c_{ZCM,M1}$ and $c_{FSM,M1}$, respectively. Further, for the experimental sound velocities corrected for diffraction using Method 2, the best agreement with the modelled sound velocity was found at $25°C$. Here, $c_{ZCM,M2}$ and $c_{FSM,M2}$ agreed to within 744 and 988 ppm of c_{UNESCO}, respectively. The biggest deviation was found at $45°C$, with an agreement of 874 and 1202 ppm for $c_{ZCM,M2}$ and $c_{FSM,M2}$, respectively.

Benus did not use the FSM on saline water, but found a maximum deviation of 213 ppm from the modelled sound velocity using the ZCM on a six-period pulse in saline water at 20 ppt salinity. This is better than the best agreement found in this work. The reason for the better agreement might be due to the diffraction correction suiting the measurement cell better. The diffraction correction method in [84] is derived for the solid buffer method, while the two diffraction correction methods used here are two extremes. The modelled sound velocity lies between the two extremes, which is expected

[40]. A diffraction correction method derived specifically for the three-way pulse method has not been identified.

For the experimental sound velocities corrected for diffraction using Method 1 in saline water at 35 ppt salinity, the best agreement with the modelled sound velocity was also found at at 45°C. Here, $c_{ZCM,M1}$ and $c_{FSM,M1}$ agreed to within 1325 and 1006 ppm of c_{UNESCO}, respectively. The biggest deviation was found at 25°C for the ZCM, where an agreement of 1453 ppm was observed. For the FSM, the biggest deviation was found at 30°C, where the agreement is within 1196 ppm. Further, for the experimental sound velocities corrected for diffraction using Method 2, the best agreement with the modelled sound velocity was found at 25°C for the ZCM and 30°C for the FSM. Here, $c_{ZCM,M2}$ and $c_{FSM,M2}$ agreed to within 795 and 1022 ppm of c_{UNESCO}, respectively. The biggest deviation was found at 45°C, with an agreement of 949 and 1236 ppm for $c_{ZCM,M2}$ and $c_{FSM,M2}$, respectively. The reason to why $c_{FSM,M1}$ was furthest away from, and $c_{FSM,M2}$ was closest to, c_{UNESCO} at 30°C is that the modelled sound velocity increased at a higher rate than the experimental sound velocities at low temperatures, cf. Fig. 5.17. Such decrease in normalized sound velocity only occurred once throughout the project, which was during the first measurement series in saline water at 35 ppt with the FSM. Initially, it was assessed whether the decrease could be caused by the waterbath lid not covering the complete opening. It was found that the opening in the water bath had to be covered in order to increase the temperature beyond approximately 40°C. Thus, a lid was placed on the waterbath from the beginning to keep the conditions equal during all measurements. If the lid were slightly displaced at any point, water would be more exposed to the surrounding air, causing heat to escape. This, combined with the fact that the temperature probe is placed to the side in the measurement cell, could result in erroneously results. However, such error would presumably affect the experimental sound velocities measured with the ZCM the same way, and is consequently assumed to not be the source of this deviating trend.

For the experimental sound velocities corrected for diffraction using Method 1 in saline water at 50 ppt salinity, the best agreement with the modelled sound velocity was also found at at 45°C. Here, $c_{ZCM,M1}$ and $c_{FSM,M1}$ agreed to within 1351 and 1035 ppm of c_{UNESCO}, respectively. The biggest deviation was found at 25°C, with an agreement of 1502 and 1186 ppm for $c_{ZCM,M1}$ and $c_{FSM,M1}$, respectively. Further, for the experimental sound velocities corrected for diffraction using Method 2, the best agreement with the modelled sound velocity was found at 25°C. Here, $c_{ZCM,M2}$ and $c_{FSM,M2}$ agreed to within 761 and 1032 ppm of c_{UNESCO}, respectively. The biggest deviation was found at 45°C, with an agreement of 877 and 1212 ppm for $c_{ZCM,M2}$ and $c_{FSM,M2}$, respectively.

Unfortunately, there are no model for the sound velocity in Exxsol D120 oil, and the exact composition of hydrocarbons in the oil is unknown. Therefore, the experimental sound velocities in Exxsol D120 oil cannot be compared to a modelled sound velocity. However, the sound velocity was observed to be decreasing at increasing temperatures, which was expected [43]. Also, the deviation between measurement series 1 and 2 in Exxsol D120 oil almost never exceeds 0.04 m/s. One exception is found here for the sound velocity measured with the ZCM at 40°C in the uncycled oil, where the deviation reached 0.08 m/s, corresponding to an agreement within approximately 61 ppm of each other. The

agreement between measurement series 1 and 2 contributes to having more confidence in the results.

Another observation that was made for the Exxsol D120 oil is that the experimental sound velocity was higher in the temperature cycled oil with about 0.1 to 0.2 m/s. The temperature cycled oil is cycled once from 25 to 45°C, and then back to 25°C before being tested. This cycling might have changed the composition of the oil as different hydrocarbons evaporates at different temperatures, cf. Section 2.1.2, and could be the reason to why the sound velocities were higher for the cycled oil.

Studying the figures in Section 5.4, it is clear that the ZCM always measured approximately 0.3 to 0.7 m/s lower than the FSM in both distilled and saline water. However, this was not the case for Exxsol D120 oil, where the ZCM measured around 0.2 m/s higher than the FSM. Upon further investigation, it was found that the reason might be due to MATLAB struggling with defining the zerocrosses in the pulses. Only the steady state part of the pulses is applied in both signal processing methods and they are defined from the zerocrosses, cf. Section 3.7.1 and 3.7.2. Fig. 6.1a shows an extract of Pulse A after the transient parts have been removed, and the potential source to the deviation between the ZCM and FSM is enlarged in Fig. 6.1b.
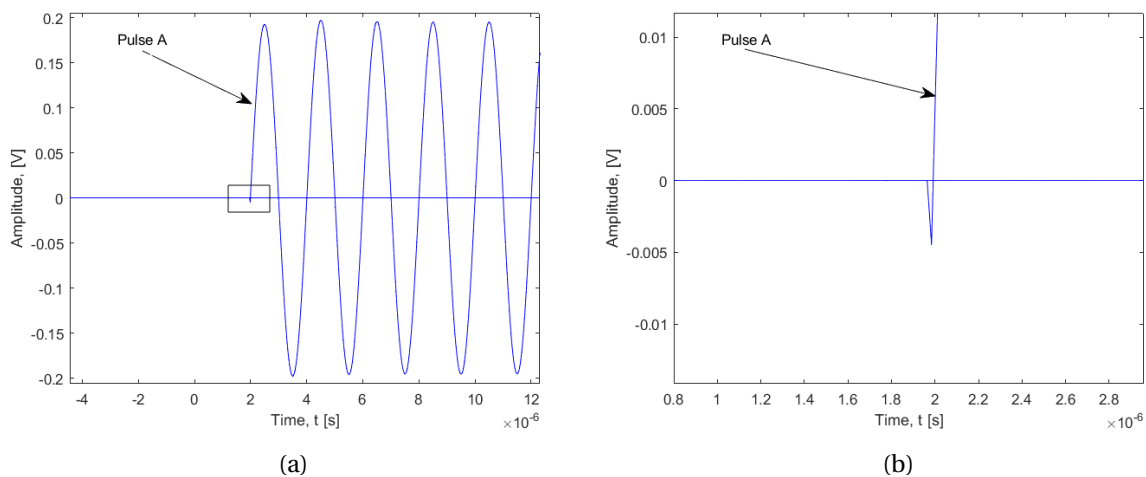
Figure 6.1: Start of the steady state part in Pulse A. The signal generator was set to generate a ten-period pulse at 500 kHz and 10 V, and the oscilloscope has averaged the waveform 512 times. The sample is distilled water at approximately 25°C. (a) Extract of Pulse A, (b) Enlargement of the highlighted area in (a).

In the MATLAB-script presented in Appendix E.3.4, the zerocrosses are used to define where the steady state parts start and end. Fig. 6.1 shows that an erroneously detection of the start of the steady state part of Pulse A has occurred. It seems like MATLAB defines the start of the steady state part somewhat earlier than what it should. The time shift between the two zerocrosses in Fig. 6.1b is approximately $5.6 \cdot 10^{-8}$ s. If MATLAB treats all zerocrosses in Pulse A as if they were $5.6 \cdot 10^{-8}$ s earlier, it would cause a corresponding change in measured sound velocity of approximately -0.5 m/s, given that the sample is distilled water at 25°C. Further testing showed that the error was somewhat fluctuating depending on temperature and salinity, and also occurred for Pulse B, but with a lesser magnitude. However, in Exxsol D120 oil, the error seemed to be in the opposite direction, as shown

in Fig. 6.2.
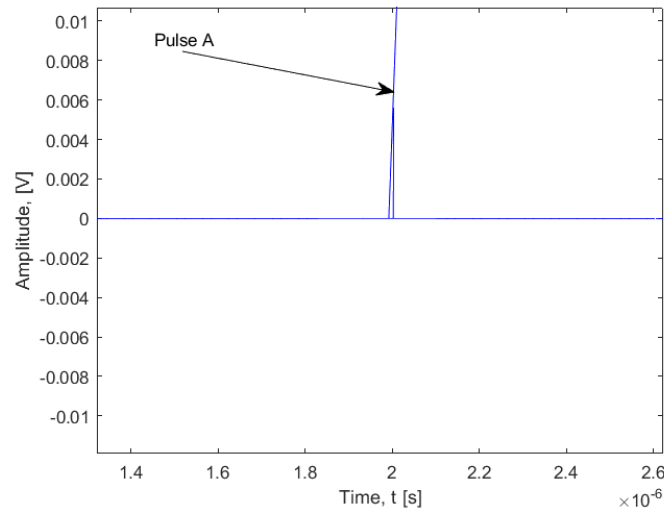
Figure 6.2: Enlargement of the error corresponding to the error in Fig. 6.1b, but in Exxsol D120 oil instead of distilled water. The signal generator was set to generate a ten-period pulse at 500 kHz and 10 V, and the oscilloscope has averaged the waveform 512 times. The temperature was approximately $25°C$.

Here, it seems like MATLAB has overestimated the zerocrossing time, causing the change in measured sound velocity to be positive instead of negative. This corresponds well with the results found for Exxsol D120 oil, where the ZCM measured a higher sound velocity than the FSM. These errors were not observed until after all measurement series had been completed, and new measurement series have not been conducted due to time limits.

During measurements, it was found that the FSM sometimes resulted in erroneously sound velocities. The measurements could be running smoothly, and then suddenly jump such that the sound velocities measured with the FSM were around 18 m/s too high or too low. An example of the sudden jumps in experimental sound velocity is shown in Fig. 6.3.
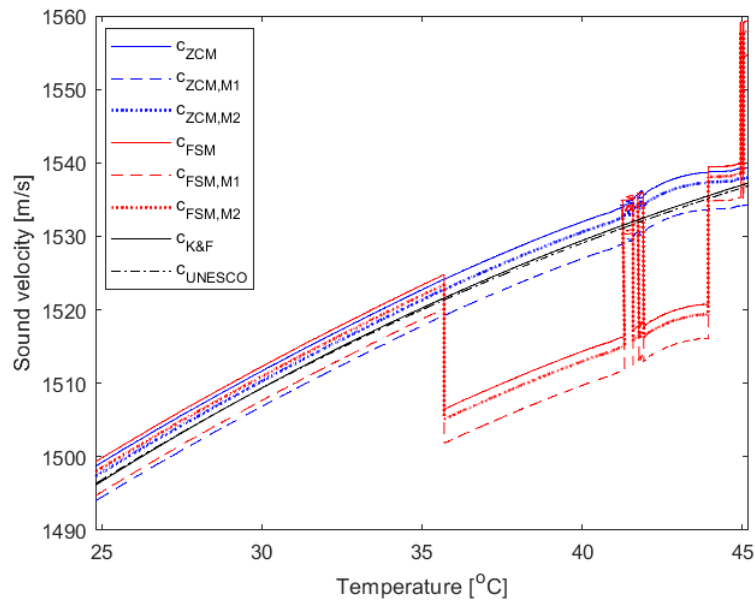
Figure 6.3: Measured and theoretical sound velocity in distilled water from 25 to 45°C. The measured values are found using the steady state portion of a ten period pulse and averaging the waveform 512 times. The theoretical values for $c_{K\&F}$ and c_{UNESCO} are calculated using Eq. 2.1 and D.1, respectively.

In the example above, measurements were running smoothly until approximately 35.7°C. Here, the FSM suddenly started measuring sound velocities about 18 m/s too low. Then, at 41.2°C, the measurements started fluctuating between being seemingly correct and 18 m/s too low. The bulge around 43 − 44°C is a result of removing the lid and stirring the sample with a cold metal rod to eliminate air bubbles (this was later swapped with a plastic rod with the same temperature as the sample to avoid a change in rate at which the temperature increased). At around 45°C, the FSM measured sound velocities about 18 m/s higher than what it presumably should. The errors occurred for both distilled water and saline water at 20 ppt salinity.

After further investigation, it was found that the jumps might be due to a $2n\pi$ phase ambiguity occurring in the FSM. The first jump in Fig. 6.3 is found at 35.69°C. Here, c_{FSM} decreases from 1524.84 m/s to 1506.51 m/s. This corresponds to a time shift of 2.0 μs, which, in turn, corresponds a to phase shift of 2π at 500 kHz. According to [45?], the phase angle might be subject to $2n\pi$ phase ambiguities if the pulses are not shifted to the start of the time window prior to the unwrapping process. By shifting the pulses to the start, as shown in Fig. 6.4b, the number of "jumps" in the phase might be reduced [95]. Fig. 3.43c shows what these jumps may look like after unwrapping. There could potentially be hundreds of such jumps present if the pulses are not shifted to the start, and if one of these jumps is distorted by noise, there will be an error in the measured sound velocity [95]. The probability of errors is thus higher if the pulses are not shifted. It should, however, also be noted that if the noise distorts an equal amount of phase jumps in Pulse A and B, the results should be valid [95]. On the basis of this, it is assumed that the noise distorted an unequal amount of phase jumps whenever the experimental sound velocity were erroneous. Consequently, the pulses were attempted circularly rotated to the start of the time window at a point where the measured sound velocity was "incorrect", and

the problem was found to be resolved. Circularly rotation of the pulses were thereafter performed whenever such errors occurred.
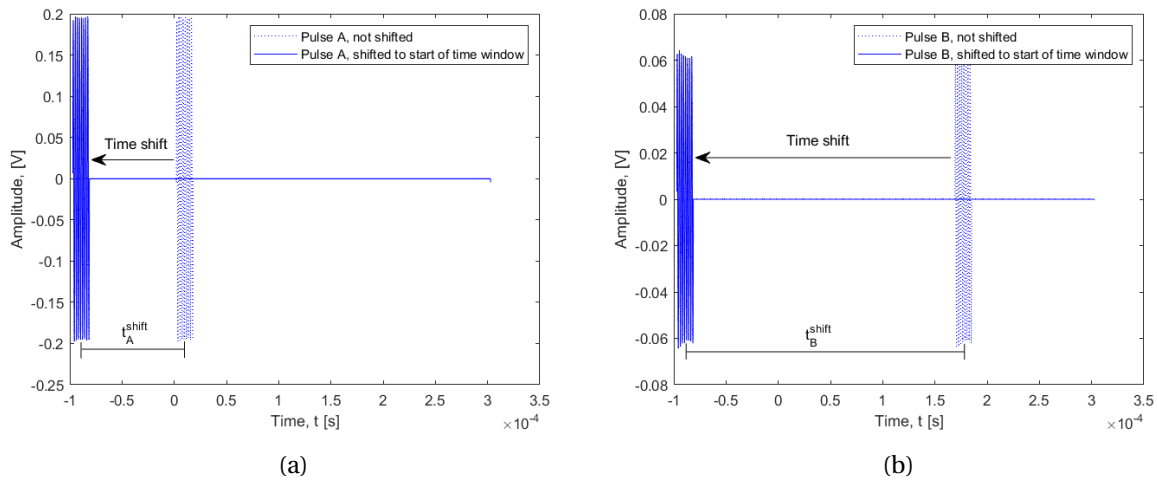
Figure 6.4: Shifting of the pulses to the start of the time window. The signal generator was set to generate a ten-period pulse at 500 kHz frequency and 10 V amplitude. The oscilloscope has averaged the waveform 512 times. (a) Pulse A, (b) Pulse B.

Since Pulse B is shifted further than Pulse A, the time shifting must be compensated for when the sound velocity is calculated. This was treated in MATLAB by adding a time shift $t^{shift} = t_B^{shift} - t_A^{shift}$ to the transit time difference Δt, see Appendix E.3.4.

The experimental sound velocity as a function of frequency was further investigated for distilled water, 50 ppt saline water and uncycled Exxsol D120 oil. The examined frequency span is from 275 kHz to 600 kHz in steps of 25 kHz. Fig. 5.12, **??** and 5.22 show the results graphically. A similar trend can be seen for all three cases, where the experimental sound velocities are found to be higher at lower frequencies. The cause is thought to be an amplitude reduction of the pulses, resulting in a reduced SNR. The measurements seemed to stabilize around 375 kHz for distilled and saline water, and around 425 kHz for Exxsol D120 oil, suggesting that the amplitude reduced at a slightly faster rate in the oil. Having said that, the measurements were rather stable from 425 to 600 kHz in all liquids, indicating a potential for using the measurement cell at frequencies other than 500 kHz which was chosen for this project. This can be of interest when sound velocity measurements are to be carried out on dispersive media. Frequencies higher than 600 kHz have not been investigated as XSENS Flow Solutions' desired frequency range is 200-500 kHz.

6.1.2 Factors that may have affected the measured sound velocities

Although the experimental sound velocities in this work seemed to be fairly accurate, with the modelled sound velocity lying between the two diffraction corrected sound velocities, it is important to recognize factors that may have affected the results.

Firstly, it should be noted that problems occurred during the heating process. As the temperature in-

creased, air bubbles gathered around the whole area of the cavity, including the transducer surfaces. Consequently, both the lid on the water bath and on the measurement cell had to be detached regularly to remove the air bubbles. The measurements has therefore been performed under rather unstable conditions. When the lid on the waterbath was removed, the temperature increased at a slower rate, and detaching of the measurement cell lid might have resulted in a slight change in sample composition due to evaporation. However, the conductivity measurements presented in Table 5.24 indicates that the change in sample composition due to evaporation were negligible, and no sudden change in experimental sound velocity due to a rate of change in temperature has been observed.

On the topic of temperature, it should be mentioned that the temperature sensor was accidentally mounted in the measurement cell before it had been calibrated. It was attached with strong glue, and had to be punched out of the measurement cell with great force. This resulted in some bulges on the tip of the probe, but testing indicated that the measured temperature were unaffected by the mistake.

The pressure in the laboratory was not constant throughout the measurement series. The maximum deviation in hydrostatic pressure across all measurement series was $\Delta P = 1.031 - 1.004$ bar $= 0.027$ bar. For distilled water at $25°C$, a change of 0.027 bar corresponds to a change of $4.53 \cdot 10^{-3}$ m/s in c_{UNESCO} and $4.52 \cdot 10^{-3}$ m/s in $c_{K\&F}$. It is thus assumed that the pressure fluctuations did not have a significant impact on the results.

Further, the distilled water used in this work is filtered with a system called Milli-Q [120]. The system produces pyrogen- and RNase-free ultrapure water through a purification system that combines ultrafiltration technologies and ultraviolet photo-oxidation, making the water ultra-low in organics [120]. Kinsler et. al. does not state the degree of purity of the water that the model is empirically derived from, and might therefore not be completely representative for the experimental sound velocities in distilled water found in this work. This might be the cause to the slightly different rates at which the experimental and modelled sound velocities increased in distilled water. Similarly, the difference in rate at which the experimental and modelled sound velocities increased in saline water could be due to the UNESCO-algorithm being empirically derived from measurements in sea water containing several different minerals. The UNESCO-algorithm is also not validated for temperatures above $40°C$ and salinity above 40 ppt [12].

Several other models describing the sound velocity as a function of temperature and pressure also exist. Some examples are the Mackenzie equation [121], Coppens' equation [122] and the NPL equation [115]. They are all found empirically, and the range of validity varies slightly. A more thorough examination of the models is required in order to have more confidence regarding comparisons between experimental and modelled sound velocities.

After all measurement series were finished, a small leakage was observed between the transmitting transducer and the cell wall in which it is mounted. The leakage was not observed before several days after completing the last measurement series. It is thus unknown when the leakage occurred, but it is assumed that a small gap between the transmitting transducer and cell wall arose as a result of thermal expansion during one of the measurement series. The thermal expansion coefficient of plex-

iglas and steel differs. While plexiglas has a linear thermal expansion coefficient of approximately $\alpha_T = 7.25 \cdot 10^{-5} {}^\circ C^{-1}$ [60, 61, 62], 303 stainless steel, which is the steel type of the transducer casing [63, 64], has a thermal expansion coefficient of approximately $\alpha_T = 1.73 \cdot 10^{-5} {}^\circ C^{-1}$ [65]. The plexiglass and transducer casing therefore expands at different rates as the temperature increases. In [10], such different thermal expansion rates resulted in small cracks in the measurement cell. Similar cracks is not observed in the measurement cell used here. It is thus assumed that there is only a small rift in the solidified glue between the cell wall and the transducer. The magnitude of the leakage is difficult to quantify, as it might depend on the temperature due to thermal expansion. However, at room temperature, almost no liquid is able to penetrate through the rift. Also, the experimental sound velocities corresponds well to the modelled sound velocities, suggesting that the leakage has not affected the results with great magnitude.

The temperature points at which the sound velocities are found differs slightly for each measurement series. Hence, the tabulated data in Section 5.4 is found by linearly interpolating between the two measurements closest to, and on either side of each temperature point in the tables. The curves representing the experimental sound velocities are not smooth, but more jagged, as illustrated in Fig. 6.5. The figure is an extract of Fig. 5.9a at around $30^\circ C$, showing that the measured sound velocities are fluctuating up and down even if the temperature is constantly increasing. The fluctuations are probably a result of different noise sources, and are one of the reasons as to why there is some inconsistency between the listed results found during measurement series 1 and 2.
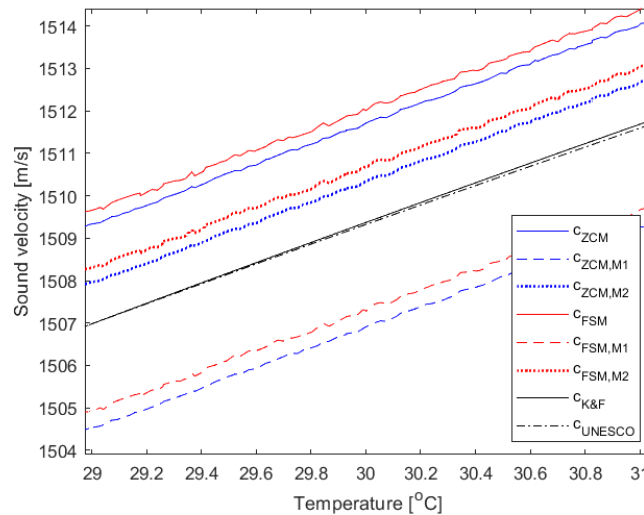
Figure 6.5: Extract of Fig. 5.9a around $30^\circ C$. The measured values are found using the steady state portion of a ten period pulse and averaging the waveform 512 times. The theoretical values for $c_{K\&F}$ and c_{UNESCO} are calculated using Eq. 2.1 and D.1, respectively.

Lastly, it should be taken into consideration that the transducers are not ideal. Specifications for each transducer is provided in Appendix B. The test forms show that the center frequency is not exactly 500 kHz, and the signal waveforms are slightly different. There may also be an imperfect symmetry inside the transducers, and the mounting of the transducers in the measurement cell is not flaw-

less. A non-perfect placement of the transducers could affect the measured sound velocities, but the transducer distance measurements in Section 5.3 suggests that the transducers have been mounted fairly accurate. On the topic of transducers, it should also be mentioned that thermal expansion in the transducer casing and inside the transducers has not been taken into account due to the interior of the transducers being unknown. In addition, possible interfering mode-converted shear waves generated at the transducer surface upon reflection at the sample-transducer interface has not been investigated in this work.

6.2 Uncertainty discussion

Two uncertainties are investigated in this work: (1) Estimated measurement uncertainty calculated according to the uncertainty model presented in Section 4.2, for which an example is given in Section 5.5, and (2) uncertainty in terms of deviation from the modelled sound velocity.

The normalized sound velocities are presented graphically throughout Section 5.4, and the deviation up to 1000 ppm from the modelled sound velocity is marked in green. $c_{ZCM,M2}$ is the only experimental sound velocity that is within 1000 ppm of the modelled sound velocity for all measurement series. However, if the estimated measurement uncertainty of the experimental sound velocities are taken into account, both $c_{FSM,M1}$ and $c_{FSM,M2}$ are within 1000 ppm of the modelled sound velocity. This is illustrated for $c_{FSM,M1}$ in Fig. 6.6.
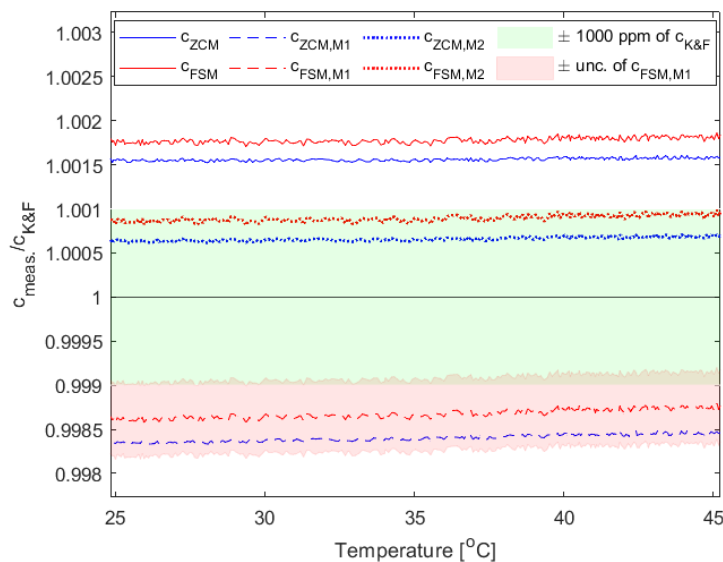
Figure 6.6: Normalised measured sound velocity in distilled water from 25 to $45°C$, with respect to the theoretical values calculated using Eq. 2.1. The measured values are found using the steady state portion of a ten period pulse and averaging the waveform 512 times. The figure corresponds to Fig. 5.10a, but with the estimated measurement uncertainty of $c_{FSM,M1}$ included.

The tabulated results in Section 5.4 show that the estimated relative measurement uncertainty calculated according to the uncertainty model presented in Section 4.2 varies between 368 and 428 ppm

across all measurement series. To illustrate how the uncertainty changes over the complete temperature span, the relative expanded uncertainty of both the experimental sound velocities and the two modelled sound velocities are plotted as a function of temperature in Fig. 6.7a. The uncertainties correspond to the relative expanded uncertainties associated to each respective measurement in the first measurement series for distilled water. All uncertainties are calculated with the MATLAB script presented in Appendix E.3.5.
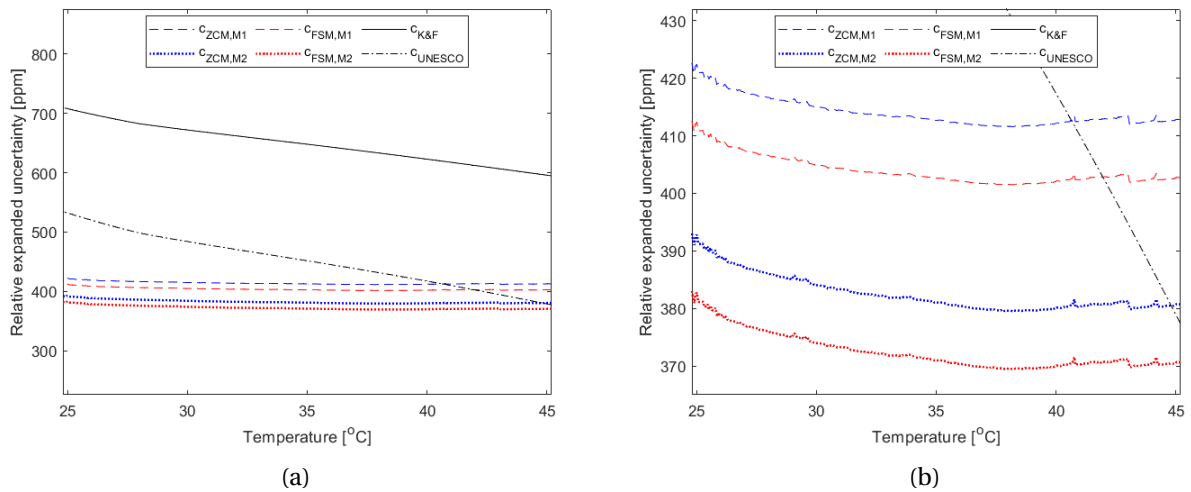
Figure 6.7: Relative expanded uncertainties at 95% confidence level calculated according to the uncertainty models presented in Chapter 4 for the first measurement series in distilled water. (b) is an extract of (a), highlighting the uncertainty of the experimental sound velocities.

Fig. 6.7a shows that the uncertainty of the experimental sound velocities is relatively stable, while the uncertainty of both modelled sound velocities decreases when the temperature increases. The decrease in the uncertainty of $c_{K\&F}$ and c_{UNESCO} is mainly due to the sensitivity coefficients in Eq. 4.57 and 4.60 decreasing as the temperature increases. A small decrease in relative uncertainty is also observed at low temperatures for the experimental sound velocities. Then, as the temperature becomes higher, the relative uncertainty seems to stabilize. This corresponds well with the figures showing the experimental sound velocities graphically in Section 5.4. It is clear that the experimental sound velocities are increasing fastest at the lowest temperatures, and more slowly at the highest temperatures. The same applies for the modelled sound velocities.

Moreover, some fluctuations can be seen in the measured uncertainties. The fluctuations are due to the uncertainty contributions that are measured for each data acquisition. For example, it was found that the uncertainty due to discretization of the pulses, $u(\Delta t)_{dis.}$, for which a model is derived in Section 4.2.4, was fluctuating throughout the measurement series. The fluctuations are thought to be a result of incoherent noise caused by vibrations from the waterbath. How this affects the total relative expanded uncertainty is illustrated in Fig. 6.8, where clear fluctuations were observed at the very start of the measurement series when the heating in the waterbath was initiated.
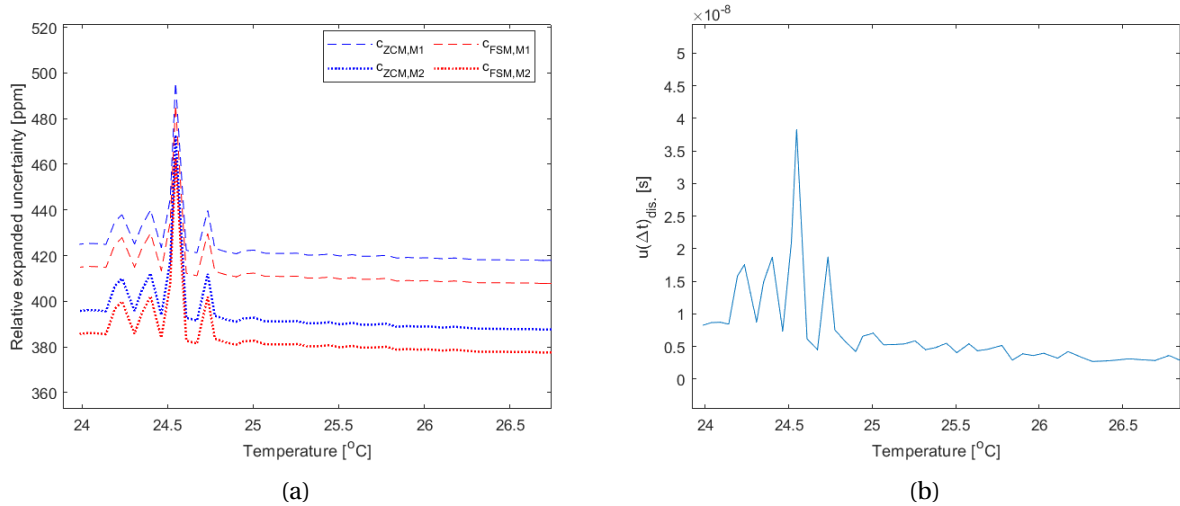
Figure 6.8: Measured uncertainties calculated according to the uncertainty models presented in Section 4.2. (a) Relative expanded uncertainty of the experimental sound velocities at 95% confidence level, (b) Absolute uncertainty in transit time difference due to discretization of the pulses, $u(\Delta t)_{dis.}$, at 95% confidence level.

The shape of the fluctuations in Fig. 6.8b, is clearly present in Fig. 6.8a, which indicates that the incoherent noise can have a big impact on the relative uncertainty of the experimental sound velocities. It also explains why the measured uncertainty in measurement series 1 and 2 for each sample differs slightly. The distinct "jumps" in Fig. 6.7b are thought to be caused by movement of the coaxial cables connecting the transducers to the electrical instruments. Also, at around $43°C$, there is a sudden decrease in uncertainty. The cause of this decrease has not been identified, but is thought to be a result of the cables being more separated from the walls of the waterbath, and thus being less prone to vibrations hereafter.

From the tabulated relative uncertainties in Section 5.4, it is clear that the ZCM results in a higher uncertainty than the FSM. The reason is found in the uncertainty of the transit time difference, $u(\Delta t)$. Here, the uncertainty contributions are dependent on which signal processing method is used. It was found that the uncertainty due to a spread in time shift of zerocrossing pairs in Pulse A and B in the ZCM was $7.64 \cdot 10^{-9}$ s in distilled water at $25°C$, cf. Table 5.33. This is higher than the uncertainty due to abruptly truncating the pulses to extract the steady state part prior to calculating the DFT in the FSM, which was found to be $7.87 \cdot 10^{-10}$ s, cf. Table 5.33. Hence, the relative expanded uncertainty of $c_{ZCM,M1}$ and $c_{ZCM,M2}$ is higher than that of $c_{FSM,M1}$ and $c_{FSM,M2}$.

It is also observed that diffraction correction Method 1 entails a higher relative uncertainty than diffraction correction Method 2. This is due to diffraction correction Method 1 resulting in a lower experimental sound velocity than Method 2, and because Method 1 carries a higher absolute uncertainty than Method 2, cf. calculations in Table 5.36 and 5.37. According to Table 5.40, the uncertainty of the correction term is the biggest uncertainty contributor to the uncertainty of c. This is mainly due to the uncertainty of the effective transducer radius. Arising problems caused all but the two first measurement series for each transducer to be distorted, see Section **??**. Consequently, the effective

transducer radii are estimated from only two sets of data. The uncertainty of the effective transducer radii is thus relatively high, entailing a relatively high uncertainty also in the diffraction correction.

Upon further thoughts, it has been acknowledged that a coverage factor of $k = 1$ would be more fitting for the uncertainty of the correction term, due to the lack of measurements of a_{eff}. If k is changed from 2 to 1, the resulting relative expanded uncertainty of c would be 655 ppm instead of 422 ppm, using the same values as in Table 5.40. This is still lower than 1000 ppm, which was the desired limit set for this project.

6.3   Potential improvements

Although the relative expanded uncertainty of the experimental measurements are well below 1000 ppm, some improvements of the measurement cell could certainly be made. Firstly, the temperature sensor used in this work is three-wired. It is specified by the manufacturer to have Class A type accuracy [79], meaning that the uncertainty of the sensor is $0.2°C$ at $T = 25°C$. The sensor was opted for due to its small size. The small size reduces disturbances in the sound field by not blocking the propagation path of the signals in the side lobes. However, it was found that the side lobes only contribute with a small part to the uncertainty of the transit time difference due to coherent noise, cf. Section 5.5.1. Consequently, although it would have been bigger in size, a four-wired temperature sensor might have been more sufficient as they are more accurate [87?]. Benus [84] used a four-wired JUMO STEAMTemp Temperaturegiver RTD [123] with 1/10 DIN Class B type accuracy. By interpolating the tabulated data in [109], which follows [113], this corresponds to an uncertainty of $0.045°C$ (95% confidence level) at $25°C$. By swapping this with the uncertainty of the three-wired temperature sensor in Table 5.3, the expanded uncertainty of the temperature measurements at 95% confidence level is reduced from $0.2757°C$ to $0.195°C$ according to the uncertainty budget.

It was found that the experimental sound velocities in this work fluctuated less than the experimental sound velocities found in [84], presumably due to the longer pulse length used here. Thus, it is believed that an even longer pulse length could reduce the fluctuations even more. In Section 3.3.2, it was shown that Pulse A would interfere with side wall reflections if the pulse length is longer than three periods, ref. Fig. 3.20. However, the maximum dB-level of the interfering side lobes is only -47.62 dB, and has been found to not cause a significant increase in the measurement uncertainty. Also, in Section 5.5.1, the worst case resulting time shift due to coherent noise was found from the SNR between Pulse B and the trailing noise, which corresponds to the lowest SNR over the complete waveform. A corresponding uncertainty was found and has been included in the uncertainty budgets. Consequently, if the pulse length was to be made longer, it would not affect the uncertainty of the measurements. It should be noted, however, that the uncertainty due to coherent noise was calculated for distilled water at $25°C$, and the SNR might be different in another medium with a different temperature.

A volume limit of 0.5 l was set for the measurement cell prior to the designing phase. This restricted

a lot of possibilities regarding the shape and dimensions of the cell, as far field conditions were desirable, cf. Section 3.2.2. The design was made under the assumption that sound velocities would be measured down to approximately 1154 m/s. Using the nominal transducer radii of the V318-SU transducers, this corresponds to a Rayleigh distance of 123.5 mm. In other words, the transducer separation distance presumably had to be at least 123.5 mm to obtain far field conditions for all measurements in this project. With a volume limit of 0.5 l, this entailed a relatively long and narrow shape of the measurement cell. However, in this work, the lowest measured sound velocity was 1285.00 m/s, see Table 5.28. Using this value and also swapping the nominal transducer radius with the mean of the effective transducer radii, a new Rayleigh distance of 114.3 mm is found. Thus, the measurement cell could have been shorter in length and less narrow, without disrupting far field conditions.

Simple trigonometric calculations along with the sound field analysis presented in Section 3.3 show that a wider cell would increase the time difference between arrival of the signals of interest and the side wall reflections, and thus reduce coherent noise. A tentative design for the measurement cell with new dimensions is shown in Fig. 6.9. The resulting change in arrivals of the signals of interest and side wall reflections is shown in Fig. 6.10.
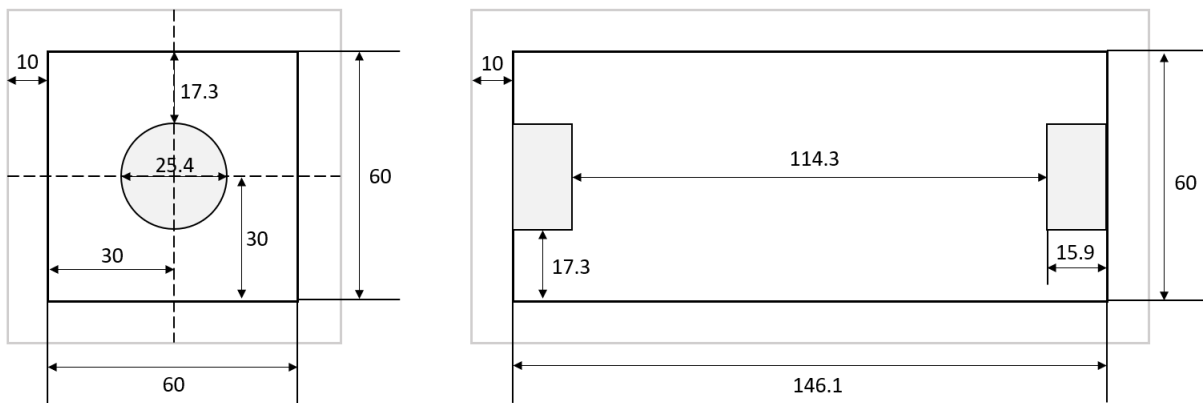
Figure 6.9: Proposed new and improved tentative dimensions of the measurement cell based on the results found in this work. The thickness of the cell walls are kept the same, and the dimensions keeps the volume at 0.5 l. Dimensions are in mm.
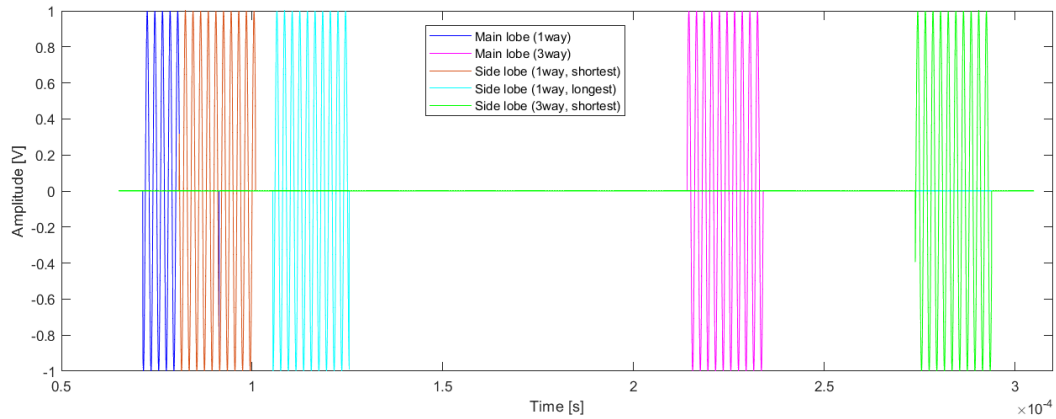
Figure 6.10: One-way signal of interest, shortest travelling one-way side wall reflection, longest travelling one-way side wall reflection, three-way signal of interest, and shortest travelling three-way side wall reflection plotted along the same time axis for the new cell dimensions. The pulse length is set to 10 periods and the sound speed of the medium is set to 1593 m/s, which corresponds to the sound speed in 50 ppt saline water at $60°C$.

Comparison of Fig. 6.10 with Fig. 3.20 shows that the first five periods of Pulse A avoids side wall reflections in the new cell design, as opposed to the 3 periods in the original design. Thus, if the measurement cell does not require to perform measurements on liquids with lower sound velocity, the new tentative design is assumed to be more accurate.

The new design is primarily created with avoidance of side wall reflections in mind. However, in Section 3.3.2 and 3.3.3, some testing were done with metal blocks and a steel plate to investigate how the waveform could be affected. It was found that the metal blocks increased the amplitude of Pulse B and reduced the amplitude of the trailing noise. However, the noise prior to Pulse B increased and made it difficult to define the start of the signal. From Fig. 3.20, it has already been found that Pulse B is not prone to side wall reflections. The connection between the placement of the metal blocks and the change in noise is thus unclear. It might be caused by a change in the sound waves that propagate into the actual cell walls, and follows the wall around to the receiving transducer. The same applies for the change in noise due to the steel plate being mounted flush with the receiving transducer. As side wall reflections presumably should be absent around pulse B, the change in signal could, again, be due to noise propagating inside the actual cell walls. Such noise has not been investigated in this work, but might be necessary in order to design an even more accurate measurement cell.

Lastly, the measurement cell should ideally be constructed based on the effective transducer radii and the actual sound field. If the measurement cell was customized based on these factors, it would most likely be more accurate, as the nominal transducer radii and the theoretical sound field are not completely representative. Late arrival of the transducers unfortunately restricted these possibilities.

Chapter 7

Conclusions and further work

7.1 Conclusions

In this project, a measurement cell based on the 3-way pulse method for sound velocity measurements has been developed. The measurement cell has been tested on distilled water, saline water and Exxsol D120 oil over a temperature span from approximately $25°C$ to $45°C$ to determine whether the method is well suited to construct a measurement cell of high precision.

For all sound velocity measurements, the steady state part of a 500 kHz ten-period pulse has been processed to find the experimental sound velocities. Signal processing has been performed through two different methods: The zerocrossing method (ZCM) and the Fourier spectrum method (FSM). Additionally, two different diffraction correction methods was applied to the sound velocities. Thus, a total of four diffraction corrected experimental sound velocities have been found for each measured temperature in the liquid samples. The experimental sound velocities have been compared to modelled sound velocities calculated according to the equation presented by Kinsler et. al. [29] and to the UNESCO-algorithm [11, 12]. The results show that the experimental sound velocities are greater than the modelled sound velocities when diffraction correction Method 2 is applied, and less than the modelled sound velocities when diffraction correction Method 1 is applied.

For distilled water, the best agreement with the modelled sound velocity was found to be 628 ppm at $45°C$ using the ZCM and diffraction correction Method 2. On the contrary, the ZCM and diffraction correction Method 1 demonstrated the worst agreement, where the experimental sound velocity agreed to within 1624 ppm of the modelled sound velocity. The FSM showed agreements between these two values over the complete temperature span. The same trend has been found for all experiments on saline water. Across all sound velocity measurements, the best agreement with the modelled sound velocity was found to be 744, 795 and 761 ppm for 20, 35 and 50 ppt salinity, respectively. On the opposite side, the worst agreement with the modelled sound velocity was 1501, 1453 and 1502 ppm for the same respective salinity values. All the best agreements where found with the ZCM and diffraction correction Method 2, while all the worst agreements where found with the ZCM and diffraction correction Method 1.

The experimental sound velocities in Exxsol D120 oil have not been compared to a modelled sound velocity. However, a maximum deviation of only 61 ppm was found between measurement series 1 and 2 for both the uncycled and temperature cycled oil, increasing the confidence in the results. It has also been observed that the experimental sound velocity was generally 0.1 to 0.2 m/s higher in the temperature cycled oil, indicating that the composition of the oil had been slightly affected by the temperature cycling.

Associated relative expanded uncertainties at 95% confidence level have been calculated for the experimental sound velocities using the uncertainty models presented in Chapter 4. An example uncertainty budget for the relative expanded uncertainty at 95% confidence level for the experimental sound velocity in distilled water at $25°C$ has been carried out. The uncertainty was found to be 422 ppm, which is within the 1000 ppm limit that was set for the project. Across all sound velocity measurements, the uncertainty generally fluctuated between 368 and 428 ppm.

From the example uncertainty budget, it has been found that the diffraction correction contributes the most to the total relative expanded uncertainty of the experimental sound velocity. Of the 422 ppm, 197 ppm are due to diffraction correction, which is nearly half of the total. Further, the uncertainty of the transducer separation distance and transit time difference was found to contribute with 155 ppm and 67 ppm, respectively, while uncertainty in thermal expansion only contributed with 3 ppm.

It has been acknowledged that a coverage factor $k = 1$ would be more appropriate for the uncertainty of the correction term, and potentially some other uncertainty contributors, to have more confidence in not underestimating the measurement uncertainty. The current budgeted uncertainty is low enough to allow for such changes and still not exceed the desired limit of 1000 ppm. The measurement cell has thus shown great potential in regards to a low measurement uncertainty. However, since there is a deviation between the results found with ZCM and FSM, and the two diffraction correction methods reduce the experimental sound velocities to either side of the modelled sound velocities, it is concluded that further investigation of the signal processing methods and diffraction correction in the 3-way pulse method is desirable before the measurement cell can be used for high precision sound velocity measurements.

7.2 Further work

Since only two sets of measurements were carried out for each liquid sample, it would be of interest to investigate the repeatability further by performing more measurements. The measurement cell was also planned to be tested on oils other than Exxsol D120, but time constraints prevented this. Moreover, the experimental sound velocity was carried out for frequencies between 275 and 600 kHz, where the results were found to be stable above 425 kHz. In further work, one could test the measurement cell at other frequencies to investigate its potential at frequencies other than the frequencies tested in this project.

The two diffraction correction methods applied in this project are two extremes, and it was assumed that the modelled sound velocity would lie between the experimental sound velocities corrected with the two methods [40]. This was indeed found to be the case. In further work, it would be interesting to investigate diffraction correction in the 3-way pulse method more thoroughly, e.g. through finite element modelling in COMSOL.

Uncertainty in diffraction correction was found to be the main uncertainty contributor in the measurement cell. By carrying out more measurements of the effective transducer radii, it is assumed that the uncertainty could be reduced significantly. Also, thermal expansion of the transducers are neglected in this work due to the internal structure of them being unknown. Since both transducers are penetrating into the cavity of the measurement cell, further investigation of how the transducers change shape as the temperature changes is desirable.

Finally, the initial plan was to develop a measurement cell that could also measure the sound velocity in pressurized liquids. However, that would require a more complex measurement cell containing valves, a pressure sensor and reinforced cell walls. This was not feasible within the scope of the project, and may thus be a topic for further work.

References

[1] A.-M. O. Mohamed, M. El Gamal, and A. Y. Zekri, "Effect of salinity and temperature on water cut determination in oil reservoirs," *Journal of Petroleum Science and Engineering*, vol. 40, no. 3-4, pp. 177–188, 2003.

[2] S. Fisher, *Science and skepticism in the seventeenth century: The atomism and scientific method of Pierre Gassendi*.   City University of New York, 1997.

[3] D. Ragni, F. Avallone, and D. Casalino, "Measurement techniques for aeroacoustics: from aerodynamic comparisons to aeroacoustic assimilations," *Measurement Science and Technology*, vol. 33, no. 6, p. 062001, 2022.

[4] G. Horváth-Szabó, H. Høiland, and E. Høgseth, "An automated apparatus for ultrasound velocity measurements improving the pulse-echo-overlap method to a precision better than 0.5 ppm in liquids," *Review of scientific instruments*, vol. 65, no. 5, pp. 1644–1648, 1994.

[5] P. Norli, P. Lunde, and M. Vestrheim, "Investigation of precision sound velocity measurement methods as reference for ultrasonic gas flow meters," in *IEEE Ultrasonics Symposium, 2005.*, vol. 3.   IEEE, 2005, pp. 1443–1447.

[6] S. Zeroug and S. Bose, "Recent advances in the use of acoustics across the frequency spectrum in the oil and gas industry," in *AIP Conference Proceedings*, vol. 1949, no. 1.   AIP Publishing LLC, 2018, p. 020014.

[7] J. P. Bentley, *Principles of Measurements Systems*, 4th ed.   Harlow: Pearson/Prentice Hall, 2005.

[8] XSENS Flow Solutions, Bergen, Norway, Available at: https://xsensflow.com/, Last Accessed: 25.05.22.

[9] Weatherford International, Inc., Houston, Texas, USA, Available at: https://www.weatherford.com/products-and-services/production/production-4-0/flow-measurement/multiphase-flow-measurement/, Last Accessed: 25.05.22.

[10] O. Nesse, "Sound Propagation in Emulsions," Ph.D. dissertation, University of Bergen, Dept. of Physics and Technology, Bergen, Norway, Jan. 1998.

[11] C.-T. Chen and F. J. Millero, "Speed of sound in seawater at high pressures," *The Journal of the Acoustical Society of America*, vol. 62, no. 5, pp. 1129–1135, 1977.

[12] G. S. Wong and S.-m. Zhu, "Speed of sound in seawater as a function of salinity, temperature, and pressure," *The Journal of the Acoustical Society of America*, vol. 97, no. 3, pp. 1732–1736, 1995.

[13] V. A. Del Grosso, "New equation for the speed of sound in natural waters (with comparisons to other equations)," *The Journal of the Acoustical Society of America*, vol. 56, no. 4, pp. 1084–1091, 1974.

[14] P. Lunde and M. Vestrheim, "Precision Sound Velocity Cell for Natural Gas at High Pressure. Phase 1- Feasibility study." *Christian Michelsen Research*, Ref. nr.: CMR-98-A10039, Bergen, Norway, Dec. 1998.

[15] P. Norli, "Sound Velocity Cell for Gas Characterization," Ph.D. dissertation, University of Bergen, Dept. of Physics and Technology, Bergen, Norway, Aug. 2007.

[16] P. Kortbeek, M. Muringer, N. Trappeniers, and S. Biswas, "Apparatus for sound velocity measurements in gases up to 10 kbar: Experimental data for argon," *Review of scientific instruments*, vol. 56, no. 6, pp. 1269–1273, 1985.

[17] G. Benedetto, R. M. Gavioso, P. Albo, S. Lago, D. M. Ripa, and R. Spagnolo, "Speed of sound in pure water at temperatures between 274 and 394 k and at pressures up to 90 mpa," *International journal of thermophysics*, vol. 26, no. 6, pp. 1667–1680, 2005.

[18] W. Zhang and J. Schouten, "The sound velocity of a mixture of he and n2 up to 10 kbar and from 157 k to 298 k," *Fluid phase equilibria*, vol. 79, pp. 211–220, 1992.

[19] W. Wagner and A. Pruß, "The iapws formulation 1995 for the thermodynamic properties of ordinary water substance for general and scientific use," *Journal of physical and chemical reference data*, vol. 31, no. 2, pp. 387–535, 2002.

[20] E. P. Papadakis, "Ultrasonic phase velocity by the pulse-echo-overlap method incorporating diffraction phase corrections," *The Journal of the Acoustical Society of America*, vol. 42, no. 5, pp. 1045–1051, 1967.

[21] ——, "Ultrasonic attenuation and velocity in three transformation products in steel," *Journal of Applied Physics*, vol. 35, no. 5, pp. 1474–1482, 1964.

[22] ——, "New, compact instrument for pulse-echo-overlap measurements of ultrasonic wave transit times," *Review of Scientific Instruments*, vol. 47, no. 7, pp. 806–813, 1976.

[23] J. E. May, "Precise measurement of time delay," in *1958 IRE National Convention*. IEEE, 1958, pp. 134–142.

[24] F. Foudzi and I. Ihara, "Development of polygonal buffer rods for ultrasonic pulse-echo measurements," in *Journal of Physics: Conference Series*, vol. 520, no. 1. IOP Publishing, 2014, pp. 1–4.

[25] C. K. Jen, L. Piche, and J. F. Bussiere, "Long isotropic buffer rods," *The Journal of the Acoustical Society of America*, vol. 88, no. 1, pp. 23–25, 1990.

[26] C. K. Jen, B. Cao, K. T. Nguyen, C. A. Loong, and J. G. Legoux, "On-line ultrasonic monitoring of a die-casting process using buffer rods," *Ultrasonics*, vol. 35, no. 5, pp. 335–344, 1997.

[27] M. Solberg, "Absolute sound velocity measurements in liquid using the three-way three way pulse method," Master's thesis, University of Bergen, Dept. of Physics and Technology, Bergen, Norway, Sep. 2009.

[28] P. Lunde, P. Norli, M. Vestrheim, and R. A. Kippersund, "Precision sound velocity cell as reference for gas quality measurement in ultrasonic flow meters," in *Proceedings of the 30th Scandinavian Symposium on Physical Acoustics*, Geilo, Norway, Jan. 2007.

[29] L. E. Kinsler, A. R. Frey, A. B. Coppens, and J. V. Sanders, *Fundamentals of Acoustics*, 4th ed. USA: John Wiley & Sons, Inc., 2000.

[30] W. Sachse and Y.-H. Pao, "On the determination of phase and group velocities of dispersive waves in solids," *Journal of applied Physics*, vol. 49, no. 8, pp. 4320–4327, 1978.

[31] P. M. Morse and K. U. Ingard, *Theoretical acoustics.* Princeton, New Jersey, USA: Princeton university press, 1986.

[32] W. D. Wilson, "Speed of sound in sea water as a function of temperature, pressure, and salinity," *The Journal of the Acoustical Society of America*, vol. 32, no. 6, pp. 641–644, 1960.

[33] E. R. Anderson, "Sound speed in seawater as a function of realistic temperature - salinity - pressure domains," *Naval undersea research and development center, San Diego, CA. 92132*, vol. 243, pp. 1–58, 1971.

[34] H. D. Young and R. A. Freedman, *University Physics with Modern Physics*, 14th ed. Harlow, England: Pearson Education Limited, 2015.

[35] S. Gröber, M. Vetter, B. Eckert, and H. Jodl, "World pendulum—a distributed remotely controlled laboratory (rcl) to measure the earth's gravitational acceleration depending on geographical latitude," *European journal of physics*, vol. 28, no. 3, pp. 603–613, 2007.

[36] National Physical Laboratory, "Technical guides - speed of sound in sea-water," 2000, Available at: https://www.comm-tec.com/library/technical_papers/speedsw.pdf, 2000.

[37] N. P. Fofonoff and R. C. Millard, "Algorithms for computation of fundamental properties of seawater," *Unesco technical papers in marine science*, vol. 44, pp. 1–53, 1983.

[38] The Engineering Toolbox, "Evaporation from a Water Surface," Available at: https://www.engineeringtoolbox.com/evaporation-water-surface-d_690.html, Last Accessed: 07.06.22.

[39] A. B. Bhatia, *Ultrasonic absorption: an introduction to the theory of sound absorption and dispersion in gases, liquids, and solids.* New York, USA: Dover publications, Inc., 1985.

[40] Lunde, P., Rommetveit, T., *Personal communication with supervisors*, University of Bergen, Dept. of Physics and Technology, Bergen, Norway, 2021-2022.

[41] V. Simanzhenkov and R. Idem, *Crude oil chemistry.* New York, USA: Crc Press, 2003.

[42] M. C. K. de Oliveira, L. R. Miranda, A. B. de Carvalho, and D. F. S. Miranda, "Viscosity of water-in-oil emulsions from different american petroleum institute gravity brazilian crude oils," *Energy & Fuels*, vol. 32, no. 3, pp. 2749–2759, 2018.

[43] Z. Wang, A. M. Nur, and M. L. Batzle, "Acoustic velocities in petroleum oils," in *SPE Annual Technical Conference and Exhibition*, no. SPE-18163-MS. OnePetro, Oct. 1988.

[44] J. Hogendoorn, A. Boer, M. Zoeteweij, O. Bousché, R. Tromp, R. de Leeuw, P. Moeleker, M. Appel, and H. de Jong, "Magnetic resonance multiphase flow meter: Gas flow measurement principle and wide range testing results," in *Proceedings of the 32nd International North Sea Flow Measurement Workshop, St. Andrews, Scotland*, 2014, pp. 21–24.

[45] M. Saether, "Elastic wave velocities and attenuation under methane hydrate growth in Bentheim Sandstone - Measurements and modelling," Ph.D. dissertation, University of Bergen, Dept. of Physics and Technology, Bergen, Norway, Sep. 2018.

[46] H. Fossaa, "Ultrasound Phantom for Myocardium," Master's thesis, University of Bergen, Dept. of Physics and Technology, Bergen, Norway, Oct. 2011.

[47] M. Vestrheim, *Lecture notes in PHYS373- Acoustic measurement systems.* Course at the University of Bergen, Dept. for Physics and Technology, Bergen, Norway, 2013.

[48] A. S. Khimunin, "Numerical calculation of the diffraction corrections for the precise measurement of ultrasound absorpsjon," *Acta Acustica united with Acustica*, vol. 27, no. 4, pp. 173–181, 1972.

[49] ——, "Numerical calculation of the diffraction corrections for the precise measurement of ultrasound phase velocity," *Acta Acustica united with Acustica*, vol. 35, no. 3, pp. 192–200, 1975.

[50] E. Bjorndal, K.-E. Froysa, and S.-A. Engeseth, "A novel approach to acoustic liquid density measurements using a buffer rod based measuring cell," *ieee transactions on ultrasonics, ferroelectrics, and frequency control*, vol. 55, no. 8, pp. 1794–1808, 2008.

[51] J. Krautkramer and H. Krautkramer, *Ultrasonic Testing of Materials*, 2nd ed. Berlin, Germany: Springer-Verlag, 1977.

[52] F. B. Hildebrand, *Introduction to Numerical Analysis*, 2nd ed. New York, USA: Dover publications, Inc., 1987.

[53] J. A. Hossack and B. A. Auld, "Multiple layer transducers for broadband applications," *IEEE 1991 Ultrasonic Symposium*, pp. 605–610, Dec. 1991.

[54] V. M. Nascimento, V. L. S. N. Button, J. M. Maia, E. T. Costa, and E. J. V. Oliveira, "Influence of backing and maching layers in ultrasound transducer performance," *Proc. SPIE 5035, Medical Imaging 2003: Ultrasonic Imaging and Signal Processing*, vol. 5035, pp. 1208–1217, 2003.

[55] M. Vestrheim, *Lecture notes in PHYS272- Acoustic Transducers.* Course at the University of Bergen, Dept. of Physics and Technology, Bergen, Norway, 2007.

[56] H. Ilham, M. Salim, R. Jenal, and T. Hayashi, "Guided wave matching layer using a quarter of wavelength technique," in *Applied Mechanics and Materials*, vol. 833. Bäch, Switzerland: Trans Tech Publications Ltd., Aug. 2016, pp. 59–68.

[57] P. Lunde, *Lecture notes in PHYS271 - Acoustics.* Course at the University of Bergen, Dept. of Physics and Technology, Bergen, Norway, 2009.

[58] A. D. Pierce, *Acoustics, An introduction to Its Physical Principles and Applications*, 2nd ed. Pennsylvania, USA: Acoustical Society of America, 1989.

[59] Brenntag, "Exxsol d grade dearomatised hydrocarbons," Available at: https://www.brenntag.com/media/documents/uk_ireland/exxsol_d_grade_dearomatised_hydrocarbons_brenntag.pdf, Last Accessed: 27.05.2022.

[60] The Engineering Toolbox, "Thermal expansion - linear expansion coefficients," Available at: https://www.engineeringtoolbox.com/linear-expansion-coefficients-d_95.html, Last Accessed: 31.05.2022.

[61] Carville Ltd., "How thermally stable is acrylic or plexiglass (pmma)," Available at: https://www.carvilleplastics.com/how-thermally-stable-is-acrylic-or-plexiglass-pmma/, Last Accessed: 31.05.2022.

[62] Induflex A/S, "How big is the heat expansion of acrylic?" Available at: https://www.pmma.dk/acryl_expansion.aspx?Lang=en-GB, Last Accessed: 31.05.2022.

[63] Olympus America, Inc., "Ultrasonic Transducers - Wedges, Cables, Test Blocks," Available at: http://www.materialevaluation.gr/pdf/Flaw_Detectors/Transducers_And_Probes/UltraSonic_Transducers_Pana_UT_EN_201603.pdf, July 2019, Last Accessed: 03.06.2022.

[64] ——, "Immersion Transducer – V318-SU," Available at: https://datasheets.globalspec.com/ds/3074/OlympusAmericaInc/9715413A-C90B-4957-ABB0-3B4D80BA5ADC, Last Accessed: 05.06.2022.

[65] Metals4U, "303 Stainless Steel," Available at: https://www.metals4u.co.uk/blog/303-stainless-steel, Last Accessed: 14.06.2022.

[66] K. K. Andersen, "Reciprocity calibration of ultrasonic piezoelectric disks in air," Master's thesis, University of Bergen, Dept. of Physics and Technology, Bergen, Norway, Nov. 2015.

[67] R. Hauge, "Finite element modeling of ultrasound measurement systems for gas. comparison with experiments in air." Master's thesis, University of Bergen, Dept. of Physics and Technology, Bergen, Norway, June 2013.

[68] P. He and J. Zheng, "Acoustic dispersion and attenuation measurement using both transmitted and reflected pulses," *Ultrasonics*, vol. 39, no. 1, pp. 27–32, 2001.

[69] X. Lurton, *An introduction to Underwater Acoustics*, 2nd ed.   Chichester, UK: Springer, 2010.

[70] K. D. Lohne, P. Lunde, and M. Vestrheim, "Measurements and 3d simulations of ultrasonic directive beam transmission through a water-immersed steel plate," *Proceedings of the 34th Scandinavian Symposium on Physical Acoustics*, vol. 30, pp. 1–29, Geilo, Norway, Jan. 2011.

[71] D. T. Blackstock, *Fundamentals of Physical Acoustics*, 1st ed.   Austin, Texas, USA: John Wiley & Sons, Inc., 2000.

[72] M. R. Ebadi, "Coherent and incoherent seismic noise attenuation using parabolic radon transform and its application in environmental geophysics," *Modeling Earth Systems and Environment*, vol. 3, no. 18, pp. 1–12, Abadan, Iran, Feb. 2017.

[73] MATLAB, *version 9.9.0 (R2020b)*.   Natick, Massachusetts: The MathWorks Inc., 2020.

[74] Olympus America, inc., "Olympus ultrasonic transducers," Available at: https://www.olympus-ims.com/en/ultrasonic-transducers/, Last Accessed: 13.03.22.

[75] Thyssenkrupp Materials, "Stainless steel 303 1.4305," Available at: https://www.thyssenkrupp-materials.co.uk/stainless-steel-303-14305.html, Last Accessed: 02.05.2022.

[76] GE Infrastructure, "Sound speeds and pipe size data," *GE Infrastructure Sensing Inc.*, pp. 1–23, Billerica, Massachusetts, USA, Aug. 2004.

[77] Keysight Technologies, "33500B and 33600A Series Trueform Waveform Generators," Aug. 2021, Available at: https://www.keysight.com/zz/en/assets/7018-05928/data-sheets/5992-2572.pdf, Last Accessed: 08.06.2022.

[78] Tektronix, "Mixed Signal Oscilloscopes MSO3000 Series, DPO3000 Series Datasheet," Sep. 2010, Available at: https://www.farnell.com/datasheets/866445.pdf, Last Accessed: 05.06.2022.

[79] RS Components AS, "RS PRO PT100 Sensor, 3mm Dia, 30mm Long, 3 Wire, Probe, Class A +250° Max," Available at: https://no.rs-online.com/web/p/rtd-sensors/4573710, Last Accessed: 01.03.2022.

[80] InstrumentationTools, "What is RTD Accuracy?" Available at: https://instrumentationtools.com/rtd-accuracy/, Last Accessed: 03.02.2022.

[81] Dracal Technologies, "USB 2/3 Wire RTD Sensor To USB Adapter ," Available at: https://www.dracal.com/wp-content/uploads/2021/09/Dracal-RTD_23-Datasheet.pdf, Last Accessed: 02.06.2022.

[82] Keison Products, "5 Stirred thermostatic baths and circulators," Available at: http://www.keison.co.uk/products/grantinstruments/StirredThermostaticBathsAndCirculators.pdf, Last Accessed: 22.06.2022.

[83] J. Hovem, *Ray Trace Modeling of Underwater Sound Propagation*, SINTEF, Trondheim, Norway, Nov. 2013, pp. 1–49.

[84] H. D. S. Benus, "Measurement cell for sound speed in liquids: Pulse-echo buffer rod method," Master's thesis, University of Bergen, Dept. of Physics and Technology, Bergen, Norway, May 2022.

[85] A. DeLancey, "When to Use a 3 Wire RTD," Aug. 2016, Available at: https://blog.wika.us/products/temperature-products/3-wire-rtd/, Last Accessed: 08.06.2022.

[86] Instrumentationtools, "Difference Between 2 wire RTD, 3 wire RTD, and 4 wire RTD's," Available at: https://instrumentationtools.com/difference-between-2-3-and-4-wire-rtds/, Last Accessed: 09.07.2022.

[87] Omega Engineering, "What is the Difference Between a 2, 3, and 4 Wire RTD?" Available at: https://www.omega.com/en-us/resources/rtd-2-3-4-wire-connections, Last Accessed: 18.07.2022.

[88] WIKA Alexander Wiegand SE Co. KG, "Operating limits and tolerances of platinum resistance thermometers per DIN EN IEC 60751," Available at: https://www.wika.com/media/Technical-information/English/ds_in0017_en_co.pdf, Nov. 2020, Last Accessed: 14.03.2022.

[89] R. Radetić, M. Pavlov-Kagadejev, and N. Milivojević, "The analog linearization of pt100 working characteristic," *Serbian Journal of Electrical Engineering*, vol. 12, no. 3, pp. 345–357, 2015.

[90] Paroscientific, Inc. Digiquartz Pressure Instrumentation, "Digiquartz Intelligent Barometers and Barometric Standards," Available at: http://www.coastal-usa.com/paros.pdf, Last Accessed: 02.06.2022.

[91] Precision Acoustics, "1.0 mm needle hydrophone (NH1000)," Available at: https://www.acoustics.co.uk/wp-content/uploads/2022/03/NH1000-1.0mm-Needle-hydrophone-TDS-V1-0222.pdf, Last Accessed: 13.07.2022.

[92] M. Aanes, "Interaction of piezoelectric transducer excited ultrasonic pulsed beams with a fluid-embedded viscoelastic plate. Finite element modeling, angular spectrum modeling and measurements," Ph.D. dissertation, University of Bergen, Dept. of Physics and Technology, Bergen, Norway, Dec. 2013.

[93] J. H. McClellan, R. W. Schafer, and M. A. Yoder, *DSP First*, 2nd ed. Harlow, England: Pearson Education Limited, 2016.

[94] R. A. Adams and C. Essex, *Calculus: A Complete Course*, 8th ed. Canada: Prentice Hall Canada, 2013.

[95] M. M. Sæther, *Personal communication*, University of Bergen, Dept. of Physics and Technology, Bergen, Norway, 2022.

[96] K. W. Winkler and T. Plona, "Technique for measuring ultrasonic velocity and attenuation spectra in rocks under pressure," *Journal of Geophysical Research: Solid Earth*, vol. 87, no. B13, pp. 10 776–10 780, Ridgefield, Connecticut, USA, Dec. 1982.

[97] J. Wu and F. Cubberley, "Measurement of velocity and attenuation of shear waves in bovine compact bone using ultrasonic spectroscopy," *Ultrasound in medicine & biology*, vol. 23, no. 1, pp. 129–134, Burlington, Vermont, USA, May 1997.

[98] E. O. Brigham, *The Fast Fourier Transform and its applications.* Prentice Hall, Englewood Cliffs, New Jersey, USA, 1988.

[99] S. Winder, *Analog and Digital Filter Design*, 2nd ed. USA: Newnes, 2002.

[100] J. Heath, "Digital filters vs. analog filters," *Electrical Engineering News and Products*, pp. 1208–1217, Virginia, USA, Oct. 2016.

[101] Krohn-Hite Corporation, "Model 3940 3Hz to 2MHz, High-Pass/Low-Pass Butterworth/Bessel Programmable Filter," Available at: https://www.krohn-hite.com/3940Data.pdf, Last Accessed: 12.03.2022.

[102] R. E. Crochiere and L. R. Rabiner, "Interpolation and decimation of digital signals - a tutorial review," *Proceedings of the IEEE*, vol. 69, no. 3, pp. 300–331, Mar. 1981.

[103] D. G. E. Robertson and J. J. Dowling, "Design and responses of butterworth and critically damped digital filters," *Journal of Electromyography and Kinesiology*, vol. 13, no. 6, pp. 569–573, Dec. 2003.

[104] C. S. Bretherton, *Lecture notes: Lecture 16: Filter design and Butterworth filters.* Course at the University of Washington, USA, 2014.

[105] Joint Committee for Guides in Metrology (ISO), Guide 100:2008, *Evaluation of measurement data - Guide to the expression of uncertainty in measurement*, 1st ed. Geneva, Switzerland: International Organisation for Standardisation, 2008.

[106] International Organization for Standardization ISO 5168:2005, *Measurement of fluid flow - Procedures for the evaluation of uncertainties*, 2nd ed., Geneva, Switzerland, 2005.

[107] P. Lunde and K.-E. Frøysa, "Handbook of Uncertainty Calculations. Ultrasonic Fiscal Gas Metering Stations," *Christian Michelsen Research AS*, Dec. 2001, Bergen, Norway, Rapp. nr. ISBN: 82-556-1009-3.

[108] Acromag, "Criteria for Temperature Sensor Selection of T/C and RTD Sensor Types - The Basics of Temperature Measurement using RTDs," Tech. Rep., no. 8500-917A, Wixom, USA.

[109] ATP Instrumentation Ltd, "Pt100 Accuracy and Probe Classification," Available at: https://atp-instrumentation.co.uk/blogs/articles/pt100-accuracy-and-probe-classification, Last Accessed: 02.06.2022.

[110] Fluke Corporation, "Fluke 1586A Super-DAQ Precision Temperature Scanner," Available at: https://www.fluke.com/en-us/product/calibration-tools/temperature-calibrators/fluke-calibration-1586a, Last Accessed: 02.06.2022.

[111] Sylvac SA, "Instruction for use caliper s_cal pro," April 2008, Available at: https://www.sylvac.ch/download-en/manuals/instruction-for-use-caliper-s-cal-pro/viewdocument/1, Last Accessed: 02.06.2022.

[112] P. Lunde, K.-E. Frøysa, and M. Vestrheim, "GARUSO - Version 1.0. Uncertainty model for Multipath Ultrasonic Transit Time Gas Flow Meters," Christian Michelsen Research AS, Bergen, Norway, Tech. Rep. CMR-97-A10014, Sept 1997.

[113] The International Electrotechnical Commission (IEC), "Industrial platinum resistance thermometers and platinum temperature sensors (IEC 60751:2008)," Standard, July 2008, DIN EN 60751:2009-05.

[114] MeterLab, "CMD210 Conductivity meter- Operating instructions," Available at: https://pdf.indiamart.com/impdf/24943910855/MY-96244901/meterlab-cmd-210-conductivity-meter.pdf, Last Accessed: 15.06.2022.

[115] C. C. Leroy, S. P. Robinson, and M. J. Goldsmith, "A new equation for the accurate calculation of sound speed in all oceans," *The Journal of the Acoustical Society of America*, vol. 124, no. 5, pp. 2774–2782.

[116] J. C. Goold, J. D. Bennell, and S. E. Jones, "Sound velocity measurements in spermaceti oil under the combined influences of temperature and pressure," *Deep Sea Research Part I: Oceanographic Research Papers*, vol. 43, no. 7, pp. 961–969, 1996.

[117] S. Mia and N. Ohno, "Relation between low temperature fluidity and sound velocity of lubricating oil," *Tribology international*, vol. 43, no. 5-6, pp. 1043–1047, 2010.

[118] E. Howells and E. Norton, "Parameters affecting the velocity of sound in transformer oil," *IEEE Transactions on Power Apparatus and Systems*, vol. PAS-103, no. 5, pp. 1111–1115, 1984.

[119] J.-L. Daridon and B. Lagourette, "Ultrasonic velocity of liquid tridecane and tetradecane as a function of temperature and pressure," *High Temp.–High Pres*, vol. 32, pp. 83–87, 2000.

[120] Merck, "Lab Water Purification Systems," Available at: https://www.merckmillipore.com/NO/en/products/water-purification/xWqb.qB.E3QAAAE_Rg53.Lxj,nav, Last Accessed: 15.06.2022.

[121] K. V. Mackenzie, "Nine-term equation for sound speed in the oceans," *The Journal of the Acoustical Society of America*, vol. 70, no. 3, pp. 807–812, 1981.

[122] A. B. Coppens, "Simple equations for the speed of sound in neptunian waters," *The Journal of the Acoustical Society of America*, vol. 69, no. 3, pp. 862–863, 1981.

[123] JUMO, "Push-in resistance thermometers in steam-tight version," Available for download: http://www.jumo.no/produkter/sensorer-og-automatisering/temperatur/rtd-temperaturf%C3%B8lere/oversikt-over-rtd-temperaturf%C3%B8lere/902830/jumo-steamtemp-temperaturgiver-rtd-pt100---pt1000-i-vann--og-damptett-utf%C3%B8relse-902830.html, Last Accessed: 30.07.2022.

[124] A. Williams Jr, "The piston source at high frequencies," *The Journal of the Acoustical Society of America*, vol. 23, no. 1, pp. 1–6, 1951.

[125] AnalystPrep, "Key properties of the normal distribution," Oct. 2019, Available at: https://analystprep.com/cfa-level-1-exam/quantitative-methods/key-properties-normal-distribution/, Last Accessed: 12.04.2022.

[126] H. Zhang, Z. Liu, H. Huang, and L. Wang, "Ftsgd: An adaptive stochastic gradient descent algorithm for spark mllib," in *2018 IEEE 16th Intl Conf on Dependable, Autonomic and Secure Computing, 16th Intl Conf on Pervasive Intelligence and Computing, 4th Intl Conf on Big Data Intelligence and Computing and Cyber Science and Technology Congress (DASC/PiCom/DataCom/CyberSciTech)*. IEEE, 2018, pp. 828–835.

Appendix A

Diffraction correction calculations

A.1 Numerical solution of Khimunin's integral for diffraction correction

In this project, two different diffraction correction methods are used in sound velocity calculations. Both approaches are based on Khimunin's diffraction correction integral [48, 49], cf. Section 2.3.1. In order to validate the calculations in this work, the tabulated values found by Khimunin using a BESM-4 computer is compared to own values found using the MATLAB-script presented in Appendix E.1.1. As Khimunin used Simpson's method to calculate the diffraction correction integral, the same approach is used here. The results are provided at the end of this appendix.

Assuming a uniformly vibrating circular plane piston, Khimunin expressed the deviation from plane wave propagation as

$$D^{diff} = \frac{\langle p \rangle_A}{p^{plane}}, \tag{A.1}$$

where $\langle p \rangle_A$ is the averaged free field sound pressure over the surface of a measurement area $A = \pi a^2$ equal to the active surface of the transmitting transducer, at distance $z = d$, and p^{plane} is the plane wave pressure at the same distance. The principle is illustrated in Fig. A.1. The transducer and the measurement area are assumed to be placed in an infinite uniform media without absorption.
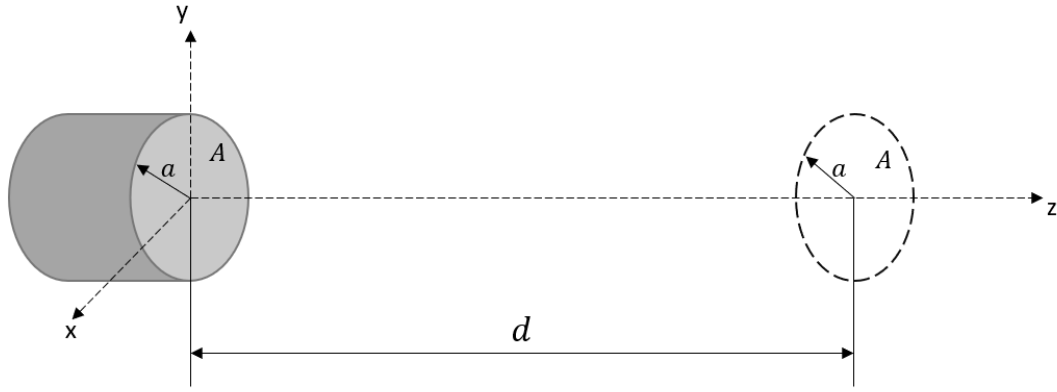
Figure A.1: The active surface of the transducer is placed in the xy-plane with its center at origo. Sound waves propagates along the z-axis towards the measurement area located at $z = d$. The transducer surface and the measurement area are axially concentric.

Using Williams' mathematical description of diffraction from a plane circular piston in an infinite rigid baffle [124], Khimunin derived the following diffraction correction formula, assuming continuous waves:

$$D^{dif}(z, k) = 1 - \frac{4}{\pi} \int_0^{\pi/2} e^{-ikz\left(\sqrt{1+4\left(\frac{a}{z}\right)^2 \cos^2 \theta} - 1\right)} \sin^2 \theta \, d\theta. \tag{A.2}$$

Here, a is the radius of the active surface of the transducer (and the measurement area), $k = \omega/c$ is the wave number and θ is the integration variable. The plane wave term has been extracted from the equation. Moreover, Khimunin expressed the modulus, $|D^{dif}|$, of the diffraction correction as [48]

$$|D^{dif}| = \frac{\langle p(z, k) \rangle_A}{p_p(z, k)} = \sqrt{A^2 + B^2}, \tag{A.3}$$

where A and B are defined as

$$A = 1 - C\frac{4}{\pi}\cos(kz) - D\frac{4}{\pi}\sin(kz) \tag{A.4}$$

and

$$B = D\frac{4}{\pi}\cos(kz) - C\frac{4}{\pi}\sin(kz), \tag{A.5}$$

respectively. The coefficients C and D are given as

$$C = \int_0^{\pi/2} \cos[k\sqrt{z^2 + 4a^2 cos^2\theta}] \sin^2 \theta \, d\theta \tag{A.6}$$

and

$$D = \int_0^{\pi/2} \sin[k\sqrt{z^2 + 4a^2 \cos^2 \theta}] \sin^2 \theta \, d\theta, \tag{A.7}$$

respectively. Khimunin further used Eqs. A.4 amd A.5 to define the phase of the diffraction correction

as [49]

$$\angle D^{dif} = \tan^{-1}\left(\frac{B}{A}\right). \tag{A.8}$$

The modulus and phase of the diffraction correction is found by solving Eqs. A.6 and A.7 numerically. The integrals can be solved using Simpsons integration method, given as [52]

$$\int_a^b f(x)dx \approx \frac{h}{3}\left(f_0 + f_n + 4 \cdot \sum_{i=1,3,5}^{n-1} f_i + 2 \cdot \sum_{i=2,4,6}^{n-2} f_i\right) \tag{A.9}$$

where $[a, b]$ is the integration range, h is the segment size and f is the expression to be integrated.

Khimunin used a constant transducer radius of $a = 10$ mm and a set of i different wave numbers, $k_1, k_2, ..., k_i$, when he calculated the modulus and phase of the diffraction correction. Also, in the tabulated values calculated by Khimunin (Table 6.4b and 6.4b), the ka-number is rounded off. The Fresnel parameter [55], given as

$$S = \frac{2\pi z}{ka^2}, \tag{A.10}$$

is therefore used to calculate the exact values for ka. For example, for $ka = 40$, $a = 10$ mm and $S = 1$, solving Eq. A.10 for z shows that

$$z = \frac{ka \cdot a}{2\pi} \approx 64mm. \tag{A.11}$$

This value for z can further be used to find the exact wave number, given as

$$k = \frac{2\pi z}{Sa^2} = 4.0212 \ mm^{-1}. \tag{A.12}$$

Consequently, the exact ka-number is $ka = 40.212$. Khimunin uses the rounded off ka-values 10, 15, 20, 25, 30, 40, 60, 100, 200, 400 and 1000. He also uses S-values from 0.05 to 10 with different steps. To be consistent, the same values for ka and S are used when the modulus and phase of the diffraction correction is calculated in MATLAB. Khimunin reports an uncertainty of $1 \cdot 10^{-4}$ for the tabulated values.

In the following, four tables are presented. Table A.1 and A.3 provides values calculated by Khimunin for the modulus and phase of the diffraction correction, respectively, while the corresponding values calculated in MATLAB are given Table A.2 and A.4, respectively. The difference between Khimunin's tabulated values and the corresponding values calculated in MATLAB is for the most part within the uncertainty. The biggest deviations is found for low values of S when $ka = 1000$. This applies for both the modulus and the phase of the diffraciton correction. However, in this work, the ka-value lies between 19 at the lowest and 27 at max. In this region, the values are almost identical with a few exceptions. The calculated diffraction correction in this work is therefore assumed to be valid.

Table A.1: Khimunin's tabulated values of the modulus of the diffraction correction. The ka-values are rounded off. The table corresponds to Table 1 in [48].

S \ ka	10	15	20	25	30	40	60	100	200	400	1000
0.05	0.9713	0.9547	0.9625	0.9514	0.9517	0.9546	0.9514	0.9514	0.9512	0.9511	0.9509
0.1	0.9605	0.9308	0.9304	0.9327	0.9324	0.9301	0.9323	0.9308	0.9308	0.9312	0.9318
0.15	0.9473	0.9284	0.9228	0.9229	0.9216	0.9185	0.9188	0.9164	0.9175	0.9165	0.9161
0.2	0.9292	0.9191	0.9104	0.9010	0.9075	0.9068	0.9040	0.9040	0.9056	0.9055	0.9053
0.25	0.9075	0.8969	0.8899	0.9003	0.8914	0.8937	0.8962	0.8937	0.8956	0.8952	0.8950
0.3	0.8862	0.8787	0.8905	0.8837	0.8900	0.8823	0.8863	0.8824	0.8844	0.8851	0.8853
0.35	0.8690	0.8744	0.8846	0.8752	0.8732	0.8809	0.8735	0.8750	0.8770	0.8775	0.8776
0.4	0.8581	0.8774	0.8657	0.8760	0.8685	0.8644	0.8705	0.8713	0.8705	0.8701	0.8701
0.45	0.8534	0.8762	0.8552	0.8606	0.8669	0.8642	0.8578	0.8568	0.8573	0.8577	0.8576
0.5	0.8533	0.8660	0.8572	0.8480	0.8502	0.8569	0.8592	0.8580	0.8569	0.8566	0.8566
0.55	0.8560	0.8501	0.8586	0.8490	0.8431	0.8417	0.8449	0.8473	0.8483	0.8485	0.8487
0.6	0.8587	0.8350	0.8509	0.8509	0.8465	0.8403	0.8367	0.8357	0.8352	0.8355	0.8356
0.65	0.8598	0.8252	0.8367	0.8435	0.8447	0.8430	0.8398	0.8367	0.8367	0.8365	0.8364
0.7	0.8582	0.8219	0.8225	0.8294	0.8335	0.8368	0.8377	0.8376	0.8374	0.8374	0.8375
0.75	0.8536	0.8236	0.8146	0.8166	0.8194	0.8233	0.8262	0.8277	0.8282	0.8283	0.8284
0.8	0.8461	0.8271	0.8131	0.8098	0.8097	0.8111	0.8128	0.8140	0.8146	0.8147	0.8147
0.85	0.8363	0.8297	0.8158	0.8096	0.8069	0.8052	0.8048	0.8049	0.8048	0.8050	0.8050
0.9	0.8250	0.8296	0.8192	0.8127	0.8092	0.8058	0.8038	0.8028	0.8024	0.8024	0.8024
0.95	0.8129	0.8262	0.8207	0.8158	0.8127	0.8092	0.8068	0.8054	0.8049	0.8046	0.8048
1	0.8007	0.8194	0.8190	0.8165	0.8144	0.8119	0.8097	0.8088	0.8083	0.8082	0.8082
1.1	0.7789	0.7996	0.8056	0.8074	0.8077	0.8079	0.8077	0.8076	0.8074	0.8074	0.8074
1.2	0.7632	0.7774	0.7847	0.7882	0.7899	0.7915	0.7927	0.7930	0.7933	0.7933	0.7933
1.3	0.7541	0.7591	0.7642	0.7671	0.7690	0.7706	0.7717	0.7724	0.7727	0.7727	0.7727
1.4	0.7513	0.7474	0.7490	0.7503	0.7514	0.7525	0.7532	0.7536	0.7538	0.7538	0.7539
1.5	0.7531	0.7425	0.7409	0.7408	0.7409	0.7410	0.7412	0.7413	0.7413	0.7413	0.7413
1.6	0.7577	0.7432	0.7393	0.7379	0.7373	0.7366	0.7362	0.7361	0.7358	0.7360	0.7360
1.7	0.7633	0.7473	0.7421	0.7399	0.7388	0.7377	0.7369	0.7366	0.7364	0.7364	0.7364
1.8	0.7689	0.7529	0.7473	0.7448	0.7428	0.7421	0.7411	0.7407	0.7405	0.7404	0.7404
1.9	0.7736	0.7586	0.7531	0.7505	0.7491	0.7478	0.7468	0.7463	0.7461	0.7460	0.7461
2	0.7769	0.7635	0.7584	0.7560	0.7547	0.7534	0.7250	0.7520	0.7518	0.7517	0.7517
2.1	0.7786	0.7670	0.7626	0.7604	0.7592	0.7581	0.7573	0.7568	0.7566	0.7565	0.7565
2.2	0.7787	0.7689	0.7652	0.7633	0.7622	0.7613	0.7605	0.7601	0.7599	0.7599	0.7599
2.3	0.7772	0.7691	0.7660	0.7647	0.7636	0.7627	0.7621	0.7618	0.7616	0.7617	0.7616
2.4	0.7740	0.7677	0.7652	0.7639	0.7630	0.7625	0.7620	0.7618	0.7616	0.7616	0.7615
2.5	0.7699	0.7648	0.7628	0.7617	0.7612	0.7606	0.7602	0.7600	0.7599	0.7599	0.7599
2.6	0.7645	0.7605	0.7590	0.7582	0.7577	0.7573	0.7570	0.7568	0.7567	0.7568	0.7567
2.7	0.7580	0.7551	0.7540	0.7533	0.7530	0.7527	0.7525	0.7523	0.7523	0.7522	0.7522
2.8	0.7508	0.7488	0.7479	0.7474	0.7472	0.7470	0.7468	0.7467	0.7464	0.7466	0.7466
2.9	0.7429	0.7415	0.7409	0.7407	0.7405	0.7403	0.7406	0.7398	0.7401	0.7397	0.7401
3	0.7341	0.7336	0.7333	0.7331	0.7330	0.7329	0.7328	0.7328	0.7327	0.7327	0.7327
3.5	0.6972	0.6881	0.6884	0.6883	0.6886	0.6887	0.6886	0.6887	0.6887	0.6888	0.6888
4	0.6380	0.6394	0.6399	0.6406	0.6404	0.6403	0.6406	0.6406	0.6406	0.6406	0.6406
4.5	0.5915	0.5929	0.5934	0.5936	0.5937	0.5939	0.5938	0.5941	0.5941	0.5941	0.5941
5	0.5488	0.5501	0.5504	0.5507	0.5508	0.5511	0.5511	0.5512	0.5512	0.5512	0.5512
5.5	0.5105	0.5117	0.5120	0.5121	0.5122	0.5124	0.5125	0.5125	0.5125	0.5125	0.5125
6	0.4762	0.4772	0.4775	0.4776	0.4778	0.4779	0.4780	0.4780	0.4780	0.4780	0.4780
6.5	0.4456	0.4466	0.4468	0.4469	0.4470	0.4471	0.4472	0.4472	0.4472	0.4472	0.4472
7	0.4184	0.4191	0.4194	0.4195	0.4196	0.4196	0.4196	0.4197	0.4198	0.4198	0.4197
7.5	0.3940	0.3947	0.3949	0.3949	0.3950	0.3950	0.3950	0.3951	0.3951	0.3951	0.3951
8	0.3722	0.3726	0.3728	0.3729	0.3729	0.3729	0.3730	0.3731	0.3731	0.3731	0.3731
8.5	0.3523	0.3529	0.3530	0.3530	0.3531	0.3531	0.3531	0.3532	0.3532	0.3532	0.3532
9	0.3345	0.3348	0.3350	0.3351	0.3351	0.3351	0.3351	0.3352	0.3352	0.3352	0.3352
9.5	0.3183	0.3186	0.3188	0.3188	0.3188	0.3188	0.3188	0.3189	0.3189	0.3189	0.3189
10	0.3035	0.3037	0.3038	0.3039	0.3039	0.3039	0.3040	0.3040	0.3040	0.3040	0.3040

Table A.2: Modulus of the diffraction correction calculated using MATLAB [73]. The ka-values in the table are rounded off, but the exact values are used in the calculations.

S \ ka	10	15	20	25	30	40	60	100	200	400	1000
0.05	0.9713	0.9547	0.9625	0.9515	0.9516	0.9546	0.9515	0.9514	0.9512	0.9511	0.9514
0.1	0.9604	0.9308	0.9304	0.9326	0.9324	0.9301	0.9322	0.9308	0.9309	0.9312	0.9308
0.15	0.9473	0.9284	0.9228	0.9230	0.9211	0.9185	0.9187	0.9167	0.9175	0.9163	0.9167
0.2	0.9291	0.9191	0.9104	0.9019	0.9075	0.9070	0.9040	0.9040	0.9056	0.9055	0.9040
0.25	0.9075	0.8969	0.8898	0.9002	0.8915	0.8937	0.8962	0.8934	0.8956	0.8952	0.8934
0.3	0.8862	0.8787	0.8905	0.8837	0.8900	0.8823	0.8863	0.8824	0.8844	0.8851	0.8824
0.35	0.8690	0.8744	0.8846	0.8752	0.8734	0.8806	0.8733	0.8750	0.8770	0.8775	0.8750
0.4	0.8580	0.8775	0.8658	0.8760	0.8694	0.8644	0.8705	0.8715	0.8705	0.8701	0.8715
0.45	0.8534	0.8762	0.8552	0.8606	0.8669	0.8641	0.8578	0.8568	0.8573	0.8575	0.8568
0.5	0.8535	0.8660	0.8572	0.8479	0.8502	0.8569	0.8592	0.8580	0.8569	0.8566	0.8580
0.55	0.8561	0.8502	0.8586	0.8490	0.8431	0.8418	0.8448	0.8473	0.8483	0.8486	0.8473
0.6	0.8588	0.8350	0.8509	0.8509	0.8465	0.8403	0.8366	0.8357	0.8355	0.8355	0.8357
0.65	0.8598	0.8252	0.8364	0.8435	0.8448	0.8430	0.8398	0.8377	0.8367	0.8365	0.8377
0.7	0.8583	0.8220	0.8226	0.8294	0.8336	0.8368	0.8378	0.8377	0.8375	0.8375	0.8377
0.75	0.8536	0.8236	0.8145	0.8164	0.8194	0.8233	0.8263	0.8277	0.8282	0.8284	0.8277
0.8	0.8461	0.8271	0.8131	0.8098	0.8097	0.8110	0.8129	0.8140	0.8146	0.8147	0.8140
0.85	0.8363	0.8297	0.8158	0.8095	0.8069	0.8053	0.8049	0.8049	0.8050	0.8050	0.8049
0.9	0.8250	0.8295	0.8192	0.8127	0.8091	0.8058	0.8037	0.8028	0.8025	0.8024	0.8028
0.95	0.8129	0.8261	0.8207	0.8158	0.8126	0.8092	0.8067	0.8054	0.8049	0.8048	0.8054
1	0.8007	0.8194	0.8190	0.8165	0.8144	0.8119	0.8099	0.8088	0.8083	0.8082	0.8088
1.1	0.7789	0.7995	0.8056	0.8073	0.8078	0.8079	0.8077	0.8075	0.8075	0.8074	0.8075
1.2	0.7630	0.7774	0.7848	0.7881	0.7899	0.7915	0.7925	0.7931	0.7933	0.7933	0.7931
1.3	0.7540	0.7590	0.7642	0.7671	0.7687	0.7705	0.7717	0.7724	0.7727	0.7727	0.7724
1.4	0.7513	0.7473	0.7490	0.7504	0.7513	0.7524	0.7532	0.7536	0.7538	0.7539	0.7536
1.5	0.7531	0.7425	0.7410	0.7408	0.7408	0.7410	0.7412	0.7413	0.7413	0.7413	0.7413
1.6	0.7577	0.7432	0.7394	0.7379	0.7372	0.7366	0.7362	0.7361	0.7360	0.7360	0.7361
1.7	0.7633	0.7472	0.7421	0.7399	0.7388	0.7377	0.7369	0.7366	0.7364	0.7364	0.7366
1.8	0.7689	0.7528	0.7473	0.7447	0.7434	0.7421	0.7411	0.7406	0.7404	0.7404	0.7406
1.9	0.7736	0.7586	0.7531	0.7505	0.7492	0.7478	0.7468	0.7463	0.7461	0.7460	0.7463
2	0.7769	0.7635	0.7584	0.7560	0.7547	0.7534	0.7525	0.7520	0.7518	0.7517	0.7520
2.1	0.7786	0.7670	0.7626	0.7604	0.7592	0.7581	0.7572	0.7568	0.7566	0.7566	0.7568
2.2	0.7787	0.7689	0.7651	0.7633	0.7623	0.7612	0.7605	0.7601	0.7600	0.7599	0.7601
2.3	0.7772	0.7691	0.7660	0.7644	0.7636	0.7627	0.7621	0.7618	0.7616	0.7616	0.7618
2.4	0.7742	0.7677	0.7651	0.7639	0.7632	0.7625	0.7620	0.7617	0.7616	0.7616	0.7617
2.5	0.7699	0.7648	0.7628	0.7618	0.7612	0.7606	0.7602	0.7600	0.7599	0.7599	0.7600
2.6	0.7645	0.7606	0.7590	0.7582	0.7578	0.7573	0.7570	0.7568	0.7568	0.7567	0.7568
2.7	0.7581	0.7552	0.7540	0.7534	0.7530	0.7527	0.7525	0.7523	0.7523	0.7523	0.7523
2.8	0.7508	0.7488	0.7479	0.7475	0.7472	0.7470	0.7468	0.7467	0.7467	0.7467	0.7467
2.9	0.7429	0.7416	0.7410	0.7407	0.7405	0.7403	0.7402	0.7401	0.7401	0.7401	0.7401
3	0.7344	0.7337	0.7333	0.7331	0.7330	0.7329	0.7328	0.7328	0.7328	0.7328	0.7328
3.5	0.6872	0.6881	0.6884	0.6886	0.6886	0.6887	0.6887	0.6888	0.6888	0.6888	0.6888
4	0.6381	0.6395	0.6400	0.6403	0.6404	0.6405	0.6406	0.6406	0.6406	0.6406	0.6406
4.5	0.5915	0.5929	0.5934	0.5937	0.5938	0.5939	0.5940	0.5941	0.5941	0.5941	0.5941
5	0.5488	0.5501	0.5506	0.5508	0.5509	0.5511	0.5511	0.5512	0.5512	0.5512	0.5512
5.5	0.5105	0.5116	0.5120	0.5122	0.5123	0.5124	0.5125	0.5125	0.5125	0.5125	0.5125
6	0.4762	0.4772	0.4776	0.4777	0.4778	0.4779	0.4780	0.4780	0.4780	0.4780	0.4780
6.5	0.4457	0.4465	0.4468	0.4470	0.4470	0.4471	0.4472	0.4472	0.4472	0.4472	0.4472
7	0.4184	0.4191	0.4194	0.4195	0.4196	0.4196	0.4197	0.4197	0.4197	0.4197	0.4197
7.5	0.3940	0.3946	0.3949	0.3949	0.3950	0.3951	0.3951	0.3951	0.3951	0.3951	0.3951
8	0.3721	0.3726	0.3728	0.3729	0.3729	0.3730	0.3730	0.3730	0.3730	0.3731	0.3730
8.5	0.3524	0.3528	0.3530	0.3530	0.3531	0.3531	0.3531	0.3532	0.3532	0.3532	0.3532
9	0.3345	0.3349	0.3350	0.3351	0.3351	0.3351	0.3352	0.3352	0.3352	0.3352	0.3352
9.5	0.3183	0.3186	0.3187	0.3188	0.3188	0.3188	0.3189	0.3189	0.3189	0.3189	0.3189
10	0.3035	0.3038	0.3039	0.3039	0.3039	0.3040	0.3040	0.3040	0.3040	0.3040	0.3040

Table A.3: Khimunin's tabulated values of the phase of the diffraction correction. The ka-values are rounded off. The table corresponds to Table 1 in [49].

S \ ka	10	15	20	25	30	40	60	100	200	400	1000
0.05	0.0604	0.0727	0.0575	0.0535	0.0584	0.0537	0.0523	0.0538	0.0532	0.0530	0.0530
0.1	0.0839	0.0780	0.0846	0.0836	0.0819	0.0771	0.0753	0.0765	0.0762	0.0767	0.0762
0.15	0.1116	0.0925	0.0919	0.0943	0.0991	0.0931	0.0956	0.0962	0.0953	0.0941	0.0947
0.2	0.1373	0.1212	0.1209	0.1154	0.1084	0.1094	0.1094	0.1097	0.1119	0.1105	0.1101
0.25	0.1566	0.1416	0.1271	0.1243	0.1291	0.1228	0.1243	0.1275	0.1254	0.1245	0.1243
0.3	0.1677	0.1451	0.1341	0.1463	0.1380	0.1421	0.1366	0.1398	0.1415	0.1413	0.1412
0.35	0.1713	0.1451	0.1589	0.1466	0.1572	0.1505	0.1505	0.1547	0.1543	0.1540	0.1535
0.4	0.1707	0.1559	0.1732	0.1650	0.1581	0.1657	0.1673	0.1625	0.1608	0.1606	0.1605
0.45	0.1701	0.1770	0.1725	0.1839	0.1793	0.1703	0.1714	0.1751	0.1767	0.1769	0.1772
0.5	0.1727	0.1991	0.1770	0.1848	0.1920	0.1921	0.1862	0.1828	0.1817	0.1815	0.1814
0.55	0.1800	0.2141	0.1946	0.1877	0.1909	0.1981	0.2022	0.2024	0.2020	0.2021	0.2020
0.6	0.1921	0.2197	0.2160	0.2041	0.1991	0.1985	0.2016	0.2041	0.2056	0.2055	0.2056
0.65	0.2080	0.2193	0.2308	0.2251	0.2186	0.2126	0.2093	0.2084	0.2083	0.2082	0.2082
0.7	0.2264	0.2180	0.2354	0.2386	0.2370	0.2329	0.2287	0.2264	0.2254	0.2252	0.2251
0.75	0.2454	0.2204	0.2343	0.2423	0.2453	0.2464	0.2455	0.2446	0.2441	0.2439	0.2439
0.8	0.2644	0.2286	0.2336	0.2411	0.2455	0.2497	0.2521	0.2535	0.2533	0.2535	0.2534
0.85	0.2808	0.2421	0.2379	0.2411	0.2443	0.2483	0.2514	0.2531	0.2539	0.2539	0.2539
0.9	0.2954	0.2589	0.2482	0.2468	0.2474	0.2491	0.2510	0.2521	0.2528	0.2528	0.2528
0.95	0.3066	0.2770	0.2632	0.2584	0.2567	0.2558	0.2555	0.2560	0.2561	0.2562	0.2563
1	0.3149	0.2946	0.2806	0.2743	0.2712	0.2685	0.2668	0.2663	0.2660	0.2660	0.2659
1.1	0.3237	0.3229	0.3144	0.3090	0.3061	0.3024	0.2999	0.2986	0.2981	0.2979	0.2979
1.2	0.3248	0.3389	0.3381	0.3360	0.3345	0.3327	0.3314	0.3305	0.3301	0.3301	0.3300
1.3	0.3222	0.3440	0.3489	0.3502	0.3505	0.3508	0.3508	0.3507	0.3505	0.3506	0.3505
1.4	0.3211	0.3429	0.3505	0.3536	0.3554	0.3565	0.3578	0.3582	0.3584	0.3584	0.3586
1.5	0.3233	0.3409	0.3484	0.3520	0.3539	0.3559	0.3573	0.3579	0.3583	0.3584	0.3584
1.6	0.3302	0.3418	0.3475	0.3505	0.3522	0.3540	0.3553	0.3560	0.3562	0.3564	0.3565
1.7	0.3421	0.3471	0.3507	0.3527	0.3539	0.3551	0.3560	0.3566	0.3568	0.3569	0.3568
1.8	0.3583	0.3577	0.3591	0.3600	0.3611	0.3613	0.3617	0.3620	0.3623	0.3622	0.3622
1.9	0.3779	0.3730	0.3725	0.3724	0.3725	0.3726	0.3727	0.3728	0.3728	0.3728	0.3729
2	0.4002	0.3925	0.3901	0.3893	0.3890	0.3886	0.3884	0.3884	0.3884	0.3884	0.3884
2.1	0.4242	0.4139	0.4110	0.4096	0.4089	0.4084	0.4089	0.4077	0.4076	0.4075	0.4076
2.2	0.4494	0.4378	0.4341	0.4324	0.4315	0.4307	0.4302	0.4298	0.4297	0.4296	0.4297
2.3	0.4751	0.4628	0.4587	0.4569	0.4558	0.4548	0.4541	0.4538	0.4536	0.4536	0.4536
2.4	0.5016	0.4884	0.4842	0.4821	0.4812	0.4800	0.4792	0.4788	0.4787	0.4786	0.4786
2.5	0.5270	0.5143	0.5099	0.5079	0.5098	0.5056	0.5049	0.5045	0.5044	0.5043	0.5043
2.6	0.5525	0.5401	0.5357	0.5338	0.5326	0.5315	0.5307	0.5304	0.5301	0.5301	0.5300
2.7	0.5776	0.5655	0.5612	0.5592	0.5582	0.5571	0.5564	0.5559	0.5558	0.5557	0.5557
2.8	0.6021	0.5905	0.5863	0.5843	0.5833	0.5823	0.5815	0.5812	0.5814	0.5810	0.5809
2.9	0.6259	0.6148	0.6108	0.6090	0.6079	0.6069	0.6053	0.6057	0.6056	0.6055	0.6056
3	0.6488	0.6383	0.6346	0.6328	0.6318	0.6309	0.6302	0.6298	0.6297	0.6296	0.6296
3.5	0.7529	0.7449	0.7420	0.7404	0.7399	0.7392	0.7384	0.7384	0.7383	0.7383	0.7383
4	0.8394	0.8328	0.8309	0.8299	0.8295	0.8291	0.8286	0.8283	0.8283	0.8283	0.8283
4.5	0.9105	0.9061	0.9043	0.9036	0.9033	0.9027	0.9028	0.9025	0.9024	0.9024	0.9024
5	0.9702	0.9668	0.9658	0.9649	0.9644	0.9641	0.9640	0.9640	0.9640	0.9640	0.9640
5.5	1.0204	1.0178	1.0169	1.0165	1.0164	1.0159	1.0156	1.0157	1.0156	1.0156	1.0156
6	1.0631	1.0612	1.0604	1.0602	1.0601	1.0597	1.0599	1.0595	1.0595	1.0595	1.0595
6.5	1.1000	1.0983	1.0979	1.0977	1.0974	1.0975	1.0972	1.0971	1.0971	1.0971	1.0971
7	1.1320	1.1308	1.1301	1.1303	1.1299	1.1301	1.1298	1.1298	1.1297	1.1297	1.1299
7.5	1.1602	1.1589	1.1587	1.1587	1.1584	1.1583	1.1583	1.1583	1.1583	1.1583	1.1583
8	1.1850	1.1840	1.1835	1.1834	1.1832	1.1833	1.1834	1.1834	1.1834	1.1834	1.1843
8.5	1.2068	1.2060	1.2059	1.2055	1.2057	1.2054	1.2056	1.2055	1.2055	1.2055	1.2055
9	1.2266	1.2258	1.2255	1.2254	1.2255	1.2254	1.2254	1.2254	1.2254	1.2254	1.2254
9.5	1.2443	1.2435	1.2434	1.2432	1.2433	1.2431	1.2430	1.2432	1.2432	1.2432	1.2432
10	1.2602	1.2596	1.2595	1.2593	1.2594	1.2594	1.2593	1.2593	1.2593	1.2592	1.2592

Table A.4: Phase of the diffraction correction calculated using MATLAB [73]. The ka-values in the table are rounded off, but the exact values are used in the calculations.

S \ ka	10	15	20	25	30	40	60	100	200	400	1000
0.05	0.0603	0.0727	0.0574	0.0535	0.0586	0.0537	0.0522	0.0538	0.0531	0.0531	0.0538
0.1	0.0839	0.0780	0.0846	0.0838	0.0819	0.0771	0.0753	0.0766	0.0764	0.0768	0.0766
0.15	0.1116	0.0925	0.0919	0.0943	0.0991	0.0932	0.0956	0.0963	0.0953	0.0942	0.0963
0.2	0.1373	0.1212	0.1209	0.1150	0.1084	0.1093	0.1095	0.1097	0.1118	0.1105	0.1097
0.25	0.1567	0.1417	0.1272	0.1242	0.1291	0.1228	0.1244	0.1277	0.1254	0.1245	0.1277
0.3	0.1677	0.1451	0.1341	0.1463	0.1380	0.1420	0.1366	0.1398	0.1414	0.1413	0.1398
0.35	0.1712	0.1451	0.1589	0.1466	0.1566	0.1512	0.1502	0.1547	0.1544	0.1540	0.1547
0.4	0.1707	0.1559	0.1732	0.1650	0.1580	0.1658	0.1672	0.1627	0.1609	0.1606	0.1627
0.45	0.1701	0.1770	0.1725	0.1839	0.1793	0.1703	0.1714	0.1751	0.1767	0.1771	0.1751
0.5	0.1726	0.1991	0.1770	0.1849	0.1921	0.1921	0.1862	0.1828	0.1817	0.1815	0.1828
0.55	0.1799	0.2141	0.1946	0.1877	0.1910	0.1982	0.2021	0.2025	0.2022	0.2021	0.2025
0.6	0.1920	0.2198	0.2160	0.2041	0.1991	0.1985	0.2016	0.2041	0.2052	0.2055	0.2041
0.65	0.2080	0.2192	0.2306	0.2249	0.2189	0.2125	0.2093	0.2084	0.2083	0.2083	0.2084
0.7	0.2264	0.2179	0.2354	0.2386	0.2370	0.2329	0.2287	0.2264	0.2254	0.2251	0.2264
0.75	0.2455	0.2204	0.2343	0.2424	0.2454	0.2464	0.2456	0.2446	0.2441	0.2440	0.2446
0.8	0.2640	0.2286	0.2336	0.2410	0.2455	0.2497	0.2521	0.2530	0.2533	0.2534	0.2530
0.85	0.2809	0.2421	0.2379	0.2411	0.2443	0.2483	0.2514	0.2531	0.2537	0.2539	0.2531
0.9	0.2952	0.2589	0.2482	0.2468	0.2474	0.2491	0.2510	0.2521	0.2526	0.2528	0.2521
0.95	0.3066	0.2771	0.2632	0.2584	0.2567	0.2558	0.2558	0.2560	0.2561	0.2562	0.2560
1	0.3151	0.2947	0.2807	0.2743	0.2712	0.2685	0.2669	0.2663	0.2660	0.2660	0.2663
1.1	0.3238	0.3230	0.3145	0.3090	0.3058	0.3024	0.2999	0.2986	0.2981	0.2980	0.2986
1.2	0.3247	0.3390	0.3381	0.3361	0.3346	0.3328	0.3313	0.3305	0.3301	0.3301	0.3305
1.3	0.3225	0.3441	0.3489	0.3502	0.3506	0.3508	0.3507	0.3507	0.3506	0.3506	0.3507
1.4	0.3211	0.3429	0.3505	0.3537	0.3553	0.3568	0.3578	0.3582	0.3584	0.3585	0.3582
1.5	0.3233	0.3409	0.3484	0.3520	0.3540	0.3559	0.3573	0.3580	0.3583	0.3584	0.3580
1.6	0.3303	0.3416	0.3475	0.3506	0.3523	0.3540	0.3553	0.3560	0.3563	0.3563	0.3560
1.7	0.3422	0.3471	0.3507	0.3527	0.3539	0.3552	0.3561	0.3566	0.3568	0.3568	0.3566
1.8	0.3584	0.3578	0.3591	0.3600	0.3606	0.3613	0.3618	0.3620	0.3622	0.3622	0.3620
1.9	0.3780	0.3731	0.3725	0.3725	0.3725	0.3726	0.3728	0.3728	0.3729	0.3729	0.3728
2	0.4002	0.3921	0.3901	0.3893	0.3890	0.3887	0.3885	0.3884	0.3883	0.3883	0.3884
2.1	0.4242	0.4140	0.4109	0.4096	0.4090	0.4083	0.4079	0.4077	0.4076	0.4076	0.4077
2.2	0.4494	0.4378	0.4341	0.4324	0.4315	0.4307	0.4301	0.4298	0.4297	0.4296	0.4298
2.3	0.4752	0.4628	0.4587	0.4568	0.4558	0.4548	0.4541	0.4537	0.4536	0.4536	0.4537
2.4	0.5011	0.4885	0.4841	0.4821	0.4811	0.4800	0.4792	0.4789	0.4787	0.4787	0.4789
2.5	0.5270	0.5144	0.5099	0.5079	0.5068	0.5057	0.5049	0.5045	0.5044	0.5043	0.5045
2.6	0.5526	0.5401	0.5357	0.5337	0.5326	0.5315	0.5307	0.5303	0.5302	0.5301	0.5303
2.7	0.5776	0.5656	0.5613	0.5593	0.5582	0.5571	0.5563	0.5559	0.5558	0.5557	0.5559
2.8	0.6021	0.5905	0.5863	0.5844	0.5833	0.5823	0.5816	0.5812	0.5810	0.5810	0.5812
2.9	0.6259	0.6148	0.6108	0.6089	0.6079	0.6069	0.6062	0.6058	0.6057	0.6056	0.6058
3	0.6490	0.6384	0.6346	0.6328	0.6318	0.6309	0.6302	0.6298	0.6297	0.6296	0.6298
3.5	0.7529	0.7449	0.7420	0.7407	0.7400	0.7392	0.7387	0.7385	0.7383	0.7383	0.7385
4	0.8391	0.8332	0.8310	0.8300	0.8295	0.8290	0.8286	0.8284	0.8283	0.8283	0.8284
4.5	0.9106	0.9061	0.9045	0.9037	0.9033	0.9029	0.9026	0.9025	0.9024	0.9024	0.9025
5	0.9702	0.9668	0.9655	0.9650	0.9647	0.9644	0.9641	0.9640	0.9640	0.9640	0.9640
5.5	1.0205	1.0178	1.0169	1.0164	1.0162	1.0159	1.0158	1.0157	1.0156	1.0156	1.0157
6	1.0633	1.0612	1.0604	1.0601	1.0599	1.0597	1.0596	1.0595	1.0595	1.0595	1.0595
6.5	1.1001	1.0985	1.0979	1.0976	1.0974	1.0973	1.0972	1.0971	1.0971	1.0971	1.0971
7	1.1322	1.1308	1.1303	1.1301	1.1300	1.1298	1.1298	1.1297	1.1297	1.1297	1.1297
7.5	1.1602	1.1591	1.1587	1.1585	1.1584	1.1583	1.1582	1.1582	1.1582	1.1582	1.1582
8	1.1849	1.1840	1.1836	1.1835	1.1834	1.1833	1.1833	1.1832	1.1832	1.1832	1.1832
8.5	1.2069	1.2061	1.2058	1.2057	1.2056	1.2056	1.2055	1.2055	1.2055	1.2055	1.2055
9	1.2265	1.2259	1.2256	1.2255	1.2255	1.2254	1.2254	1.2253	1.2253	1.2253	1.2253
9.5	1.2442	1.2436	1.2434	1.2433	1.2433	1.2432	1.2432	1.2432	1.2432	1.2431	1.2432
10	1.2601	1.2596	1.2595	1.2594	1.2593	1.2593	1.2593	1.2593	1.2592	1.2592	1.2593

A.2   Influence of transducer radius and transducer distance on diffraction correction

Diffraction correction is the main contributor to the correction term t^{corr} in Eqs. 2.36 and 2.52. It is also one of the main contributors to the total uncertainty of the measured sound velocity. Consequently, the influence of the transducer radius a and transducer distance L on diffraction correction is investigated further in this appendix.

The diffraction correction is calculated according to the two methods explained in Section 2.3.1. The diffraction correction's dependency on transducer radius and transducer distance is dependent on which method is used. For Method 1, an increase in diffraction correction is obtained by decreasing a and increasing L. Contrastingly, for Method 2, an increase in diffraction correction is obtained by increasing a and decreasing L.

Four figures are presented in the following, illustrating how the diffraction correction varies due to changes in a and L. Fig. A.2 shows how the diffraction correction calculated using Method 1 is dependent on a, while keeping L constant. Fig. A.3 shows how the diffraction correction calculated using Method 1 is dependent on L, while keeping a constant. Fig. A.4 shows how the diffraction correction calculated using Method 2 is dependent on a, while keeping L constant. Fig. A.5 shows how the diffraction correction calculated using Method 2 is dependent on L, while keeping a constant. In Fig. A.3 and A.5, the transducer radius is set to be $a = 9.705$ mm, which corresponds to the mean of the measured effective transducer radius of the transmitting transducer. In Fig. A.2 and A.4, the transducer distance is set to be 125.002 mm, which corresponds to the transducer distance at 25° C. In all four figures, the frequency of the sound waves is set to be 500 kHz, and the sound velocity is 1500 m/s. The calculations are performed in MATLAB, using the script presented in Appendix E.1.2.
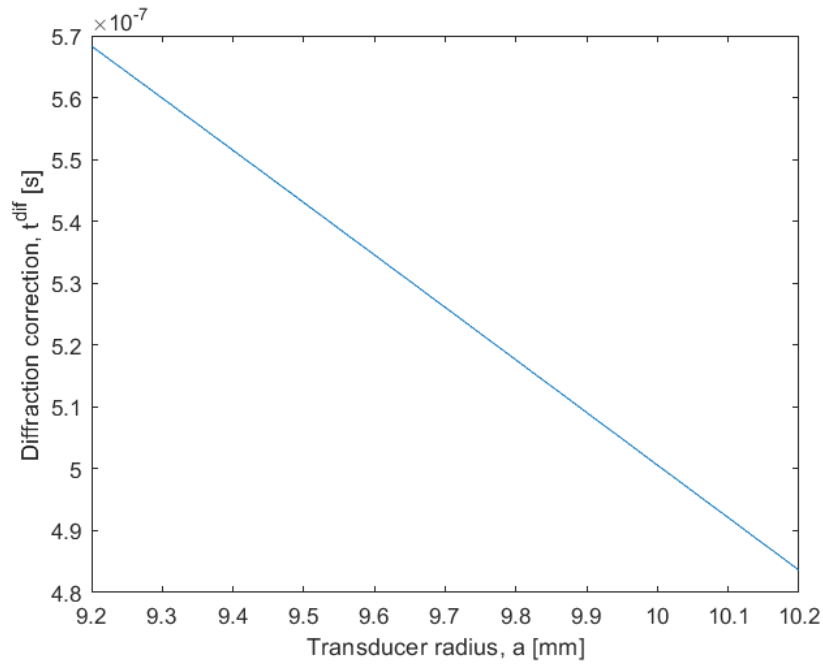
Figure A.2: Diffraction correction calculated using Method 1 as a function of transducer radius values from 9.2 mm to 10.2, covering all measured effective transducer radii. The transducer distance is set to be 125.002 mm, with the sound waves having frequency 500 kHz and propagating at 1500 m/s.
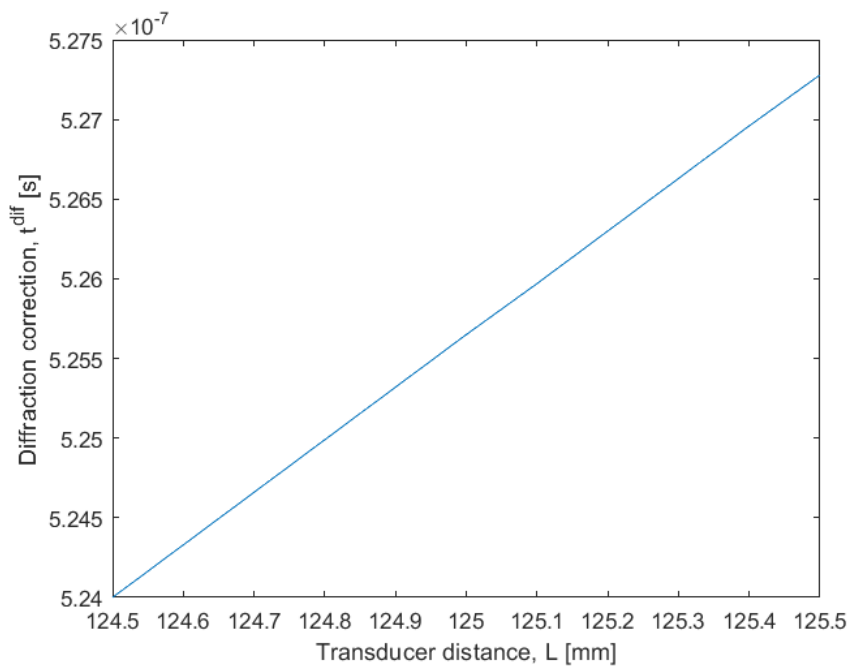
Figure A.3: Diffraction correction calculated using Method 1 as a function of transducer distance values from 124.5 mm to 125.5 mm, covering all transducer distances in this work. The transducer radius is set to be 9.705 mm, with the sound waves having frequency 500 kHz and propagating at 1500 m/s.
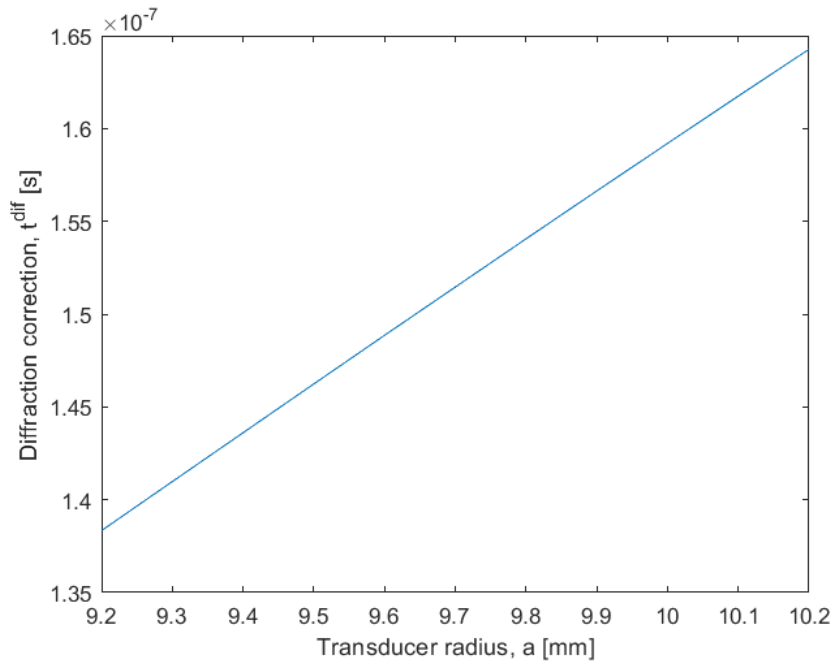
Figure A.4: Diffraction correction calculated using Method 2 as a function of transducer radius values from 9.2 mm to 10.2, covering all measured effective transducer radii. The transducer distance is set to be 125.002 mm, with the sound waves having frequency 500 kHz and propagating at 1500 m/s.
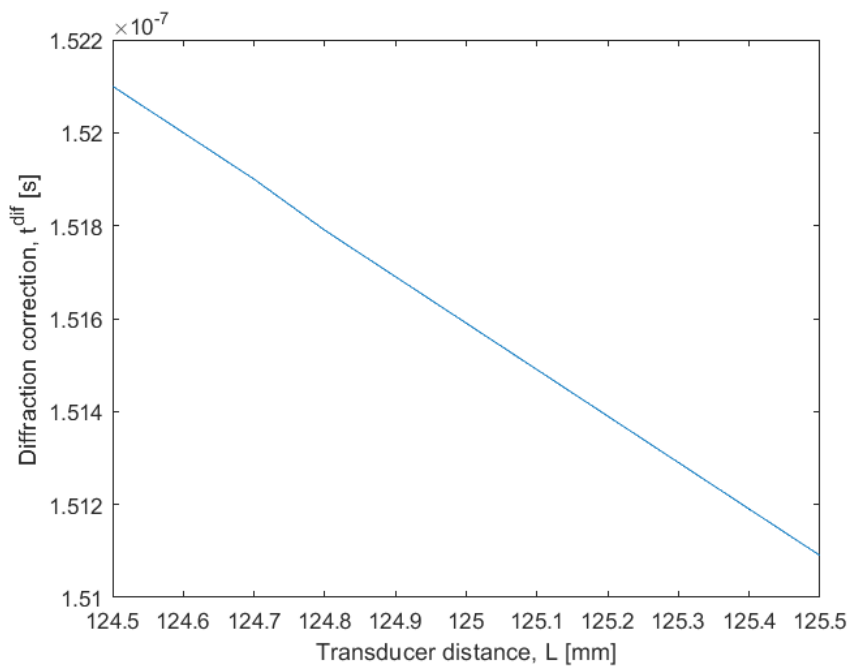
Figure A.5: Diffraction correction calculated using Method 2 as a function of transducer distance values from 124.5 mm to 125.5 mm, covering all transducer distances in this work. The transducer radius is set to be 9.705 mm, with the sound waves having frequency 500 kHz and propagating at 1500 m/s.

Appendix B

Test form certificates for transducers

B.1 Test form certificate for transmitting transducer

B.2   Test form certificate for receiving transducer

OLYMPUS

Tel: 781-419-3900
www.olympus-ims.com

TRANSDUCER DESCRIPTION

PART NO.: V318
SERIAL NO: 1339737
DESIGNATION: IMMERSION

FREQUENCY: 0.50 MHz
ELEMENT SIZE: .75 in. DIA.

TEST INSTRUMENTATION

FLAW DETECTOR: Epoch 600; S/N: 130527005
TEST PROGRAM: TP103-4
CABLE: RG-58 A/U LENGTH: 4FT

TEST CONDITIONS

PULSER SETTING: Energy: 100 Volt; Damping: 400 Ohm; Shape: Spike
RECEIVER SETTING: Gain: 44 dB; Filter: DC - 10.0 MHz
TARGET: 5.0 IN. SILICA   WATER PATH: 1.011 in
JOB CODE: TP210

MEASUREMENTS PER ASTM E1065

WAVEFORM DURATION:
  -14DB LEVEL -- 2.873 US
  -20DB LEVEL -- 3.312 US
  -40DB LEVEL -- 4.274 US

SPECTRUM MEASURANDS:
  CENTER FREQ. ----- 0.54 MHz
  PEAK FREQENCY -- 0.51 MHz
  -6DB BANDWIDTH -- 82.33 %
        F#: 0.5

COMMENTS:

SPECTRUM BASED ON GATED PORTION OF SIGNAL AS MARKED

** ACCEPTED

TECHNICIAN (14)   DATE: 09-07-2021

This Certificate may not be reproduced except in full without written approval of OSSA

SIGNAL WAVEFORM

(VOLT)
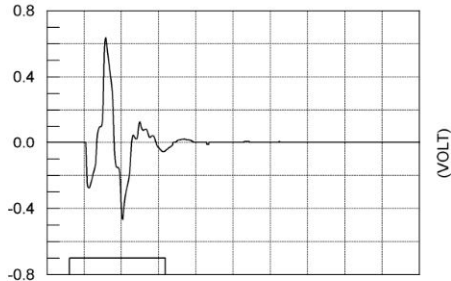
(2 USEC / DIVISON)

FREQUENCY SPECTRUM

0.32   0.76

(MHz)
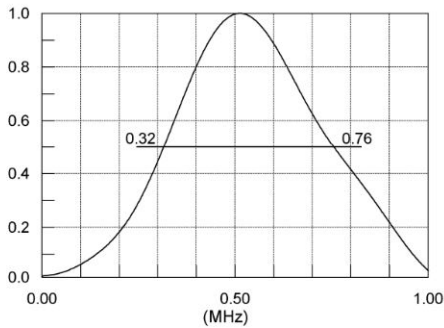
TP103 Rev. A

Appendix C

Uncertainty standards

One of the main goals in this thesis is to create a measurement cell which is capable of measuring the sound velocity in liquids with a relative expanded uncertainty (95% confidence level) of 1000 ppm at max. Consequently, correct treatment of uncertainties are both important and necessary. To clarify the uncertainty notations and calculations used in this work, some uncertainty standards are given in this appendix. All uncertainty calculations follows *ISO GUM* [105].

C.1 Evaluation of uncertainties

Evaluation of uncertainty is often separated into type A evaluation of uncertainty and type B evaluation of uncertainty. While type A evaluation of uncertainty concerns statistical methods used on data collected from a series of measurements, type B evaluation is essentially data collected from anything but the experiment itself.

C.1.1 Type A evaluation of uncertainty

According to ISO GUM, an uncertainty is classified as a type A uncertainty if the uncertainty is evaluated from statistics such as the arithmetic mean, standard deviation and degrees of freedom. The arithmetic mean is the average value of a set of measurements. It is given as [105]

$$\bar{x} = \frac{1}{n} \sum_{i=1}^{n} x_i \tag{C.1}$$

where n is the number of independent repeated observations and x_i are the individual observations. The individual observations will differ in value because of random variations such as noise. The arithmetic mean can be used to calculate the standard deviation, σ, given as [105]

$$\sigma = \sqrt{\frac{1}{n-1} \sum_{i=1}^{n} (x_i - \bar{x})^2} \tag{C.2}$$

The standard deviation characterizes the dispersion about the mean value.

In addition to calculating the arithmetic mean and the standard deviation, the degrees of freedom, v, should always be included in type A uncertainty evaluations. It is defined as the number of values that can vary freely in the final calculation of a statistic:

$$v = n - 1 \tag{C.3}$$

It can be used to estimate coverage factors and determine confidence intervals.

C.1.2 Type B evaluation of uncertainty

Type B evaluation of uncertainty concerns uncertainty contributions from non-experimental factors. Some examples are datasheets, calibration reports, manuals from manufacturer, industry guides and other available information. More often than not, the confidence level for type B uncertainties are not available. In such cases, one have to assume a coverage factor for the uncertainty. Normally, a coverage factor $k = 2$ (95% confidence level) can be assumed for most type B uncertainties [105]. However, if there are no available information about the uncertainty of an instrument, or the instrument is very worn, it might be more reasonable to assume $k = 1$ (68% confidence level). In this work, $k = 2$ is mainly assumed, but with some exceptions.

C.1.3 Combined standard uncertainty

Both type A and type B uncertainties are included in the combined uncertainty of a measurement. If a type B uncertainty has a given confidence level, division by the associated coverage factor results in the corresponding standard uncertainty. For type A uncertainties, the standard uncertainty corresponds to the standard deviation divided by the square root of the number of independent repeated observations [105]:

$$u(\bar{x}) = \frac{\sigma}{\sqrt{n}} \tag{C.4}$$

If a parameter $y = f(x_1, x_2, ..., x_N)$ is measured using more than one instrument, or is calculated from a formula containing several other measured parameters, the standard uncertainty of each such term, x_i, $i = 1, 2, ..., N$, can be used to find the combined standard uncertainty of y, given as [105]

$$u_c(y) = \sqrt{\sum_{i=1}^{N} \left(\frac{\partial f}{\partial x_i} \right)^2 u^2(x_i)} \tag{C.5}$$

Here, $u^2(x_i)$ is the standard uncertainty and $\frac{\partial f}{\partial x_i}$ is the sensitivity coefficient for term number i. The squared product of the standard uncertainty and the sensitivity coefficient is equal to the variance of term number i. In other words, the combined standard uncertainty of a parameter y is equal to the

square root of the sum of variances constituting $u_c(y)$.

Further, the combined expanded uncertainty, $U(y)$ of y can be found by multiplying the combined standard uncertainty by a coverage factor, k, i.e.

$$U(y) = u_c(y) \cdot k, \tag{C.6}$$

where $k = 2$ for a 95% confidence level. This corresponds to the *absolute* combined expanded uncertainty at 95% confidence level. Additionally, the *relative* combined standard uncertainty can be found by dividing $u_c(y)$ by y, i.e.

$$E_y = \frac{u_c(y)}{y}. \tag{C.7}$$

C.2   Uncertainty distributions

Confidence levels and coverage factors for various measurements are given together with a *probability distribution*. The probability distribution of a measurement is the mathematical function that describes the probabilities of occurrence of various outcomes for said measurement (KILDE). The most common probability distributions are the *normal* distribution and the *rectangular* distribution, which will be explained in the following.

C.2.1   Normal distribution

When an uncertainty is specified to have a 95% confidence level with coverage factor $k = 2$, it means that there is a 95% chance that a measured value will lie within 95% of a *normal* distribution. A normal distribution is a continuous probability distribution for a random variable with real value. They are regularly used in statistics to represent such random variables whose distributions are unknown [94]. Measurement errors often have distributions that are nearly normal. This is due to the central limit theorem. It states that a sum of independent random variables converges towards a normal distribution when the number of variables goes to infinity (KILDE). The shape of the normal distribution is shown in Fig. C.1.
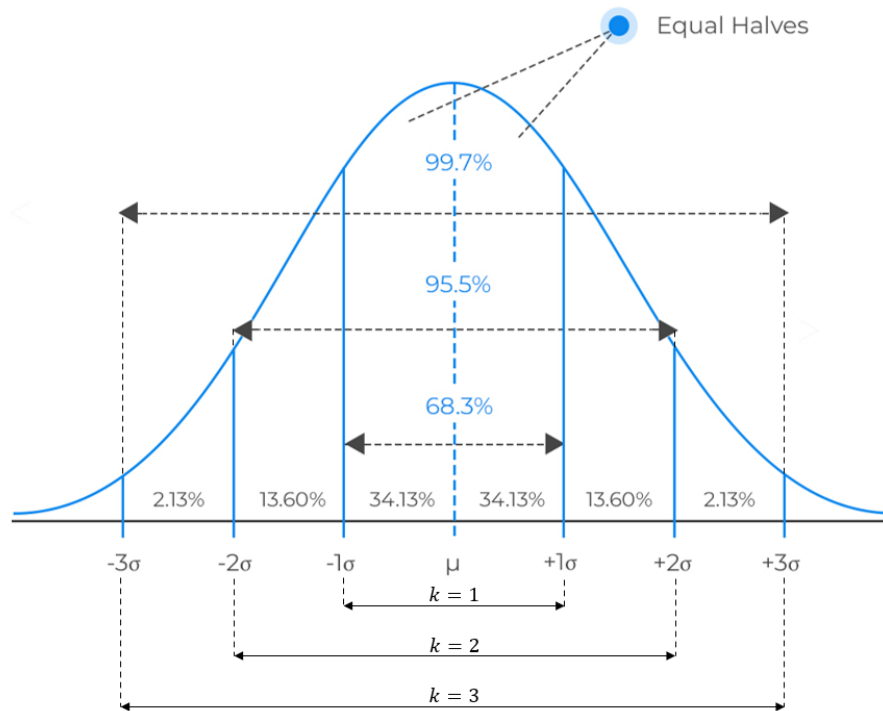
Figure C.1: Normal distribution with coverage factors and corresponding number of standard deviations from the mean. The normal distribution is symmetric, and is split into two equal halves. The figure is a modified version of the figure found in [125].

As indicated in Fig. C.1, about 68% of values in a normal distribution is less than one standard deviation away from the mean. Similarly, two standard deviations from the mean covers about 95% of the values, and about 99.7% of values are within three standard deviations. In other words, a coverage factor of $k = 1$ corresponds to approximately a 68% confidence level; $k = 2$ corresponds to approximately a 95% confidence level; and $k = 3$ corresponds to approximately a 99.7% confidence level. This is known as the 68-95-99.7 empirical rule [126].

C.2.2 Rectangular distribution

A rectangular distribution has determined bounds where an arbitrary outcome is 100% certain to lie between these bounds. All possible outcomes are equally probable in a rectangular distribution [105]. If the bounds of the distribution are $\pm a$, a measurement x_i will have values of $-a < x < +a$ with a 100% confidence level and coverage factor $\sqrt{3}$ [94]. The rectangular distribution is illustrated in Fig. C.2.
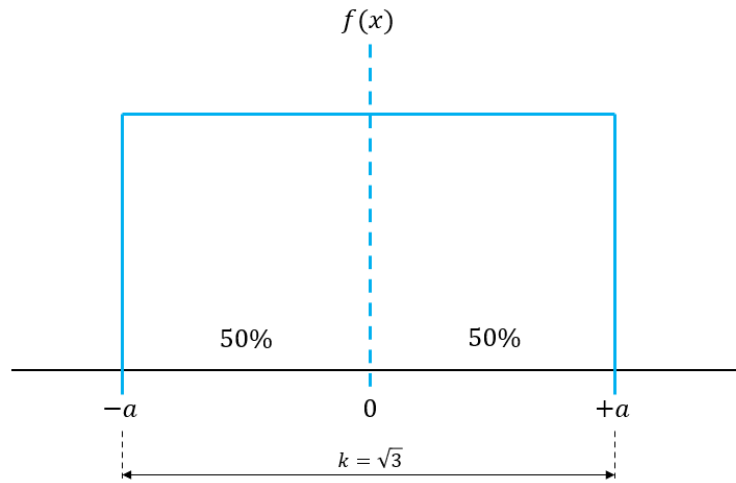
Figure C.2: Rectangular distribution with coverage factor $k = \sqrt{3}$.

Appendix D

The UNESCO-algorithm

The UNESCO-algorithm consists of the following set of Equations [11, 12]:

$$
\begin{aligned}
c(S, T, P) = \quad & Cw(T,P) + A(T,P)S + B(T,P)S^{3/2} + D(T,P)S^2 \\[2ex]
Cw(T, P) = \quad & \left(C_{00} + C_{01}T + C_{02}T^2 + C_{03}T^3 + C_{04}T^4 + C_{05}T^5\right) + \\
& \left(C_{10} + C_{11}T + C_{12}T^2 + C_{13}T^3 + C_{14}T^4\right)P + \\
& \left(C_{20} + C_{21}T + C_{22}T^2 + C_{23}T^3 + C_{24}T^4\right)P^2 + \\
& \left(C_{30} + C_{31}T + C_{32}T^2\right)P^3 \\[2ex]
A(T, P) = \quad & \left(A_{00} + A_{01}T + A_{02}T^2 + A_{03}T^3 + A_{04}T^4\right) + \\
& \left(A_{10} + A_{11}T + A_{12}T^2 + A_{13}T^3 + A_{14}T^4\right)P + \\
& \left(A_{20} + A_{21}T + A_{22}T^2 + A_{23}T^3\right)P^2 + \\
& \left(A_{30} + A_{31}T + A_{32}T^2\right)P^3 \\[2ex]
B(T, P) = \quad & B_{00} + B_{01}T + (B_{10} + B_{11}T)P \\[2ex]
D(T, P) = \quad & D_{00} + D_{10}P,
\end{aligned}
\tag{D.1}
$$

where T is temperature in degrees Celsius, P is hydrostatic pressure in bar and S is salinity in Practical Salinity Units (parts per thousand). The numerical values of the coefficients are given in Table D.1.

Table D.1: Numerical values for the coefficients in Eq. D.1 [12].

Coefficients	Numerical values	Coefficients	Numerical values
C_{00}	1402.388	A_{02}	$7.166 \cdot 10^{-5}$
C_{01}	5.03830	A_{03}	$2.008 \cdot 10^{-6}$
C_{02}	$-5.81090 \cdot 10^{-2}$	A_{04}	$-3.21 \cdot 10^{-8}$
C_{03}	$3.3432 \cdot 10^{-4}$	A_{10}	$9.4742 \cdot 10^{-5}$
C_{04}	$-1.47797 \cdot 10^{-6}$	A_{11}	$-1.2583 \cdot 10^{-5}$
C_{05}	$3.1419 \cdot 10^{-9}$	A_{12}	$-6.4928 \cdot 10^{-8}$
C_{10}	0.153563	A_{13}	$1.0515 \cdot 10^{-8}$
C_{11}	$6.8999 \cdot 10^{-4}$	A_{14}	$-2.0142 \cdot 10^{-10}$
C_{12}	$-8.1829 \cdot 10^{-6}$	A_{20}	$-3.9064 \cdot 10^{-7}$
C_{13}	$1.3632 \cdot 10^{-7}$	A_{21}	$9.1061 \cdot 10^{-9}$
C_{14}	$-6.1260 \cdot 10^{-10}$	A_{22}	$-1.6009 \cdot 10^{-10}$
C_{20}	$3.1260 \cdot 10^{-5}$	A_{23}	$7.994 \cdot 10^{-12}$
C_{21}	$-1.7111 \cdot 10^{-6}$	A_{30}	$1.100 \cdot 10^{-10}$
C_{22}	$2.5986 \cdot 10^{-8}$	A_{31}	$6.651 \cdot 10^{-12}$
C_{23}	$-2.5353 \cdot 10^{-10}$	A_{32}	$-3.391 \cdot 10^{-13}$
C_{24}	$1.0415 \cdot 10^{-12}$	B_{00}	$-1.922 \cdot 10^{-2}$
C_{30}	$-9.7729 \cdot 10^{-9}$	B_{01}	$-4.42 \cdot 10^{-5}$
C_{31}	$3.8513 \cdot 10^{-10}$	B_{10}	$7.3637 \cdot 10^{-5}$
C_{32}	$-2.3654 \cdot 10^{-12}$	B_{11}	$1.7950 \cdot 10^{-7}$
A_{00}	1.389	D_{00}	$1.727 \cdot 10^{-3}$
A_{01}	$-1.262 \cdot 10^{-2}$	D_{10}	$-7.9836 \cdot 10^{-6}$

D.1   Sensitivity coefficients for the uncertainty of the UNESCO-algorithm

The uncertainty of the UNESCO-algorithm is found by differentiating Eq. D.1 with respect to salinity, S, temperature, T, and pressure, P. The sensitivity coefficients are given in the following:

Sound velocity differentiated with respect to salinity

$$\frac{\partial c}{\partial S} = \frac{\partial Cw}{\partial S} + \frac{\partial A \cdot S}{\partial S} + \frac{\partial B \cdot S^{3/2}}{\partial S} + \frac{\partial D \cdot S^2}{\partial S}$$

$$\frac{\partial Cw}{\partial S} = 0$$

$$\frac{\partial A \cdot S}{\partial S} = \left(A_{00} + A_{01} T + A_{02} T^2 + A_{03} T^3 + A_{04} T^4 \right) +$$
$$\left(A_{10} + A_{11} T + A_{12} T^2 + A_{13} T^3 + A_{14} T^4 \right) P +$$
$$\left(A_{20} + A_{21} T + A_{22} T^2 + A_{23} T^3 \right) P^2 +$$
$$\left(A_{30} + A_{31} T + A_{32} T^2 \right) P^3$$

(D.2)

$$\frac{\partial B \cdot S^{3/2}}{\partial S} = \frac{3}{2} \left(B_{00} + B_{01} T + (B_{10} + B_{11} T) P \right) S^{1/2}$$

$$\frac{\partial D \cdot S^2}{\partial S} = 2 \left(D_{00} + D_{10} P \right) S$$

Sound velocity differentiated with respect to temperature

$$\frac{\partial c}{\partial T} = \frac{\partial Cw}{\partial T} + \frac{\partial A}{\partial T} S + \frac{\partial B}{\partial T} S^{3/2} + \frac{\partial D}{\partial T} S^2$$

$$\frac{\partial Cw}{\partial T} = \left(C_{01} + 2C_{02} T + 3C_{03} T^2 + 4C_{04} T^3 + 5C_{05} T^4 \right) +$$
$$\left(C_{11} + 2C_{12} T + 3C_{13} T^2 + 4C_{14} T^3 \right) P +$$
$$\left(C_{21} + 2C_{22} T + 3C_{23} T^2 + 4C_{24} T^3 \right) P^2 +$$
$$\left(C_{31} + 2C_{32} T \right) P^3$$

$$\frac{\partial A}{\partial T} = \left(A_{01} + 2A_{02} T + 3A_{03} T^2 + 4A_{04} T^3 \right) +$$
$$\left(A_{11} + 2A_{12} T + 3A_{13} T^2 + 4A_{14} T^3 \right) P +$$
$$\left(A_{21} + 2A_{22} T + 3A_{23} T^2 \right) P^2 +$$
$$\left(A_{31} + 2A_{32} T \right) P^3$$

(D.3)

$$\frac{\partial B}{\partial T} = B_{01} + B_{11} P$$

$$\frac{\partial D}{\partial T} = 0$$

Sound velocity differentiated with respect to pressure

$$\frac{\partial c}{\partial P} = \quad \frac{\partial Cw}{\partial P} + \frac{\partial A}{\partial P} S + \frac{\partial B}{\partial P} S^{3/2} + \frac{\partial D}{\partial P} S^2$$

$$\begin{aligned} \frac{\partial Cw}{\partial P} = \quad & \left(C_{10} + C_{11} T + C_{12} T^2 + C_{13} T^3 + C_{14} T^4 \right) + \\ & 2 \left(C_{20} + C_{21} T + C_{22} T^2 + C_{23} T^3 + C_{24} T^4 \right) P + \\ & 3 \left(C_{30} + C_{31} T + C_{32} T^2 \right) P^2 \end{aligned}$$

$$\begin{aligned} \frac{\partial A}{\partial P} = \quad & \left(A_{10} + A_{11} T + A_{12} T^2 + A_{13} T^3 + A_{14} T^4 \right) + \\ & 2 \left(A_{20} + A_{21} T + A_{22} T^2 + A_{23} T^3 \right) P + \\ & 3 \left(A_{30} + A_{31} T + A_{32} T^2 \right) P^2 \end{aligned} \tag{D.4}$$

$$\frac{\partial B}{\partial P} = \quad B_{10} + B_{11} T$$

$$\frac{\partial D}{\partial P} = \quad D_{10}$$

The numerical values of the coefficients are given in Table D.1.

Appendix E

MATLAB-scripts

E.1 Diffraction correction

E.1.1 Khimunin_test.m

```matlab
1   clear all, close all, clc
2
3   %%%% KHIMUNIN TEST %%%%
4
5   a = 9.50e-3; %Transducer radius [mm]
6   n = 10000; %Number of steps for simpson integration
7   theta = 0:(pi/2)/n:pi/2; %Angle [rad]
8
9   f = 500000; %Frequency [Hz]
10  w = 2*pi*f; %Angular frequency [rad/s]
11  c = 1500; %Sound Velocity [m/s]
12  k = w/c; %Wave number [m^-1]
13
14  %k = [1.0053, 1.5079, 2.0106, 2.5133, 3.0159, 4.0212, 6.0319,...
15  %    10.053, 20.106, 40.212, 10.053]; %Wave number [m^-1]
16
17  %ka = [5 10 20 50 100]; %ka-number
18  ka = 100;
19
20  S = 0:0.005:5; %Dimensionless distance
21
22  %Besselfunctions:
23  J0 = besselj(0,2*pi./S);
24  J1 = besselj(1,2*pi./S);
25
26
27  %The diffraction correction calculated numerically by using k, a and z as
28  %variables. The equation implemented: (3) page 174 (Khimunin, 1972).
29
30  for l = 1:length(S)
31      for j = 1:length(k)
32
33          %Find z from equation for S:
34          z(l,j) = S(l) * k(j) * a^2 / (2*pi);
35
36      for m = 1:length(theta)
37
38          %The function which is to be integrated, calculated at m number
39          %of values of theta.
40
41           C(l,m) = cos(k*(z(l)^2+4*a^2*(cos(theta(m)))^2)^0.5)*(sin(theta(m)))^2;
42           D(l,m) = sin(k*(z(l)^2+4*a^2*(cos(theta(m)))^2)^0.5)*(sin(theta(m)))^2;
43
44
45          %Diffraction correction calculated by using eq. 5.40 in PHYS373
46          %lecture notes (for comparison)
47          h(l,m) = exp(-i*((ka^2*S(l))/(2*pi)) * ((1+((4*pi)/(S(l)*ka))^2 * ...
48              (cos(theta(m)))^2)^0.5-1))*(sin(theta(m)))^2;
49
50      end
51
52      %Numerical calculation of the integrals C and D
53
54      C_sum(l) = ((C(l,1))+ 2*sum(C(l,(3:2:end-2)))+ 4*sum(C(l,(2:2:end)))+ ...
55          C(l,length(theta)))*theta(2)/3;
55      D_sum(l) = ((D(l,1))+ 2*sum(D(l,(3:2:end-2)))+ 4*sum(D(l,(2:2:end)))+ ...
56          D(l,length(theta)))*theta(2)/3;
56
57      A(l) = 1 - C_sum(l)*4/pi*cos(k*z(l))-D_sum(l)*4/pi*sin(k*z(l));
```

```matlab
58        B(l) = D_sum(l)*4/pi*cos(k*z(l))-C_sum(l)*4/pi*sin(k*z(l));
59
60        %Diffraction correction (amplitude and phase) from eq. (3) in Khimunin, 1972.
61        Dne_abs(l)  =(A(l)^2+B(l)^2)^0.5;
62        Dne_phase(l) = atan(B(l)./A(l));
63
64        %Total diffraction correction from eq. (5.40) in PHYS373 lecture notes.
65        Dneh(l) = 1 - 4/pi*theta(2)*(sum(h(l,:))-0.5*(h(l,1)+h(l,length(theta))));
66
67
68    end
69 end
70
71 %Amplitude and phase of diffraction correction from eq. (5.40) in PHYS373
72 %lecture notes.
73 Dneh_abs = abs(Dneh);
74 Dneh_phase = atan(imag(Dneh)./real(Dneh));
75
76
77
78 plot(S,Dneh_abs)
79 xlabel("S")
80 ylabel("Amplitude")
81 f1 = figure;
82 plot(S,Dneh_phase)
83 xlabel("S")
84 ylabel("Phase [rad]")
```

E.1.2 Diffraction_M1vM2.m

```matlab
1  clear all, close all, clc
2
3  %Script used to investigate the difference in diffraction correction
4  %between Method 1 and Method 2, and to find the uncertainty of the
5  %diffraction correction.
6
7
8  freq = 500000; %Frequency [Hz
9  w = 2*pi*freq; %Angular frequency [rad/s]
10 c_uncorr = 1492.1; %Uncorrected sound velocity [m/s]
11 k = 2*pi*freq./c_uncorr; %Wavenumber [m^-1]
12 a_eff = 9.52e-3; %Effective transducer radius [m]
13 n = 10000; %Number of steps for Simpson integration
14 theta = 0:(pi/2)/n:(pi/2); %Angles [rad]
15 z_1way = 125.018e-3; % Length between transducers [m]
16 z_3way = 3*z_1way;
17 %z_1way = linspace(12.5e-3 - 1e-3, 12.5e-3 + 1e-3, length(c_uncorr));
18 h = (theta(end) - theta(1))/n;
19
20
21 for m = 1:length(theta)
22     D_diff_A_integral(m) = ...
           exp(-1i*k*z_1way*((sqrt(1+4*(a_eff/(z_1way))^2*(cos(theta(m)))^2))-1))...
23         *(sin(theta(m)))^2; %Diff.corr. integral for signal A
24     D_diff_B_integral(m) = ...
           exp(-1i*k*z_3way*((sqrt(1+4*(a_eff/(z_3way))^2*(cos(theta(m)))^2))-1))...
25         *(sin(theta(m)))^2; %Diff.corr. integral for signal B
26 end
27
28 D_diff_A = 1 - 4/pi*(4*sum(D_diff_A_integral(3:2:end-1)) + ...
       2*sum(D_diff_A_integral(2:2:end-2)) + D_diff_A_integral(1) + ...
       D_diff_A_integral(length(theta)))*h/3; %Diff.corr for signal A
29 phase_diff_A = angle(D_diff_A); %Angle of diff.corr for signal A
30 t_diff_A = phase_diff_A./w; %Time shift due to diffraction for signal A
31
32 %D_diff_B = D_diff_A; %Diff.corr for signal B
33 D_diff_B = 1 - 4/pi*(4*sum(D_diff_B_integral(3:2:end-1)) + ...
       2*sum(D_diff_B_integral(2:2:end-2)) + D_diff_B_integral(1) + ...
       D_diff_B_integral(length(theta)))*h/3; %Diff.corr for signal B
34 phase_diff_B = angle(D_diff_B); %Angle of diff.corr for signal B
35 t_diff_B = phase_diff_B./w; %Time shift due to diffraction for signal B
36
37
38 total_diff = t_diff_B-t_diff_A
```

E.2 Sound field simulations

E.2.1 beampropagation.m

```matlab
1  clear all, close all, clc
2  %%%%% This script simulates propagation of the side lobes in the
```

```matlab
 3   % measurement cell using ray tracing %%%%%
 4
 5   %%% Joachim Gjesdal Kristensen, 09.05.21 %%%
 6
 7
 8   %%% Dimensions of the cell %%%
 9   trans_hei = 31.75e-3; % Transducer height [m]
10   trans_pen = 15.875e-3; % Transducer penetration depth [m]
11   %cell_volume = 0.5*10^-3; %[m^3]
12   cell_length = 0.125 + 2*trans_pen; %[m]
13   cell_width = 0.057;   %[m]
14   trans_dia_OD = 19.05e-3; % Nominal diameter of active surface of transducer [m]
15   trans_rad = 19.05e-3/2; % Nominal radius of active surface of transducer [m]
16
17
18   c_sample = 1593; %Sound velocity in sample [m/s]
19   f = 500000; %Frequency [Hz]
20   w = 2*pi*f; %Angular frequency [rad/s]
21   rayleigh_distance = pi*(trans_rad)^2*f/c_sample % [m]
22
23
24   %%%%% Calculate the angles of the lobes %%%%%
25   theta_1 = asind(5.15/(w*trans_rad/c_sample)); %MAX sidelobe 1
26   theta_2 = asind(8.42/(w*trans_rad/c_sample)); %MAX sidelobe 2
27   theta_3 = asind(11.62/(w*trans_rad/c_sample)); %MAX sidelobe 3
28   theta_4 = asind(14.70/(w*trans_rad/c_sample)); %MAX sidelobe 4
29
30   node_1 = asind(3.83/(w*trans_rad/c_sample)); %First node
31   node_2 = asind(7.02/(w*trans_rad/c_sample)); %Second node
32   node_3 = asind(10.17/(w*trans_rad/c_sample)); %Third node
33   node_4 = asind(13.32/(w*trans_rad/c_sample)); %Fourth node
34   node_5 = asind(16.47/(w*trans_rad/c_sample)); %Fifth node
35
36   %%% Angles for the complete lobes %%%
37   %angle_2 = [0:2:node_1]; %To investigate the whole main lobe
38   %angle_2 = [node_1:(node_2-node_1)/6:node_2]; %To investigate the whole first sidelobe
39   %angle_2 = [node_2:(node_3-node_2)/6:node_3]; %To investigate the whole second sidelobe
40   %angle_2 = [node_3:(node_4-node_3)/6:node_4]; %To investigate the whole third sidelobe
41   %angle_2 = [node_4:(node_5-node_4)/6:node_5]; %To investigate the whole fourth sidelobe
42
43   %angle_2 = [theta_1,theta_2,theta_3,theta_4]; %To investigate only maximums
44   angle_2 = [20.723] %Shortest 1 way
45   %angle_2 = [6.155] %Shortest 3 way
46   %angle_2 = [5]; %For testing
47
48
49
50   %%%%% Colours for plotting %%%%%
51   b = [0 0.4470 0.7410];
52   o = [0.8500 0.3250 0.0980];
53   y = [0.9290 0.6940 0.1250];
54   p = [0.4940 0.1840 0.5560];
55   g = [0.4660 0.6740 0.1880];
56   lb = [0.3010 0.7450 0.9330];
57   r = [0.6350 0.0780 0.1840];
58
59   vector_colors = {b,o,y,p,g,lb,r,b,o,y,p,g,lb,r,b,o,y,p,g,lb,r,b,o,y,p,g,lb,r};
60
61   angle_1 = 90 - angle_2; %Angle with respect to horizontal axis
62
63
64
65   %%%%% Plotting shape of measurement cell %%%%%
66   plot((cell_width/2+(trans_dia_OD/2)), trans_pen)
67   hold on
68   xlabel("Width of cell [m]")
69   ylabel("Length of cell [m]")
70   xlim([0,cell_width])
71   ylim([0,cell_length])
72   plot((cell_width/2-(trans_dia_OD/2)), trans_pen)
73   line([cell_width/2-(trans_dia_OD/2), cell_width/2+(trans_dia_OD/2)],...
74       [trans_pen, trans_pen])
75   line([cell_width/2-(trans_dia_OD/2), cell_width/2+(trans_dia_OD/2)],...
76       [cell_length-trans_pen, cell_length-trans_pen])
77   line([cell_width/2-(trans_dia_OD/2), cell_width/2-(trans_dia_OD/2)],...
78       [0,trans_pen])
79   line([cell_width/2+(trans_dia_OD/2), cell_width/2+(trans_dia_OD/2)],...
80       [0,trans_pen])
81   line([cell_width/2-(trans_dia_OD/2), cell_width/2-(trans_dia_OD/2)],...
82       [cell_length,cell_length-trans_pen])
83   line([cell_width/2+(trans_dia_OD/2), cell_width/2+(trans_dia_OD/2)],...
84       [cell_length,cell_length-trans_pen])
85
86   % Temperature sensor:
87   % line([0.047, 0.047], [0,0.03])
88   % line([0.05, 0.05], [0,0.03])
89   % line([0.047,0.05], [0.03,0.03])
90
91
92   %%%%% Caculating propagation time for main lobe %%%%%
93   t_main_dir = (cell_length-(2*trans_pen)) / c_sample; %direct
94   t_main_ref = 3*t_main_dir; %reflected
95
96
97   corner_1 = atand((cell_length-trans_pen)/(cell_width/2)); %Angle from transducer to top ...
        right corner
98
99
100
101  %%%%% RAY TRACING %%%%%
102  for i = 1:length(angle_2)
103
104
105      timeABD(i) = 0;
```

```
106        timeABE(i) = 0;
107        timeGHI(i) = 0;
108        timeGHIJL(i) = 0;
109        timeGHIJM(i) = 0;
110        timeGR(i) = 0;
111        timeGRSTU(i) = 0;
112        timeGY(i) = 0;
113        timeGYZB1(i) = 0;
114        timeGYZC1(i) = 0;
115        timeGE1F1G1I1(i) = 0;
116        timeGE1F1G1J1(i) = 0;
117
118
119
120        %Finding the beams that hits upper wall first
121        if angle_1(i) > corner_1
122            prop_1(i) = (cell_length-trans_pen) / (tand(angle_1(i))); %Horizontal distance ...
                   from transducer
123            plot([cell_width/2,cell_width/2 + prop_1(i)], ...
                   [trans_pen,cell_length],"color",vector_colors{i});
124            lengthA(i) = sqrt((prop_1(i))^2 + (cell_length-trans_pen)^2);
125            timeA(i) = lengthA(i)/c_sample;
126            corner_2(i) = atand(cell_length / (cell_width/2 - prop_1(i))); %Angle from ...
                   first reflection to bottom right corner
127
128            if angle_1(i) < corner_2(i) %TR1
129                prop_2(i) = (cell_width/2 - prop_1(i)) * (tand(angle_1(i))); %Vertical ...
                       distance from top to right after first reflection
130                plot([cell_width/2 + ...
                       prop_1(i),cell_width],[cell_length,cell_length-prop_2(i)],"color",...
131                    vector_colors{i});
132                lengthB(i) = sqrt((cell_width-(cell_width/2 + prop_1(i)))^2 + prop_2(i)^2);
133                timeB(i) = lengthB(i)/c_sample;
134                prop_4(i) = (cell_length-prop_2(i)) / (tand(angle_1(i))); %Horizontal ...
                       distance from right towards transducer after second reflection
135
136
137                if prop_4(i) < (cell_width/2 - trans_rad) %TRB
138                    prop_3(i) = (cell_length - prop_2(i)) / tand(angle_1(i)); %Horizontal ...
                           distance from right towards transducer after second reflection
139                    plot([cell_width - prop_3(i), cell_width], [0, cell_length - ...
                           prop_2(i)],"color",vector_colors{i})
140                    lengthC(i) = sqrt((prop_3(i))^2 + (cell_length-prop_2(i))^2);
141                    timeC(i) = lengthC(i)/c_sample;
142                    timeABC(i) = timeA(i) + timeB(i) + timeC(i);
143
144
145                    %Here I find the shortest time for a signal (in a sidelobe)
146                    %to the receiver after 3way propagation. This time
147                    %will then be used to find the maximum pulselength.
148                    % prop_X(i) = (cell_width/2 - trans_rad - prop_3(i)) * tand(angle_1(i));
149                    % plot([cell_width/2+trans_rad,cell_width-prop_3(i)], ...
150                    %     [prop_X(i),0],"color",vector_colors{i})
151                    % lengthK1(i) = sqrt((((cell_width-prop_3(i))...
152                    %     -(cell_width/2+trans_rad))^2 + (prop_X(i))^2);
153                    % timeK1(i) = lengthK1(i)/c_sample;
154                    % timeABCK1(i) = timeA(i) + timeB(i) + timeC(i) + timeK1(i);
155
156
157                else %TRB
158                    prop_5(i) = cell_length - prop_2(i) - trans_pen; %Vertical distance ...
                           from right to trans_pen after second reflection
159                    prop_6(i) = prop_5(i) / tand(angle_1(i)); %Horizontal distance from ...
                           right towards transducer
160
161                    if prop_6(i) < (cell_width/2 - trans_rad) %TRB2
162                        hos_1(i) = cell_width/2 - trans_rad - prop_6(i);
163                        mot_1(i) = hos_1(i) * tand(angle_1(i));
164                        prop_7(i) = trans_pen - mot_1(i);
165                        plot([cell_width/2 + trans_rad, cell_width], ...
                               [prop_7(i),cell_length-prop_2(i)],"color",vector_colors{i})
166                        lengthD(i) = sqrt((cell_width - (cell_width/2 + trans_rad))^2 + ...
                               (cell_length-prop_2(i) - prop_7(i))^2);
167                        timeD(i) = lengthD(i)/c_sample;
168                        timeABD(i) = timeA(i)+timeB(i)+timeD(i);
169
170                    else %(if prop_6(i) > (cell_width/2 - trans_rad)) %TRTr1
171                        prop_7(i) = (cell_width/2 + trans_rad) - prop_6(i); %Horizontal ...
                               distance from left transducer side to where beam cross ...
                               transducer top
172                        plot([cell_width/2 - trans_rad + prop_7(i), cell_width], ...
                               [trans_pen, cell_length-prop_2(i)], "color",vector_colors{i})
173                        lengthE(i) = sqrt((prop_6(i))^2 + ...
                               ((cell_length-prop_2(i))-trans_pen)^2);
174                        timeE(i) = lengthE(i)/c_sample;
175                        timeABE(i) = timeA(i) + timeB(i) + timeE(i);
176                    end
177
178                end
179
180            else %TB1
181                prop_2(i) = (cell_length) / tand(angle_1(i)); %Vertical distance from top ...
                       to bottom after first reflection
182                plot([cell_width/2 + prop_1(i), cell_width/2 + prop_1(i) + prop_2(i)], ...
                       [cell_length, 0], "color",vector_colors{i})
183                lengthF(i) = sqrt((prop_2(i))^2 + (cell_length)^2);
184                timeF(i) = lengthF(i)/c_sample;
185                timeAF(i) = timeA(i) + timeF(i);
186
187            end
188
189
190        %Finding the beams that hits the right wall first
```

```
191        else
192            prop_1(i) = (cell_width/2) * (tand(angle_1(i))); %Vertical distance from ...
                   trans_pen to first reflection on right wall
193            plot([cell_width/2, cell_width], [trans_pen, trans_pen + ...
                   prop_1(i)],"color",vector_colors{i})
194            lengthG(i) = sqrt((cell_width/2)^2 + (prop_1(i))^2);
195            timeG(i) = lengthG(i)/c_sample;
196            prop_2(i) = (cell_length-trans_pen-prop_1(i)) / tand(angle_1(i)); %Horizontal ...
                   distance from right wall towards transducer
197
198            if prop_2(i) < (cell_width/2 - trans_rad) % RT1
199                plot([cell_width, cell_width-prop_2(i)], [trans_pen+prop_1(i), ...
                       cell_length], "color",vector_colors{i})
200                lengthH(i) = sqrt((prop_2(i))^2 + (cell_length-trans_pen-prop_1(i))^2);
201                timeH(i) = lengthH(i)/c_sample;
202                prop_5(i) = cell_width/2 - trans_rad - prop_2(i);
203                prop_6(i) = prop_5(i) * tand(angle_1(i));
204
205                if prop_6(i) < trans_pen %RT7 + RT8
206                    plot([cell_width/2+trans_rad, ...
                           cell_width-prop_2(i)],[cell_length-prop_6(i),cell_length], ...
                           "color",vector_colors{i})
207                    lengthI(i) = sqrt(((cell_width-prop_2(i))-(cell_width/2+trans_rad))^2 + ...
                           (prop_6(i))^2);
208                    timeI(i) = lengthI(i)/c_sample;
209                    timeGHI(i) = timeG(i) + timeH(i) + timeI(i);
210                    prop_10(i) = (cell_width/2 - trans_rad) * tand(angle_1(i));
211                    plot([cell_width/2+trans_rad, cell_width],[cell_length-prop_6(i), ...
                           cell_length-prop_6(i)-prop_10(i)], "color",vector_colors{i})
212                    lengthJ(i) = sqrt((cell_width/2 - trans_rad)^2 + (prop_10(i))^2);
213                    timeJ(i) = lengthJ(i)/c_sample;
214                    prop_11(i) = (cell_length-prop_6(i)-prop_10(i)) / tand(angle_1(i));
215
216                    if prop_11(i) < (cell_width/2 - trans_rad) %RT8
217                        plot([cell_width-prop_11(i),cell_width],[0,cell_length-prop_6(i)...
                               -prop_10(i)], "color",vector_colors{i})
218                        lengthK(i) = sqrt((prop_11(i))^2 + ...
219                               (cell_length-prop_6(i)-prop_10(i))^2);
220                        timeK(i) = lengthK(i)/c_sample;
221                        timeGHIJK(i) = timeG(i) + timeH(i) + timeI(i) + timeJ(i) + timeK(i);
222
223
224                    else %(if prop_11(i) > (cell_width/2 - trans_rad))    RT8
225                        prop_12(i) = cell_length-prop_6(i)-prop_10(i)-trans_pen;
226                        prop_13(i) = prop_12(i) / tand(angle_1(i));
227
228                        if prop_13(i) < cell_width/2 - trans_rad %RT8
229                            hos_4(i) = cell_width/2 - trans_rad - prop_13(i);
230                            mot_4(i) = hos_4(i) * tand(angle_1(i));
231                            plot([cell_width/2+trans_rad,cell_width], ...
                                   [trans_pen-mot_4(i),cell_length-prop_6(i)-prop_10(i)], ...
                                   "color",vector_colors{i})
232                            lengthL(i) = sqrt((cell_width/2-trans_rad)^2 + ...
                                   ((cell_length-prop_6(i)-prop_10(i))-(trans_pen-mot_4(i)))^2)
233                            timeL(i) = lengthL(i)/c_sample;
234                            timeGHIJL(i) = timeG(i) + timeH(i) + timeI(i) + timeJ(i) + ...
                                   timeL(i);
235
236                        else %(prop_13(i) > cell_width/2 - trans_rad)    RT7 + RT8 + RT9
237                            prop_14(i) = prop_13(i) - (cell_width/2 - trans_rad);
238                            plot([cell_width-prop_13(i), cell_width],[trans_pen,...
                                   cell_length-prop_6(i)-prop_10(i)],"color",vector_colors{i})
239                            lengthM(i) = sqrt((prop_13(i))^2 + ...
                                   ((cell_length-prop_6(i)-prop_10(i))-(trans_pen))^2);
240                            timeM(i) = lengthM(i)/c_sample;
241                            timeGHIJM(i) = timeG(i) + timeH(i) + timeI(i) + timeJ(i) + ...
                                   timeM(i);
242
243
244                        end
245
246                    end
247
248
249                else %(prop_6(i) > trans_pen) %RT7
250                    prop_7(i) = cell_width-prop_2(i);
251                    prop_8(i) = prop_7(i) * tand(angle_1(i));
252
253                    if prop_8(i) < cell_length %RT7
254                        plot([cell_width-prop_2(i), 0], [cell_length, ...
                               cell_length-prop_8(i)],"color",vector_colors{i})
255                        lengthN(i) = sqrt((cell_width-prop_2(i))^2 + (prop_8(i))^2);
256                        timeN(i) = lengthN(i)/c_sample;
257                        prop_9(i) = (cell_length - prop_8(i)) / tand(angle_1(i));
258                        plot([0,prop_9(i)], [cell_length-prop_8(i), ...
                               0],"color",vector_colors{i})
259                        lengthO(i) = sqrt((prop_9(i))^2 + (cell_length - prop_8(i))^2);
260                        timeO(i) = lengthO(i)/c_sample;
261                        timeGHNO(i) = timeG(i) + timeH(i) + timeN(i) + timeO(i);
262
263
264                    else %(if prop_8(i) > cell_length)  RT10
265                        prop_9(i) = (cell_length - trans_pen) / tand(angle_1(i));
266
267                        if prop_9(i) > (cell_width/2 + trans_rad - prop_2(i)) %RT7 + RT10
268                            prop_10(i) = trans_pen / tand(angle_1(i));
269                            plot([cell_width-prop_2(i)-prop_9(i)-prop_10(i), ...
                                   cell_width-prop_2(i)],[0,cell_length],"color",vector_colors{i})
270                            lengthP(i) = sqrt((prop_9(i) + prop_10(i))^2 + cell_length^2);
271                            timeP(i) = lengthP(i)/c_sample;
272                            timeGHP(i) = timeG(i) + timeH(i) + timeP(i);
273
274                        else %(prop_9(i) < (cell_width/2 + trans_rad - prop_2(i)))
275                            prop_11(i) = (cell_length - trans_pen) / tand(angle_1(i));
```

```matlab
276                 plot([cell_width-prop_2(i)-prop_11(i), cell_width-prop_2(i)],...
277                     [trans_pen,cell_length],"color",vector_colors{i})
278                 lengthQ(i) = sqrt((prop_11(i))^2 + (cell_length - trans_pen)^2);
279                 timeQ(i) = lengthQ(i)/c_sample;
280                 timeGHQ(i) = timeG(i) + timeH(i) + timeQ(i);
281
282                 end
283
284
285             end
286
287         end
288
289     else %RT2   (if prop_2(i) > (cell_width/2 - trans_rad))
290         prop_3(i) = cell_length - 2*trans_pen - prop_1(i); %Vertical distance from ...
                first reflection up towards trans_pen
291         prop_4(i) = prop_3(i) / tand(angle_1(i)); %Horizontal distance from right ...
                wall towards upper transducer
292
293         if prop_4(i) < (cell_width/2 - trans_rad) %RT2 + RT5 + RT6
294             hos_1(i) = cell_width/2 - trans_rad - prop_4(i);
295             mot_1(i) = hos_1(i) * tand(angle_1(i));
296             plot([cell_width, cell_width/2 + trans_rad], [trans_pen+prop_1(i), ...
                    cell_length-trans_pen+mot_1(i)], "color",vector_colors{i})
297             lengthR(i) = sqrt((cell_width/2 - trans_rad)^2 + ...
                    ((cell_length-trans_pen+mot_1(i))-(trans_pen+prop_1(i)))^2)
298             timeR(i) = lengthR(i)/c_sample;
299             timeGR(i) = timeG(i) + timeR(i);
300             hos_2(i) = (trans_pen - mot_1(i)) / tand(angle_1(i)); %Horizontal ...
                    distance from rigth transducer wall towards right cell wall
301             plot([cell_width/2 + trans_rad, cell_width/2 + trans_rad + ...
                    hos_2(i)],[cell_length-trans_pen+mot_1(i),cell_length], ...
                    "color",vector_colors{i})
302             lengthS(i) = sqrt((hos_2(i))^2 + (trans_pen - mot_1(i))^2);
303             timeS(i) = lengthS(i)/c_sample;
304             mot_2(i) = (cell_width/2 - trans_rad - hos_2(i)) * tand(angle_1(i)); ...
                    %Vertical distance from top along right wall
305             plot([cell_width/2+trans_rad+hos_2(i), cell_width],[cell_length, ...
                    cell_length-mot_2(i)],  "color",vector_colors{i})
306             lengthT(i) = sqrt((cell_width - (cell_width/2+trans_rad+hos_2(i)))^2 + ...
                    (mot_2(i))^2);
307             timeT(i) = lengthT(i)/c_sample;
308             hos_3(i) = (cell_length - mot_2(i) - trans_pen) / tand(angle_1(i));   %RT6
309
310
311             if hos_3(i) < cell_width/2 + trans_rad %RT16
312                 plot([cell_width-hos_3(i),cell_width],[trans_pen,...
313                     cell_length-mot_2(i)],"color",vector_colors{i})
314                 lengthU(i) = sqrt((hos_3(i))^2 + ((cell_length-mot_2(i))-trans_pen)^2);
315                 timeU(i) = lengthU(i)/c_sample;
316
317             else %(if hos_3(i) > cell_width/2 + trans_rad) RT6
318                 hos_4(i) = trans_pen / tand(angle_1(i));
319
320                 if cell_width > hos_3(i)+hos_4(i) && hos_3(i)+hos_4(i) > ...
                        cell_width/2 + trans_rad % RT6
321                     plot([cell_width-hos_3(i)-hos_4(i), cell_width],[0, ...
                            cell_length-mot_2(i)], "color",vector_colors{i})
322                     lengthV(i) = sqrt((hos_3(i) + hos_4(i))^2 + ...
                            (cell_length-mot_2(i))^2);
323                     timeV(i) = lengthV(i)/c_sample;
324                     timeGRSTV(i) = timeG(i) + timeR(i) + timeS(i) + timeT(i) + ...
                            timeV(i);
325
326                 else %(hos_3(i)+hos_4(i) > cell_width) RT6
327                     mot_3(i) = cell_width * tand(angle_1(i))
328                     plot([0, cell_width],[cell_length-mot_2(i)-mot_3(i), ...
                            cell_length-mot_2(i)],"color",vector_colors{i})
329                     lengthW(i) = sqrt((cell_width)^2 + (mot_3(i))^2);
330                     timeW(i) = lengthW(i)/c_sample;
331
332                     prop_25(i) = cell_length - mot_2(i) - mot_3(i);
333                     prop_26(i) = prop_25(i) / tand(angle_1(i)); %IF-statement for ...
                            prop_26?
334                     plot([0,prop_26(i)],[prop_25(i),0],"color",vector_colors{i})
335                     lengthX(i) = sqrt((prop_25(i))^2 + (prop_26(i))^2);
336                     timeX(i) = lengthX(i)/c_sample;
337                     timeGRSTWX(i) = timeG(i) + timeR(i) + timeS(i) + timeT(i) + ...
                            timeW(i) + timeX(i);
338
339                 end
340
341
342             end
343
344         elseif cell_width/2 - trans_rad < prop_4(i) && prop_4(i) < cell_width/2 + ...
                trans_rad %RT3
345             plot([cell_width, cell_width-prop_4(i)],[trans_pen+prop_1(i), ...
                    trans_pen+prop_1(i)+prop_3(i)], "color",vector_colors{i})
346             lengthY(i) = sqrt((prop_3(i))^2 + (prop_4(i))^2);
347             timeY(i) = lengthY(i)/c_sample;
348             timeGY(i) = timeG(i) + timeY(i);
349             prop_20(i) = (cell_width - prop_4(i)) * tand(angle_1(i));
350             plot([0,cell_width-prop_4(i)],[cell_length-trans_pen-prop_20(i),...
351                 cell_length-trans_pen],"color",vector_colors{i})
352
353             lengthZ(i) = sqrt((cell_width-prop_4(i))^2 + (prop_20(i))^2);
354             timeZ(i) = lengthZ(i)/c_sample;
355             prop_21(i) = (cell_length-trans_pen-prop_20(i)) / tand(angle_1(i)); ...
                    %RT11 + RT12 + RT13
356
357             if prop_21(i) < cell_width/2 - trans_rad %RT12
```

```
358                    plot([0,prop_21(i)], [cell_length-trans_pen-prop_20(i), 0], ...
                           "color",vector_colors{i})
359                    lengthA1(i) = sqrt((prop_21(i))^2 + ...
                           (cell_length-trans_pen-prop_20(i))^2);
360                    timeA1(i) = lengthA1(i)/c_sample;
361                    timeGYZA1(i) = timeG(i) + timeY(i) + timeZ(i) + timeA1(i);
362
363                else  %(if prop_21(i) > cell_width/2 - trans_rad)    RT11 + RT12
364                    prop_22(i) = (prop_21(i) - (cell_width/2 - trans_rad)) * ...
                           tand(angle_1(i));
365
366                    if prop_22(i) < trans_pen %RT11
367                        plot([0,cell_width/2 - ...
                               trans_rad],[cell_length-trans_pen-prop_20(i),prop_22(i)],...
368                           "color",vector_colors{i})
369                        lengthB1(i) = sqrt((cell_width/2 - trans_rad)^2 + ...
                               ((cell_length-trans_pen-prop_20(i))-(prop_22(i)))^2);
370                        timeB1(i) = lengthB1(i)/c_sample;
371                        timeGYZB1(i) = timeG(i) + timeY(i) + timeZ(i) + timeB1(i);
372
373                    else %(if prop_22(i) > trans_pen)    %RT13
374                        prop_23(i) = prop_22(i) - trans_pen;
375                        prop_24(i) = prop_23(i) / tand(angle_1(i));
376
377                        if prop_24(i) < trans_dia_OD %RT13
378                        plot([0, cell_width/2-trans_rad+prop_24(i)],[cell_length...
379                           -trans_pen-prop_20(i),trans_pen],"color",vector_colors{i})
380                        lengthC1(i) = sqrt((cell_width/2-trans_rad+prop_24(i))^2 + ...
                               ((cell_length-trans_pen-prop_20(i))-(trans_pen))^2);
381                        timeC1(i) = lengthC1(i)/c_sample;
382                        timeGYZC1(i) = timeG(i) + timeY(i) + timeZ(i) + timeC1(i);
383
384                        else %(if prop_24(i) > trans_dia)   RT13.5
385                            plot([0,prop_21(i)],[cell_length-trans_pen-prop_20(i),0],...
386                               "color",vector_colors{i}) %May need if-statement
387                            lengthD1(i) = sqrt((prop_21(i))^2 + ...
                                   (cell_length-trans_pen-prop_20(i))^2);
388                            timeD1(i) = lengthD1(i)/c_sample;
389                            timeGYZD1(i) = timeG(i) + timeY(i) + timeZ(i) + timeD1(i);
390
391                        end
392
393                    end
394
395                end
396
397
398
399            else  %RT14 (if prop_4(i) > cell_width/2 + trans_rad
400                prop_28(i) = (prop_3(i) + trans_pen) / tand(angle_1(i));
401                %prop_27(i) = prop_28(i) - (cell_width/2 + trans_rad);
402
403                if prop_28(i) < cell_width
404                %if prop_27(i) < (cell_width/2 - trans_rad) %RT14
405                    plot([cell_width-prop_28(i),cell_width],[cell_length,cell_length...
406                       -trans_pen-prop_3(i)],"color",vector_colors{i})
407                    lengthE1(i) = sqrt((prop_28(i))^2 + (prop_3(i) + trans_pen)^2);
408                    timeE1(i) = lengthE1(i)/c_sample;
409                    prop_30(i) = (cell_width-prop_28(i)) * tand(angle_1(i));
410                    plot([0,cell_width-prop_28(i)],[cell_length-prop_30(i),cell_length],...
411                       "color",vector_colors{i})
412                    lengthF1(i) = sqrt((cell_width-prop_28(i))^2 + (prop_30(i))^2);
413                    timeF1(i) = lengthF1(i)/c_sample;
414                    prop_31(i) = cell_width * tand(angle_1(i));
415
416                    plot([0,cell_width],[cell_length-prop_30(i),cell_length-prop_30(i)...
417                       -prop_31(i)],"color",vector_colors{i})
418                    lengthG1(i) = sqrt((cell_width)^2 + (prop_31(i))^2);
419                    timeG1(i) = lengthG1(i)/c_sample;
420
421                    prop_33(i) = cell_length - prop_30(i) - prop_31(i);
422                    prop_32(i) = prop_33(i) / tand(angle_1(i));
423
424                    if prop_32(i) < cell_width/2 - trans_rad; %RT14
425                        plot([cell_width-prop_32(i),cell_width],[0,prop_33(i)],"color",...
426                           vector_colors{i})
427                        lengthH1(i) = sqrt((prop_32(i))^2 + (prop_33(i))^2);
428                        timeH1(i) = lengthH1(i)/c_sample;
429                        timeGE1F1G1H1(i) = timeG(i) + timeE1(i) + timeF1(i) + timeG1(i) ...
                               + timeH1(i);
430
431                    else %RT15 (if prop_32(i) > cell_width/2 - trans_rad)
432                        prop_33(i) = (prop_32(i) - (cell_width/2 - trans_rad)) * ...
                               tand(angle_1(i));
433
434                        if prop_33(i) < trans_pen %RT15
435                            plot([cell_width/2+trans_rad,cell_width],[prop_33(i),...
436                               cell_length-prop_30(i)-prop_31(i)],"color",vector_colors{i})
437                            lengthI1(i) = sqrt((cell_width/2 - trans_rad)^2 + ...
                                   ((cell_length-prop_30(i)-prop_31(i))-(prop_33(i)))^2);
438                            timeI1(i) = lengthI1(i)/c_sample;
439                            timeGE1F1G1I1(i) = timeG(i) + timeE1(i) + timeF1(i) + ...
                                   timeG1(i) + timeI1(i);
440
441                        else %RT16 (prop_33(i) > trans_pen)
442                            prop_34(i) = (prop_33(i) - trans_pen) / tand(angle_1(i));
443                            plot([cell_width/2+trans_rad-prop_34(i),cell_width],...
444                               [trans_pen,cell_length-prop_30(i)-prop_31(i)],"color",...
445                               vector_colors{i})
446                            lengthJ1(i) = ...
                                   sqrt((cell_width-(cell_width/2+trans_rad-prop_34(i)))^2 ...
                                   + ((cell_length-prop_30(i)-prop_31(i))-(trans_pen))^2);
447                            timeJ1(i) = lengthJ1(i)/c_sample;
```

```
448                                        timeGE1F1G1J1(i) = timeG(i) + timeE1(i) + timeF1(i) + ...
                                               timeG1(i) + timeJ1(i);
449
450                                    end
451
452                                end
453
454                            else %if prop_27(i) > (cell_width/2 - trans_rad) %RT15
455                                prop_29(i) = (cell_width - prop_4(i)) * tand(angle_1(i));
456                                plot([0,cell_width], [cell_length-trans_pen+prop_29(i), ...
                                       trans_pen+prop_1(i)],"color",vector_colors{i})
457                                lengthK1(i) = sqrt((cell_width)^2 + ...
                                       ((cell_length-trans_pen+prop_29(i))-(trans_pen+prop_1(i)))^2);
458                                timeK1(i) = lengthK1(i)/c_sample;
459
460
461                            end
462
463                        end
464
465                    end
466
467                end
468
469   end
```

E.2.2   Directivity.m

```
1   close all, clear all, clc
2
3   %%% This script plots the directivity of the sound field from the transducer %%%
4
5
6   f = 5e5; %Frequency [Hz]
7   c = 1593; %Sound velocity [m/s]
8   k = 2*pi*f/c; %Wave number [m^-1]
9   a = ((9.71 + 9.63)/2)*10^-3; %Transducer radius [m]
10  %theta = [15.2848, 24.9850, 35.3920, 47.3041];
11  theta = [0:0.001:90]; %Angles [deg]
12  x = k*a*sind(theta);
13  J = besselj(1,x); %Bessel function
14  H = abs((2*J)./x);
15  Hlog = 20*log10(H.^2);
16  pt = plot(theta,Hlog);
17  ylim([-100, 0])
18  %title("dB-level as function of angle")
19  xlabel("Angle [\circ]")
20  ylabel("20log(H(\theta)_{tot})")
21  datatip(pt,15.628,-35.1403)
22  datatip(pt,26.191,-47.6223)
23  datatip(pt,37.538,-55.9141)
24  datatip(pt,20.721,-64.7659)
```

E.3   Signal Processing scripts

E.3.1   Main.m

```
1   clear all
2
3   %%% Main script for data acquisition, calculations and plotting.
4   %%% Based on a "Timer" function scheduling MATLAB commands to be executed.
5   % Explanation: The script initiates oscilloscope through InitScope.m, reads
6   % data from oscilloscope through DPRRead.m, finds the sound velocities
7   % through SOS_calculation.m and the corresponding uncertainties through
8   % Uncertainty_calculation.m.
9
10  %%% Joachim Gjesdal Kristensen, last edited 14.05.22 %%%
11
12
13  [id_scope] = InitScope(); %Connecting to oscilloscope
14  ch = 2; %Channel used on oscilloscope
15
16  WF_file = ['WF_',datestr(now,'dd_mm_HH_MM_SS'),'.txt']; %Creating file name for waveform
17  Data_file = ['Data_',datestr(now,'dd_mm_HH_MM_SS'),'.txt']; %Creating file name for all ...
        data
18  Data_file_open = fopen(Data_file,'at'); %Opens Data_file in text mode for writing. ...
        Appends data to end of file.
19
20
21  delay = 3; %Seconds between runs
22  executions = 10000; %Number of measurements (number of times this program is run). Use ...
        ctrl + c if it proves excessive.
```

```matlab
23
24
25  t = timer; %Creates empty timer object to schedule execution of MATLAB commands
26
27  %Setting graphics object properties:
28  %set(t, 'StartDelay', delay); %Sets the delay between start of timer and first ...
        execution equal to "delay" seconds
29  set(t, 'Period', delay); %Sets the delay between executions equal to "delay" seconds
30  set(t, 'StartDelay', delay); %Sets the delay between start of timer and first execution ...
        equal to "delay" seconds
31  set(t, 'TasksToExecute', executions); %Sets the number of times the timer callback ...
        function is executed equal to "executions" times.
32  set(t, 'ExecutionMode', 'fixedRate'); %Defines starting point of 'Period' property to ...
        be immediately after the timer callback function is added to the MATLAB execution ...
        queue.
33
34  t.StartFcn = {@StartDataAcquisition, id_scope, ch, WF_file, Data_file_open}; %Specify ...
        value of StartFcn callback.
35  t.TimerFcn = {@DataAcquisition, id_scope, ch, WF_file, Data_file_open}; %Specify value ...
        of TimerFcn callback.
36  t.StopFcn = {@StopDataAcquisition, id_scope, ch, WF_file, Data_file_open}; %Specify ...
        value of StopFcn callback.
37
38  start(t); %Starting timer
39  pause(20000); %Time it takes inbetween starting and stopping timer. (Only sometimes?).
40  stop(t); %Stopping timer
41  delete(t); %Deleting timer
42
43
44  %Plotting
45  Plotting(Data_file)
46
47  function[c_ZC,c_ZC_corr_M1] = StartDataAcquisition(¬, ¬, id_scope,ch, ...
        WF_file,Data_file_open) %Commands in StartDataAcquisition is executed when timer starts
48      [x,wf] = DPORead(id_scope,ch); %Acquire time and amplitude values from oscilloscope
49
50      [¬,Dracal_data] = system(['usbtenkiget -s E18753 -i 0 -x 3']); %Acquire data from ...
            temperature sensor via Dracal
51      findDigits = regexp(Dracal_data,"\d+.\d*","match"); % See explanation below
52      % \d :  Begins with any numeric digit from 0-9 (number before decimal)
53      % + :   A numeric digit can occur one or more times (\d now represents one OR MORE ...
            consecutive digits. Needed if temperature is 10 degrees or more.)
54      % . :   Next is any single character (will conveniently be "." in this case)
55      % \d* :  Matches any number of consecutive digits (after decimal)
56      % "match" :  regexp returns substring that match "\d+.\d*" in Dracal_data
57      T_str = findDigits(1); %Measured temperature in text form is the first cell
58      T_org = str2double(T_str); %Measured temperature converted from text to number. To ...
            be calibrated...
59
60      [y_D,pulse_length,T,c_ZC,c_ZC_corr_M1,c_ZC_corr_M2,c_FSM,c_FSM_corr_M1,c_FSM_corr_M2,...
61          c_Frey,c_Chen,ppm_c_ZC_M1, ppm_c_ZC_M2, ppm_c_FSM_M1, ppm_c_FSM_M2, ppm_c_Frey,...
62          ppm_c_Chen, std_Deltat, u_t0, Deltat, t_corr_ZC_M1, t_corr_ZC_M2, t_corr_FSM_M1,...
63          t_corr_FSM_M2] = SOS_calculation(x,wf,T_org); %Calculating speed of sound
64
65      %Plotting waveform live
66      hLine = plot(y_D); %Plot to be updated live
67      StripChart("initialize",gca) %Initialize plot (gca creates cartesian axes object)
68
69      err = 0 ; %Needed later in case error occurs(?). 0 = no error, 1 = error
70
71      %Writing waveform to the WF_file text file
72      writematrix(y_D,WF_file);
73
74      %Writing formatted data to the Data_file text file (%s = string, %d = integer)
75      fprintf(Data_file_open, '%s %s %s %s %s %s %s %s %s %s %s %s %s %s %s %s %s %s ...
          %s %s %s %s %s\n', "Date","Time","Temperature","Pulse_length","c_ZC",...
76          "c_ZC_corr_M1","ppm_c_ZC_M1","c_ZC_corr_M2","ppm_c_ZC_M2","c_FSM",...
77          "c_FSM_corr_M1","ppm_c_FSM_M1","c_FSM_corr_M2","ppm_c_FSM_M2","c_Frey",...
78          "ppm_c_Frey","c_Chen","ppm_c_Chen","Error","std_Deltat","u_t0","Deltat",...
79          "t_corr_ZC_M1", "t_corr_ZC_M2", "t_corr_FSM_M1", "t_corr_FSM_M2");
80
81      fprintf(Data_file_open,'%s %s %d %d %d %d %d %d %d %d %d %d %d %d %d %d %d %d %d ...
          %d %d %d %d %d %d \n',datestr(now,'dd_mm_yyyy'),datestr(now,'HH_MM_SS'),T,...
82          pulse_length, c_ZC,c_ZC_corr_M1,ppm_c_ZC_M1,c_ZC_corr_M2,ppm_c_ZC_M2,c_FSM,...
83          c_FSM_corr_M1,ppm_c_FSM_M1,c_FSM_corr_M2,ppm_c_FSM_M2,c_Frey,ppm_c_Frey,c_Chen,...
84          ppm_c_Chen, err, std_Deltat, u_t0, Deltat, t_corr_ZC_M1, t_corr_ZC_M2,...
85          t_corr_FSM_M1, t_corr_FSM_M2);
86
87      %Displaying some data in command window
88      info = sprintf("TimeStart = %s Temperature = %s c_ZC = %s c_FSM = %s c_Frey = %s ...
            c_Chen = %s",datestr(now,'HH_MM_SS'),T,c_ZC,c_FSM,c_Frey,c_Chen);
89      disp(info);
90  end
91
92  function [c_ZC,c_ZC_corr_M1] = DataAcquisition(¬, ¬, id_scope,ch,WF_file, ...
        Data_file_open) %Commands in DataAcquisition is executed when timer executes
93      [x,wf] = DPORead(id_scope,ch); %Acquire time and amplitude values from oscilloscope
94
95      [¬,Dracal_data] = system(['usbtenkiget -s E18753 -i 0 -x 3']); %Acquire data from ...
            temperature sensor via Dracal
96      findDigits = regexp(Dracal_data,"\d+.\d*","match"); % See explanation below
97      % \d :  Begins with any numeric digit from 0-9 (number before decimal)
98      % + :   A numeric digit can occur one or more times (\d now represents one OR MORE ...
            consecutive digits. Needed if temperature is 10 degrees or more.)
99      % . :   Next is any single character (will conveniently be "." in this case)
100     % \d* :  Matches any number of consecutive digits (after decimal)
101     % "match" :  regexp returns substring that match "\d+.\d*" in Dracal_data
102     T_str = findDigits(1); %Measured temperature in text form is the first cell
103     T_org = str2double(T_str); %Measured temperature converted from text to number. To ...
            be calibrated...
104
105     [y_D,pulse_length,T,c_ZC,c_ZC_corr_M1,c_ZC_corr_M2,c_FSM,c_FSM_corr_M1,c_FSM_corr_M2,...
106         c_Frey,c_Chen,ppm_c_ZC_M1, ppm_c_ZC_M2, ppm_c_FSM_M1, ppm_c_FSM_M2, ppm_c_Frey,...
```

```
107            ppm_c_Chen, std_Deltat, u_t0, Deltat, t_corr_ZC_M1, t_corr_ZC_M2, t_corr_FSM_M1,...
108            t_corr_FSM_M2] = SOS_calculation(x,wf,T_org); %Calculating speed of sound
109
110        %Plotting waveform live
111        hLine = plot(y_D); %Plot to be updated live
112        StripChart('Update',hLine,y_D) %Updates plot with new waveform
113
114        %Writing waveform to the WF_file text file
115        %try, catch, end allows for overriding of the default error behavior
116        err = 0;
117        try
118            writematrix(y_D,WF_file,"WriteMode","Append"); %Appends new waveform below the ...
                   existing waveforms in WF_file
119        catch
120            disp('Error: Could not write waveform');
121            err = 1; %0 = no error, 1 = error
122        end
123
124        %Writing formatted data to the Data_file text file (%s = string, %d = integer)
125        fprintf(Data_file_open,'%s %s %d %d %d %d %d %d %d %d %d %d %d %d %d %d %d %d ...
                 %d %d %d %d %d %d \n',datestr(now,'dd_mm_yyyy'),datestr(now,'HH_MM_SS'),T,...
126            pulse_length, c_ZC,c_ZC_corr_M1,ppm_c_ZC_M1,c_ZC_corr_M2,ppm_c_ZC_M2,c_FSM,...
127            c_FSM_corr_M1,ppm_c_FSM_M1,c_FSM_corr_M2,ppm_c_FSM_M2,c_Frey,ppm_c_Frey,c_Chen,...
128            ppm_c_Chen, err, std_Deltat, u_t0, Deltat, t_corr_ZC_M1, t_corr_ZC_M2,...
129            t_corr_FSM_M1, t_corr_FSM_M2);
130
131        %Displaying some data in command window
132        info = sprintf("Time = %s Temperature = %s c_ZC = %s c_FSM = %s c_Frey = %s c_Chen ...
                = %s",datestr(now,'HH_MM_SS'),T,c_ZC,c_FSM,c_Frey,c_Chen);
133        disp(info);
134
135        pause(1) %(?)
136    end
137
138    function [c_ZC,c_ZC_corr_M1] = StopDataAcquisition(¬, ¬, id_scope,ch,WF_file, ...
           Data_file_open) %Commands in StopDataAcquisition is executed when timer stops
139        [x,wf] = DPORead(id_scope,ch); %Acquire time and amplitude values from oscilloscope
140
141        [¬,Dracal_data] = system(['usbtenkiget -s E18753 -i 0 -x 3']); %Acquire data from ...
               temperature sensor via Dracal
142        findDigits = regexp(Dracal_data,"\d+.\d*","match"); % See explanation below
143        % \d :  Begins with any numeric digit from 0-9 (number before decimal)
144        % + :  A numeric digit can occur one or more times (\d now represents one OR MORE ...
               consecutive digits. Needed if temperature is 10 degrees or more.)
145        % . :  Next is any single character (will conveniently be "." in this case)
146        % \d* :  Matches any number of consecutive digits (after decimal)
147        % "match" :  regexp returns substring that match "\d+.\d*" in Dracal_data
148        T_str = findDigits(1); %Measured temperature in text form is the first cell
149        T_org = str2double(T_str); %Measured temperature converted from text to number. To ...
               be calibrated...
150
151        [y_D,pulse_length,T,c_ZC,c_ZC_corr_M1,c_ZC_corr_M2,c_FSM,c_FSM_corr_M1,c_FSM_corr_M2,...
152            c_Frey,c_Chen,ppm_c_ZC_M1, ppm_c_ZC_M2, ppm_c_FSM_M1, ppm_c_FSM_M2, ppm_c_Frey,...
153            ppm_c_Chen, std_Deltat, u_t0, Deltat, t_corr_ZC_M1, t_corr_ZC_M2, t_corr_FSM_M1,...
154            t_corr_FSM_M2] = SOS_calculation(x,wf,T_org); %Calculating speed of sound
155
156        %Plotting waveform live
157        hLine = plot(y_D); %Plot to be updated live
158        StripChart('Update',hLine,y_D) %Updates plot with new waveform
159
160        err = 0;
161
162        %Writing waveform to the WF_file text file
163        writematrix(y_D,WF_file,"WriteMode","Append"); %Appends new waveform below the ...
               existing waveforms in WF_file
164
165        %Writing formatted data to the Data_file text file (%s = string, %d = integer)
166        fprintf(Data_file_open,'%s %s %d %d %d %d %d %d %d %d %d %d %d %d %d %d %d %d %d ...
                 %d %d %d %d %d %d \n',datestr(now,'dd_mm_yyyy'),datestr(now,'HH_MM_SS'),T,...
167            pulse_length, c_ZC,c_ZC_corr_M1,ppm_c_ZC_M1,c_ZC_corr_M2,ppm_c_ZC_M2,c_FSM,...
168            c_FSM_corr_M1,ppm_c_FSM_M1,c_FSM_corr_M2,ppm_c_FSM_M2,c_Frey,ppm_c_Frey,c_Chen,...
169            ppm_c_Chen, err, std_Deltat, u_t0, Deltat, t_corr_ZC_M1, t_corr_ZC_M2,...
170            t_corr_FSM_M1, t_corr_FSM_M2);
171        fclose(Data_file_open); %Closes the open Data_file
172
173        %Displaying some data in command window
174        info = sprintf("TimeEnd = %s Temperature = %s c_ZC = %s c_FSM = %s c_Frey = %s ...
               c_Chen = %s",datestr(now,'HH_MM_SS'),T,c_ZC,c_FSM,c_Frey,c_Chen);
175        disp(info);
176    end
```

E.3.2   InitScope.m

```
1    function [id_scope] = InitScope()
2    %% InitScope()
3    % Initialize Tektronix oscilloscope over USB
4    % Created by Magne Vestrheim
5    % Adjusted 2021-10 by Audun Oppedal Pedersen:
6    % - use 16-bit data
7    % - clean up old code (it stays available as earlier revision in GitLab)
8    % - update from the deprecated visa statement to visadev
9    % - update from fprintf to write (corresponding to visadev)
10
11
```

```matlab
12  %% Identify oscilloscope
13  % dlist = visadevlist();
14  % Unable to make this work with NI-VISA and 2021b per 2021-10.
15
16  id_scope = visadev('USB0::0x0699::0x0410::C024018::INSTR'); % Auduns PC
17  write(id_scope, 'DATA:ENCDG SRIBINARY;WIDTH 2');
```

E.3.3   DPORead.m

```matlab
1   %% DPORead.m
2   % Created by Magne Vestrheim
3   % Adjusted 2021-11-04 by Audun Oppedal Pedersen:
4   % - Byte order and word length controlled by InitScope (16-bit)
5   % - Cleaned up old code (still found in GitLab)
6   % - Using visadev in InitScope instead of the deprecated visa statement:
7   % => Update from the deprecated binblockread function to readbinblock
8   % => Update from fprintf and freadf to write and read
9   % - Corrected an error in the calculation of wf. Now including YOF.
10
11  % Use the DPO3000 Series Programmer Guide when editing the script.
12
13  %function [x,wf,tidsskala] = DPORead(id_scope,ch,samples)
14  function [x,wf,tidsskala] = DPORead(id_scope,ch)
15
16  noB = 2; % Number of bytes per word (8-bit if 1, 16-bit if 2, ...)
17  % set(id_scope,'InputBufferSize',noB*samples); % Buffer size in the computer
18
19  % fopen(id_scope);
20  % fprintf(id_scope,['DAT:SOU CH' num2str(ch)]); % Velge kanal. ch=1 betyr CH1
21  write(id_scope,['DAT:SOU CH' num2str(ch)]); % Velge kanal. ch=1 betyr CH1
22
23  % Record length per visible time interval, affecting the sample rate
24  pause(2)
25  rec_len = str2double(writeread(id_scope,'HOR:RECO?'));
26  if nargin() == 3
27      if samples > rec_len
28          warning('The record length is set too low. Adjusting and waiting 10 s...')
29          write(id_scope,['HOR:RECO ' num2str(samples)]); % New record length
30          pause(10);
31      elseif samples < rec_len
32          warning('Retrieving less than the record length (full view).')
33      end
34  else
35      samples = rec_len;
36  end
37
38  % Set what samples to retrieve
39  write(id_scope,'DAT:START 1');
40  write(id_scope,['DAT:STOP ' num2str(samples)]);
41
42  % Read the data
43  write(id_scope,'CURV?');
44  % dd = query(id_scope,'CURV?');
45  % pause(.2);
46  % ff = query(id_scope,'BUSY?');
47  if noB == 2
48      ydata = readbinblock(id_scope,'int16');
49  elseif noB == 1
50      ydata = readbinblock(id_scope,'int8');
51  else
52      error('Unsupported word length');
53  end
54  flush(id_scope); % Flush the termination character from the scope
55
56  %% Scaling of the data
57  % Horizontal scaling
58  tidsskala = str2double(writeread(id_scope,'HOR:SCA?'));
59  % Horizontal offset
60  xze = str2double(writeread(id_scope,'WFMO:XZE?'));
61  % Horizontal increment
62  xin = str2double(writeread(id_scope,'WFMO:XIN?'));
63  % Vertical multiplying factor
64  ymu = str2double(writeread(id_scope,'WFMO:YMU?'));
65  % Vertical offset
66  yze = str2double(writeread(id_scope,'WFMO:YZE?'));
67  % Digital vertical offset
68  yof = str2double(writeread(id_scope,'WFMO:YOF?'));
69
70  % Time vector
71  x = (0:(length(ydata)-1))*xin + xze;
72  % Voltage/current vector
73  wf = (ydata-yof)*ymu + yze;
74
75  %save("waveform70.mat", "x", "wf")
```

E.3.4   SOS_calculation.m

```matlab
1  %This script uses a sampled waveform to calculate the sound velocity in
2  %liquids using the zerocrossing method and the Fourier spectrum method.
3
4  %%% Joachim Gjesdal Kristensen, Last edited: 14.05.22 %%%
5
6
7  function ...
      [y_D,pulse_length,T,c_ZC,c_ZC_corr_M1,c_ZC_corr_M2,c_FSM,c_FSM_corr_M1,c_FSM_corr_M2,...
8      c_Frey,c_Chen,ppm_c_ZC_M1,ppm_c_ZC_M2,ppm_c_FSM_M1,ppm_c_FSM_M2,ppm_c_Frey,...
9      ppm_c_Chen, std_Deltat, u_t0, Deltat, t_corr_ZC_M1, t_corr_ZC_M2, t_corr_FSM_M1,...
10     t_corr_FSM_M2] = SOS_calculation(x,wf,T_org);
11
12 %% Variables that must be updated before doing measurements %%
13
14 pulse_length = 10; %Number of periods in generated pulse
15 const = 14; %Constant added to pulse_length to find number of zerocrossings in pulse. ...
      Dependent on pulse_length.
16          %Pulse_length = 1,2,3,5,10 ---> const = 5,6,7,9,14, etc.
17 Dec1 = 5; %For decimation (to find zerocrosses)
18 Dec2 = 1; %For decimation (if needed for filtering)
19 scope_span = 0.4; %Vertical span in oscilloscope display
20 P_0 = 1.020; %Pressure measured in lab before starting a measurement series [bar]
21 S = 0; %Salinity of water [g/liter] (parts per thousand)
22 noise_fraction = 2/10; %Approximate first fraction of the signal where there is only ...
      incoherent noise
23 signal_fraction = 6/10; %Fraction of the signal excluding Pulse B
24 TresholdA = 0.01; %Lower than first peak of pulse A, but higher than noise.
25 TresholdB = 0.001; %Lower than first peak of pulse B, but higher than noise.
26 ss_start = 5; %Number of zerocrossings before steady-state part of signal begins.
27 ss_end = 4; %Number of zerocrossings before steady-state part of signal ends.
28 timeAB = x(length(x)*signal_fraction); %Arbitrary time between signal A and B [s]. Will ...
      change depending on signal generator. Used to separate signal A and B later
29
30
31
32
33
34 %% Constants %%
35
36 T_0 = 22.8; %Reference temperature [C]
37 L_0 = 125.0e-3; %Transducer distance at reference temperature [m]
38 freq = 500000; %Frequency of generated signal [Hz]
39 w = 2*pi*freq; %Angular frequency of generated signal [rad/s]
40 a_eff = 9.71e-3; %Effective element radius of transmitting transducer [m]
41
42
43
44
45 %% Temperature correction (calibration) %%
46
47 alpha_org = 0.003908299841; %Original coefficient [C^-1]
48 beta_org = -5.7749974e-7; %Original coefficient [C^-2]
49 R = 100*(1 + alpha_org*T_org + beta_org*T_org^2); %Characteristic equation for Pt100 [Ohm]
50
51 alpha = 3.733e-3; %New coefficient [C^-1]
52 beta = -4.784e-7; %New coefficient [C^-2]
53 R_0 = 100.3; %New coefficient [Ohm]
54
55 T = (-alpha*R_0 + sqrt(alpha^2*R_0^2 - 4*beta*R_0*(R_0 - R)))/(2*beta*R_0); ...
      %Characteristic equation for Pt100, solved for T [C]
56
57
58
59
60 %% Calculating pressure %%
61
62 %%%%% Coefficients in equation for density in seawater:
63 b0 = 8.24493e-1;
64 b1 = -4.0899e-3;
65 b2 = 7.6438e-5;
66 b3 = -8.2467e-7;
67 b4 = 5.3875e-9;
68 c0 = -5.72466e-3;
69 c1 = 1.0227e-4;
70 c2 = -1.6546e-6;
71 d0 = 4.8314e-4;
72 a0 = 999.842594;
73 a1 = 6.793952e-2;
74 a2 = -9.095290e-3;
75 a3 = 1.001685e-4;
76 a4 = -1.120083e-6;
77 a5 = 6.536332e-9;
78
79 % Equation for density as a function of temperature and salinity:
80 rho_0 = a0 + a1*T + a2*T^2 + a3*T^3 + a4*T^4 + a5*T^5;
81
82 rho = rho_0 + (b0 + b1*T + b2*T^2 + b3*T^3 + b4*T^4)*S +...
83     (c0 + c1*T + c2*T^2)*S^(3/2) + d0*S^2;
84
85 %Calculating pressure:
86 g = 9.81; %Gravity acceleration [m/s2]
87 h = 29.5e-3; %Depth of center of transducer [m]
88 pascal2bar = 10e-5; %Pascal to bar conversion
89 P = rho*g*h*pascal2bar + P_0; %Hydrostatic pressure [bar]
90 P_atm = 1.01325; %Atmospheric pressure [bar]
91 P_gauge = P - P_atm; %Gauge pressure [bar]
92
93 % For uncertainty calculations later
94 d_rho_d_T = a1 + 2*a2*T + 3*a3*T^2 + 4*a4*T^3 + 5*a5*T^4 + ...
95     (b1 + 2*b2*T + 3*b3*T^2 + 4*b4*T^3)*S + ...
96     (c1 + 2*c2*T)*S^(3/2);
97
98 d_rho_d_S = b0 + b1*T + b2*T^2 + b3*T^3 + b4*T^4 + ...
99     (3/2) * (c0 + c1*T + c2*T^2) * S^(1/2) + 2*d0*S;
```

```matlab
100
101
102
103
104 %% Thermal expansion of measurement cell %%
105
106 alpha_T = 0.0725e-3; %Linear thermal expansion coefficient of plexiglass [C^-1]
107 K_T = 1 + alpha_T * (T-T_0); %Thermal expansion coefficient
108 L = K_T*L_0; %Transducer distance at temperature T [m]
109
110
111
112
113 %% Resolution and incoherent noise %%
114
115 %%%%% Incoherent noise:
116 for i = 1:20000 %Using the part of the signal where there is only incoherent noise ...
        (before arrival of pulse A)
117     wf_square(i) = wf(i)^2; %Square of each sample
118 end
119 wf_mean = mean(wf_square); %Mean of samples
120 wf_rms = sqrt(wf_mean); %Root-mean-square of samples
121 u_V_inc = sqrt(2) * wf_rms; %Uncertainty due to incoherent noise
122
123 %%%%% Bits:
124 bits = 8; %Vertical resolution of oscilloscope [bits]
125 Delta_Vq = scope_span/(2^bits - 1); %Quantisation interval [V]
126 u_V_bit = Delta_Vq/2; %Uncertainty due to bit resolution (quantisation error) [V]
127
128 %%%%% Total:
129 u_V = sqrt(u_V_inc^2 + u_V_bit^2); %Uncertainty in sampled voltage amplitudes
130
131 ts = (x(end) - x(1))/100000; %Sampling period
132
133
134
135
136 %% Decimating, filtering, zero-padding %%
137
138 fs = (length(x)-1)/(x(end-1)-x(1)); %Sampling frequency used to sample the signal [Hz]
139 x1 = x; %Assigning original time values to x1 (for decimation when running script ...
        several times)
140 y1 = wf; %Assigning original amplitude values to y1 (for decimation when running script ...
        several times)
141
142 %%%%% Decimation and downsampling:
143 y_D = decimate(y1,Dec1); %Resamples waveform at 1/Dec1 times the original sample rate ...
        after lowpass filtering
144 if round(length(x1)/Dec1) ≠ length(x1)/Dec1 %Handles cases where the number of samples ...
        divided by decimation factor is not an integer
145     x_D = linspace(x1(1),x1(end),(length(x1))/Dec1 + 1); %Resamples x-axis at 1/Dec1 ...
            times the original sample rate
146 else
147     x_D = linspace(x1(1),x1(end),(length(x1))/Dec1); %Resamples x-axis at 1/Dec1 times ...
            the original sample rate
148 end
149 fs_D = fs/Dec1; %1/D times the original sample rate
150
151 % noise_mean = mean(y_D(1:round(length(y_D)*noise_fraction))); %Mean of incoherent noise
152 % y_D = y_D - noise_mean; %Shifted signal such that mean of coherent noise (first part ...
        of total signal) is zero
153
154
155 % Additional decimation (if needed for filtering)
156 y_D = decimate(y_D,Dec2);
157 if round(length(x_D)/Dec2) ≠ length(x_D)/Dec2
158     x_D = linspace(x_D(1),x_D(end),(length(x_D))/Dec2 + 1);
159 else
160     x_D = linspace(x_D(1),x_D(end),(length(x_D))/Dec2);
161 end
162 fs_D = fs_D/Dec2;
163
164
165 % Filtering
166 N = 4; %Order of Butterworth filter
167 Wn = [1e5, 1e6] / (fs_D / 2); %Defines the passband of the filter (cutoff freq). Divide ...
        by (fs_D / 2) to fulfill Nyquist
168 [B, A] = butter(N, Wn); %Returns Butterworth filter coefficients B (numerator) and A ...
        (denominator)
169 [y_D] = filtfilt(B, A, y_D); %Decimated and filtered waveform
170 %butter returns the transfer function coefficients of a Nth order lowpass
171 %digital Butterworth filter. B = coefficients in numerator. A =
172 %coefficients in denominator.
173 %filtfilt uses the constructed Butterworth filter on the waveform y_D, and
174 %compensates for the phase shift.
175
176
177
178
179 %Finding first index of Pulse A:
180 [pksA,pks_idxA] = ...
        findpeaks(y_D(1:round(length(y_D)*signal_fraction)),'MinPeakHeight',TresholdA); ...
        %Finds peaks and indices of Pulse A
181 for i = pks_idxA(1):-1:1 %Starting at first peak in Pulse A and going backwards
182     if pksA(1) - y_D(i) > pksA(1) %Equivalent to: if y_D(i) < zero...
183         i_A_min = i; %... then i_A_min is defined as index i, and the loop breaks.
184         break
185     end
186 end
187
188 %Finding last index of Pulse A:
189 A_vec = -1; %Needed since index of start of Pulse A is the last negative value, and the ...
        first peak is positive
190 for i = i_A_min:length(y_D) %Looping from first point in Pulse A
```

```matlab
191         if sign(y_D(i)) ≠ sign(y_D(i+1))
192             A_vec = A_vec + 1; %Number of sign swaps
193             if A_vec == pulse_length + const %If number of sign swaps is equal to the ...
                    number of zerocrossings in the pulse...
194                 i_A_max = i; %... then the last index, i_A_max, of the pulse is found, and ...
                        the loop breaks.
195                 break
196             end
197         end
198     end
199
200     %Finding first index of Pulse B:
201     [pksB,pks_idxB] = ...
            findpeaks(y_D(round(length(y_D)*signal_fraction):end),'MinPeakHeight',TresholdB); ...
                %Finds peaks and indices of Pulse B
202     pks_idxB = pks_idxB + round(length(y_D)*signal_fraction); %Starting at first peak in ...
            Pulse B and going backwards
203     for i = pks_idxB(1):-1:1 %Starting at first peak in Pulse B and going backwards
204         if pksB(1) - y_D(i) > pksB(1) %Equivalent to: if y_D(i) < zero...
205             i_B_min = i; %... then i_B_min is defined as index i, and the loop breaks.
206             break
207         end
208     end
209
210     %Finding last index of Pulse B:
211     B_vec = -1; %Needed since index of start of Pulse B is the last negative value, and the ...
            first peak is positive
212     for i = i_B_min:length(y_D) %Looping from first point in Pulse B
213         if sign(y_D(i)) ≠ sign(y_D(i+1))
214             B_vec = B_vec + 1; %Number of sign swaps
215             if B_vec == pulse_length + const %If number of sign swaps is equal to the ...
                    number of zerocrossings in the pulse...
216                 i_B_max = i; %... then the last index, i_B_max, of the pulse is found, and ...
                        the loop breaks.
217                 break
218             end
219         end
220     end
221
222     %%%%% Zero-padding
223     % for i = 1:length(y_D)
224     %     if i ≤ i_A_min | i ≥ i_A_max && i ≤ i_B_min | i ≥ i_B_max
225     %         y_D(i) = 0;
226     %     end
227     % end
228
229
230
231
232     %% Finding zerocrosses and uncertainty in zerocrosses %%
233
234     ys = sign(y_D); %Finds the sign of each y-value (1, 0 or -1)
235     ysd = diff(ys); %Finds the difference between two consecutive elements in ys
236     myZC = find(ysd≠0); %Finds the indices in ysd where the value is not 0. Those are the ...
            indices closest to the zerocrosses. It is the indeces of y_D BEFORE it switches sign.
237
238     clear myZC_idx ZC_x_B_idx ZC_x_A_idx ZC_x_B ZC_x_A ZC_y_B ZC_y_A
239
240     for zc = 1:length(myZC) %Looping through all indices closest to the zerocrosses
241
242         if myZC(zc) ≥ i_A_min && myZC(zc) ≤ i_A_max | myZC(zc) ≥ i_B_min && myZC(zc) ≤ i_B_max
243
244             myZC_idx(zc) = myZC(zc);
245
246             x_zc_interval = x_D((myZC(zc)):(myZC(zc)+1)); %Vector of time values for ...
                    indices BEFORE and AFTER zerocrosses
247             y_zc_interval = y_D((myZC(zc)):(myZC(zc)+1)); %Vector of amplitude values for ...
                    indices BEFORE and AFTER zerocrosses
248
249             Δ_V(zc) = y_zc_interval(end) - y_zc_interval(1); %Voltage difference between ...
                    point before and after the actual zerocrossing
250             error_t0(zc) = ts/Δ_V(zc) * u_V; %Error for each zerocrossing time
251
252             if y_zc_interval(1) == y_zc_interval(2) %Handles situation where a zerocross is ...
                    exactly at zero. Happens at start and end of pulses because of zero-padding.
253                 myZCx(zc) = x_D(myZC(zc)); %Time of zerocrosses exactly at zero
254                 myZCy(zc) = y_D(myZC(zc)); %Amplitude of zerocrosses excatly at zero (=0)
255
256             else                                    %Handles situation where a zerocross is ...
                    not excactly at zero using linear interpolation.
257                 myZCx(zc) = interp1(y_zc_interval,x_zc_interval,0); %Time of zerocrosses ...
                        found through linear interpolation
258                 myZCy(zc) = interp1(x_D,y_D,myZCx(zc)); %Amplitude of zerocrosses found ...
                        through linear interpolation (very close to 0)
259             end
260         else
261             myZCx(zc) = 1;
262             myZCy(zc) = 1;
263         end
264     end
265
266     myZC_idx = transpose(nonzeros(myZC_idx));
267
268     myZCx = myZCx(myZCx ≠ 1);
269     myZCy = myZCy(myZCy ≠ 1);
270
271
272     % myZCx = transpose(nonzeros(myZCx));
273     % myZCy = transpose(nonzeros(myZCy));
274
275     u_t0 = sum(error_t0)/length(error_t0); %Uncertianty in zerocrossing time
276
277
278
```

```matlab
279
280  %% Zerocrossing method %%
281
282  %%%%% Separating signal A and B:
283  for i = 1:length(myZCx)
284      if myZCx(i) < timeAB %Signal A arrives before this time. Signal B arrives after.
285          ZC_x_A(i) = myZCx(i); %Array of times for zerocrosses in Signal A
286          ZC_y_A(i) = myZCy(i); %Array of amplitudes for zerocrosses in Signal A (should ...
                 be close to 0)
287          ZC_x_A_idx(i) = myZC_idx(i);
288      else
289          ZC_x_B(i-length(ZC_x_A)) = myZCx(i); %Array of times for zerocrosses in Signal B
290          ZC_y_B(i-length(ZC_y_A)) = myZCy(i); %Array of amplitudes for zerocrosses in ...
                 Signal B (should be close to 0)
291          ZC_x_B_idx(i) = myZC_idx(i);
292      end
293  end
294
295  ZC_x_B_idx = transpose(nonzeros(ZC_x_B_idx));
296
297
298  for i = ss_start:length(ZC_x_A)-ss_end;
299      Deltat_vec(i) = ZC_x_B(i) - ZC_x_A(i);
300  end
301
302  Deltat_vec = transpose(nonzeros(Deltat_vec));
303  std_Deltat = std(Deltat_vec);
304  Deltat = mean(Deltat_vec);
305
306
307
308
309
310  %% Fourier spectrum method %%
311
312  P_pow = nextpow2(length(x_D)); %returns the first P_pow such that 2.^P_pow ≥ ...
                 abs(length(X_D))
313  Q = 2.^P_pow; %First power of two higher than abs(length(X_D))
314  freq_fft = (0:Q-1)/(Q-1)*fs_D; %Array of frequencies for plotting sound velocity ...
                 against frequency
315
316  Signal_A = zeros(size(x_D)); %Buffer signal A
317  Signal_B = zeros(size(x_D)); %Buffer signal B
318
319  % i_A = find(x_D ≥ ZC_x_A(1) & x_D ≤ ZC_x_A(end)); %Finding all the indexes for Signal A
320  % i_B = find(x_D ≥ ZC_x_B(1) & x_D ≤ ZC_x_B(end)); %Finding all the indexes for Signal B
321
322  % i_A = i_A_min:1:i_A_max; %Finding all the indexes for Signal A
323  % i_B = i_B_min:1:i_B_max; %Finding all the indexes for Signal B
324
325  i_A = ZC_x_A_idx(ss_start):1:ZC_x_A_idx(end-ss_end); %Finding all the indexes for ...
                 Signal A
326  i_B = ZC_x_B_idx(ss_start):1:ZC_x_B_idx(end-ss_end); %Finding all the indexes for ...
                 Signal B
327
328  Signal_A(i_A) = y_D(i_A); %All amplitude-values corresponding to the indices i_A ...
                 (representing pulse A)
329  Signal_B(i_B) = y_D(i_B); %All amplitude-values corresponding to the indices i_B ...
                 (representing pulse B)
330
331  %If time shifting of Pulse A and B is needed:
332  %Shift_A = circshift(Signal_A,-i_A(1)); %Shifts Signal_A to the start.
333  %t_Shift_A = x(i_A(1)) - x(1); %The time that Signal_A is shifted.
334  %Shift_B = circshift(Signal_B,-i_B(1)); %Shifts Signal_B to the start.
335  %t_Shift_B = x(i_B(1)) - x(1); %The time that Signal_B is shifted.
336
337  fourier_A = fft(Signal_A, Q); %The N1-point discrete Fourier transform of SignalA.
338  fourier_B = fft(Signal_B, Q); %The N1-point discrete Fourier transform of SignalB.
339
340  mag_A = abs(fourier_A); %Magnitude of DFT of SignalA
341  mag_B = abs(fourier_B); %Magnitude of DFT of SignalB
342
343  phase_A = angle(fourier_A); %Wrapped phase of DFT of SignalA
344  phase_B = angle(fourier_B); %Wrapped phase of DFT of SignalB
345
346  theta_fft = unwrap(angle(fourier_B./fourier_A));
347  %theta_fft = angle(fourier_B./fourier_A);
348  theta_FSM = interp1(freq_fft,theta_fft,500000);
349
350  Signal = zeros(size(x_D)); %Buffer total signal
351  Signal(i_A) = y_D(i_A); %Inserting signal A
352  Signal(i_B) = y_D(i_B); %Inserting signal B
353
354
355
356
357  %% Coefficients and equations needed to calculate speed of sound in seawater %%
358
359  %%%%% Coefficients in equations for sound velocity in seawater:
360  C00 = 1402.388;
361  A02 = 7.166e-5;
362  C01 = 5.03830;
363  A03 = 2.008e-6;
364  C02 = -5.81090e-2;
365  A04 = -3.21e-8;
366  C03 = 3.3432e-4;
367  A10 = 9.4742e-5;
368  C04 = -1.47797e-6;
369  A11 = -1.2583e-5;
370  C05 = 3.1419e-9;
371  A12 = -6.4928e-8;
372  C10 = 0.153563;
373  A13 = 1.0515e-8;
374  C11 = 6.8999e-4;
```

```matlab
375  A14 = -2.0142e-10;
376  C12 = -8.1829e-6;
377  A20 = -3.9064e-7;
378  C13 = 1.3632e-7;
379  A21 = 9.1061e-9;
380  C14 = -6.1260e-10;
381  A22 = -1.6009e-10;
382  C20 = 3.1260e-5;
383  A23 = 7.994e-12;
384  C21 = -1.7111e-6;
385  A30 = 1.100e-10;
386  C22 = 2.5986e-8;
387  A31 = 6.651e-12;
388  C23 = -2.5353e-10;
389  A32 = -3.391e-13;
390  C24 = 1.0415e-12;
391  B00 = -1.922e-2;
392  C30 = -9.7729e-9;
393  B01 = -4.42e-5;
394  C31 = 3.8513e-10;
395  B10 = 7.3637e-5;
396  C32 = -2.3654e-12;
397  B11 = 1.7950e-7;
398  A00 = 1.389;
399  D00 = 1.727e-3;
400  A01 = -1.262e-2;
401  D10 = -7.9836e-6;
402
403  %%%%% Equations constituting final equation for speed of sound in seawater:
404  Cw = (C00 + C01*T + C02*T^2 + C03*T^3 + C04*T^4 + C05*T^5) + ...
405       (C10 + C11*T + C12*T^2 + C13*T^3 + C14*T^4)*P + ...
406       (C20 + C21*T + C22*T^2 + C23*T^3 + C24*T^4)*P^2 + ...
407       (C30 + C31*T + C32*T^2)*P^3;
408
409  A = (A00 + A01*T + A02*T^2 + A03*T^3 + A04*T^4) + ...
410      (A10 + A11*T + A12*T^2 + A13*T^3 + A14*T^4)*P + ...
411      (A20 + A21*T + A22*T^2 + A23*T^3)*P^2 + ...
412      (A30 + A31*T + A32*T^2)*P^3;
413
414  B = B00 + B01*T + (B10 + B11*T)*P;
415
416  D = D00 + D10*P;
417
418
419
420  %% For uncertainty calculations of theoretical sound velocity
421
422  % For distilled water, c_Frey
423  d_c_d_PG = 0.159 + 2.8*10^-4*T + 2.4 * 10^-6*T^2;
424
425  d_c_d_T = 4.88 - 0.0964*T + 405*10^-6*T^2 + 2.8*10^-4*P_gauge + 4.8*10^-6*T*P_gauge;
426
427
428  % For seawater, c_Chen
429  d_Cw_d_P = (C10 +C11*T +C12*T^2 +C13*T^3 +C14*T^4) +...
430      2*(C20 +C21*T +C22*T^2 +C23*T^3 +C24*T^4)*P +...
431      3*(C30 +C31*T +C32*T^2)*P^2;
432
433  d_A_d_P = (A10 + A11*T + A12*T^2 + A13*T^3 + A14*T^4) +...
434      2*(A20 + A21*T + A22*T^2 + A23*T^3)^P +...
435      3*(A30 + A31*T + A32*T^2)*P^2;
436
437  d_B_d_P = B10 + B11*T;
438
439  d_D_d_P = D10;
440
441  d_c_d_P = d_Cw_d_P + d_A_d_P*S + d_B_d_P*S^(3/2) + d_D_d_P*S^2;
442
443
444
445  d_Cw_d_T = (C01 + 2*C02*T + 3*C03*T^2 + 4*C04*T^3 + 5*C05*T^4) +...
446      (C11 + 2*C12*T + 3*C13*T^2 + 4*C14*T^3)*P +...
447      (C21 + 2*C22*T + 3*C23*T^2 + 4*C24*T^3)*P^2+...
448      (C31 + 2*C32*T)*P^3;
449
450  d_A_d_T = (A01 + 2*A02*T + 3*A03*T^2 + 4*A04*T^3) +...
451      (A11 + 2*A12*T + 3*A13*T^2 + 4*A14*T^3)*P +...
452      (A21 + 2*A22*T + 3*A23*T^2)*P^2+...
453      (A31 + 2*A32*T)*P^3;
454
455  d_B_d_T = B01 + B11*P;
456
457  d_D_d_T = 0;
458
459  d_c_d_T2 = d_Cw_d_T + d_A_d_T*S + d_B_d_T*S^(3/2) + d_D_d_T*S^(2);
460
461
462
463  d_Cw_d_S = 0;
464
465  d_AS_d_S = (A00 + A01*T + A02*T.^2 + A03*T.^3 + A04*T.^4) + ...
466      (A10 + A11*T + A12*T.^2 + A13*T.^3 + A14*T.^4).*P + ...
467      (A20 + A21*T + A22*T.^2 + A23*T.^3).*P.^2 + ...
468      (A30 + A31*T + A32*T.^2).*P.^3;
469
470  d_BS_d_S = (3/2)*(B00 + B01*T + (B10 + B11*T)*P)*S^(1/2);
471
472  d_DS_d_S = 2*(D00 + D10*P)*S;
473
474  d_c_d_S = d_Cw_d_S + d_AS_d_S + d_BS_d_S + d_DS_d_S;
475
476
477
478
479  %% Speed of sound calculations (without diffraction correction) %%
```

```matlab
480
481 %Calculating the speed of sound using zerocrossing method
482 c_ZC = 2*L/(mean(Deltat_vec));
483
484 %Calculating speed of sound using Fourier spectrum method
485 c_FSM = -4*pi*freq*L./theta_FSM;
486
487 %Calculating the theoretical speed of sound of distilled water using Kinsler and Frey
488 c_Frey = 1402.7 + 488 * (T/100) - 482 * (T/100)^2 + 135 * (T/100)^3 +...
489     (15.9 + 2.8 * (T/100) + 2.4 * (T/100)^2) * (P_gauge/100);
490 %c_Frey = 0.00249*T^2 - 3.831*T + 1457;
491
492 %Calculating the theoretical speed of sound of seawater using Chen and Millero
493 c_Chen = Cw + A*S + B*S^(3/2) + D*S^2;
494
495
496
497
498
499 %% Diffraction correction %%
500
501 n = 1000; %Number of intervals for Simpson integration
502 theta = 0:(pi/2)/n:(pi/2); %Angles [rad]
503 z_1way = L; %Axial distance from surface of transmitting transducer [m]
504 z_3way = 3*L;
505 h = (theta(end) - theta(1))/n; %Segment size in Simpson integration
506
507
508 %%% For c_zerocrosses:
509 k_zc = 2*pi*freq/c_ZC; %Wavenumber in sample [1/m]
510
511 %Method 1:
512 for m = 1:length(theta)
513     D_diff_A_integral_zc_M1(m) = exp(-1i*k_zc*z_1way*((sqrt(1+4*(a_eff/(z_1way))^2*...
514         (cos(theta(m)))^2))-1))*(sin(theta(m)))^2; %Diff.corr. integral for signal A
515 end
516
517 D_diff_A_zc_M1 = 1 - 4/pi*(4*sum(D_diff_A_integral_zc_M1(3:2:end-1)) + ...
        2*sum(D_diff_A_integral_zc_M1(2:2:end-2)) + D_diff_A_integral_zc_M1(1) + ...
        D_diff_A_integral_zc_M1(length(theta)))*h/3; %Diff.corr for signal A
518
519 phase_diff_A_zc_M1 = angle(D_diff_A_zc_M1); %Angle of diff.corr for signal A
520 t_diff_A_zc_M1 = -phase_diff_A_zc_M1./w; %Time shift due to diff.corr for signal A
521
522 phase_diff_B_zc_M1 = 3*angle(D_diff_A_zc_M1); %Angle of diff.corr for signal B
523 t_diff_B_zc_M1 = -phase_diff_B_zc_M1./w; %Time shift due to diff.corr for signal B
524
525
526 %Method 2:
527 for m = 1:length(theta)
528     D_diff_A_integral_zc_M2(m) = exp(-1i*k_zc*z_1way*((sqrt(1+4*(a_eff/(z_1way))^2*...
529         (cos(theta(m)))^2))-1))*(sin(theta(m)))^2; %Diff.corr. integral for signal A
530     D_diff_B_integral_zc_M2(m) = exp(-1i*k_zc*z_3way*((sqrt(1+4*(a_eff/(z_3way))^2*...
531         (cos(theta(m)))^2))-1))*(sin(theta(m)))^2; %Diff.corr. integral for signal B
532 end
533
534 D_diff_A_zc_M2 = 1 - 4/pi*(4*sum(D_diff_A_integral_zc_M2(3:2:end-1)) + ...
        2*sum(D_diff_A_integral_zc_M2(2:2:end-2)) + D_diff_A_integral_zc_M2(1) + ...
        D_diff_A_integral_zc_M2(length(theta)))*h/3; %Diff.corr for signal A
535 phase_diff_A_zc_M2 = angle(D_diff_A_zc_M2); %Angle of diff.corr for signal A
536 t_diff_A_zc_M2 = -phase_diff_A_zc_M2./w; %Time shift due to diff.corr for signal A
537
538 D_diff_B_zc_M2 = 1 - 4/pi*(4*sum(D_diff_B_integral_zc_M2(3:2:end-1)) + ...
        2*sum(D_diff_B_integral_zc_M2(2:2:end-2)) + D_diff_B_integral_zc_M2(1) + ...
        D_diff_B_integral_zc_M2(length(theta)))*h/3; %Diff.corr for signal B
539 phase_diff_B_zc_M2 = angle(D_diff_B_zc_M2); %Angle of diff.corr for signal B
540 t_diff_B_zc_M2 = -phase_diff_B_zc_M2./w; %Time shift due to diff.corr for signal B
541
542
543
544
545 %%% For c_FSM:
546 k_FSM = 2*pi*freq/c_FSM; %Wavenumber in sample [1/m]
547
548 %Method 1:
549 for m = 1:length(theta)
550     D_diff_A_integral_FSM_M1(m) = exp(-1i*k_FSM*z_1way*((sqrt(1+4*(a_eff/(z_1way))^2*...
551         (cos(theta(m)))^2))-1))*(sin(theta(m)))^2; %Diff.corr. integral for signal A
552 end
553
554 D_diff_A_FSM_M1 = 1 - 4/pi*(4*sum(D_diff_A_integral_FSM_M1(3:2:end-1)) + ...
        2*sum(D_diff_A_integral_FSM_M1(2:2:end-2)) + D_diff_A_integral_FSM_M1(1) + ...
        D_diff_A_integral_FSM_M1(length(theta)))*h/3; %Diff.corr for signal A
555
556 phase_diff_A_FSM_M1 = angle(D_diff_A_FSM_M1); %Angle of diff.corr for signal A
557 t_diff_A_FSM_M1 = -phase_diff_A_FSM_M1./w; %Time shift due to diff.corr for signal A
558
559 phase_diff_B_FSM_M1 = 3*angle(D_diff_A_FSM_M1); %Angle of diff.corr for signal B
560 t_diff_B_FSM_M1 = -phase_diff_B_FSM_M1./w; %Time shift due to diff.corr for signal B
561
562 %Method 2:
563 for m = 1:length(theta)
564     D_diff_A_integral_FSM_M2(m) = exp(-1i*k_FSM*z_1way*((sqrt(1+4*(a_eff/(z_1way))^2 ...
565         *(cos(theta(m)))^2))-1))*(sin(theta(m)))^2; %Diff.corr. integral for signal A
566     D_diff_B_integral_FSM_M2(m) = exp(-1i*k_FSM*z_3way*((sqrt(1+4*(a_eff/(z_3way))^2 ...
567         *(cos(theta(m)))^2))-1))*(sin(theta(m)))^2; %Diff.corr. integral for signal B
568 end
569
570 D_diff_A_FSM_M2 = 1 - 4/pi*(4*sum(D_diff_A_integral_FSM_M2(3:2:end-1)) + ...
        2*sum(D_diff_A_integral_FSM_M2(2:2:end-2)) + D_diff_A_integral_FSM_M2(1) + ...
        D_diff_A_integral_FSM_M2(length(theta)))*h/3; %Diff.corr for signal A
571 D_diff_B_FSM_M2 = 1 - 4/pi*(4*sum(D_diff_B_integral_FSM_M2(3:2:end-1)) + ...
        2*sum(D_diff_B_integral_FSM_M2(2:2:end-2)) + D_diff_B_integral_FSM_M2(1) + ...
        D_diff_B_integral_FSM_M2(length(theta)))*h/3; %Diff.corr for signal B
572
```

```
573  phase_diff_A_FSM_M2 = angle(D_diff_A_FSM_M2); %Angle of diff.corr for signal A
574  t_diff_A_FSM_M2 = -phase_diff_A_FSM_M2./w; %Time shift due to diff.corr for signal A
575
576  phase_diff_B_FSM_M2 = angle(D_diff_B_FSM_M2); %Angle of diff.corr for signal B
577  t_diff_B_FSM_M2 = -phase_diff_B_FSM_M2./w; %Time shift due to diff.corr for signal B
578
579
580  %% Speed of sound calculations (with diffraction correction) %%
581
582  %Calculating the speed of sound using zerocrossing method
583  c_ZC_corr_M1 = 2*L / ((Deltat) - (t_diff_B_zc_M1 - t_diff_A_zc_M1));
584  c_ZC_corr_M2 = 2*L / ((Deltat) - (t_diff_B_zc_M2 - t_diff_A_zc_M2));
585
586
587  %Calculating speed of sound using Fourier spectrum method
588  c_FSM_corr_M1 = -4*pi*freq*L./(theta_FSM - (phase_diff_B_FSM_M1 - phase_diff_A_FSM_M1));
589  c_FSM_corr_M2 = -4*pi*freq*L./(theta_FSM - (phase_diff_B_FSM_M2 - phase_diff_A_FSM_M2));
590
591
592
593
594
595  %% For uncertainty calculations %%
596  t_corr_ZC_M1 = t_diff_B_zc_M1 - t_diff_A_zc_M1; %Correction term in zerocrossing method ...
         using Method 1
597  t_corr_ZC_M2 = t_diff_B_zc_M2 - t_diff_A_zc_M2; %Correction term in zerocrossing method ...
         using Method 2
598  t_corr_FSM_M1 = t_diff_B_FSM_M1 - t_diff_A_FSM_M1; %Correction term in Fourier spectrum ...
         method using Method 1
599  t_corr_FSM_M2 = t_diff_B_FSM_M2 - t_diff_A_FSM_M2; %Correction term in Fourier spectrum ...
         method using Method 2
600
601
602  [ppm_c_ZC_M1, ppm_c_ZC_M2, ppm_c_FSM_M1, ppm_c_FSM_M2, ppm_c_Frey, ppm_c_Chen] = ...
         Uncertainty_calculation(L_0, T, T_0, alpha_T, K_T,P_0, d_rho_d_T, d_rho_d_S, ...
         d_c_d_PG, d_c_d_T, d_c_d_P, d_c_d_T2, d_c_d_S, rho, P, u_t0, std_Deltat, Deltat, ...
         t_corr_ZC_M1, t_corr_ZC_M2, t_corr_FSM_M1, t_corr_FSM_M2,c_ZC_corr_M1, ...
         c_ZC_corr_M2, c_FSM_corr_M1, c_FSM_corr_M2, c_Frey, c_Chen);
```

E.3.5   Uncertainty_calculation.m

```
1   % This script calculates the uncertainties associated with the sound velocities
2   % found in SOS_calculation.m
3
4   %%% Joachim Gjesdal Kristensen, Last edited: 14.05.22 %%%
5
6
7   function [ppm_c_ZC_M1, ppm_c_ZC_M2, ppm_c_FSM_M1, ppm_c_FSM_M2, ppm_c_Frey, ppm_c_Chen] ...
         = Uncertainty_calculation(L_0, T, T_0, alpha_T, K_T,P_0, d_rho_d_T, d_rho_d_S, ...
         d_c_d_PG, d_c_d_T, d_c_d_P, d_c_d_T2, d_c_d_S, rho, P, u_t0, std_Deltat, Deltat, ...
         t_corr_ZC_M1, t_corr_ZC_M2, t_corr_FSM_M1, t_corr_FSM_M2,c_ZC_corr_M1, ...
         c_ZC_corr_M2, c_FSM_corr_M1, c_FSM_corr_M2, c_Frey, c_Chen);
8
9   %% Uncertainty in length measurements
10
11  u_L0_caliper = 0.03e-3; %Uncertainty in caliper, k = 2
12  u_L0_resolution = 0.01e-3; %Uncertainty due to caliper resolution, k = 2
13  u_L0_repeatability = 0.0021e-3; %Uncertainty due to repeatability of measurements, k = 2
14  u_L0_surface = 0.0011e-3; %Uncertainty due to roughness and orietation of transducer ...
         surfaces, k = 1
15
16  uc_L0_68 = sqrt((u_L0_caliper/2)^2 + (u_L0_resolution/2)^2 + (u_L0_surface)^2 + ...
         (u_L0_repeatability)^2); %Combined standard uncertainty of L_0
17  uc_L0_95 = 2*uc_L0_68; %Expanded uncertainty (95% confidence level, k = 2)
18  rel_uc_L0_95 = uc_L0_95 / L_0; %Relative expanded uncertainty (95% confidence level, k ...
         = 2)
19  ppm_L0 = rel_uc_L0_95 * 10^6; %Relative expanded uncertainty (95% confidence level, k = ...
         2) in ppm
20
21
22
23  %% Uncertainty in temperature measurements
24
25  u_T_PT100 = 0.15 + 0.002*T; %Uncertainty in temp. sensor. Class A accuracy. k = 2
26  u_T_drift = 0.05; %Uncertainty due to drift in temp sensor, k = 2
27  u_T_refPT100 = 0.001*T + 0.02; %Uncertainty in reference temp. sensor.
28  u_T_refdrift = 0.05; %Uncertainty due to drift in reference temp sensor, k = 2
29  if T > 28
30      u_T_scanner = 0.005 + 0.003*(T-28) + 0.15; %Uncertainty of Fluke 1586A scanner, k = 2
31  else
32      u_T_scanner = 0.005 + 0.15; %Uncertainty of Fluke 1586A scanner, k = 2
33  end
34  u_T_dev = 0.0003079*T^2 - 0.03288*T + 0.6663; %Deviation between referense temp. sensor ...
         and calibrated temp. sensor. Found from curve fitting, k = 2
35  u_T_rtdusb = 0.05; %Uncertainty in RTD-USB adapter, k = 2
36  u_T_var = 0.003; %Uncertainty due to observed temp. variation during measurements, k = ...
         sqrt(3)
37
38  uc_T_68 = sqrt((u_T_PT100/2)^2 + (u_T_drift/2)^2 + (u_T_refPT100/2)^2 +...
39      (u_T_refdrift/2)^2 + (u_T_scanner/2)^2 + (u_T_dev/3)^2 + (u_T_rtdusb/2)^2 + ...
         (u_T_var/sqrt(3))^2); %Combined standard uncertainty of L_0
40  uc_T_95 = 2*uc_T_68; %Expanded uncertainty (95% confidence level, k = 2)
41  rel_uc_T_95 = uc_T_95 / T; %Relative expanded uncertainty (95% confidence level, k = 2)
42  ppm_T = rel_uc_T_95 * 10^6; %Relative expanded uncertainty (95% confidence level, k = ...
         2) in ppm
```

```
43
44
45
46  %% Uncertainty in thermal expansion
47  u_alphaT = 4.5e-6; %Uncertainty in linear thermal expansion coeff. k = sqrt(3)
48  u_DeltaT = sqrt(uc_T_68^2 + 0.2^2); %Uncertainty in the temperature difference \Delta ...
        T, k = 1
49
50  Delta_T = T - T_0; %Temperature difference
51
52  uc_KT_68 = sqrt((Delta_T*(u_alphaT/sqrt(3))/2)^2 + (alpha_T*(u_DeltaT))^2); %Combined ...
        standard uncertainty of L_0
53  uc_KT_95 = 2*uc_KT_68; %Expanded uncertainty (95% confidence level, k = 2)
54  rel_uc_KT_95 = uc_KT_95 / K_T; %Relative expanded uncertainty (95% confidence level, k ...
        = 2)
55  ppm_KT = rel_uc_KT_95 * 10^6; %Relative expanded uncertainty (95% confidence level, k = ...
        2) in ppm
56
57
58
59  %% Uncertainty in pressure measurements
60  u_P0_barometer = 0.00015*P_0; %Uncertainty in barometer, k = 2
61  u_P0_resolution = 0.00001; %Uncertainty due to resolution of barometer, k = 2
62  u_P0_var = 5e-5; %Uncertainty due to variation in pressure during measurements, k = sqrt(3)
63  u_S = 1e-4; %Uncertainty due to scale resolution for salinity adjustments, k = 1
64  u_h = sqrt((u_L0_caliper/2)^2 + (u_L0_resolution/2)^2 + (u_L0_repeatability/2)^2); ...
        %Uncertainty due to transducer depth, k = 1
65
66  g = 9.819481148; %Gravitational acceleration [m/s2]
67  h = 29.5e-3; %Transducer depth [m]
68
69  uc_P_68 = sqrt((u_P0_barometer/2)^2 + (u_P0_resolution/2)^2 + (u_P0_var/sqrt(3))^2 + ...
        (10e-5*g*h*d_rho_d_T*(uc_T_95/2))^2 + ...
70      (10e-5*g*h*d_rho_d_S*u_S)^2 + (10e-5*rho*g*u_h)^2); %Combined standard uncertainty ...
        of P
71  uc_P_95 = uc_P_68*2; %Expanded uncertainty (95% confidence level, k = 2)
72  rel_uc_P_95 = uc_P_95 / P; %Relative expanded uncertainty (95% confidence level, k = 2)
73  ppm_P = rel_uc_P_95 * 10^6; %Relative expanded uncertainty (95% confidence level, k = ...
        2) in ppm
74
75
76
77
78  %% Uncertainty in transit time
79
80  u_Deltat_osc = 4e-10; %Uncertainty due to oscilloscope resolution, k = 2
81  u_Deltat_var = std_Deltat; %Uncertainty due to time variation between zerocrossings, k ...
        = 1
82  u_Deltat_cohnoise = 1.3235e-9; %Uncertainty due to coherent noise, k = 2
83  u_Deltat_dis = u_t0; %Uncertainty due to descretization of signals, k = 2
84  u_Deltat_waterbath = 1e-10; %Uncertainty due to water bath, k = 1
85  u_Deltat_filt = 1.15e-9; %Uncertainty due to filtering, k = 1
86  u_Deltat_trunc = 7.868e-10; %Uncertainty due to truncating the signal, k = 1
87
88  %%% ZCM:
89  uc_Deltat_68_ZC = sqrt((u_Deltat_osc/2)^2 + u_Deltat_var^2 + u_Deltat_filt^2 ...
90      +(u_Deltat_cohnoise/2)^2 + (u_Deltat_dis/2)^2 + u_Deltat_waterbath^2); %Combined ...
        standard uncertainty of Deltat
91  uc_Deltat_95_ZC = uc_Deltat_68_ZC*2; %Expanded uncertainty (95% confidence level, k = 2)
92  rel_uc_Deltat_95_ZC = uc_Deltat_95_ZC / Deltat; %Relative expanded uncertainty (95% ...
        confidence level, k = 2)
93  ppm_Deltat_ZC = rel_uc_Deltat_95_ZC * 10^6; %Relative expanded uncertainty (95% ...
        confidence level, k = 2) in ppm
94
95  %%% FSM:
96  uc_Deltat_68_FSM = sqrt((u_Deltat_osc/2)^2 + u_Deltat_trunc^2 + u_Deltat_filt^2 ...
97      +(u_Deltat_cohnoise/2)^2 + (u_Deltat_dis/2)^2 + u_Deltat_waterbath^2); %Combined ...
        standard uncertainty of Deltat
98  uc_Deltat_95_FSM = uc_Deltat_68_FSM*2; %Expanded uncertainty (95% confidence level, k = 2)
99  rel_uc_Deltat_95_FSM = uc_Deltat_95_FSM / Deltat; %Relative expanded uncertainty (95% ...
        confidence level, k = 2)
100 ppm_Deltat_FSM = rel_uc_Deltat_95_FSM * 10^6; %Relative expanded uncertainty (95% ...
        confidence level, k = 2) in ppm
101
102
103
104 %% Uncertainty in correction term (uncertainty due to diffraction correction)
105
106 u_tcorr_dif_M1 = 0.02386e-6; %Uncertainty due to diffraction correction, k = 1 due to ...
        limited measurements of a_eff
107 u_tcorr_dif_M2 = 0.00734e-6; %Uncertainty due to diffraction correction, k = 1 due to ...
        limited measurements of a_eff
108
109 uc_tcorr_68_M1 = sqrt(u_tcorr_dif_M1^2); %Combined standard uncertainty of tcorr
110 uc_tcorr_95_M1 = uc_tcorr_68_M1*2; %Expanded uncertainty (95% confidence level, k = 2)
111 uc_tcorr_68_M2 = sqrt(u_tcorr_dif_M2^2); %Combined standard uncertainty of tcorr
112 uc_tcorr_95_M2 = uc_tcorr_68_M2*2; %Expanded uncertainty (95% confidence level, k = 2)
113
114 rel_uc_tcorr_95_ZC_M1 = uc_tcorr_95_M1 / t_corr_ZC_M1; %Relative expanded uncertainty ...
        (95% confidence level, k = 2)
115 rel_uc_tcorr_95_ZC_M2 = uc_tcorr_95_M2 / t_corr_ZC_M2; %Relative expanded uncertainty ...
        (95% confidence level, k = 2)
116 rel_uc_tcorr_95_FSM_M1 = uc_tcorr_95_M1 / t_corr_FSM_M1; %Relative expanded uncertainty ...
        (95% confidence level, k = 2)
117 rel_uc_tcorr_95_FSM_M2 = uc_tcorr_95_M2 / t_corr_FSM_M2; %Relative expanded uncertainty ...
        (95% confidence level, k = 2)
118
119 ppm_tcorr_ZC_M1 = rel_uc_tcorr_95_ZC_M1 * 10^6; %Relative expanded uncertainty (95% ...
        confidence level, k = 2) in ppm
120 ppm_tcorr_ZC_M2 = rel_uc_tcorr_95_ZC_M2 * 10^6; %Relative expanded uncertainty (95% ...
        confidence level, k = 2) in ppm
121 ppm_tcorr_FSM_M1 = rel_uc_tcorr_95_FSM_M1 * 10^6; %Relative expanded uncertainty (95% ...
        confidence level, k = 2) in ppm
```

```
122  ppm_tcorr_FSM_M2 = rel_uc_tcorr_95_FSM_M2 * 10^6; %Relative expanded uncertainty (95% ...
         confidence level, k = 2) in ppm
123
124
125
126
127  %% Uncertainty in measured sound velocity
128
129  d_c_d_L0_ZC_M1 = 2*K_T/(Deltat - t_corr_ZC_M1);
130  d_c_d_KT_ZC_M1 = 2*L_0/(Deltat - t_corr_ZC_M1);
131  d_c_d_Deltat_ZC_M1 = -2*K_T*L_0/(Deltat - t_corr_ZC_M1)^2;
132  d_c_d_tcorr_ZC_M1 = 2*K_T*L_0/(Deltat - t_corr_ZC_M1)^2;
133
134  d_c_d_L0_ZC_M2 = 2*K_T/(Deltat - t_corr_ZC_M2);
135  d_c_d_KT_ZC_M2 = 2*L_0/(Deltat - t_corr_ZC_M2);
136  d_c_d_Deltat_ZC_M2 = -2*K_T*L_0/(Deltat - t_corr_ZC_M2)^2;
137  d_c_d_tcorr_ZC_M2 = 2*K_T*L_0/(Deltat - t_corr_ZC_M2)^2;
138
139  d_c_d_L0_FSM_M1 = 2*K_T/(Deltat - t_corr_FSM_M1);
140  d_c_d_KT_FSM_M1 = 2*L_0/(Deltat - t_corr_FSM_M1);
141  d_c_d_Deltat_FSM_M1 = -2*K_T*L_0/(Deltat - t_corr_FSM_M1)^2;
142  d_c_d_tcorr_FSM_M1 = 2*K_T*L_0/(Deltat - t_corr_FSM_M1)^2;
143
144  d_c_d_L0_FSM_M2 = 2*K_T/(Deltat - t_corr_FSM_M2);
145  d_c_d_KT_FSM_M2 = 2*L_0/(Deltat - t_corr_FSM_M2);
146  d_c_d_Deltat_FSM_M2 = -2*K_T*L_0/(Deltat - t_corr_FSM_M2)^2;
147  d_c_d_tcorr_FSM_M2 = 2*K_T*L_0/(Deltat - t_corr_FSM_M2)^2;
148
149
150  uc_c_68_ZC_M1 = sqrt((d_c_d_L0_ZC_M1*uc_L0_68)^2 + (d_c_d_tcorr_ZC_M1*uc_tcorr_68_M1)^2 ...
         + ...
151      (d_c_d_Deltat_ZC_M1*uc_Deltat_68_ZC)^2 + (d_c_d_KT_ZC_M1*uc_KT_68)^2); %Combined ...
             standard uncertainty of tcorr
152  uc_c_95_ZC_M1 = uc_c_68_ZC_M1*2; %Expanded uncertainty (95% confidence level, k = 2)
153  rel_uc_c_95_ZC_M1 = uc_c_95_ZC_M1 / c_ZC_corr_M1; %Relative expanded uncertainty (95% ...
         confidence level, k = 2)
154  ppm_c_ZC_M1 = rel_uc_c_95_ZC_M1 * 10^6; %Relative expanded uncertainty (95% confidence ...
         level, k = 2) in ppm
155
156  uc_c_68_ZC_M2 = sqrt((d_c_d_L0_ZC_M2*uc_L0_68)^2 + (d_c_d_tcorr_ZC_M2*uc_tcorr_68_M2)^2 ...
         + ...
157      (d_c_d_Deltat_ZC_M2*uc_Deltat_68_ZC)^2 + (d_c_d_KT_ZC_M2*uc_KT_68)^2); %Combined ...
             standard uncertainty of tcorr
158  uc_c_95_ZC_M2 = uc_c_68_ZC_M2*2; %Expanded uncertainty (95% confidence level, k = 2)
159  rel_uc_c_95_ZC_M2 = uc_c_95_ZC_M2 / c_ZC_corr_M2; %Relative expanded uncertainty (95% ...
         confidence level, k = 2)
160  ppm_c_ZC_M2 = rel_uc_c_95_ZC_M2 * 10^6; %Relative expanded uncertainty (95% confidence ...
         level, k = 2) in ppm
161
162  uc_c_68_FSM_M1 = sqrt((d_c_d_L0_FSM_M1*uc_L0_68)^2 + ...
         (d_c_d_tcorr_FSM_M1*uc_tcorr_68_M1)^2 + ...
163      (d_c_d_Deltat_FSM_M1*uc_Deltat_68_FSM)^2 + (d_c_d_KT_FSM_M1*uc_KT_68)^2); %Combined ...
             standard uncertainty of tcorr
164  uc_c_95_FSM_M1 = uc_c_68_FSM_M1*2; %Expanded uncertainty (95% confidence level, k = 2)
165  rel_uc_c_95_FSM_M1 = uc_c_95_FSM_M1 / c_FSM_corr_M1; %Relative expanded uncertainty ...
         (95% confidence level, k = 2)
166  ppm_c_FSM_M1 = rel_uc_c_95_FSM_M1 * 10^6; %Relative expanded uncertainty (95% ...
         confidence level, k = 2) in ppm
167
168  uc_c_68_FSM_M2 = sqrt((d_c_d_L0_FSM_M2*uc_L0_68)^2 + ...
         (d_c_d_tcorr_FSM_M2*uc_tcorr_68_M2)^2 + ...
169      (d_c_d_Deltat_FSM_M2*uc_Deltat_68_FSM)^2 + (d_c_d_KT_FSM_M2*uc_KT_68)^2); %Combined ...
             standard uncertainty of tcorr
170  uc_c_95_FSM_M2 = uc_c_68_FSM_M2*2; %Expanded uncertainty (95% confidence level, k = 2)
171  rel_uc_c_95_FSM_M2 = uc_c_95_FSM_M2 / c_FSM_corr_M2; %Relative expanded uncertainty ...
         (95% confidence level, k = 2)
172  ppm_c_FSM_M2 = rel_uc_c_95_FSM_M2 * 10^6; %Relative expanded uncertainty (95% ...
         confidence level, k = 2) in ppm
173
174
175
176
177  %% Uncertainty in theoretical sound velocity in distilled water
178
179  u_c_Frey_model = 0.05/100 * c_Frey; % Uncertainty in Frey's formula for theoretical ...
         sound velocity in distilled water, k = 2
180
181  uc_c_Frey_68 = sqrt((d_c_d_PG*uc_P_68)^2 + (d_c_d_T*uc_T_68)^2 + (u_c_Frey_model/2)^2); ...
         %Combined standard uncertainty of c_Frey
182  uc_c_Frey_95 = uc_c_Frey_68*2; %Expanded uncertainty (95% confidence level, k = 2)
183  rel_uc_c_Frey_95 = uc_c_Frey_95 / c_Frey; %Relative expanded uncertainty (95% ...
         confidence level, k = 2)
184  ppm_c_Frey = rel_uc_c_Frey_95 * 10^6; %Relative expanded uncertainty (95% confidence ...
         level, k = 2) in ppm
185
186
187
188
189  %% Uncertainty in theoretical sound velocity in seawater
190  u_S_scale = 1e-4; % Uncertainty in the scale used to adjust salinity
191  u_c_Chen_model = 0.15; % Uncertainty in the UNESCO formula for theoretical sound ...
         velocity in seawater
192
193  uc_c_Chen_68 = sqrt((d_c_d_P*uc_P_68)^2 + (d_c_d_T2*uc_T_68)^2 + ...
194      (d_c_d_S*u_S_scale)^2 + (u_c_Chen_model)^2); %Combined standard uncertainty of c_Chen
195  uc_c_Chen_95 = uc_c_Chen_68*2; %Expanded uncertainty (95% confidence level, k = 2)
196  rel_uc_c_Chen_95 = uc_c_Chen_95 / c_Chen; %Relative expanded uncertainty (95% ...
         confidence level, k = 2)
197  ppm_c_Chen = rel_uc_c_Chen_95 * 10^6; %Relative expanded uncertainty (95% confidence ...
         level, k = 2) in ppm
198
199
200  %end
```